University of Potsdam

Doctoral Thesis

Source parameters of the major historical earthquakes in the Tien-Shan region from the late 19^{th} to the early 20^{th} century

By

Galina Kulikova

A cumulative thesis submitted in fulfilment of the requirements for the degree of "doctor rerum naturalium"
(Dr. rer. nat.)

in the

Institute of Earth and Environmental Science

Faculty of Science

February 2016

Published online at the
Institutional Repository of the University of Potsdam:
URN urn:nbn:de:kobv:517-opus4-88370
http://nbn-resolving.de/urn:nbn:de:kobv:517-opus4-88370

Declaration of Authorship

I, Galina Kulikova, declare that this thesis titled, 'Source parameters of the major historical earthquakes in the Tien-Shan region from the late 19^{th} to the early 20^{th} century' and the work presented in it are my own. I confirm that:

- This work was done wholly while in candidature for a research (Dr. rer. nat.) degree at the University of Potsdam.
- To my knowledge, no any part of this thesis has previously been submitted for a degree or any other qualification at this University or any other institution.
- Where I have consulted the published work of others, this is always clearly attributed.
- Where I have quoted from the work of others, the source is always given. With the exception of such quotations, this thesis is entirely my own work.
- I have acknowledged all main sources of help.
- Where the thesis is based on work done by myself jointly with others, I have made clear exactly what was done by others and what I have contributed myself.

Declaration of Authorship for Publications

For the three publications presented in this thesis the author did the following:

1.
   - collected and digitized the data
   - developed the software codes for processing methods
   - analyzed the results
   - wrote the complete manuscript
2.
   - collected and digitized the data
   - adjusted the existing software codes for landslide source modeling
   - analyzed of the results
   - wrote 90% of the manuscript
3.
   - described previously published studies and the current seismicity
   - translated the original reports from Russian
   - digitized the seimogram and prepared the corresponding figures and tables
   - wrote the corresponding parts of the paper, about 40%

Author signature:
Galina Kulikova

Supervisor signature:
apl. Prof. Dr. Frank Krüger

"You know me as a very smart man. Don't you think that if I were wrong, I would know it?"

Sheldon Cooper

Abstract

The Tien-Shan and the neighboring Pamir region are two of the largest mountain belts in the world. Their deformation is dominated by intermontane basins bounded by active thrust and reverse faulting. The Tien-Shan mountain belt is characterized by a very high rate of seismicity along its margins as well as within the Tien-Shan interior. The study area of the here presented thesis, the western part of the Tien-Shan region, is currently seismically active with small and moderate sized earthquakes. However, at the end of the 19th beginning of the 20th century, this region was struck by a remarkable series of large magnitude (M>7) earthquakes, two of them reached magnitude 8.

Those large earthquakes occurred prior to the installation of the global digital seismic network and therefore were recorded only by analog seismic instruments. The processing of the analog data brings several difficulties, for example, not always the true parameters of the recording system are known. Another complicated task is the digitization of those records - a very time-consuming and delicate part. Therefore a special set of techniques is developed and modern methods are adapted for the digitized instrumental data analysis.

The main goal of the presented thesis is to evaluate the impact of large magnitude M≥7.0 earthquakes, which occurred at the turn of 19th to 20th century in the Tien-Shan region, on the overall regional tectonics. A further objective is to investigate the accuracy of previously estimated source parameters for those earthquakes, which were mainly based on macroseismic observations, and re-estimate them based on the instrumental data. An additional aim of this study is to develop the tools and methods for faster and more productive usage of analog seismic data in modern seismology.

In this thesis, the ten strongest and most interesting historical earthquakes in Tien-Shan region are analyzed. The methods and tool for digitizing and processing the analog seismic data are presented. The source parameters of the two major M≥8.0 earthquakes in the Northern Tien-Shan are re-estimated in individual case studies. Those studies are published as peer-reviewed scientific articles in reputed journals. Additionally, the Sarez-Pamir earthquake and its connection with one of the largest landslides in the world, Usoy landslide, is investigated by seismic modeling. These results are also published as a research paper.

With the developed techniques, the source parameters of seven more major earthquakes in the region are determined and their impact on the regional tectonics was investigated. The large magnitudes of those earthquakes are confirmed by instrumental data. The focal mechanism of these earthquakes were determined providing evidence for responsible faults or fault systems.

Zusammenfassung

Der Tien-Shan und die angrenzende Pamir Region sind zwei der größten Gebirgszüge der Welt. Deformation findet hier hauptsächlich an aktiven Auf- und Abschiebungszonen statt, welche intermontane Becken umschließen. Der Tien-Shan Gebirgszug ist sowohl an den Störungszonen als auch innerhalb der Becken durch eine hohe Seismizitätsrate charakterisiert. Das Untersuchungsgebiet der hier präsentierten Dissertation, der westliche Bereich der Tien-Shan Region, ist in den letzten Jahrzehnten durch das Auftreten kleiner und mittlerer Erdbeben gekennzeichnet. Jedoch wurde diese Region an der Wende zum 20. Jahrhundert von einer Reihe außergewöhnlich starker Erdbeben (M>7) heimgesucht. Zwei von ihnen erreichten sogar die Magnitude 8.

Diese starken Erdbeben ereigneten sich vor der Installation eines globalen, digitalen seismischen Netzwerks und wurden daher nur von analogen seismischen Instrumenten aufgezeichnet. Die Bearbeitung von analogen Daten birgt mehrere Schwierigkeiten, z.B. sind die wahren Werte der Instrumentencharakterisitik nicht immer bekannt. Ein weiterer komplizierter Teil ist die Digitalisierung dieser Aufzeichnungen, die sehr zeitaufwändig und diffizil ist. Um diesen und weiteren Schwierigkeiten zu begegnen, wurden in der vorliegenden Arbeit spezielle Techniken zur Digitalisierung analoger, seismischer Daten und moderne Methoden der Datenanalyse speziell für digitalisierte, analoge Daten adaptiert.

Das Hauptziel der hier präsentierten Dissertation ist die Auswertung der Auswirkungen von starken Erdbeben (Magnitude 7.0) auf die regionale Tektonik, welche zur Jahrhundertwende zum 20. Jahrhundert in der Tian Shan Region stattgefunden haben. Eine weitere Zielsetzung ist die Überprüfung der Genauigkeit von früher bestimmten Herdparametern dieser Erdbeben, welche hauptsächlich auf makroseismischen Untersuchungen beruhen, und deren erneute Bestimmung mithilfe instrumenteller Daten. Außerdem sollen in dieser Arbeit die notwendigen Werkzeuge und Methoden für die schnellere und produktivere Nutzung von analogen, seismischen Daten für zukünftige Studien in der modernen Seismologie entwickelt werden.

In dieser Arbeit werden die zehn stärksten und interessantesten historischen Erdbeben der Tien-Shan Region analysiert. Es werden Methoden und Werkzeuge für die Digitalisierung und Bearbeitung von analogen seismischen Daten vorgestellt. Die Herdparameter der zwei bedeutendsten Erdbeben mit M∼8 im nördlichen Tien-Shan werden erneut bestimmt und in separaten, detaillierten Fallstudien behandelt. Diese Studien sind als wissenschaftlich begutachtete Artikel in renommierten Fachzeitschriften publiziert. Zusätzlich wurde das Sarez-Pamir Erdbeben und seine Verbindung mit einem der größten Erdrutsche der Welt, dem Usoy Erdrutsch, basierend auf seismischer Modellierung untersucht. Diese Ergebnisse sind ebenfalls in einem wissenschaftlichen Aufsatz veröffentlicht.

Mit den hier entwickelten Methoden wurden die Herdparameter der sieben stärksten Erdbeben in der Region bestimmt und ihre Auswirkung auf die regionale Tektonik untersucht. Die Magnituden dieser Erdbeben wurden mit Hilfe instrumental aufgezeichneter Daten bestätigt. Die Herdflächenlösungen dieser Erdbeben wurden bestimmt und geben Hinweise auf die möglichen verantwortlichen Störungen.

Acknowledgements

The successful completion of this thesis was only possible with help and support of many people whom I sincerely acknowledge. I would like to express my deepest gratitude to my supervisor apl. Prof. Dr. Frank Krüger for being great adviser during my PhD. I would like to thank Frank Krüger for encouraging my research and for allowing me to grow as a research scientist; for sharing with me his wide knowledge in the field of geophysics and seismology; and for supporting my ideas with enthusiasms. I also thank Prof. Dr. Torsten Dahm, Prof. Dr. Frank Scherbaum, Dr. Matthias Ohrnberger and Dr. Angela Landgraf for additional advice on my research and on my career.

This PhD work was a part of PROGRESS project (http: //www.earth-in-progress.de) and I sincerely thank the German Federal Ministry of Education and Research for the financial support. Moreover I would like to express my gratitude to Prof. Dr. Manfred Strecker, apl. Prof. Dr. Frank Krüger and Dr. Angela Landgraf for providing extra financial support. I also thank Graduate School of Potsdam University for ″Completion scholarship″, Faculty of Mathematik and Natural Sciences of Potsdam University for ″Bridge scholarship″, and TIPTIMON project, which provided additional financial support during my PhD work.

I would like to express my deepest gratitude to all the people who helped to collect the historical seismograms (the names are presented in the Table *F.1*, Appendix *F*)- without you this work would not be possible. Also I would like to express my great appreciation to Dr James Dewey and Dr Josep Batllo for their valuable and constructive suggestions during my work with historical data.

A special thanks goes to my family especially to my dearest aunt Natalya and my sister Tamara who always loved and supported me extremely and unconditionally; who always found encouraging words and made me laugh at problems; who also applied their own language skills and knowledge in geophysics to help me in my progress; and who always believed in my success much more that I did myself.

I would like to express the greatest appreciation to my most beloved boyfriend Lutz Ehlert; who has been great moral support for me; who has comforted me at the moments of weakness and encouraged to continue towards my goal no matter what; who has advised and helped in developing my programming skills; and who has sacrificed his own vacation and leisure time for the sake of my PhD work.

I would also like to thank my friends; Olga Zakharova, Polina Kim, Antonia Runge, Jhosnella Sayago, Kunduz Mendibaeva who supported and encouraged me to strive towards my goal. I am particularly grateful to my dear friends; Xeniya Kozina, Stefanie Donner and Yvonne Qualao, who helped me in writing with their language correction, and also gave advice in developing my scientific knowledge and skills.

Additional thanks goes to my officemates; Tobias Müller-Wrana, Sanjay Singh Bora, Christian Molkenthin, Katrin Hannemann and Agostiny-Marrios Lontsi, for supporting nice and friendly working atmosphere in the office and for fun moments we had together. I would also like to thank my colleagues: Ines Münch, Daniel Vollmer, Birgit Fabian and Cornelia Becker, for their technical and administration support; and Annabel Händel, Conny Hammer, Marius Kriegerowski, Nicolas Kühn, Carsten Riggelsen and Brigitte Knapmeyer-Endrun; for being the greatest working group ever, where friendliness, respect and scientific encouragement prevail. My particular gratitude is expressed to the best secretary of all times Tanja Klaka-Tauscher, for helping with all the office work and documents preparation, and for being a great friend and adviser in daily life.

Symbols

M_0	scalar seismic moment	N·m
M_w	moment magnitude	
m_B	body wave magnitude	
M_S	surface wave magnitude	
L	rupture length	m
W	rupture width	m
A	rupture area	m^2
μ	shear modulus	N/m^2
D	slip	m
V	case magnification of an instrument	
T_0	free period of an instrument	s
h	damping constant	
ω	angular frequency	$rads^{-1}$

THIS THESIS IS DEDICATED TO MY DEAREST AND MOST BELOVED GRANDPARENTS, WHO PASSED AWAY DURING MY PHD WORK.

YOU WILL ALWAYS LIVE IN MY MEMORY AND MY HEART.

Contents

List of Figures

List of Tables

Chapter 1

Introduction

The deformation of the Tien-Shan mountain belt is characterized by a high level of seismic activity. Currently this seismic activity is confined to weak and moderate sized earthquakes. However at the turn of 19th to 20th century the region was struck by a remarkable series of major earthquakes, two of them likely exceeded magnitude M8.0. Additionally, a number of large M>7.0 earthquakes occurred in the 20th century, before the era of digital seismic records.

The Tien-Shan and the neighboring Pamir region are two of the largest mountain belts in the world, which rose due to the India and Eurasia plates convergence. Active deformation of the Tien-Shan is distributed through the whole intracontinental mountain belt. It consist of intermontane basins bounded by active thrust and reverse faulting. The occurrence of large magnitude (M∼8.0) earthquakes on intracontinental thrust faults is a rare case in seismology which causes particular interest to the Tien-Shans tectonic features (see section *1.2*). Due to complex history and frequent change of the political regimes on this territory it is hard to find a reliable catalog of historical seismic events. *Kalmetieva et al.* [2009] presented a catalog which according to their information is complete for M>6.9 events from 1770. It is seen from this catalog that there was no comparable sequence of major earthquakes in the last ∼250 years. However, the available data are not sufficient to draw any conclusions about the seismic cycle and recurrence intervals. The Tien-Shan can be compared to other regions in the world showing intracontinental seismicity such as Northern India (with well know devastating Gujarat earthquake in 2001), Wenchuan in China (which produced for example the 2008 Sichuan thrust earthquake), the seismic activity in Northern Iran, or the historical strong earthquakes observed in Mongolia. From all these examples only Mongolia has shown strong earthquakes as a sequence throughout 20th century with several M>7.5 earthquakes but unlike Tien-Shan this region is dominated by strike-slip faulting. Other regions have shown intracontinental earthquakes as single and unexpected events.

Continuous seismic recording is an important tool in understanding the kinematics and dynamics of tectonic processes accompanied by earthquakes. However the seismic instrumentry is very young in comparison to the age of geological processes and seismically active structures. The first analog seismic records are a little more then 100 years old, and the valuable modern digital recording started in 1970s. The collection, preservation and digitization of analog seismic records can provide an essential source of information for the detailed study of earthquake source parameters in the last 120 years.

1.1 The major historical earthquakes in the Tien-Shan region

At the end of the 19th century (1885-1889) the Tien-Shan region was struck by three major earthquakes. Later on they were followed by strong M≥7.0 earthquakes continuing through the 20th century (Figure *1.1*). The majority of these earthquakes have been recorded only by analog seismic instruments and the seismograms are only available on paper or microfilms. In order to use these seismic records for earthquake processing they have to be digitized and converted into one of the modern seismic data formats. This procedure is very delicate and requires a large effort to collect the seismograms from different archives worldwide, and additional very time consuming work to digitize the records. Due to this enormous workload in pre-processing the data, comprehensive studies based on the analogue seismic records are rare in modern seismology. As a result, the source parameters of the large earthquakes in the Tien-Shan region remained poorly investigated. All the knowledge about those earthquakes is based on macroseismic observations, seismic bulletins information and geological studies. There have been a few studies trying to determine source information such as depth and focal mechanism of those earthquakes. However, they were based on a limited dataset and the authors themselves admitted their data weaknesses [*Chen & Molnar*, 1977; *Molnar & Ghose*, 2000].

Earthquakes with such a large magnitude must have been recorded by the majority of the existing seismic stations worldwide, and although not all of those seismic records are available nowadays, a proper collection of seismograms for further studies can be obtained. The true information about the source parameters of those historical earthquakes is of crucial importance for the understanding of regional tectonic and deformation processes in the Tien-Shan region. Moreover, this findings are of great interest for the studies aiming to estimate seismic hazard in the region, where nowadays the risk is much higher due to an increase of population by a factor of 50 compared to the beginning of the 1900s.

Each of the major earthquakes shown in Figure *1.1* is fascinating in its own way. Every earthquake is unique and extremely important for the understanding of the deformation process occurring in the Tien-Shan region. Due to the complicated processing of the analogue seismic data this study is limited to the 10 most interesting earthquakes. In the following, the main reasons for including each of these earthquakes into the study are explained.

The Tien-Shan remarkable earthquakes sequence started with the 1885 M6.9 Belovodsk earthquake, which caused severe destruction in the epicenter area and was felt on a long distance, causing also some damage in the capital of Kyrgyzstan, Bishkek. *Kalmetieva et al.* [2009] reported that this earthquake initiated a 20 km long surface rupture and up to 2 m vertical offsets. The occurrence of this earthquake was a turning point for the scientific interest to the Northern Tien-Shan region for the Russian Geographical Society. Subsequently, two years after, when in 1887 the M7.3 Verny earthquake occurred, the first geological expedition was sent to the epicenter region to investigate all the effects of the earthquake. The earthquake was catastrophic for the city of Verny (currently Almaty, former capital of Kazakhstan). It destroyed almost all buildings and caused many casualties [*Nurmagambetov*, 1999]. The results of the geological expedition investigations were then published in a report describing the damage. Till now, this report remains the main source of information for this earthquake [*Mushketov*, 1890].

Unfortunately, the Belovodsk and Verny earthquakes occurred prior to the development of the global seismic instrumentation, and no seismic records are available. The occurrence of the 1885 and 1887 earthquakes initiated the development of "construction rules", which was basically the first seismic code for this seismically active region. Following this seismic code in rebuilding the

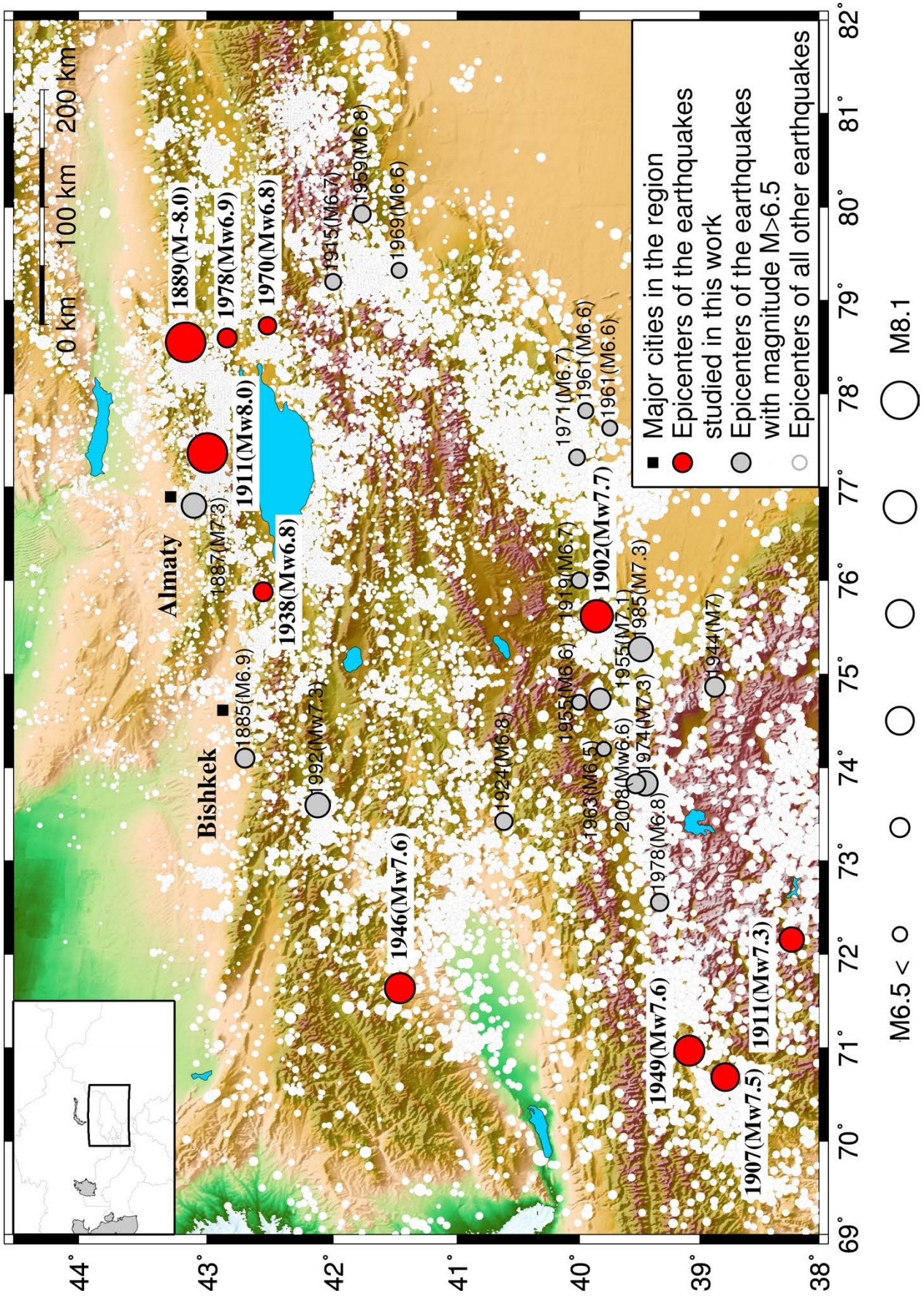
0 km 100 km 200 km
Major cities in the region
Epicenters of the earthquakes studied in this work
Epicenters of the earthquakes with magnitude M>6.5
Epicenters of all other earthquakes
M6.5 < o
M8.1
Almaty
Bishkek
1889(M~8.0)
1978(Mw6.9)
1970(Mw6.8)
1911(Mw8.0)
1938(Mw6.8)
1946(Mw7.6)
1902(Mw7.7)
1949(Mw7.6)
1907(Mw7.5)
1911(Mw7.3)
1887(M7.3)
1885(M6.9)
1992(Mw7.3)
1924(M6.8)
1978(M6.8)
2008(Mw6.6)
1963(M6.5)
1955(M6.6)
1919(M6.7)
1971(M6.7)
1961(M6.6)
1961(M6.6)
1915(M6.7)
1959(M6.8)
1969(M6.6)
1955(M7.1)
1985(M7.3)
1974(M7.3)
1944(M7)
69°
70°
71°
72°
73°
74°
75°
76°
77°
78°
79°
80°
81°
82°
38°
39°
40°
41°
42°
43°
44°

FIGURE 1.1: Topography map of the study area, including south and north Tien-Shan region and part of the Pamir. Red circles mark epicenters of major earthquakes (M>6.8) investigated in this study. They are signed by the year of the earthquake and its magnitude. Gray circles show further strong earthquakes (M>6.5) in the region since 1885 (not included in this study) . White circles show all earthquakes in the region from 1995 until 2009 [*Storchak et al.*, 2013; *Mikhailova et al.*, 2015]

city of Verny considerably lessened the damage caused by the next M8.3 Chilik earthquake in 1889 [*Mushketov*, 1891]. The Chilik earthquake, with its M8.3 magnitude remains the strongest earthquake registered in the Tien-Shan. The earthquake occurred in a sparsely populated area and was not a subject of a particular geological study. However, this earthquake was recorded by an early Rebeur-Paschwitz seismic instrument and the record is available for this study. A detailed study of the Chilik earthquake is presented in Appendix *A* of this work (Publication 3).

The next large earthquake which occurred in the northern Tien-Shan region, is the most remarkable - the 1911 M8.0 Chon-Kemin earthquake. This earthquake brought fascinating changes in the landscape of the mountains between Zailiskey and Kungey Alatau (Figure *1.2*) by producing a ∼200km surface rupture with up to 10 meter vertical offset and numerous landslides. The earthquake killed about people ∼400 [*Nurmagambetov*, 1999] and caused enormous damage to the buildings. The Chon-Kemin earthquake is considered to be the most interesting in the whole sequence and the main time of this PhD work is devoted to this earthquake. All the methods and techniques presented in this work are developed and tested on the Chon-Kemin earthquake dataset. The detailed study of the Chon-Kemin earthquake is presented in Chapter *2* (Publication 1). This publication includes a full description of the methodology developed in this study which is then applied to other earthquakes.

Another remarkable earthquake is the 1911 M7.3 Sarez-Pamir earthquake. Although it is smaller than the Chon-Kemin earthquake it caused as much or even more discussion in the scientific community. This earthquake has been associated with one of the largest landslides in the world. It was even speculated that the earthquake did not take place at all but it was the landslide recorded on the seismograms [*Ambraseys & Bilham*, 2012]. The investigation of the source parameters of the Sarez-Pamir earthquake and a possible solution to this controversy are presented in Chapter *3* (Publication 2). This chapter also includes a more detailed description of the data collection and digitization procedure.

In the final chapter (Chapter *4*) of this work the results of source parameter studies of seven more major earthquakes in the Tien-Shan historical earthquake sequence are presented, including the following earthquakes. The earliest and least investigated earthquake in the Southern Tien-Shan is the 1902 Kashgar (Artux) earthquake. The magnitude for this earthquake differs between M_w7.69 [*Storchak et al.*, 2013] and M_S8.3 [*Fu et al.*, 2010a]. It certainly remains the strongest earthquakes which was recorded on the Tarim and Tien-Shan convergence zone. The next one is the 1938 M6.9 Kemin-Chu earthquake, which occurred on the western edge of the fault responsible for the Chon-Kemin earthquake and is believed to be a late aftershock. Further the 1946 M7.6 Chatkal earthquake is presented in the chapter. Not much is known about this earthquake, however, it is of special importance for understanding the tectonics because it is speculated that the large Talas-Fergana strike-slip fault may be responsible for it. The 1970 M6.8 Sarykamysh and 1978 M6.9 Zhalanash-Tuup earthquakes are also investigated. Although source parameters of those earthquakes are already determined in previous studies, it is interesting to re-determine them with the methods presented here to compare the results and check the method performance. More to the south of the Tien-Shan, at the border to Pamir, two more M>7.0 earthquakes occurred, the 1907

Karatag and the 1949 Khait. However, the knowledge of the source parameters of these earthquakes is very limited. For example, in different catalogs the 1907 earthquake appears with up to 200 km epicenter location differences [*Storchak et al.*, 2013; *Kalmetieva et al.*, 2009]. It is not clear if these events still occurred on the faults in the Tien-Shan or already in the Pamir region [*Schurr et al.*, 2014].

In the two following subsections tan introduction to the tectonics of the study region and a description of the early seismic instruments are given. It is then followed by the main body of the thesis, which is composed by the individual detailed studies in the form of scientific publications devoted to the above mentioned earthquakes.

1.2 Insights into the regional tectonics

The term Tien-Shan region in geological and geophysical studies usually refers to a mountain belt located in Central Asia, which extends more than 2000 km east-west and reaches 300-400 km width (Figure *1.2*, inset map). This mountain belt has remarkable topographic relief characterized by diverse elevation between 450 m and 7000 m [*Nelson et al.*, 1987; *Fu et al.*, 2010a]. In this study I do not consider the whole Tien-Shan region, but restrict the study area to the western part of the Tien-Shan mountain belt. It covers the region in the northwestern part of the India-Eurasia collision zone, including northeastern Pamir to the south, part of the Tarim basin to the southwest and the Tien-Shan mountain belt to the north, with the Issyk-Kul lake region as an eastern border.

In general the current tectonic activity in Central Asia is attributed to India and Eurasia plates collision since the Eocene. The main convergence occurs on major east-west trending strike-slip faults in China and Mongolia [*Molnar & Tapponnier*, 1975]. However, the western part of the Tien-Shan with its numerous thrust-fold belts has been very attractive to the scientists due to the occurrence of several M>8 earthquakes. The Chinese Tien-Shan, more to the East is also known to produce large magnitude historical earthquakes [e.g. M8.3 1906 Malasi earthquake *Molnar & Qidong*, 1984], but they are not included in this study and may be investigated later with the here presented methods.

The Tien-Shan is one of the most rapidly deforming intracontinental regions in the world with about ∼20 mm/yr shortening rate [*Abdrakhmatov et al.*, 1996; *Zubovich et al.*, 2010; *Ischuk et al.*, 2013]. This shortening is expressed as crustal thickening by thrusting and folding within the mountain belt [*Tapponnier & Molnar*, 1979; *Avouac et al.*, 1993]. The mountain belt was formed following the India and Eurasia collision about 1000-2000 km to the south [*Molnar & Tapponnier*, 1975; *Abdrakhmatov et al.*, 2002]. The thrust faults and folds dominating in this region also include a left-lateral strike-slip component associated with clockwise rotation of the Tarim Basin with respect to Eurasia.

The Tien-Shan region remains currently seismically very active with small and moderate sized earthquakes. However, as mentioned above, at the end of 19th beginning of 20th century a number of large earthquakes occurred here. The seismicity is observed across the whole Tien-Shan with earthquake clusters at the plate margins as well as following crustal deformation in the Tien-Shan interior. Modern receiver function analysis [*Vinnik et al.*, 2004] and seismic tomography studies [*Makarov et al.*, 2010] show that the crustal thickness of the Tien-Shan varies from the center of the mountain belt down to the platforms (Tarim Basin, Kazakh platform, Ili Basin etc.). Crustal thickness beneath the central Tien-Shan is about 55–65 km compared to only ∼45 km beneath the Kazakh Platform to the north and the Tarim Basin to the south [*Oreshin et al.*, 2002; *Vinnik et al.*,

2002]. The style and distribution of faulting has been studied based on recent seismicity [*Nelson et al.*, 1987; *Molnar & Ghose*, 2000; *Feld et al.*, 2015]. However, the real tectonic impact of the large earthquakes, which occurred in the last century, is still missing.

1.2.1 The Northern Tien-Shan

To the North the Tien-Shan is bounded by the Kazakh platform, from the Kungey and Zailiskey Alatau ranges in the East to the Ferghana Valley on the west (Figure *1.2*). The northeastern part of this region is dominated by the historically active E-W striking Kemin-Chilik fault which, however, has shown both, sinistral and reverse motion in the past [*Molnar & Tapponnier*, 1975]. This fault controls the whole structure between the Issyk-Kul Basin and the Kazakh Platform and is believed to be responsible for the 1911 M8.0 Chon-Kemin earthquake [*Delvaux et al.*, 2001; *Arrowmith et al.*, 2015; *Kulikova & Krüger*, 2015].

The thrust and reverse faulting dominates along margins of the Kungey and Zailiskey ranges. Deformation here follows the slip along north- and south-convergent thrust and reverse faults, whereas the eastern and north-eastern side of the Issyk-Kul basin show slip on obliquely oriented strike-slip faults [*Selander et al.*, 2012]. The existence of both types of faulting in this region is confirmed by the focal mechanism of the 1978 Zhalanash-Tuup earthquake [*Ekström et al.*, 2012] being mainly a strike-slip event, whereas the 1970 Sarykamysh earthquake, located ∼40 km SSE, shows thrust faulting [*Nelson et al.*, 1987].

The special interest to this part of the Tien-Shan region is additionally caused by occurrence of several earthquakes with unusual depth. In general earthquakes in intracontinental regions are associated with shallow faults bounded to the upper crust. However, in the eastern part of the Northern Tien-Shan region several earthquakes originated in the lower crust or upper mantle, ∼40 km deep [*Alinaghi & Krüger*, 2014].

The western end of the Kemin-Chilik fault structure, characterized by differently oriented thrust faults, is the source of the 1938 M6.8 Kemin-Chu earthquake. However a candidate responsible fault or the focal mechanism for this earthquake are not known. The most western side of the Northern Tien-Shan, i.e. the Fergana valley (Figure *1.2*), shows a transpressional tectonic context due to a combination of shortening and shear mechanisms. This region is dominated by the large ∼600 km long right lateral strike-slip Talas-Fergana fault [(Figure *1.2*) *Molnar & Tapponnier*, 1975; *Ghose et al.*, 1998b] with ∼2 mm/yr slip [*Zubovich et al.*, 2010]. The region along and around this fault is currently active with small and moderate size earthquakes. However, none of these earthquakes have shown strike-slip mechanisms associated with the Talas-Fergana fault [*Nelson et al.*, 1987; *Ghose et al.*, 1998a; *Feld et al.*, 2015]. Hence, the earthquakes are associated with adjoining thrust faults. There have been a suspicion expressed by *Shirokova* [1974] and discussed by *Simpson et al.* [1981] and *Molnar & Qidong* [1984] that the Talas-Fergane fault itself is responsible for the 1946 Chatkal earthquake, but final consent has not been found.

1.2.2 The Southern Tien-Shan Pamir fault zone

The southern Tien-Shan is characterized by two main deformation processes: on the eastern part by the Tarim Basin underthrusting the Tien-Shan; and on the WSW by the Pamir overthrusting it [*Burtman*, 2013]. The underthrusting of the Tarim Basin with respect to the Tien-Shan, explains the differences in the shortening rates, e.g. the western part the Tarim Basin converges with Eurasia at 20±2 mm/yr compared to only 2-6 mm/yr within the Tien Shan. The whole north-western flank

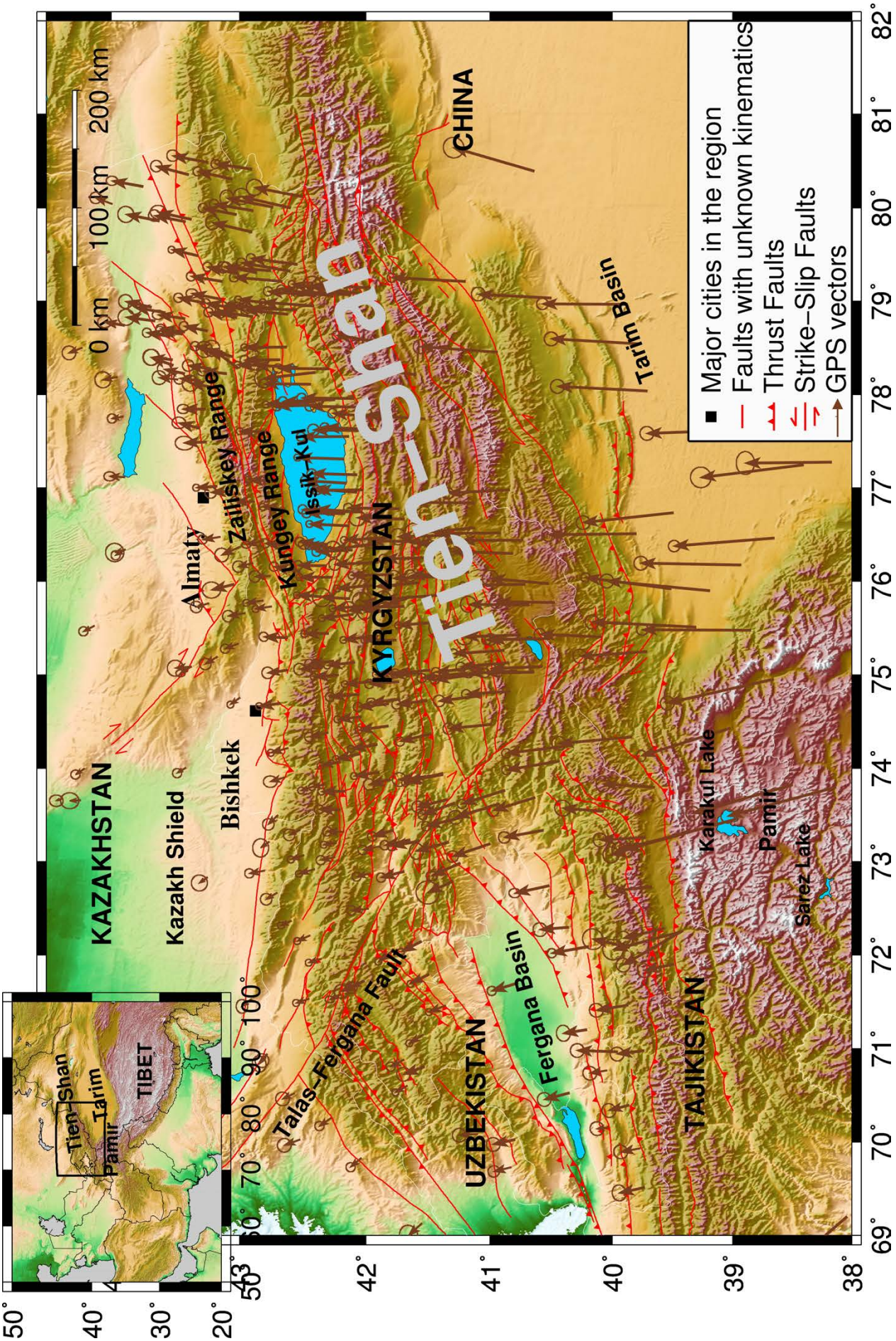
Tien–Shan
KAZAKHSTAN
KYRGYZSTAN
UZBEKISTAN
TAJIKISTAN
CHINA
Kazakh Shield
Bishkek
Almaty
Zailiskey Range
Kungey Range
Issik–Kul
Tarim Basin
Talas–Fergana Fault
Fergana Basin
Karakul Lake
Pamir
Sarez Lake
0 km
100 km
200 km
Major cities in the region
Faults with unknown kinematics
Thrust Faults
Strike–Slip Faults
GPS vectors
Tien–Shan
Tarim
Pamir
TIBET

FIGURE 1.2: Topography map of the study area with main faults marked in red. GPS velocities are relative to Eurasia and taken from *Zubovich et al.* [2010]. Main geological structures are named accordingly. Inset map (top left corner) shows location of the study area on large scale map of Central Asia indicating main geographical features.

of the Tarim Basin is characterized by very high seismicity, with modern earthquake mechanisms showing dominant thrust shallow faulting [<15km depth *Nelson et al.*, 1987; *Ghose et al.*, 1998a; *Ekström et al.*, 2012]. The 1902 ∼M8 (magnitude varies between 7.7 and 8.3 in different sources) Kashgar (Artux) earthquake occurred in the convergence zone at the north-west corner of the Tarim basin (Figure *1.2*). It then was followed by a number of M>6.0 earthquakes in the later years.

The Pamir mountain belt located southwest of the Tarim Basin (between Tarim basin and Tadjik-Afhan depression, (Figure *1.2*) was not initially planned to be included into this study. However, due to the occurrence of the particularly interesting Sarez-Pamir earthquake the study region was extended southward. The formation of Pamir, as well as the Tien-Shan, is attributed to India and Eurasia collision [*Molnar & Tapponnier*, 1975; *Tapponnier & Molnar*, 1979; *Avouac et al.*, 1993; *Fu et al.*, 2010a]. The northward indentation of the Pamir into the Tien-Shan resulted in relative displacement of the Pamir with respect to Tibet by ∼300 km northwards [*Burtman & Molnar*, 1993; *Burtman*, 2013], with current Pamir's convergence with the Tien-Shan of ∼13-15 mm/yr according to modern GPS measurements [*Zubovich et al.*, 2010; *Ischuk et al.*, 2013]. In addition to the shallow crustal seismic activity along the main Pamir thrust and currently active structures [*Schurr et al.*, 2014], the lithospheric deformation in the Pamir and the neighboring Hindu-Kush region cite[]Sippl2013a is accompanied by strong intermediate-depth (up to nearly 300 km) earthquake activity.

Current crustal deformation of the Pamir occurs along a complex mixture of normal, reverse and strike-slip faults. According to *Schurr et al.* [2014] the Pamir′s northern margins are characterized by a number of thrust-fold belts along the Trans Alai range, covering the Alai valley in the region of maximum convergence between Pamir and Tien-Shan (Figure *1.2*). At the very east of the Alai valley, where the Pamir thrust system widens and merges with the Chinese Tien-Shan, two types of faulting are observed: steep, thick-skinned north-east striking reverse faulting and sinistral strike-slip faulting along north-west trending planes, which has been attributed to the counter-clockwise rotation of the Talas-Fergana fault zone. Further west along the Trans Alai, south of the Alai valley, a few thrust earthquakes took place. However, the majority exhibited dextral strike-slip mechanisms on approximately E(SE) trending planes. At the very western edge, where Tien-Shan and Pamir collide and the Pamir thrust system bends southward (Vakhsh and Darvaz faults), the mechanisms of the earthquakes show thrust motion with a slight dextral component. This region is responsible for two large historical earthquakes, the 1907 M7.4 Karatag earthquake and the 1949 M7.4 Khait earthquake [*Storchak et al.*, 2013]. Because of poor epicenter location it is not known if the Vakhsh trust system in the Pamir is responsible for these earthquakes or if they occurred on the faults belonging to the Tien-Shan.

Although the precise epicenter of the 1911 M7.3 Sarez-Pamir earthquake is not exactly known, it is believed to be within the Pamir, not far away from the huge Usoy landslide and the Sarez lake [*Storchak et al.*, 2013; *Ambraseys & Bilham*, 2012]. The seismicity within the Pamir interior is dominated by two main structures. At first the Karakul fault system – a NNE oriented seismic structure, elongated from north-east of the Sarez lake to the NNE, crossing the Karakul lake. According to recent seismicity two types of mechanisms are observed along the Sarez-Karakul fault: a few sinistral strike-slips on the eastern side of the lake Sarez, and mainly sinistral oblique normal faulting on the southern side, the Sarez-Karakul fault system. Another dominant structure

is the fault zone on the east-south-east of the Sarez lake, where a dextral strike-slip fault zone connects the Karakorum fault with the Sarez-Murghab thrust system. It shows two dextral strike-slip earthquakes at the end of the Aksu-Murghab fault zone. From their dimension *Schurr et al.* [2014] identified these two fault structures as the only possible to be responsible for the Sarez-Pamir earthquake based on the large magnitude of the earthquake. The Sarez-Pamir earthquake did not leave any detected surface rupture and the focal mechanism of this earthquake is also not known. More detailed description of the Pamir's tectonic is presented in the Chapter *3* of this work devoted to the Sarez-Pamir earthquake.

1.3 Historical seismic instrumentation

The first attempts to record an earthquake date back to the 132 A.D. in China [*Dewey & Byerly*, 1969; *Batlló*, 2014]. After that, earthquake recording devices design has undergone several development stages in different centuries. This study does not aim to describe the progress of seismic instrumentation and the reader is kindly referred to previously published works [e.g. *Dewey & Byerly*, 1969; *Howell*, 1990; *Ferrari*, 1992; *Batlló*, 2014]. In the following, I present only main working principles and features of a few seismic instruments which operated from the beginning of the 20th century and provided seismograms for this study.

At the end of 19th beginning of 20th century rapid progress began in the development of devices for recording the earth tremors [*Dewey & Byerly*, 1969; *Batlló*, 2014]. The seismographs of this time mainly worked based on the inertia principle and consisted of some kind of pendulum and a system to recored its osculations. Mechanical recording was usually done by a pen placed at the end of the pendulum and scratching a line on a smoked paper. However a pendulum seismograph with mechanical registration was strongly influenced by friction of the pen on the paper and it required a very large mass of the pendulum to reduce this effect [e.g. *Dewey & Byerly*, 1969; *Howell*, 1990; *Ferrari*, 1992; *Schweitzer*, 2003; *Batlló*, 2014].

The first successful recording of ground motion as a function of time was done by a group of English scientist, Milne, Ewing and Gray, working in Japan at the late 1800s [*Dewey & Byerly*, 1969; *Batlló*, 2014]. Their development included common-pendulum and horizontal-pendulum seismographs and a vertical seismometer. None of those records have been collected for this study and the instruments description can be found in other studies [e.g *Milne & Gray*, 1882; *Gray*, 1883; *Ehlert*, 1898a].

The first recording of a distant earthquake belong to Ernst von Rebeur-Paschwitz in 1889 [*Rebeur-Paschwitz*, 1892a,b, 1893, 1895]. The Rebeur-Paschwitz horizontal-pendulum seismometer consisted of 10 cm long pendulum carrying a mass of only 42 grams attached to a rigid frame rotating about two bearings, each consisting of a point pressing into a socket. A mirror attached to the frame reflected a light beam from a lamp through a cylindrical lens to a rotating drum with a photographic paper fixed on it [*Dewey & Byerly*, 1969; *Fréchet & Rivera*, 2012; *Batlló*, 2014]. The Rebeur-Paschwitz seismometer was the first instrument recording on a photographic paper. Unlike the pendulum seismographs with mechanical recording, the photographic recording did not have friction in magnifying and recording. However, despite of this advantage the Rebeur-Paschwitz instrument was not as widely distributed as mechanical recorders due to the high costs of photographic paper. There was just one seismogram from the Rebeur-Paschwitz instrument available for this study. However, this record has provided the means to estimate the magnitude of the largest earthquake in the Tien-Shan region (see Chapter *A*).

The most widely distributed and successfully used early seismic instrument was the Emil Wiechert′s inverted-pendulum seismometer. Wiechert has started his development in the late 1890s and was the first one to implement a viscously-damped pendulum as a sensor in 1898 [*Dewey & Byerly*, 1969; *Agnew*, 2002; *Schweitzer*, 2003]. He afterwards modified his instrument and the final version of Wiechert′s seismometer was introduced in 1904 [*Wiechert*, 1903, 1904]. The instrument functioned as an inverted pendulum stabilized by a restoring springs applied to the top of the inertial mass and free to oscillate in any direction horizontally. Original Wiechert horizontal seismographs carried pendulums with a weight of about 1000 kg (it later was decreased to 80 kg) to overcome the friction. This allowed to achieve a magnification of 200 recorded for the periods not exceeding 10 seconds [*Wiechert*, 1903, 1904; *Dewey & Byerly*, 1969]. Maximum weight had vertical Wiechert seismograph [*Wadsworth*, 1942], with pendulum weight of 1300 kg suspended on a powerful helical springs of 8 mm steel wire. Magnification was also around 200 for periods of seismic waves not greater than 5 seconds. *Dewey & Byerly* [1969] described that ″for damping, Wiechert applied the motion of the pendulum mass to pistons which fit closely inside cylinders attached to the seismometer stand. Resistance of the air to the piston motion provided damping for the pendulum; this resistance was controlled by a valve which had the effect of regulating the amount of air space between the piston and the cylinder″. Recording of the relative motion of the pendulum inertial mass and the ground was carried out on smoked paper which was fixed on a continuously rotating (by a clockwork) drum. Time marks were put on the paper every minute by lifting up the writing index, introducing a gap in a seismogram trace [*Dewey & Byerly*, 1969; *Batlló*, 2014].

The design of the Wiechert instrument with the paper fixed on a drum and the writing index located somewhat 400 mm away from it introduced a curvature to the recorded seismogram. However with the knowledge of the instrument geometry this curvature can be corrected during the digitization process [*Cadek*, 1987]. The Wiechert seismograms, despite their curvature, have in general a good quality. This instruments operated for a very long time and have recorded almost all the earthquakes for this study. The digitization of the Wiechert records is generally well performed and the curvature can be easily corrected.

After John Milne left Japan in 1895, further instrumentation development fall in the hands of Fusakichi Omori [*Omori*, 1899] - a pupil and colleague of Milne. Omori continued working in this field and constructed horizontal-pendulum seismographs consisting of a mass on a rod, pivoting about a socket, with the mass held up by a flexible wire [*Dewey & Byerly*, 1969; *Batlló*, 2014]. This instruments were later modified into Bosch-Omori seismograph with introduction of damping and distributed worldwide in the early 20th century. Omori′s instruments had the periods of about 20 seconds [*Dewey & Byerly*, 1969; *Batlló*, 2014], which makes them better suited seismometers for the purpose of recording large magnitude teleseismic earthquakes. However, due to low magnification, of about 10, the Bosch-Omori seismograph had relatively low sensitivity and often missed small amplitudes, such as teleseimic P phases even for the M>7 earthquakes. Nevertheless, those instruments provided a significant seismograms contribution for this study, especially from Japan. The records are generally available on microfilms, which have relatively good quality and therefore are successfully digitized.

Italian seismologists also advanced in seismic instrumentation throughout 19th and 20th century, with their development of the long common-pendulum seismometers. The most widely distributed instrument was a mechanically-recording seismograph of Vicentini - ”microsismografo” [*Dewey & Byerly*, 1969]. It consisted of a heavy 100 kilogram mass suspended in a 1.5 meter-long pendulum. The relative motion of the pendulum and the ground was magnified and resolved into perpendicular components by levers, with total magnification of 80. The two horizontal seismograms were recorded on a smoked paper along the time trace. Later Vicentini added a vertical seismographs which consisted of a flat spring clamped to a wall from one side and with a oscillating mass (50 kg) at

the other end. The the mass oscillated vertically with a fundamental period of 1.2 seconds and magnification was about 130 [*Dewey & Byerly*, 1969; *Ferrari*, 1992]. Due to their construction the Vicentini seismograph records did not have a curvature and therefore were well suited for digitizing. Moreover, the smaller magnification of the instrument allowed to record the complete trace of major teleseismic earthquakes, including the full amplitude of the surface-waves. However, the absence of damping mechanism made the records very oscillatory, which complicated the identification of the different teleseismic phases and the extraction of their true amplitude.

The first electromagnetic seismic instrument - electromagnetic seismograph - was invented by Russian scientist Boris Galitzin (also sometimes written as Golitsyn) in 1905 [*Galitzin*, 1910, 1911b; *Galitzin et al.*, 1914]. This seismograph worked on the following principle: a heavy mass attached to a frame and hanging on a spring can oscillate up and down; conductive coils are placed at the ends of this frame between two strong magnets. In the absence of an earthquake the system is calm, when an earthquake occurs the mass begins to move in the magnetic field produced by the magnets, thereby inducing an electric current in the coils. After this, the current initiates motion of a galvanometer with an attached to it small mirror that reflects a light beam to a photo paper, leaving a trace of the seismogram. The photographic paper is fixed on a rotating drum, which makes one full turn per hour. The whole system is damped by a secondary magnetic field produced by the induced current in the coil.

Galitzin's electromagnetic seismograph reached magnification up to 1000 and had free period 24 seconds for horizontal and 12 seconds for vertical components [*Batlló*, 2014]. They were widely distributed in former USSR throughout the 20th century and also worldwide. This instrument became a basis for further development of the seismic instrumentation. In particular, this type of instruments were then employed in the World Wide Standardized Seismograph Network [WWSSN *Powell & Fries*, 1964].

The WWSSN installation started in 1961 [*Powell & Fries*, 1964] and contained about 120 seismic stations worldwide. Originally, the WWSSN stations recorded on paper but later those records were photographed and saved on microfilms. Several copies of the microfilm archives were made. It is known that there were two copies in the US [*Lee, William H.K.*, 2011] held at Lamont-Doherty Earth Observatory and the USGS Albuquerque Seismological Laboratory (ASL). One more microfilm chips set was stored at the British Geological Survey [*Henni & Lawrie*, 1999]. The WWSSN records for this study are taken from Strasbourg University where one more copy of the archive is stored under supervision of Prof. Dr. Luis Rivera.

Each WWSSN station was equipped with 3 component long- and short-period instruments (LP and SP respectively). In this work, only LP seismograph records from WWSSN are used, because their period band is more suited for the large magnitude teleseismic earthquakes analysis. The WWSSN-LP instruments usually had a free period of 15 seconds and the magnification varied between 750 and 1500 for different stations. The WWSSN stations recorded eight M>6.5 earthquakes in the Tien-Shan region between 1961 and 1978. Two of those earthquakes, the 1970 Sarykamysh and the 1978 Zhalanash-Tuup, are included in this study. The network provided good azimuthal coverage and the best quality analog seismic records. Digitization of these data usually caused no difficulties.

In the late 1970s, the WWSSN instruments have been replaced by "broad-band" digital seismometers, which can detect ground motions over large ranges or "bands" of periods. However, no earthquake with magnitude larger than 7 occurred in the region since then. Thus, the historical records from the older analog instruments remain an important source of data.

Publication 1

Source process of the 1911 M8.0 Chon-Kemin earthquake: investigation results by analogue seismic records.

The publication describes our detailed study about source parameters of the Chon-Kemin earthquake, the strongest instrumentally recorded earthquake in the Tien-Shan region. It is the first study about this unique earthquake based on instrumental data. Analog paper seismograms from 23 seismic stations worldwide were collected and digitized, the earthquake epicenter was relocated and the hypocenter depth was estimated. Different magnitude types (m_B, M_s, and M_w) are recalculated and the focal mechanism was determined using newly developed modification of amplitude ratios comparison method. Additionally, taking into account surface rupture information, the apparent source time duration and scalar moment of the earthquake, and a fault geometry model is proposed using the sub-events source approach and scaling relations.

This study was fully done by the author of this thesis, including data collection and digitization, development and implementation of software codes for processing methods, calculations of the source parameters, analysis of the results, and preparation of the scientific paper. The second author of the paper, apl. Prof. Frank Krüger, supervised the progress of the performed work, gave ideas, advice, and suggestions for the methods and approaches applied here. He also reviewed and corrected the manuscript several times during its preparation. Before being published the paper has been reviewed by two anonymous reviewers; with one requesting only minor changes and the second reviewer asking for a moderate revision. The comments of both reviews were regarded and the manuscript was corrected accordingly. The English language was checked by a native speaker.

REFERENCE: **Source process of the 1911 M8.0 Chon-Kemin earthquake: investigation results by analogue seismic records**, Kulikova, G. & Krüger, F., *Geophysical Journal International*, 201(3), 1891–1911. doi:10.1093/gji/ggv091.

Available at: http://gji.oxfordjournals.org/content/201/3/1891.abstract.

Publication 2

Source parameters of the Sarez-Pamir earthquake of February 18, 1911.

The publication describes the detailed study of the source parameters of the Sarez-Pamir earthquake- the strongest instrumentally recorded earthquake in the Pamir region. The study presents a new epicenter of the earthquake and its hypocenter depth located using the S-P times from the digitized waveforms and seismic bulletins. The instrumental data are also used to determine the magnitude of the earthquake and its focal mechanism using the amplitude ratios comparison, and synthetic-observed waveformfits. This study proves that the seismograms could have been produced only by an earthquake source. We confirm, using seismic modeling, that the landslide signal could not have been recorded this way on the seismic record. Additionally, the possibility of the landslide signal being superposed into the earthquake record is investigated and modeled, allowing such a scenario.

This study was mainly done by the author of this thesis, including the data collection and processing with the methods presented above (Publication 1), adjustment of existing software codes for landslide source modeling, calculation of the source parameters, analysis of the results, and preparation of the scientific paper. The second author of the paper, Dr. Bernd Schurr, has written the tectonic part of the paper and also corrected the text of the manuscript improving the English language and writing style. The third author, apl. Prof. Frank Krüger, supervised the progress of the performed work, and gave advice and suggestions for the methods and approaches applied here. He also reviewed and corrected the manuscript during its preparation. The fourth author Elisabeth Brzoska, has helped with the seismograms digitization and the preparation of the figures. The paper has been submitted to Geophysical Journal International and is awaiting reviewers scores.

REFERENCE: **Source parameters of the Sarez-Pamir earthquake February 18, 1911.**, Kulikova, G., Schurr B., Krüger, F., Brzoska, E. & Heimann, S. *Published in Geophysical Journal International, 2016, doi: 10.1093/gji/ggw069.*

Available at: https://gji.oxfordjournals.org/content/early/2016/02/19/gji.ggw069.abstract.

Publication 3

Instrumental magnitude constraints for the July, 11, 1889, Chilik earthquake.

The publication describes the Chilik earthquake, the strongest (M8.3) earthquake in the Tien-Shan region. Earlier all information about this earthquake was based on very sparse intensity data, obtained via testimonies of witnesses, and several weakly pronounced fault scarps in the epicentral region. For this publication the original intensity observation report is re-evaluated. Then, a single seismic record from the Rebeur-Paschwitz instrument in Wilhelmshaven (Germany) was found as a book reproduction and is digitized in the forms of envelope. The magnitude of the earthquake is constrained by analyzing the late coda waves of this record in comparison with that of recent events from Central Asia recorded in Germany and transferred to the Rebeur-Paschwitz instrument characteristics. Furthermore, historical magnetometer records of this earthquake are compared to those of the 1911 Chon-Kemin earthquake (where the magnitude is known), as additional constraint on the magnitude. The large M∼8.0 magnitude of the earthquake was confirmed by our investigations.

The author of this thesis has mainly contributed: 1) to the introduction of the paper by describing previously published studies and the current seismicity based on the modern local seismic catalog, including the preparation of the corresponding figures and tables; 2) to the intensity observation part of the paper, by translating the original reports of the testimonies of witnesses and preparing the picture and appendix tables related to it; 3) to the seismic data collection part by collecting necessary information about instruments and seismograms, digitizing the envelop of the seismogram and preparing the picture related to the instrument description. The main work in this publication : the coda wave analysis of major earthquakes in Asia and the Chilik earthquake in comparison with them, as well as the magnetograms analysis, is done and described by the first author of the publication, apl. Prof. Frank Krüger, with all corresponding figures and tables. Dr. Angela Landgraf is responsible for describing the geological features and tectonic settings of the region, and general supervision of the manuscript text and structure. The discussion and conclusion of the paper ae written jointly by all authors with dominant impact of the first author.

REFERENCE: **Instrumental magnitude constraints for the July, 11, 1889, Chilik earthquake.**, Krüger, F., Kulikova, G., & Landgraf, A. In: Landgraf, A., Hintersberger, E., Kübler, S., & Stein, S., (eds), *Seismicity, Fault Rupture and Earthquake Hazards in Slowly Deforming Regions, Geological Society of London, Special Publications, 432, first published on November 20, 2015, doi:10.1144/SP432.8.*

Available at:http://sp.lyellcollection.org/content/early/2015/11/19/SP432.8.abstract.

CHAPTER 2

Source process of the 1911 M8.0 Chon-Kemin earthquake: investigation results by analogue seismic records.

Kulikova G., and Krüger F.

Published in Geophysical Journal International
2015, Vol 201(3), 1891–1911.
DOI: 10.1093/gji/ggv091

SUMMARY: Several destructive earthquakes have occurred in Tien-Shan region at the beginning of 20th century. However the detailed seismological characteristics, especially source parameters of those earthquakes are still poorly investigated. The Chon-Kemin earthquake is the strongest instrumentally recorded earthquake in the Tien-Shan region. This earthquake has produced an approximately 200 km long system of surface ruptures along Kemin-Chilik fault zone and killed about ∼400 people. Several studies presented the different information on the earthquake epicentre location and magnitude, and two different focal mechanisms were also published. The reason for the limited knowledge of the source parameters for the Chon-Kemin earthquake is the complexity of old analogue records processing, digitization and analysis. In the present study the data from 23 seismic stations worldwide were collected and digitized. The earthquake epicentre was relocated to 42.996N° and 77.367E°, the hypocenter depth is estimated between 10 and 20 km. The magnitude was recalculated to m_B8.05, M_s7.94 and M_w8.02. The focal mechanism, determined from amplitude ratios comparison of the observed and synthetic seismograms, was: str=264°, dip=52°, rake=98°. The apparent source time duration was between ∼45 and ∼70 seconds, the maximum slip occurred 25 seconds after the beginning of the rupture. Two sub-events were clearly detected from the waveforms with the scalar moment ratio between them of about $\frac{1}{3}$, the third sub-event was also detected with less certainty. Taking into account surface rupture information, the fault geometry model with three patches was proposed. Based on scaling relations we conclude that the total rupture length was between ∼260-300 km and a maximum rupture width could reach ∼70 km.

2.1 Introduction

The Chon-Kemin earthquake occurred on the 3rd of January 1911 [*Bogdanovich et al.*, 1914; *Nurmagambetov*, 1999]. It caused enormous surface damage: the surface ruptures, cracks and landslides were observed around the epicentre area up-to the 200 km distant. Severe damage was observed in Almaty city (at the time called Verniy) where ∼400 citizens were killed [*Bogdanovich et al.*, 1914], almost every building was damaged and many buildings were completely destroyed. Up to the present this earthquake remains the strongest instrumentally recorded earthquake in the Northern Tien-Shan region.

The Tien-Shan mountain belt is an ∼2500 km long and 300-400 km wide orogenic belt, which serves as a boundary between the Kazakh platform in the North and the Tarim basin in the South (Figure *2.1*a) [*Selander et al.*, 2012]. The present Tien-Shan mountain belt development is assigned to the Eurasia and India convergence as a result of their collision in the Eocene, in spite of being located 1000-1500 km north of the plate boundary [*Molnar & Tapponnier*, 1975]. The dominant compression is N-S oriented with overall N-S shortening about 20 mm/year according to modern GPS observation [*Abdrakhmatov et al.*, 1996; *Zubovich et al.*, 2010]. Altogether, high seismicity in the region shows thrust and reverse faulting and therefore crustal shortening and thickening [*Tapponnier & Molnar*, 1979]. Thrust faulting plays an important role in the tectonics of the Northern Tien-Shan [*Tapponnier & Molnar*, 1979] (Figure *2.1*b,c), as it counterbalances dextral offset faults trending NW, especially on the Talas-Fergana fault (Figure *2.1*a). The Kemin-Chilik fault system, which is responsible for the Chon-Kemin earthquake, is an important reactivated structure in Northern Tien-Shan. This sinistral transpression zone reactivated in the late Pliocene following the fault zone's growth in the Late Paleozoic-Mesozoic [*Abdrakhmatov et al.*, 2013]. Overall, the mountain system between the Issyk-Kul Basin and the Kazakh shield is controlled by this structure [*Abdrakhmatov*

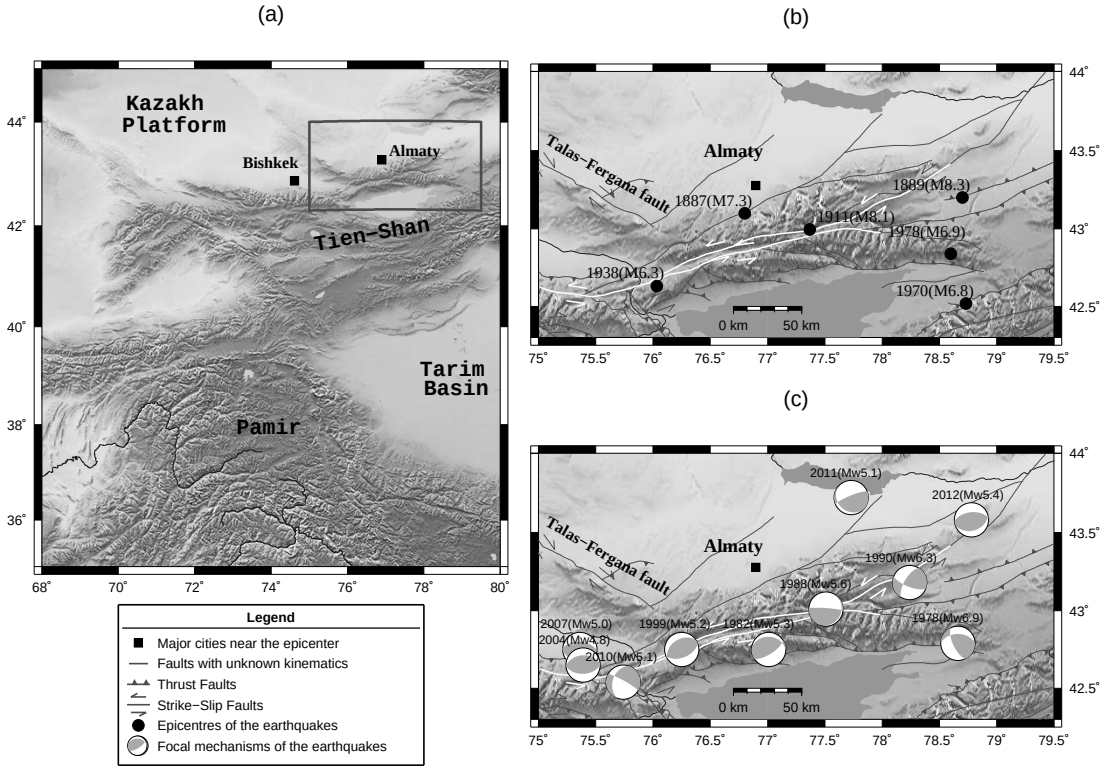

FIGURE 2.1: a)- The tectonic map of the region (the area of interest is indicated with a dark grey rectangle) and the largest cities nearby; b) - the tectonic map of the study area with the epicentres of the strongest earthquakes in the region between 1887 and 1978 (all the epicentre coordinates are taken from *Storchak et al.* [2013], except for Chon-Kemin earthquake which was relocated in this study) including the faults information [*Kalmetieva et al.*, 2009] (the faults orientation signs are described in the legend) the Kemin-Chilik fault system (also referred as Chon-Kemin-Chilik-Aksu fault system) is shown as the white strike-slip fault; c) - the tectonic map of the study area with the focal mechanisms of the modern earthquakes in the region with magnitude > 4.8 [*Ekström et al.*, 2012], the beach-balls are named by the year of the earthquake and corresponding magnitude.

et al., 2013; *Molnar & Tapponnier*, 1975; *Tapponnier & Molnar*, 1979]. The Kemin-Chilik fault is a ∼240 km-long active sinistral fault in the Northern Tien-Shan [*Delvaux et al.*, 2001] (which explains its marked strike-slip orientation on the Figure *2.1*b and c). However, in the past this fault and the connecting faults have shown both sinistral and reverse motion [*Tapponnier & Molnar*, 1979]. *Selander et al.* [2012] suggest in their study the possibility that the Kemin-Chilik sinistral fault experiences initiation of slip-partioning system of a number of high-angle (dip >45°) reverse faults, which are presently active.

Three months after the Chon-Kemin earthquake (time required by the weather conditions) a geological expedition was sent (by the Russian "Commission of the Geology Committee") to investigate the damage of the earthquake. The expedition travelled by horse around the region and very carefully mapped the appearance of earthquake effects on the surface. Afterwards, in 1914 the head of the expedition - Bogdanovich K.I. published a very detailed report, which up to now is the most quoted, reliable and well regarded work concerning to the Chon-Kemin earthquake [*Bogdanovich et al.*, 1914]. This report remains inestimable in terms of geological description of the earthquake and it is widely used for geological [*Molnar & Tapponnier*, 1975; *Delvaux et al.*, 2001; *Arrowsmith et al.*, 2005] and intensity studies [*Bindi et al.*, 2014].

The detailed and comprehensive geological studies about the Tien-Shan region in general and the Chon-Kemin earthquake in particular has been a great help for the present work. In this study we mainly refer to the works of *Arrowsmith et al.* [2005] and *Delvaux et al.* [2001], who have studied the rupture of the Chon-Kemin earthquake and have investigated the faults responsible for the earthquake. Both of these studies reported that the Chon-Kemin earthquake ruptured 5 segments of the Kemin-Chilik fault system. Successful combination of geological information and historical seismic records for an earthquake source parameters determination have been previously shown in different studies [*Kanamori et al.*, 2010; *Schlupp & Cisternas*, 2007; *Baroux et al.*, 2003; *Okal*, 2012]. An example nearest to the Chon-Kemin earthquake epicentre is the study regarding the two 1905 great continental earthquakes in Mongolia [*Schlupp & Cisternas*, 2007] - Bolnay M8.3-8.5 and Tsetserleg M8.0 (the epicentres located about 1500 km away from the epicentre of the Chon-Kemin earthquake).

The 1911 Chon-Kemin earthquake was the largest in the major earthquake sequence which took place in the Kemin-Chilik fault zone at the turn of the19th century. The sequence started on 8-June-1887 with M7.3 Verniy earthquake, which was then followed by 11-July-1889 M8.3 Chilik earthquake and concluded by 10-June-1938 M6.8 Kemin-Chu earthquake (Figure *2.1*b) [*Nurmagambetov*, 1999]. Later in the century strong earthquakes again occurred in this region on 05-June-1970 (M6.3), 24-May-1978 (M6.9) and 12-November-1990 (M6.3) [*Storchak et al.*, 2013]. The modern seismicity of the region is limited to moderate earthquakes with magnitudes $Mw \leq 5.8$, which mostly show thrust mechanisms with dips between 45○ and 65○ (Figure *2.1*c [*Ekström et al.*, 2012]). Therefore, detailed study of the Chon-Kemin earthquake, as the strongest instrumentally recorded earthquake in Northern Tien-Shan region, is of particular interest for the understanding of the regional tectonics as well as estimation of seismic hazard [*Abdrakhmatov et al.*, 2002].

The Chon-Kemin earthquake epicentre was located based on seismic data and afterwards several attempts to relocate it were made in different years (see chapter 4 on relocation). There were also two studies aiming to determine the focal mechanism of the earthquake [*Chen & Molnar*, 1977; *Molnar & Qidong*, 1984], however nothing is known about the kinematic parameters of the source from a seismological point of view. This study is directed at detailed analysis of the Chon-Kemin earthquake by employment of historical seismic records. The collected historical seismograms were digitized and then used to relocate the earthquakes epicentre, recalculate its magnitude, determine the focal mechanism and derive the kinematic source parameter with modern techniques and algorithms.

2.2 Data- collection and digitization

The Chon-Kemin earthquake would have been recorded by more than a hundred seismic stations operating at the time worldwide [*Batlló et al.*, 2008; *Schweitzer & Lee*, 2003; *Wood*, 1921; *McComb & West*, 1931]. The early seismic instruments were mainly analogue mechanical pendulums registering ground motion on smoked papers [*Fréchet & Rivera*, 2012; *Ehlert*, 1898b; *Wiechert*, 1903, 1904; *Omori*, 1899; *Milne*, 1886; *Galitzin*, 1910] , which were not designed to survive under the humidity, temperature changes or frequent transportation over the last century. Thus many seismograms have been partially lost or significantly damaged. At present, the remaining seismograms are distributed in seismic archives at different institutes and observatories worldwide.

The maximum possible number of seismograms was collected for the Chon-Kemin earthquake in the frames of this study. This includes the original analogue paper seismograms as well as microfilms (photo copies) and books or journal reproductions of original records from different archives.

Additionally the original catalogues and bulletins published at that time were collected and used as well for the earthquake relocation. Many institutions were contacted (the detailed information of each institute and personal contacts can be found in the Appendix *2.8.2*, Table *2.4*) and the seismograms were brought together trying to obtain the best possible azimuth coverage.

TABLE 2.1: Instrument constants for some of analogue instruments operating in 1911.

Station [1]	Instrument	Component	Magnification	Damping (h)	Period (T_0[sec])
API (Apia, Samoa Island)	Wiechert seismograph	NS	130.00	0.43	9.0
	Wiechert seismograph	EW	130.00	0.43	9.0
DBN (De Bilt, Netherlands)	Bosch-Omori	NS	20.00	0.40	18.0
	Bosch-Omori	EW	20.00	0.43	18.0
GTT (Goettingen, Germany)	Wiechert seismograph	NS	152.00	0.40	14.0
	Wiechert seismograph	EW	172.00	0.36	12.6
	Wiechert seismograph	Z	170.00	0.31	4.8
HAM (Hamburg, Germany)	Wiechert seismograph	NS	200.00	0.46	10.0
	Wiechert seismograph	EW	200.00	0.46	10.0
HLG (Helgoland, Germany)	Wiechert seismograph	NS	126.00	0.41	11.5
	Wiechert seismograph	EW	153.00	0.39	11.1
HNG (Hongo, Tokio, Japan)	Omori	NS	20.00	0.40	16.0
	Omori	EW	20.00	0.40	16.0
CSM (CasaMi., Ischia, Italy)	Vicentini	NS	8.00	None [2]	13.1
	Vicentini	EW	8.00	None	10.4
LEI (Leipzig, Germany)	Wiechert seismograph	NS	260.00	0.46	9.6
	Wiechert seismograph	EW	260.00	0.46	9.6
MNH (Munich, Germany)	Wiechert seismograph	NS	190.00	0.46	9.0
	Wiechert seismograph	EW	190.00	0.46	9.0
OTT (Ottawa, Canada)	Wiechert seismograph	NS	120.00	None	8.0
	Wiechert seismograph	EW	120.00	None	7.1
PUL (Pulkovo, USSR)	Galitzin	NS	856.00	0.71	18.0
	Galitzin	EW	856.00	0.71	18.0
RAV (Ravensburg, Germany)	Mainka	NS	13.00	0.33	5.0
RIV (Riverview, Australia)	Wiechert seismograph	NS	171.00	0.48	8.4
	Wiechert seismograph	EW	171.00	0.41	8.3
SIT (Sitka, Alaska)	Bosch-Omori	NS	10.00	None	17.0
	Bosch-Omori	EW	10.00	None	18.0
TAR (Taranto, Italy)	Wiechert seismograph	NS	180.00	0.40	4.5
	Wiechert seismograph	EW	180.00	0.40	4.5
TLO (Toledo, Spain)	Milne	EW	9.00	None	15.0
	Rebeuer-Ehlert	NS	123.00	0.40	7.0
	Rebeuer-Ehlert	EW	122.00	0.40	7.0
VIE (Vienna, Austria)	Wiechert seismograph	NS	160.00	0.46	9.4
	Wiechert seismograph	EW	210.00	0.40	11.2
UCC (Uccle, Belgium)	Wiechert seismograph	NS	145.00	0.40	10.7
	Wiechert seismograph	EW	165.00	0.37	10.0
	Wiechert seismograph	Z	155.00	0.33	4.8

Finally the seismic records from twenty-three seismic stations, located at distances between 3600 and 12700 km from the epicentre (Figure *2.2*), were collected. It is obvious that considerable azimuthal gaps were left: the largest– almost 180° gap is observed from SE to NW and 2 smaller 45° azimuthal gaps are seen on the ESE and NE (Figure *2.2*). In modern seismology such azimuth coverage would be considered as poor. However for an historical earthquake this amount of data is very valuable and has never before been obtained for a historical earthquake in the Tien-Shan region. Most of the records were collected from stations located in Europe (Figure *2.2*) because they were preserved in the best condition, and were most easily accessible. The availability of historical records from seismic stations in Europe has considerably improved with the EUROSEISMOS [*Michelini et al.*, 2005] project.

[1] Station abbreviation names are given by authors of this paper in 3 letters, corresponding to the closest modern seismic station name located in this region, however the precise location of the historical stations often differs from the modern one.

[2] None means that there was no damping mechanism attached to this instrument or the damping value is unknown

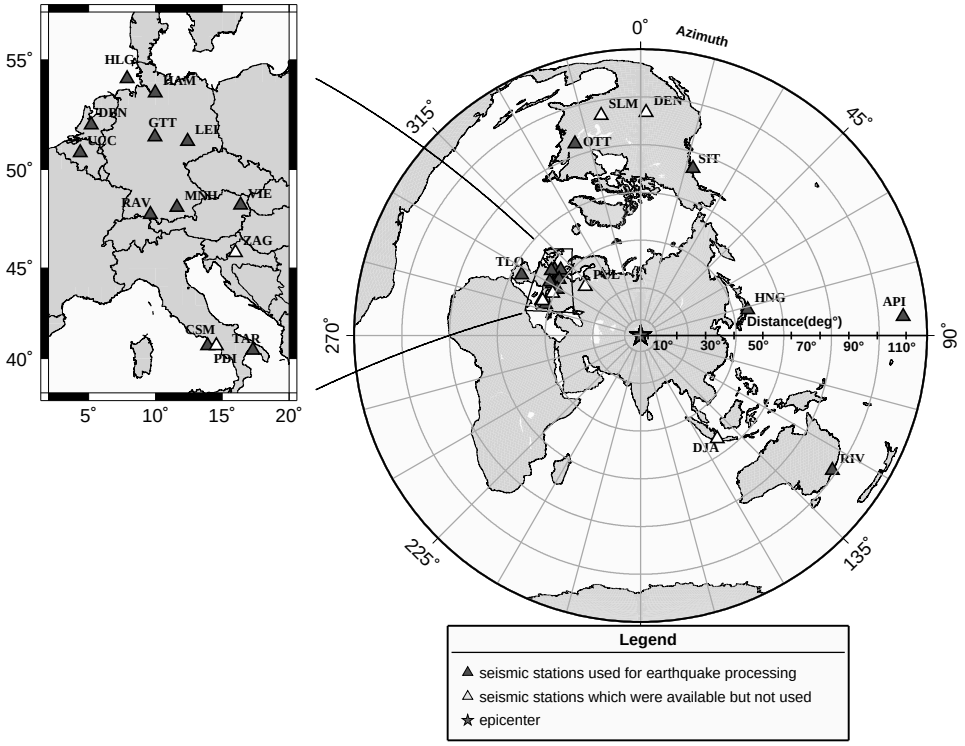

FIGURE 2.2: The distribution of seismic stations, which have recorded the Chon-Kemin earthquake in the azimuthal equidistant projection. The star at the middle represents the epicentre of the earthquake; the dark grey triangles show the stations, which were used in this study; the white triangles show the stations where seismograms were available, but did not have a high enough quality to be digitized; the station names' abbreviations are given according to the name of the nearest modern station. The inset map (top left) represents the detailed view on the seismic station distribution in Europe.

The majority of historical instruments was mechanical pendulums which were characterized by certain values of instrument constants: free period, damping and an additional parameter for the magnification of recording system, these parameters are given in the Table *2.1*, they were obtained from *Wood* [1921] and *McComb & West* [1931] or handwritten station books (Figure *2.3*). The time between different components of the early seismometers (mostly only two horizontals) was synchronized with certain time marks (minute marks). However as our investigation showed this was not always exactly achieved and has caused future complications with processing (see chapter 3.1, earthquake relocation). The vertical component was added later and was installed as an independent instrument with its own period, damping and magnification, thus our collection includes only two vertical component records.

The analogue seismic records had to be scanned with a high resolution, keeping the original size when possible (except microfilms and reproductions) in order to extract the true amplitudes and periods, after the scanned images are digitized. To date there is no universal software to digitize the historical seismograms. Our first choice was to use TESEO software for digitizing the seismograms [*Michelini et al.*, 2005; *Pintore et al.*, 2005]. The main advantage of using this software is the option for curvature correction [*Cadek*, 1987; *Schlupp & Cisternas*, 2007]. Many historical seismometers (such as widespread in Europe Wiechert instrument) were built as mechanical pendulums recording with a needle on a smoked paper which was fixed on a cylinder of a certain radius. Therefore

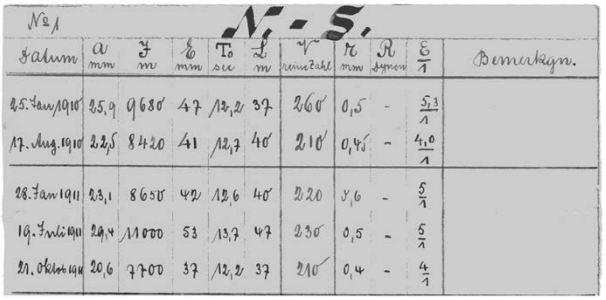

Datum	a mm	T m	ε mm	T_0 sec	L m	V Vergrößerung	κ mm	R Sgnow	ε/1	Bemerkgn.
25. Jan 1910	25,9	9680	47	12,2	37	260	0,5	-	5,3/1	
17. Aug. 1910	22,5	8420	41	12,3	40	210	0,45	-	4,0/1	
28. Jan 1911	23,1	8650	42	12,6	40	220	0,6	-	5/1	
19. Juli 1911	29,4	11000	53	13,3	47	230	0,5	-	5/1	
21. Oktober 1911	20,6	7700	37	12,2	37	210	0,4	-	4/1	

FIGURE 2.3: Example copy of handwritten station book for the seismic station in Munich (MNH), NS oriented component. The instrument constants for Wiechert seismograph in 1910-1911 years (T_0 - period, V - amplification and ϵ - damping ratio). The pre-last column of the table gives the value of damping ratio ϵ, which is then used to derive a damping constant h [*Dost & Haak*, 2002; *Scherbaum*, 2007] presented in Table *2.1*

.

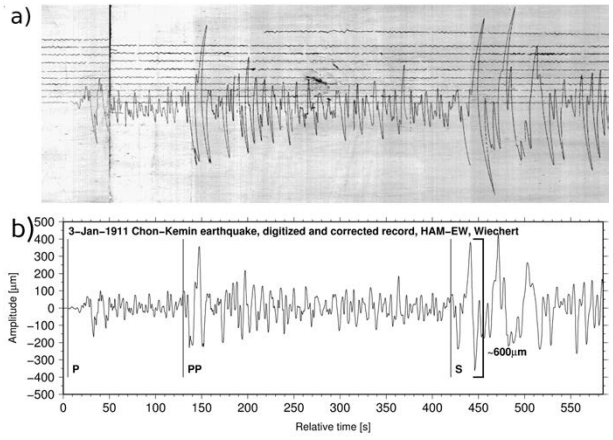

FIGURE 2.4: Examples of analogue and digitized seismograms. The top picture (a) shows a scanned paper seismogram which was recorded at Hamburg station HAM, EW oriented component, by the Wiechert seismograph. The colours are inverted and the record is cut in length to show only non-clipped part of the seismogram. The bottom picture (b) shows digitized version of the same seismogram, the amplitude of the seismogram is scaled to the true ground motion in μm and the recorded phases are named respectively.

the recorded seismograms had a curved shape and due to the geometry of the instrument and the recording mechanism the curvature was more obvious for larger amplitudes (Figure *2.4*, top). The geometric correction of such records is described by *Cadek* [1987] and *Grabrovec & Allegretti* [1994] and applied in the TESEO software [*Pintore et al.*, 2005]. For technical reasons (operating system incompatibility) a new code for digitizing seismograms was later developed on the basis of TESEO with the curvature correction method from *Cadek* [1987]using Bezier curves approximation. The results of the procedure can be seen in Figure *2.4* (bottom).

Unfortunately not all records have high enough quality for successful digitization. For this reason only thirty eight records out of fifty available ones were digitized. (More detailed information on quality of seismograms is given in the extended online version of this work in the Appendix *2.8.2* and can be accessed online.)

2.3 Earthquake location and magnitude

2.3.1 Earthquake location

The absence of radio signal techniques at the time when the Chon-Kemin earthquake occurred (1920s, *Kanamori et al.* [2010]) resulted in large uncertainties of station clock times. Moreover communication between the local and foreign institutes was often interrupted due to political reasons, which lead to the lack of seismic data exchange and resulted in each institution having its own parameters for the earthquake. Hence in several historical catalogues, published in the past, the Chon-Kemin earthquake appears with different epicentre locations and magnitudes [*Gutenberg & Richter*, 1954; *Kondorskaya et al.*, 1982; *Abe & Noguchi*, 1983; *Storchak et al.*, 2013]. The most well-known among all the epicentres listed in the literature is the *Gutenberg & Richter* [1954] epicentre, which was later considered by seismologists worldwide as the true location for the Chon-Kemin earthquake and thereafter was included in the international online catalogues [*USGS*, 2014a; *ISC*, 2015] (Figure *2.5*). Local seismologists, from the former USSR, published another epicentre for the earthquake [*Kondorskaya et al.*, 1982], Figure *2.5*. In January 2013 ISC-GEM Global Instrumental Earthquake Catalogue [*Storchak et al.*, 2013] was issued and the Chon-Kemin earthquake epicentre was relocated more to the east (Figure *2.5*). From the field observations the surface rupture for Chon-Kemin earthquake was described by geologists as being 200-km-long along Kemin-Chilik fault system, which can be seen even in the present and puts a strong constraint on the epicentre position [*Bogdanovich et al.*, 1914; *Delvaux et al.*, 2001; *Arrowsmith et al.*, 2005].

Altogether in this study, information from 34 seismic stations worldwide with 126 phase arrival times were used to relocate the earthquake epicentre. The detailed information about all the stations, phases, their arrival times, amplitudes and periods can be found in Table *2.5*, Appendix *2.8.3*. To determine the epicentre of the earthquake, the HYPOSAT software [*Schweitzer*, 2001, 2012] was used with global velocity model AK135 [*Kennett et al.*, 1995] with modified crustal structure following the CRUST 5.1 model [*Mooney et al.*, 1998]. Main priority was given to the solution based on the travel time differences and absolute arrival times were used as little as possible. Due to the above mentioned uncertainty in the station clocks we have given large initial time errors for all the arrival times: 5 sec error was given for P phase arrivals, 10 seconds for PP and S phases, and up-to 20 seconds for the SS phase arrivals. We tried to locate the earthquake epicentre using different pieces of information separately and combine them in different ways to test the stability of our location: 5 different combinations of data were tested. The results of our tests are presented in the Table *2.2*.

Table 2.2: Different locations for the Chon-Kemin earthquake depending on the dataset used.

Number	Location type	Origin time [hh:mm:ss.s]	Latitude	Longitude	Depth [km]
1	local bulletins only	23:25:58.510 ± 3.636	43.316 ± 1.85	76.642 ± 0.5867	23
2	teleseimic bulletins	23:25:46.916 ± 5.665	41.798 ± 1.1203	77.401 ± 0.6694	ND
3	all bulletins	23:25:42.823 ± 3.167	41.716 ± 0.3997	78.209 ± 0.2617	ND
4	waveforms only	23:25:49.849 ± 2.778	43.139 ± 0.5893	77.467 ± 0.3145	21.74±3.2
5	preferred location	23:25:50.716 ± 2.968	42.996 ± 0.2792	77.367 ± 0.4936	20.79±2.7

First we tried using bulletin information from local seismic stations only (distance <30 degrees) see Table *2.2* solution 1: 7 absolute arrival times corresponding to P-onset were used together with 7

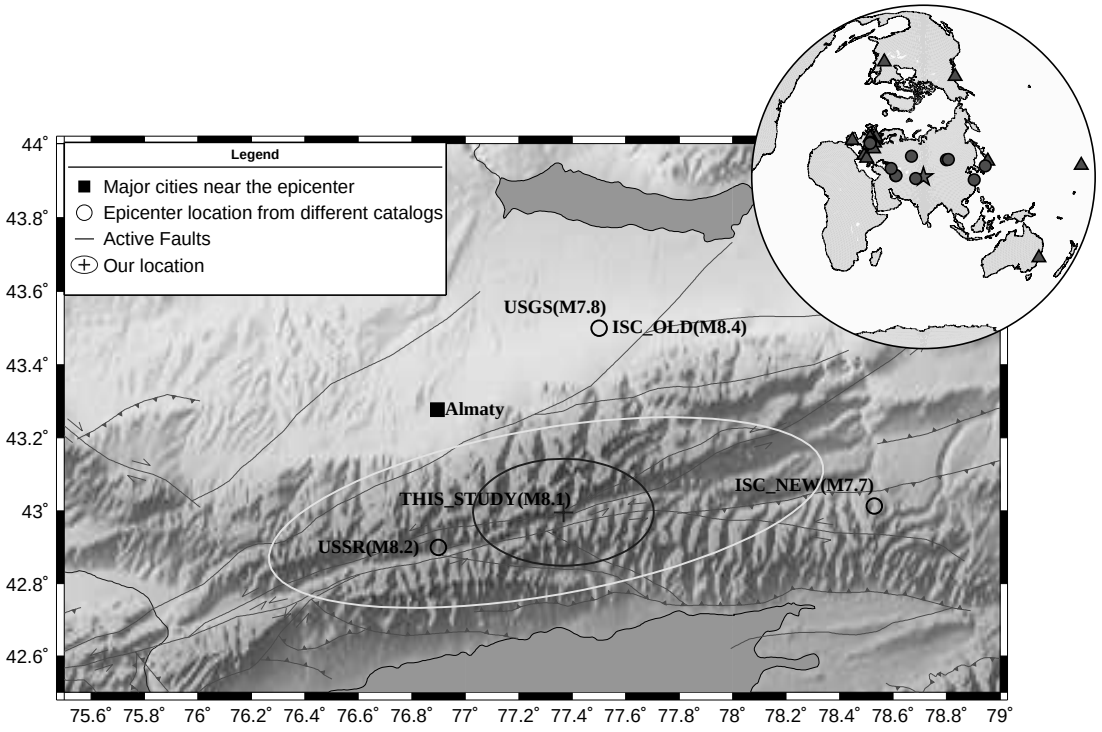

FIGURE 2.5: The topography map of Northern Tien-Shan, with active faults, showing location of Chon-Kemin earthquake from different catalogues (open black circles): USSR(M8.2) shows the location from local seismologists from the former USSR [*Kondorskaya et al.*, 1982]; USGS and ISC represent the location which appears in the USGS and ISC online catalogues [*USGS*, 2014a; *ISC*, 2015], this location is the one published by *Gutenberg & Richter* [1954]; ISC_NEW(M7.7) indicates the location published in the New ISC Catalogue [*Storchak et al.*, 2013]. The location results of this study are shown with the dark gray + with the error ellipse with one standard deviation. The white ellipse shows approximately the area where the surface rupture appeared most clearly. The inset (top right) - the map of the stations used to relocate the epicentre of the Chon-Kemin earthquake: the circles show the stations for which only bulletin information is available, the triangles show the station where the waveforms are available as well.

travel time differences (see Table *2.2*). The location error in the latitude exceeded 200 km and the origin time is shifted by almost 10 seconds in comparison with the time of catalogues. A second try (solution 2 Table *2.2*) was performed using the information from teleseismic bulletins only, absolute arrival times for the P onset for two German stations HAM and MNH (these stations were chosen because they had the same timing for the bulletin and waveforms arrivals) were used with 15 travel time differences - Δt. The epicentre is shifted very far from the observed surface rupture, almost 200 km to the south from the Chon-Kemin fault and as with the first test has very large errors in latitude. Solution 3 in Table *2.2* shows the results of combining teleseismic and local bulletin information without making use of absolute times. The solution is based on 22 Δt, the epicentre location result is not very different from solution 2, which can be explained by a larger number of teleseismic station arrival times. The error ellipse is smaller than for both test 1 and 2. For the fourth test HAM and MNH, P onset arrival times with 32 Δt from the waveforms were used. The epicentre location agrees well with the surface rupture observation. The final preferred solution (number 5 in the Table *2.2*), was obtained by combining the waveforms picked arrivals and bulletin information (HAM and MNH P onset arrival times and 38 Δt), excluding outliers. In order to

identify stations destabilising the epicentre location determination we run bootstrap tests (up 1000 times) over the stations. The hypocenter depth found in test one had very large errors, for test two and three it could not be determined at all, and for the tests 4 and 5 the depth was at about 20 km. The preferred epicentre is marked on the Figure *2.5* with dark gray indicating the error ellipse with one standard deviation. We consider this solution to be the best that can be obtained from our data set and this epicentre agrees well with the surface rupture observations (white ellipse Figure *2.5*).

2.3.2 Magnitude calculation

The magnitude of the Chon-Kemin event caused a lot of discussion among seismologists. The *Gutenberg & Richter* [1954] magnitude M8.4, as well as their epicentre, for the Chon-Kemin earthquake is often found in the literature and seismic catalogues. In 1958 Richter published an even larger magnitude M8.7 for this earthquake [*Richter*, 1958]. The local studies estimated the magnitude to be M8.2 [*Kondorskaya et al.*, 1982; *Nurmagambetov*, 1999]. These large magnitudes were then confirmed by *Abe* [1981] who gave the Chon-Kemin earthquake the estimate M_s8.4 and m_B8.1. However later in *Abe & Noguchi* [1983] the Chon-Kemin earthquake was listed with M_s7.8. *Chen & Molnar* [1977] who published a study about the source parameters of Chon-Kemin earthquake suggested M_w7.8. A recent study from *Storchak et al.* [2013] shows a lower magnitude for Chon-Kemin earthquake M7.7 and the intensity study from *Bindi et al.* [2014] gives it intensity magnitude MI_w7.6. We aim to determine the magnitude for the Chon-Kemin earthquake based on our seismic data.

We calculated the broadband body wave magnitude m_B [*Bormann & Saul*, 2009; *Bormann et al.*, 2013] for the Chon-Kemin earthquake based on the amplitude and period values measured on the digitized waveforms (see Table *2.5*, Appendix *2.8.3*). Our estimated m_B is 8.05±0.3. This value was obtained by averaging amplitudes measured for different phases. We observed that the amplitude and period values (in Table *2.5*, Appendix *2.8.3*) from the bulletins and our measured values differ from each other. This can be explained by different approaches in application of magnification factor of the instrument for reading and association of phases. If the magnitude is estimated from the bulletins amplitudes only it would be m_B8.02. The surface waves for the Chon-Kemin earthquake produced very strong oscillations and initiated instrument failure or were simply clipped for the majority of the stations. This complicates the determination of the surface wave magnitude using our data. Thus only 5 stations could be used to determine the surface waves magnitude M_s7.9 using the Prague-Moscow formula [*Karnik et al.*, 1962] (see Table *2.6*, Appendix *B*). Our estimate of M_w is presented below in section 4.

2.4 Mechanism and scalar seismic moment determination

2.4.1 Focal mechanism determination

Determination of the focal mechanism and of the scalar seismic moment M_0 of an earthquake based on moment tensor inversion is a routine procedure in modern seismology [*Dahm & Krüger*, 1999, 2014]. In frequency domain the general displacement $\tilde{u_i}(\omega)$ at a given angular frequency ω can be written as:

$$\tilde{u}_i(\omega) = \tilde{G}_{jk}(\omega) \cdot m_k \tag{2.1}$$

with $m_1 = \frac{1}{2} \cdot (M_{22} - M_{11})$, $m_2 = M_{12}$, $m_3 = M_{13}$, $m_4 = M_{23}$, $m_5 = \frac{1}{3} \cdot (\frac{1}{2} \cdot (M_{22} + M_{11}) - M_{33})$, and $m_6 = \frac{1}{3} \cdot (M_{11} + M_{22} + M_{33})$

where

M_{ij} - are the six independent components of a general moment tensor [*Aki & Richards*, 2002, 112].

G_k - are linear combinations of elements of the Green's tensor.

Inversion of the equation *2.1* for the components of the moment tensor is difficult in case of a historical earthquake dataset for a number of reasons:

1. The frequency content:
   (a) - The seismographs of the past, in comparison to modern broadband digital seismic instruments, usually had low dynamics and insufficient frequency bandwidth for teleseismic waveform modelling, especially of the large earthquake. The free period of the instruments was between 7-14 seconds for horizontal components and even less- 4-5 seconds for the vertical component. This is below the period necessary for successful teleseismic moment tensor inversion which is usually performed at about 20-50 seconds for the body waves.
   (b) - The strong oscillation produced by major earthquakes in many cases provoked a dislocation of the writing needle, which then introduced a step on the seismograms (see Figure *B.5*, Appendix *B* of the extended online version of this work). Also interpolation of time stamps during digitization is sometimes difficult and introduces small steps and kinks. Such distortion steps become more obvious in frequency domain and result in the introduction of artificial low frequencies to the recorded true ground displacement. This effect biases the moment tensor inversion procedure when we tried to increase the bandwidth by deconvolving the instrument characteristics.
2. The data quality and completeness:
   (a) - The data often have poor quality due to the low dynamics of the instruments and inability to record strong oscillation, e.g. surface waves for the Chon-Kemin earthquake.
   (b) - Sometimes single components of the instruments were lost or the instrument consisted of only one component (e.g. TLO -Milne instrument). Especially since the vertical Z component was added to the recording systems later, so for the case of the Chon-Kemin earthquake we had only two Z component records from station GTT and UCC in Europe.
   (c) - The calibration information of the instruments which was documented manually in the station books is very often not available or uncertain.
3. Rotation issue:
   (a) - Many programs which use moment tensor inversion techniques require to rotate the horizontal N and E component seismograms correctly into radial and transverse components. This is difficult for historical records because of imprecise time alignment and magnification correction between horizontal N and E components (for more details see Appendix *2.8.2*).

Taking into account these deficiencies of historical recordings, we needed a method that preferably avoids rotation and restitution of the historical seismograms. In the first step synthetic seismograms (further synthetics) were calculated with the reflectivity method [*Müller*, 1985; *Fuchs & Müller*, 1971; *Dahm & Krüger*, 2014; *Dahm et al.*, 2004; *Dahm & Krüger*, 1999] for different test depths for all stations using AK135 Global Earth Velocity model [*Kennett et al.*, 1995]. The synthetics were rotated into the local station ZNE coordinate system and historic seismograph recordings were simulated with given values for damping, free period and magnification of the respective instrument. To simulate the synthetics for mechanism and scalar moment determination we used a grid search approach based on the equation:

$$d_i(\omega) = R_{ij} \cdot \tilde{G}_{jk}(\omega) \cdot m_k \cdot S(\omega) \cdot T_i(\omega) \tag{2.2}$$

where $d_i(\omega)$ - is the observed displacement recorded on the i-th component of a historical instrument (a paper seismogram record)

R_{ij} - is a rotation matrix necessary to convert from ZRT to ZNE coordinate systems

G_{jk} and m_k - are same in the equation *2.1*

$S(\omega)$ - is a source time (moment rate) function common for all elements of the moment tensor

$T_i(\omega)$ - is a transfer function of a corresponding historical instrument - the impulse response of the i-th component of a historical seismogram

This transfer function in frequency domain can be written as a complex polynomial:

$T_i(\omega) = V_i \cdot \frac{\prod_{n=1}^{N}(i\omega - z_j)}{\prod_{n=1}^{M}(i\omega - p_j)}$

$i = \sqrt{-1}$,

V- is a constant factor (in our case magnification of the instrument),

z_j and p_j - are the zeros and the poles of the system (instrument) respectively, the poles are calculated from the corresponding damping constant h and the free period of the instrument [*Dost & Haak*, 2002; *Scherbaum*, 2007],

N - is the number of zeros,

M - is the number of poles,

In the forward modelling we use a double-couple (DC) constraint for the moment tensor by setting strike (ϕ), dip (δ) and rake (λ) angles to a specific value and calculating the corresponding moment tensor [*Bormann et al.*, 2009, 73], [*Aki & Richards*, 2002, 112],

In a grid search procedure the synthetic records were simulated with 2° spacing in strike, dip and rake angles and their amplitude ratios were compared to corresponding amplitude ratios of the observed seismograms, misfit was calculated. These procedure was done for the body waves direct and reflected phases (e.g. P, PP, S, SS, etc.). Surface waves were not used for the Chon-Kemin earthquake, as was mentioned above, because the large oscillations produced by the surface waves initiated instrument failures at most stations.

The amplitude ratios were calculated dividing the absolute values of the maximum amplitude of a specific phase by the maximum amplitude of another phase on each record separately. That means

the amplitude ratios were calculated for each record individually and amplitude ratios for different stations and components are independent from each other. The misfit was calculated with the following misfit function:

$$misfit = \frac{1}{n}\sum_{1}^{n}\frac{1}{k}\sum_{1}^{k}\sqrt{\sum_{i=1}^{m}\sum_{j>i}^{m} w_{ij}\left(\frac{|A_{d_i}|}{|A_{d_j}|} - \frac{|A_{s_i}|}{|A_{s_j}|}\right)^2} \tag{2.3}$$

where; n - is the number of stations,

k - is the number of records per station,

m - is the total number of registered phases per record,

$A_{s_i,j}$ - is the maximum phase amplitude of the synthetics,

and $A_{d_i,j}$ - is the corresponding maximum phase amplitude of the observed data.

The indices i and j are used to count the phases for each individual record (e.g. i=P, PP, S, SS, etc., j=P, PP, S, SS, etc., $i \neq j$), double counting of a specific phase is avoided.

The weighting factors w_{ij} for each amplitude ratio can be chosen from 0 to 1 based on the phase type, stations distance, quality of the record and certainty of the instrument parameters. Here we use $w_{ij} = 1$, if a specific amplitude ratio satisfies for all those points and $w_{ij} = 0$ if otherwise.

It has been proven before [*Kisslinger*, 1980; *Julian & Foulger*, 1996; *Hardebeck & Shearer*, 2003] that amplitude ratios can help to significantly constrain the focal mechanism of the earthquake. We consider the amplitude ratios to be the most reliable information for the Chon-Kemin earthquake. We also assumed that the mechanism did not change during the rupture process. Amplitude ratios do constrain strike and dip angle but not the sign of the slip vector. In order to fix all three fault orientation angles including the rake angle, polarity information is needed. In case of the Chon-Kemin earthquake no first onset polarities can be used, however, because of the known backazimuth from a specific station towards the source the overall polarity of the seismogram can be reconstructed from P-wave particle motion in the N-E plane (for details see extended online version Appendix *B.4*).

The performance of the amplitude ratios comparison method has been tested for a synthetic example and two modern large continental earthquakes more information about the tests can be found in the Appendix *C*, online). For the synthetic test we have used the same station distribution as is available for the Chon-Kemin event, taking into account the corresponding instrument characteristics. The mechanism could be recovered perfectly. The test also showed that the method had the capability to resolve the depth of the event. We performed additional tests on two modern earthquakes of comparable magnitude, which occurred in China and Pakistan, using similar azimuthal coverage as existed for the Chon-Kemin earthquake and again typical instrument characteristics of historical seismographs. The M_w8.0 Wenchuan (Sichuan) earthquake on May 12, 2008 in China was used as an example of a thrust type earthquake. This earthquake was recorded by modern digital broad band and old Wiechert analogue seismometers located close to each other, which gave the opportunity for waveform comparison (Figure *2.6*, see section 6 discussion). The M_w7.7 Balutchestan earthquake on September 24, 2013 in Pakistan was used as an example of the strike slip type earthquake. Both tests showed results (see extended online version Appendix *C*) close to the published focal mechanism solutions and centroid depths.

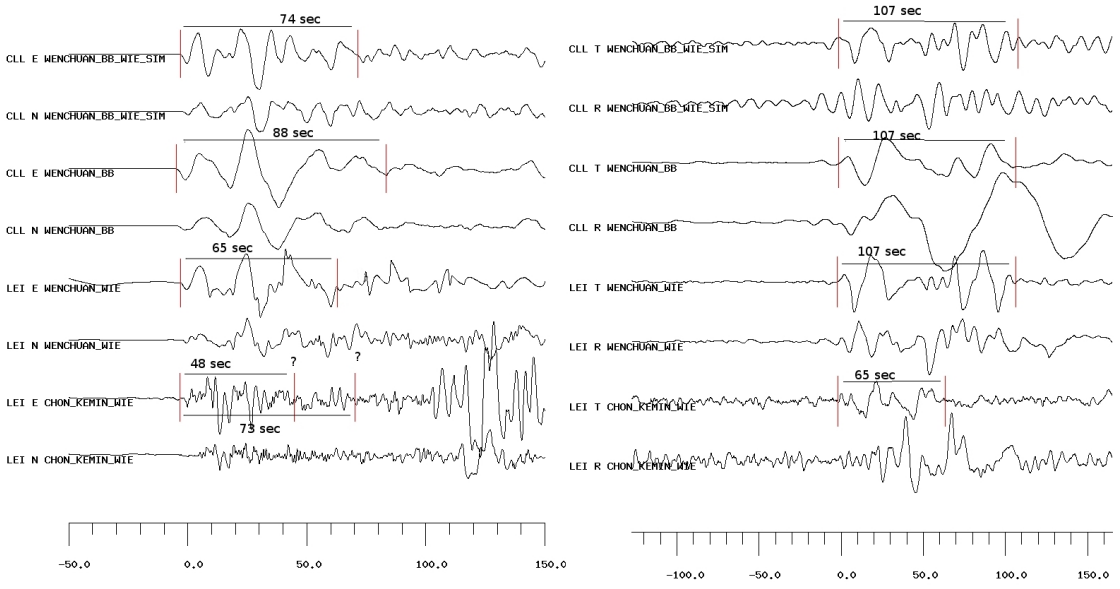

FIGURE 2.6: Comparison of the 2008, M8.0 Wenchuan earthquake and the Chon-Kemin earthquake records; P wave records on the left and SH wave on the right. The lower two traces are the records of the Chon-Kemin earthquake. The record of the 2008, M8.0 Wenchuan earthquake by the analogue Wiechert instrument (3rd and 4th traces) and on the broad-band station CLL (5th and 6th traces) located 200 meters apart; the simulated Wiechert records from the true displacement (7th and 8th traces). The duration of the P and SH waves in time is given in seconds attached to the lines showing it's length. The records show true amplitudes and are aligned in time.

From the comparison of the amplitude ratios measured on observed and synthetic seismograms the mechanism of the Chon-Kemin earthquake was determined: str/ dip/ rake = 264°±20°/ 52°±10°/ 98°±10°, which agrees with surface rupture observation and the modern seismicity in the region. The sign of the slip vector was determined from the P-wave particle motion at selected European stations. The measured data amplitude ratios were compared with synthetics calculated for different test depths using a depth increment of 2 km. The minimum misfit was found between 8 and 18 km depth (Figure *2.7* bottom left panel). The three panels on the right side of Figure *2.7* show that dip and rake angle of the mechanism are well constrained within about 10°, while the strike angle is less constrained (20°).

2.4.2 Seismic moment determination

The value of the scalar seismic moment was estimated by scaling the synthetics and observed displacement records for the given mechanism (determined above), the scaling factor in that case is proportional to the maximum scalar moment M_0. Such scaling implies that all the synthetic displacement amplitudes must be scaled to the data, which differs slightly for all the traces introducing a range of uncertainties. The main reason for those uncertainties is an error in the magnification factor for the corresponding instruments and individual station site effects. Table *2.3* represents the values for scalar moment and corresponding M_w individually for each station. The preferred scalar moment value is determined as an average of the values for different stations with one standard deviation, excluding total outliers (the values in brackets) such as stations API and TAR, which show overall very high amplitudes. The stations which are not listed in the Table *2.3* were not used

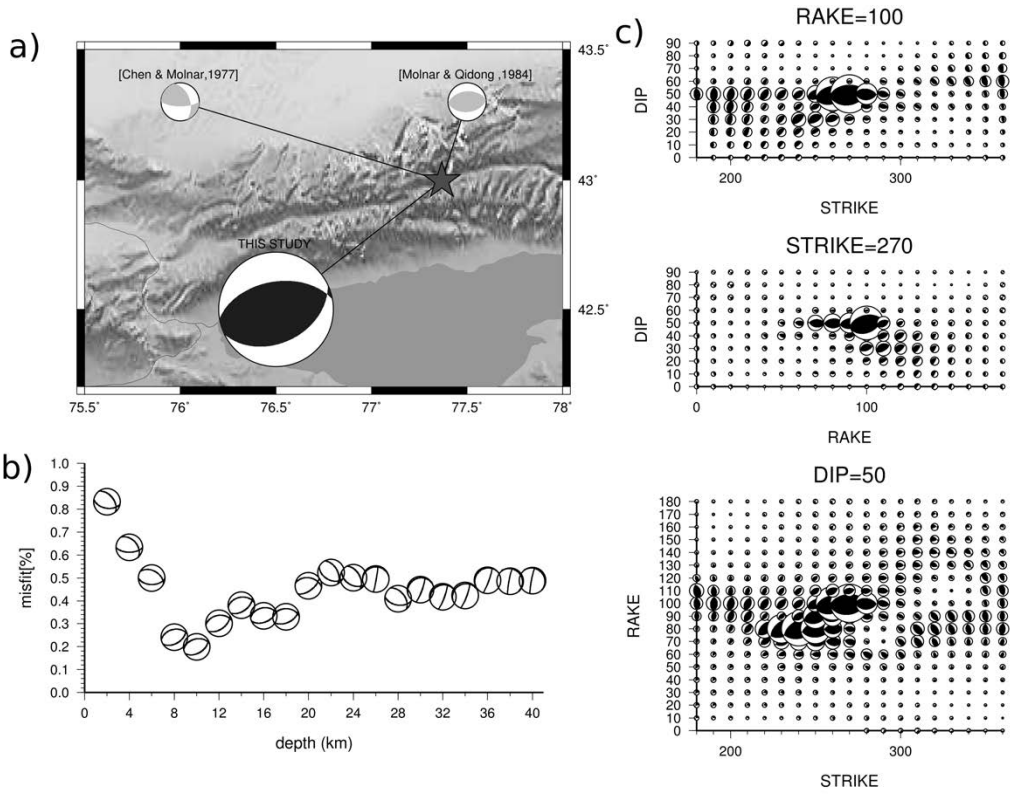

FIGURE 2.7: The results of focal mechanism determination for the Chon-Kemin earthquake based on amplitude ratios comparisons. The upper left figure (a) shows the tectonic map of the region; the epicentre is marked with the star; the grey beach balls show the focal mechanisms determined in two previous studies [*Chen & Molnar*, 1977] and [*Molnar & Qidong*, 1984]; the black beach ball shows the focal mechanism determined in this study. The lower left plot (b) shows the misfit function dynamics depending on the depth of the earthquake, showing minimum for the depth between 8 and 18 km. The three plots (c) on the right side represent the misfit function dynamics for the given rake, strike and dip accordingly.

for determination of M_0 mainly because the scaling was not possible (due to the lack of knowledge of real size of the image - the photos or microfilms of the seismograms). The scalar moment for the Chon-Kemin earthquake is estimated to be $M_0 = (1.21 \pm 0.4) \cdot 10^{21}$(Nm), which results in $M_w = 8.020 \pm 0.1$.

TABLE 2.3: Scalar moment and moment magnitude determination

#	Station	M_0	M_w
1	API	(2.47E+22)	(8.862)
2	DBN	2.36E+21	8.182
3	GTT	1.19E+21	7.984
4	HAM	1.58E+21	8.066
5	HLG	1.84E+21	8.109
6	HNG	-	-
7	CSM	9.86E+20	7.929
8	LEI	7.47E+20	7.849
9	MNH	1.23E+21	7.992
10	OTT	1.30E+21	8.010
11	PUL	-	-
12	RAV	-	-

13	RIV	1.16E+21	7.977
14	SIT	-	-
15	TAR	(5.12E+21)	(8.406)
16	TLO	1.79E+21	8.102
17	UCC	1.03E+21	7.941
18	VIE	9.53E+20	7.919
	Average	**1.35±0.5E+21**	**8.020±0.1**
	Median	**1.21±0.4E+21**	**7.988±0.1**

Figure *2.8* shows several examples of the observed and synthetic waveforms. The observed waveforms show true displacement amplitudes and the synthetics are scaled to the M_0 mentioned above. The plot mainly aims to show the amplitude fit and the amplitude ratios comparison. The waveforms fit, especially for S-waves, is far from being perfect, due to the point source approximation in the synthetics calculation. The long periods on the later part of the S-waves on European stations represent the so called "leaky mode, SPL", a high velocity surface wave component, which appears in the body waves part of the seismogram, due to its energy leakage from the multiple reflections [*Oliver*, 1961; *Phinney*, 1961]. This part of the seismogram is generated near the station, and it is hard to model it accurately with a global velocity model. The observed waveforms on PUL station are clipped, so the amplitudes do not fit to the synthetics. The more distant stations such as RIV and API are strongly disturbed and noisy, however for the station RIV the amplitude ratios fit is acceptable. The API station shows overall high amplitudes, which is believed to be partially due to wrong magnification information about the instrument and partially due to the station being located near the shoreline of a volcanic island and having special site conditions. It has to be mentioned that modelling of band-limited waveforms for such a large event like the Chon-Kemin earthquake with point source synthetics has limitations, which we focus on in the next section.

2.5 Kinematic parameters derivation

In order to derive kinematic source parameters for the Chon-Kemin earthquake we employed two datasets: observed surface rupture data reported by geological studies [*Bogdanovich et al.*, 1914; *Arrowsmith et al.*, 2005; *Delvaux et al.*, 2001] and teleseismic waveforms from the historical seismic stations. The original report from *Bogdanovich et al.* [1914] described comprehensively the surface damage after the Chon-Kemin earthquake, including detailed maps with landslides, rock-slides and surface crack locations, and the dimension of vertical offsets observed on the surface. The report described maximum vertical displacements on the surface up to 10 meter. Later, two other studies *Delvaux et al.* [2001] and *Arrowsmith et al.* [2005] followed the *Bogdanovich et al.* [1914] tracks and also documented the surface ruptures. *Arrowsmith et al.* [2005] have reported the vertical offsets observed on the surface after the Chon-Kemin earthquake in meters along the Kemin-Chilik fault zone (Figure *2.9*). The preferred maximum displacement of about ∼8 meter was observed 0.3° West from the epicentre located in our study. The average surface dislocation was about 3.2 meters and overall surface rupture extended to ∼200 km. Both *Delvaux et al.* [2001] and *Arrowsmith et al.* [2005] report 5 fault segments which ruptured during the Chon-Kemin earthquake in EW direction along the Kemin-Chilik fault. All the segments are oriented as oblique thrusts and showed both south and north dipping planes, with dip angle between 45° and 60°.

The analogue teleseismic records were used for multiple event analysis based on forward P-wave and S-wave modelling. The P and SH wave records (Figure *2.10*) allow a first estimate of the source

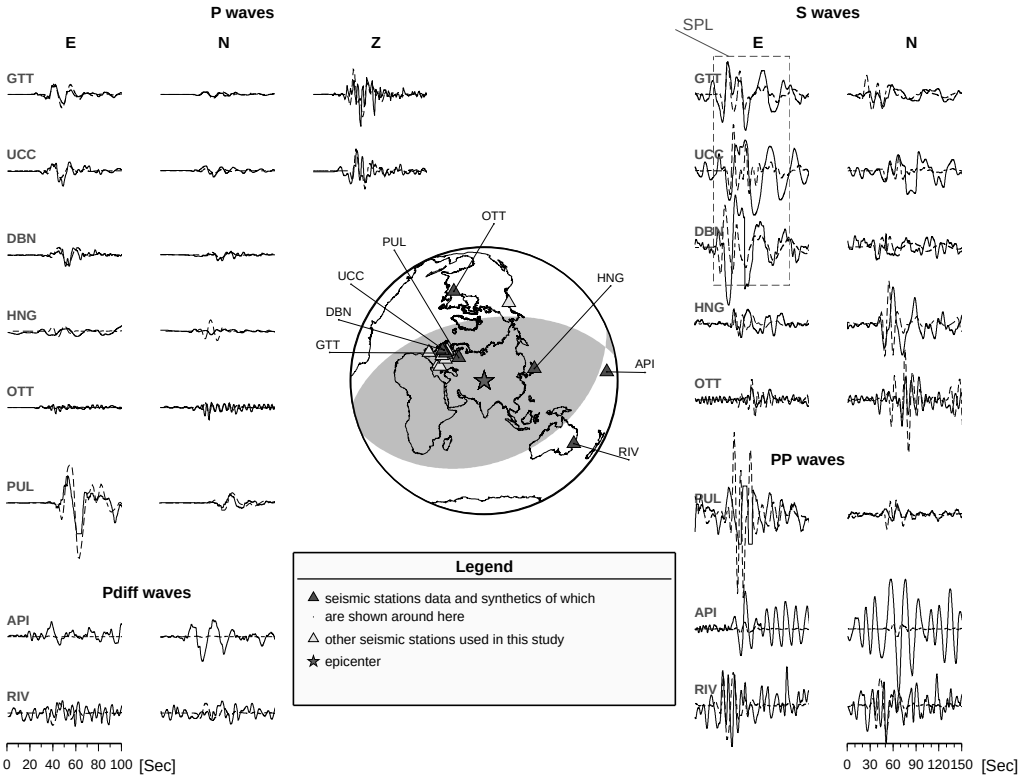

FIGURE 2.8: The synthetic and observed waveforms overlay for the Chon-Kemin earthquake. The stations location map is shown at the middle, with transparent overlay of the focal mechanism determined from amplitude ratios comparison. The stations are represented as a triangles: the dark grey triangles, accompanied by station abbreviations indicate the station the observed and synthetic data of which are shown on the left and the right sides of the plot, the white triangles show other stations which were also used to determine the mechanism and Mw of the Chon-Kemin earthquake. The left side of the plot shows the synthetic (dash lines) and observed (solid lines) data overlay for P and Pdiff waves. The right side shows the same for the S-waves and the PP-waves. On the top- right the SPL appearance is marked with a dashed rectangle. This plot shows only part of the waveforms used to determine the focal mechanism, as the whole data set is too large to be displayed here.

time duration and the number of sub-events of the Chon-Kemin earthquake. The earthquake was recorded by several European seismic stations which we use as a large aperture seismic array to align and stack the records. For P-waves this procedure is rather straightforward, because many of the stations in Europe were equipped with the same instrument type. Handling of S-waves was more problematic. We rotated a few carefully selected E and N components to isolate as much as possible the SH wave. Plotting all aligned traces together allows a rather easy differentiation between coherent source generated wavelets and coda produced by scattering near the stations. The P waves recorded on European stations (traces 8-19 Figure *2.10*) show about ∼50 seconds source duration, with two clear sub-events: The first sub-event amplitude is 3 times smaller than the second one and has a duration of ∼18 seconds, the second sub-event arrives 18 seconds after beginning of the rupture and lasts ∼32 seconds, the maximum slip occurred 25 seconds after beginning of the rupture. Some of the European stations (LEI, MNH, CSM) show an additional pulse on the P wave record ∼50 second after beginning of the rupture. This would extend the source duration up to ∼70 seconds, however it is questionable whether this pulse is related to the seismic source. The SH-wave records (traces 1-7, Figure *2.10*) are more noisy but two sub-events are also clearly observed. The

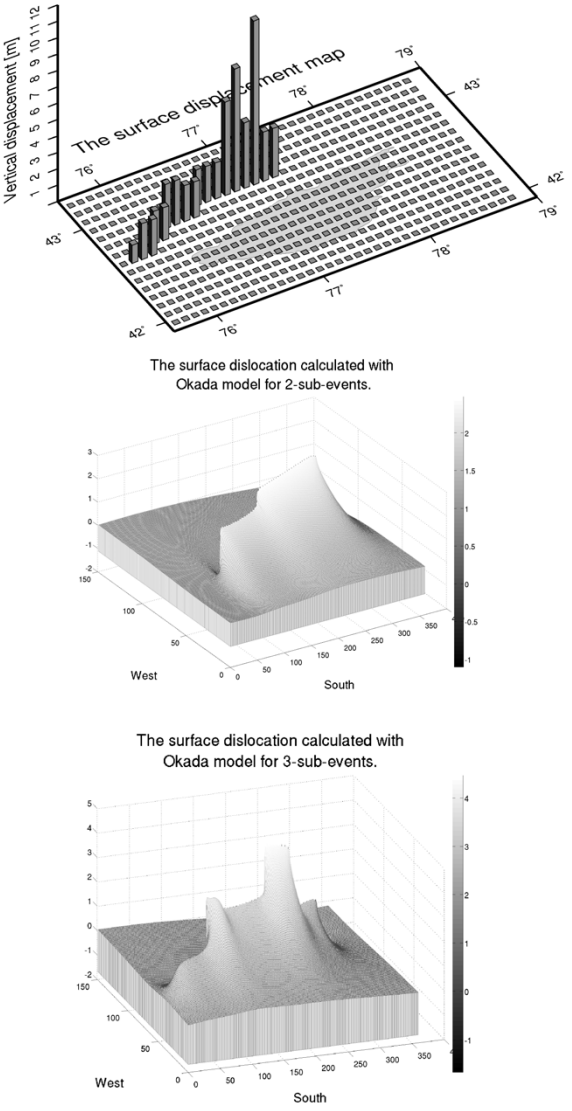

FIGURE 2.9: Top - The vertical offset observed on the surface and marked by geological expedition of Arrowsmith 2005. Middle - the surface dislocation calculated with the Okada dislocation model for an earthquake with the source parameters of the Chon-Kemin earthquake in case of 2 sub-events model where both sub-events ruptured to the surface. Bottom - the surface dislocation calculated with the Okada dislocation model in case of 3 sub-events model where two sub-events ruptured to the surface and 3rd sub-event rupture did not reach the surface.

third sub-event is partially found on a few stations (LEI and HAM).

The Kemin-Chilik fault lies in the EW direction, so comparison of the data from the stations located on the West and East are expected to show the directivity effect. However comparing the HNG seismogram in the East and the seismograms of european stations in the West no directivity is obvious. In general the Japanese seismic station HNG, which was equipped with a Bosch-Omori instrument with magnification factor of only 20, shows very small amplitudes, so that the P and SH wave duration is not clearly seen. The P wave recorded on the far away stations RIV and OTT has a very small amplitude and high noise level, and SH records from these stations suffer from superposition of SKS and S/S_{diff} and are hard to interpret.

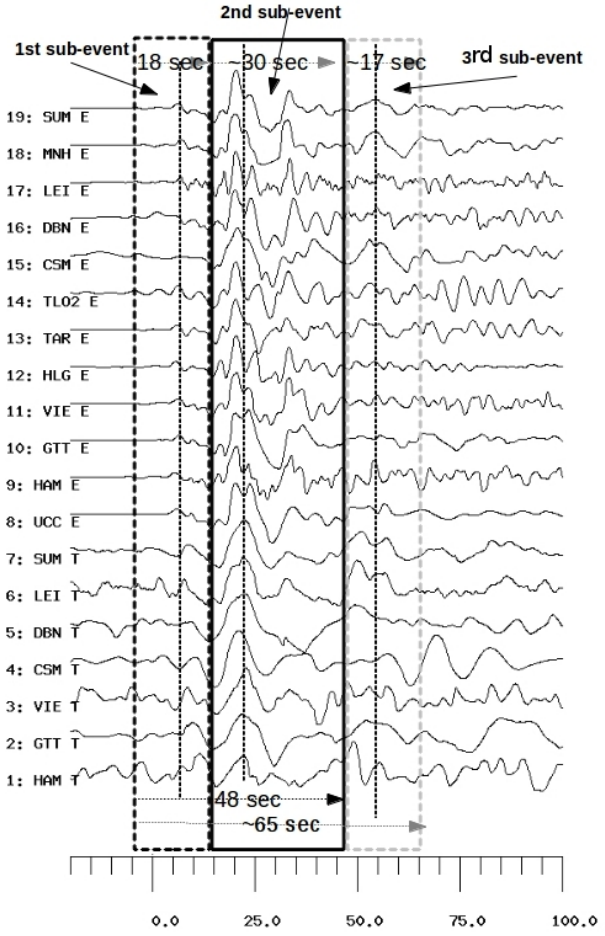

FIGURE 2.10: The P-wave and SH-wave records with corresponding station and component name. The black solid and dashed rectangles show the parts of the waveforms assigned to the first and second sub-events named accordingly. The grey dashed rectangle shows part of the seismogram assigned to the 3rd sub-event, the existence of which is discussed in the text. The duration of each sub-event is given in seconds attached to the arrow showing it's length. The records are scaled in amplitudes and aligned in time.

For our modelling we have used P and SH waves recorded mainly on the horizontal EW component of European stations. The period of the recording instruments varies between 8 and 14 seconds. The epicentre distances to the stations employed is between 42° and 60°, meaning that the PP wave which arrives between 100 and 130 seconds after the first P, is excluded from the P-wave modelling. Also the waveforms do not show clear depth phases (pP and sP). With the knowledge of the earthquakes focal mechanism obtained above we simulated synthetic waveforms with corresponding historical instrument parameters and compared them to the observed data in a grid search. For the waveform simulations we used a synthetic Greens function database calculated with the FOMOSTO tool in the PYROCKO [*Heimann*, 2014b] framework. The IASP91 velocity model [*Kennett & Engdahl*, 1991] was used in the calculation of the Greens function for several point sources. First the synthetic seismograms were created for a single point source (Figure *2.11*, top traces) located at hypocentre position. The second source is then introduced with the 0.1° shift northwards from the first source and with 1 second delay time. Following this initial step the locations and the times of both sources are allowed to shift in a grid search procedure. The sources are shifted with respect to each other in a space up to 1.5° northwards and 3.5° in the eastern direction with a step size of 0.1°, and in time with a step of one second. As a result the best waveform fit was obtained for the case, when the

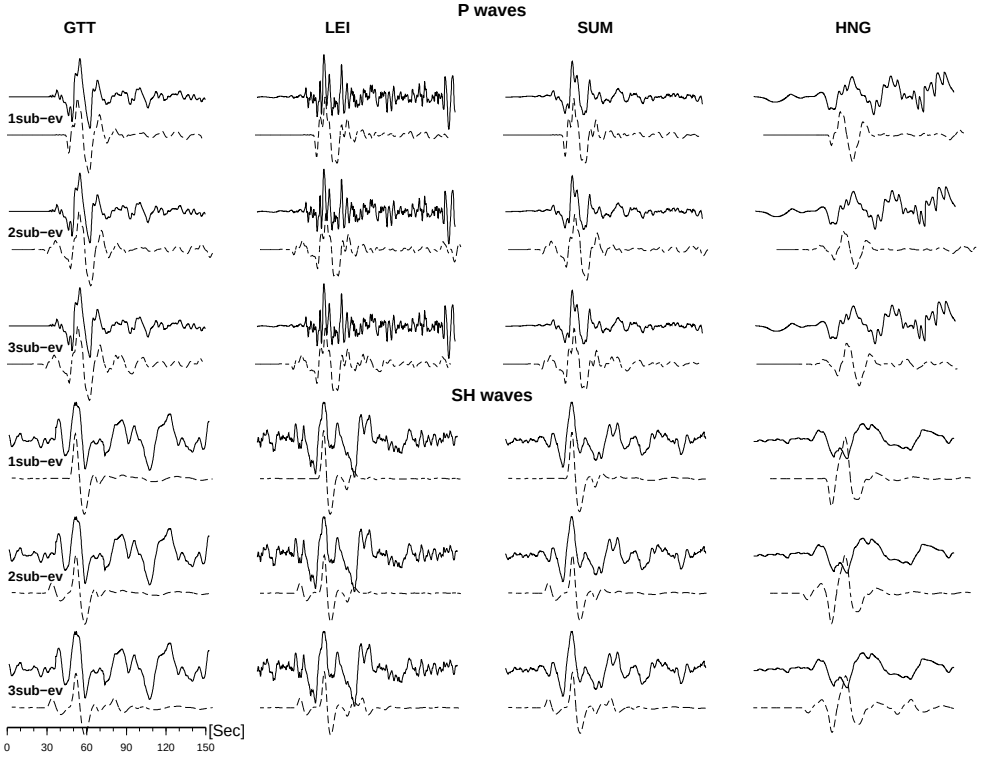

FIGURE 2.11: The synthetic and observed data waveform fit for 3 different multiple source models. The picture shows the synthetic and observed waveform fit with the corresponding station names, one column corresponds to one station, the top 3 traces show the P-waves, the bottom 3 traces show SH waves for 1,2 and 3 sub-events (sub-ev) model accordingly.

first smaller sub-event is located 52 km east from the second sub-event, and the second sub-event occurred 18 seconds after the first one (Figure *2.11*, middle traces). The moment ratio between the two sub-events is $\frac{1}{3}$ (which considering the second larger sub-event to have a maximum magnitude M_w8.02, means the first sub-event had magnitude M_w7.67). The third sub-event is then added on the same principle. The best waveform fit for the three sub-events model was found when the third sub-event occurs 52 seconds after the beginning of the rupture (first sub-event), 159 km west from the first sub-event and has magnitude M_w7.6. The third sub-event fits well to the 3rd pulse in the P and SH wave records which, however, is not observed in all records (Figure *2.11*, bottom traces). Such position and timing between the sub-events, obtained from the waveforms modelling, suggest the westward propagating rupture. Overall waveform modelling of three sub-events visually shows good waveform fit, however the misfit function shows less significant difference between the two and three sub-events models, than between the one and two sub-events model. Additionally, the modelling highlights that not all site effects and instrument parameters are correctly known, which explains some disagreement between the frequency content of the synthetic and observed data (e.g LEI, HNG).

To derive the dimensions of the fault plane (length and width) we modelled rectangular patches for the sub-events as a planar Haskell-type fault. The tests were performed for different fault lengths and widths, for a fixed depth and fixed rupture velocity in a grid search. However the waveform-fit error for different tests has shown no improvement compared to the two and three sub event point source models. Application of general scaling relations [*Blaser et al.*, 2010] leads to the following parameters: for the first smaller sub-event $L = 100km$, $W = 47km$, for the second

larger one $L = 160km$, $W = 67km$, resulting in a total rupture length of ∼260 km. In the case of the three sub-events model the third - the smallest sub-event has a length of $L = 92km$ and $W = 43km$, resulting in a overall ∼300 km long rupture. These fault length and width values taken together with the scalar seismic moment of $M_0 = 1.21 \cdot 10^{21}[N \cdot m]$ and a shear modulus of $\mu = 3.38 \cdot 10^{10}[N/m^2]$ (calculated from velocity model from *Alinaghi & Krüger* [2014]) suggest an average slip of $D \approx 3.0[m]$.

The Okada dislocation model [*Okada*, 1985] was employed in order to check the results obtained with the scaling relations, in order to estimate the resulting surface rupture. We used the above calculated fault length, width and slip values as input parameters for the Okada dislocation modelling, assuming both scenarios, i.e. when the whole fault or only part of it ruptured to the surface. The surface dislocation modelled with the Okada approach was compared to the observed surface rupture in a grid search trying to find the best fit for the calculated and observed vertical offsets. The best fit was found for two likely scenarios: either the Chon-Kemin earthquake consisted of only two sub-events which both ruptured to the surface (Figure *2.9*, middle), or it consisted of 3 sub-events but one of the smaller sub-events (first or third one) did not rupture to the surface (Figure *2.9*, bottom). The results of both test scenarios show on average around 3 m vertical offset agreeing well with 3.2 m of slip observed in geological studies [*Arrowsmith et al.*, 2005]

2.6 Discussion

The Chon-Kemin earthquake belongs to the major earthquake sequence which took place in the Northern Tien-Shan region at the turn of the 19th century. Although this sequence included several $M > 7.0$ earthquakes, only the Chon-Kemin earthquake has been recorded by well calibrated seismic instruments providing a reasonable data collection for source studies. Moreover this earthquake remains the strongest instrumentally recorded earthquake in the Northern Tien-Shan region up to the present. The uniqueness of the Chon-Kemin earthquake however serves as a limitation in the application of standard source parameter determination techniques. For example it is impossible to derive any information from the comparison of the Chon-Kemin earthquake with a similar modern event as it was done for other historical earthquakes (e.g. [*Kanamori et al.*, 2010]), simply because the Tien-Shan region has not been affected by an earthquake comparable in magnitude to Chon-Kemin since 1911. Moreover thrust intraplate earthquakes of such magnitude, are rarely observed in seismology, therefore there is no real comparison between Tien-Shan and any other region in the world. Nevertheless the present study provides a detailed analysis of the Chon-Kemin earthquake using historical seismograms, which were collected with particular effort. This dataset is presently the most complete dataset ever collected for the Chon-Kemin earthquake and has been successfully used to determine its source parameters.

The location of the earthquakes epicenter had at first shown some problems and relatively large uncertainties. Subsequently the combined usage of the digitized waveforms and the bulletin information decreased the epicenter location uncertainties to 0.6° (∼65 km). The newly located epicenter agrees well with the surface rupture assigned to the Chon-Kemin earthquake by very detailed geological studies [*Delvaux et al.*, 2001; *Arrowsmith et al.*, 2005; *Bogdanovich et al.*, 1914]. The hypocenter depth value remains the most uncertain parameter for the Chon-Kemin earthquake. However: the results of the HYPOSAT location, the absence of distinct clear depth phases, the results of the grid search over depths in the focal mechanism determination and the appearance of the earthquake rupture on the surface (large vertical offsets); all indicate a shallow depth (∼20 km), constrained to the seismogenic zone.

Different magnitude types (m_B, M_s, M_w) of the Chon-Kemin earthquake, calculated from the waveform amplitudes, show errors up to 0.3, which originates from the uncertainties in the magnification factor of the corresponding instruments (see the Appendix *B.2*) and the unmodelled site effects. However different ways of determining the magnitude - m_B and M_s directly from the measured amplitudes - and the M_w from the waveform modeling; all show that the Chon-Kemin was rather a major earthquake with magnitude between 7.9 and 8.1. This magnitude is smaller than the value 8.4 from *Gutenberg & Richter* [1954], but on the other hand it is larger than the magnitude reported by *Chen & Molnar* [1977] and the most recent from *Storchak et al.* [2013]. Thus the magnitude determined in this study is an important resource for the other studies aiming to assess seismic hazard in the region.

The focal mechanism of the Chon-Kemin earthquake presented in this study agrees very well with geological observation and the modern seismicity in the area. The amplitude ratios comparison method used to determine the mechanism is believed to be a reliable way to determine the mechanism for historical earthquakes like the Chon-Kemin event, because it is less dependent on the data quality, the exact knowledge of the historical instrument parameters and the polarities of the waveforms. The knowledge of the source mechanism determined by the amplitudes ratios comparison method was a prerequisite for more detailed source modeling aiming to derive the kinematic source parameters.

In this study we chose to model the extended source by multiple event analysis, which showed that at least two sub-events are necessary to model the waveforms. The best visual waveform fit was observed for three sub-events. However the misfit function showed relatively low resolution and the third sub-event was obvious only on some records. This leads us to the conclusion that the complex source model suggested by *Delvaux et al.* [2001] and *Arrowsmith et al.* [2005] from geological field observations including five fault segments, can neither be confirmed nor contradicted by teleseismic waveform analysis. Because the slip distribution at depth and the dip of different fault segments at depth are difficult to estimate from a surface rupture information alone, we did not try to use the geological model in its details as a prior information to model kinematic source beyond the three sub-events model. Nevertheless the simplified source model of the three rectangular patches sharing a common focal mechanism is sufficient to explain the seismological data. The scalar moments ratio of the sub-events and their distribution in space and time was determined from the waveform modeling with a reasonable value for rupture velocity of ∼2.9km/s. The absence of a strong directivity effect on the Eastern and Western stations makes inferences about the rupture propagation direction difficult. The fact that the time difference between sub-events was larger for SH waves than for P waves could be interpreted as prevailing eastward propagation of the rupture, however that is rather weak evidence due to the low data quality for SH waves. Furthermore the modeling of the sub-events location has shown that the rupture propagated from East to West. Generally ∼50 or ∼70 (in case of three sub-events) seconds rupture duration is rather short for a M_w8.0 earthquake. But the same phenomenon of short source time duration was observed for one of the 1905 great Mongolian strike-slip earthquakes [*Schlupp & Cisternas*, 2007] - the Tsetseleg M8.0 earthquake, the duration was ∼65 seconds. It should be kept in mind that there is some influence of the recording instrument, which had mainly 8-14 seconds period. For example, the 2008 Wenchuan Mw8.0 earthquake has much longer P wave duration on European stations than the Chon-Kemin earthquake. The Wenchuan earthquake was recorded by modern broadband station CLL (Colm Observatory, Germany) and a still operating analogue Wiechert instrument located just 200 m apart. The currently operating LEI station is equipped with an identical instrument to the historical LEI station but was moved from the city of Leipzig to CLL in the year 1921. Comparing those records (Figure *2.6*) it is obvious that the apparent P wave duration recorded by the broad band instrument is ∼15 seconds longer

than that from the real and simulated Wiechert instrument. It may mean that the true source time duration is longer than what we observe on the P or SH wave records of the historical instruments.

The final waveform modeling of the Chon-Kemin earthquake does not show more than three sub-events, with an overall maximum source duration of 70 seconds, which in case of unilateral rupture and taking the rupture velocity as 2.9 would produce ∼200 km rupture. However the large magnitude of all three sub-events and scaling relations suggest a longer rupture. The probability that the rupture propagated bilaterally with more dominant propagation westwards would solve this issue, it would also explain the lack of a strong directivity effect and shows good agreement with the geological five fault segments model proposed by *Arrowsmith et al.* [2005] (see Figure *2.12*).

Taking into account all the factors mentioned above we suggest that the Chon-Kemin earthquake ruptured between ∼260 and ∼300 km along the whole Kemin-Chilik fault zone. The rupture width obtained from scaling relation suggests that the rupture propagated at its maximum width down to the crust-mantel boundary (∼55km [*Vinnik et al.*, 2004; *Alinaghi & Krüger*, 2014]). The rupture started on the Eastern segment of the Kemin-Chilik fault and propagated in both directions with a stronger impulse westward (Figure *2.12*), first rupturing the small plane, then the largest sub-event occurred corresponding to maximum moment release and then the third fault segment ruptured on the western most part of the fault rupture. The average 3.1 meter slip derived from the proposed fault model is generally in a good agreement with the vertical surface displacement observed by several geological studies [*Delvaux et al.*, 2001; *Arrowsmith et al.*, 2005; *Bogdanovich et al.*, 1914].

The geological studies of *Delvaux et al.* [2001] and *Arrowsmith et al.* [2005] have observed a series of surface breaks identified as five various fault segments characterized by particular orientation, inclination, and kinematics. This complex model agrees with the three rectangular patches fault model proposed here (see Appendix *2.13*). Considering the fact that, the Kemin-Chilik strike-slip fault at depth acts as a nucleation point for a slip-partitioned system composed of numerous high-angle reverse faults forming the whole Chon-Kemin-Chilik fault system, and the fact that the ∼260-300 km rupture propagated to the Moho depths, below that nucleation point (approximately 20 km [*Selander et al.*, 2012]); it is believed that all the segments of the Kemin-Chilik fault system have been activated during these large earthquakes. Supposing that the rupture along the different shallower segments occurred simultaneously it is hard to distinguish individual smaller segments contribution to the overall source time function.

2.7 Conclusion

This study has shown that even with all the uncertainties and difficulties the historical seismograms remain an important source of information and can be successfully used to determine the source parameters of historical earthquakes.

Special effort has been spent on recovering digital seismograms from the analogue instrument recordings. From those waveforms and the historical bulletin information the earthquakes epicenter has been relocated to a position which agrees with the surface rupture. The magnitudes: m_B8.05, M_s7.94, M_w8.02; were calculated from the waveform amplitudes. Though the uncertainty of the magnitudes varies between 0.2 and 0.3 it has been clearly confirmed that the Chon-Kemin earthquake was truly the largest instrumentally recorded earthquake in the region, though the magnitude was slightly smaller than previously reported. All the amplitude values and corresponding periods are presented in the Appendix *2.8.3*.

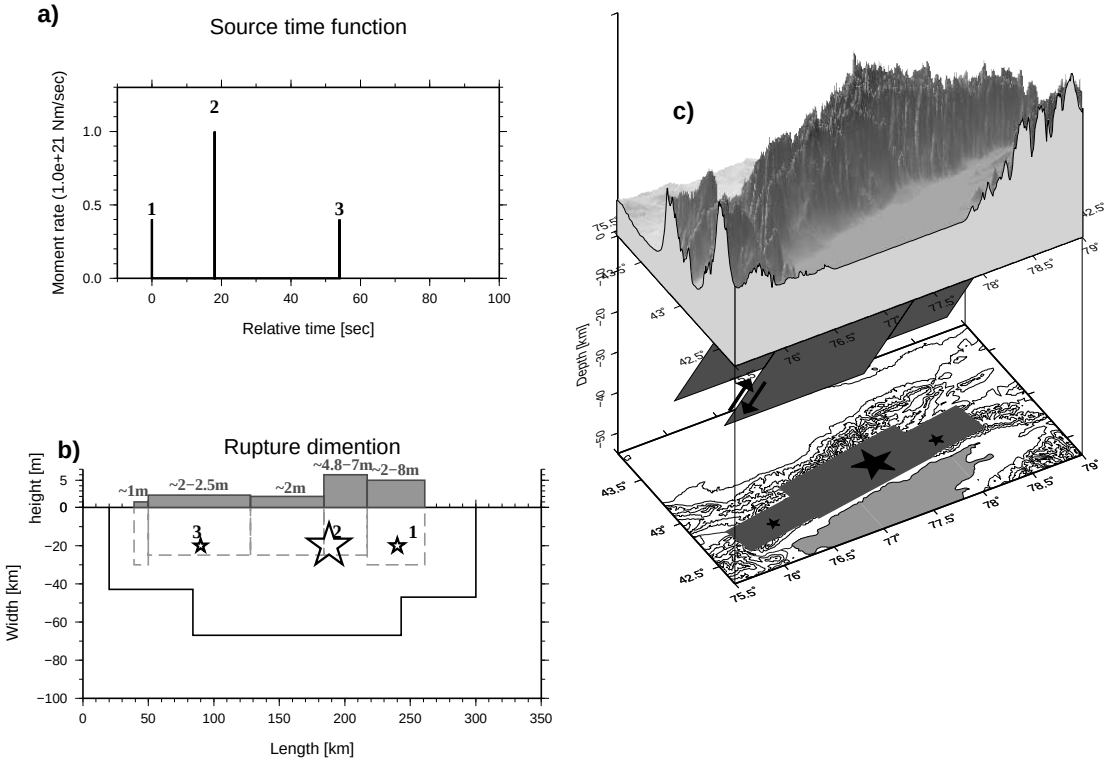

FIGURE 2.12: Description of the source parameters for the Chon-Kemin earthquake. The top (a) picture is the rough representation of the source time function as a pulse for three sub-events, the pulses are scaled to the corresponding scalar moment of each sub-event; Below this -(b)- the suggested rupture dimension and distribution of the sub-events on the rupture plane is shown. The stars show the sub-events numerated accordingly, the size of each star is proportional to the scalar seismic moment of the sub-event. The solid black line shows the extend of the rupture, obtained from three sub-events model using scaling relations. The gray dashed rectangles show the fault planes suggested by *Arrowsmith et al.* [2005], the vertical displacement observed on the surface by *Arrowsmith et al.* [2005] is shown as gray shaded rectangular blocks with corresponding height given in meter for each rectangle. The right side picture -(c) – the represents the 3D view of the Chon-Kemin source model: the bottom picture is the 2D projection of the fault planes on the regional map with sub-events marked as stars and numerated accordingly, covered on top by the topography map of the region, the relative motion of the fault planes is given with black arrows showing the dip direction.

Due to the low data quality and poorly recorded instrument characteristics the standard waveforms modeling and moment tensor inversion methods could not be applied for this earthquake. For that reason the focal mechanism was determined based on a newly developed amplitude ratios comparison method, which showed that the Chon-Kemin earthquake had a thrust mechanism with 264°N strike and 52° dip angles. This perfectly agrees with the modern moderate seismicity on the Kemin-Chilik fault system.

Knowing the focal mechanism and using the detailed surface rupture information as an additional constraint, the kinematic source parameters were derived, with application of general scaling relations and P wave modeling. It was concluded that the Chon-Kemin earthquake ruptured ∼260-300 km along the Chon-Kemin-Chilik fault propagating mainly bilaterally with prevailing propagation westwards, which explains the relative short source time duration. Usage of a multiple events approach has shown that the rupture process included at least two sub-events, with the scalar moment

ratio between them of about $\frac{1}{3}$. Also an evidence of the third sub-event was retrieved from the waveforms. According to scaling relations the length of the rupture for the first segment was about 100 km, for the second 160 km and for the third 92 km, making ∼300 km in total, assuming that the segments overlap and the rupture width was 46, 67 and 43 km respectively. The average slip of the earthquake was ∼3.0 meters, which agrees well with the average surface rupture observations, considering that the rupture reached the surface almost for the whole length (around 200 km).

This study is considered to be a valuable contribution to the general understanding of intracontinetal thrust earthquakes of such magnitudes, due to their rare occurrence. It is also of crucial importance for estimating the seismic hazard measures in the region of the Northern Tien-Shan. Additionally this study demonstrates the value of the preservation and further investigation of analogue seismic records.

Acknowledgments

We would like to express our deepest gratitude to all the people who helped us to collect the historical seismograms: Manfred Herden, Dr. Muzli, Dr. Muksin, Prof. Dr. Torsten Dahm, Marius Kriegerowski, Prof. Dr. Thomas Meier, Annika Fediuk, Kristin Burmeister, Dr. Siegfried Wendt, Pia Buchholz, Dr. Joachim Wassermann, Dr. Rudolf Widmer-Schnidrig, Marina Lopez Muga, Dr. Susana Custodio, Mr. Ivo Allegretti - without you this work would not be possible.

We are particularly grateful to the EUROSISMOS project and INGV, Rome for providing the historical seismogram database, especially we thank Dr Graziano Ferrari and Silvia Fillosa for their assistance in getting the seismograms, and Luca Arcoraci and Matteo Quintiliani for their help with TESEO software. We would like to express our very great appreciation to USGS, Golden, Colorado and particularly Dr. James Dewey for his very kind professional guidance through the data collection and digitizing process. Also special thanks should be given to the Dr. Josep Batllo for his valuable and constructive suggestions during our work with historical data.

Our grateful thanks are also extended to Tim Sonnemann for developing the seismogram digitization program; to Dr. Sebastian Heimann for providing the precalculated Greens function database and always kindly assisting in the work with Pyrocko software; to Prof. Ramon Arrowsmith for allowing to use their geological data in our research; and to Dr. Angela Landgraf for her advice and comments on geological part of this work.

This research has been done in the framework of PROGRESS project ($http://www.earth-in-progress.de/index.35.de.html$) and we sincerely thank the German Federal Ministry of Education and Research for the financial support of this project. Moreover we thank the TIPTIMON project, also funded by German Federal Ministry of Education and Research, for the additional financial help to cover some of the travel expenses.

In this work we have used open source software and would like to gratefully acknowledge: GMT - The Generic Mapping Tools developed by Paul Wessel and Walter H. F. Smith; Seismic Handler (seismic waveform analysis tool) developed by Dr. Klaus Stammler and Dr. Marcus Walther; and Pyrocko (a seismology toolbox and library) developed by Dr. Sebastian Heimann.

2.8 Appendix

2.8.1 Seismological analysis of geological source model

The *Arrowsmith et al.* [2005] and *Delvaux et al.* [2001] have presented their geological model of the source of the Chon-Kemin earthquake consisting of 5 fault segments. The *Arrowsmith et al.* [2005] have measured the dip angles and the slip on the source of each of the five segments. The summarized version of the results of *Arrowsmith et al.* [2005] investigation is presented on the Figure *2.13*. In order to check the agreement of this representation with the observed waveforms we modelled the waveforms which would be produced by a source such as suggested by *Arrowsmith et al.* [2005]. We have calculated the relative M_0 for each of the fault segments from it's slip and the area: $M_0 = \mu\vec{D}A$, μ is the shear modulus, D is the slip taken from *Arrowsmith et al.* [2005] and A - is the fault segment area (the length of the segments is know and the width was calculated from the scaling relations [*Blaser et al.*, 2010], the rupture velocity was taken from the kinematic source modelling presented in this work, as $2.9[km/s]$).

Since the geological model does not give any information of the dynamic of the rupture process we have tried modelling 3 sets of synthetic seismograms for 3 different cases of the rupture propagation, the synthetics were then compared to the observed data. First the possibility of the unilateral rupture propagating from West to East (from the segment 1 to 5) was tested, the general the waveforms fit to the observed data at the beginning, but the apparent source time duration is longer than the observed one, and the relative moment of the segments seems to differ from the observed one. The bilateral propagating rupture shows the best waveform-fit among the three tests, however it is still worse than the waveform-fit from the our three sub-event model proposed above. The East-West propagating unilateral rupture shows the worst waveform fit of all three test, also any phase shift can not be found to fit the data. Further test of different combination of bilateral and West-East propagating rupture leads to the model very similar to our there sub-events model proposed in the main body of this work. The model where the rupture start at the segment 2 (Figure *2.13*) and propagates to the east and west, triggering on the east the 2nd sub-event which can be interpreted as rupture of the segments 3-4 (Figure *2.13*) together with the realise of the largest moment, then the 3rd sub-event might explain ruptures the segments number 5.

2.8.2 Additional information on the data collection

51 seismograms from 23 seismic stations worldwide have been collected for the present study. During the time period covered by our investigation most of the stations were equipped with 2 horizontal components, instruments oriented NS and EW or NW and NE, while only 2 stations additionally had a vertical instrument (UCC and GTT). The station names and coordinates are given in Table *2.4*, including information about each institute which provided those seismic records and the contact person name. Further information about obtaining the seismograms from the mentioned institutes can be provided upon request. The information presented in the column 7 of Table 3 indicates whether the provided seismograms were available and used in the present study, as the possibility to digitize data crucially depends on the seismograms quality. Therefore the remarks on quality of each record individually as well as the description of the reasons to waive some seismograms are provided below.

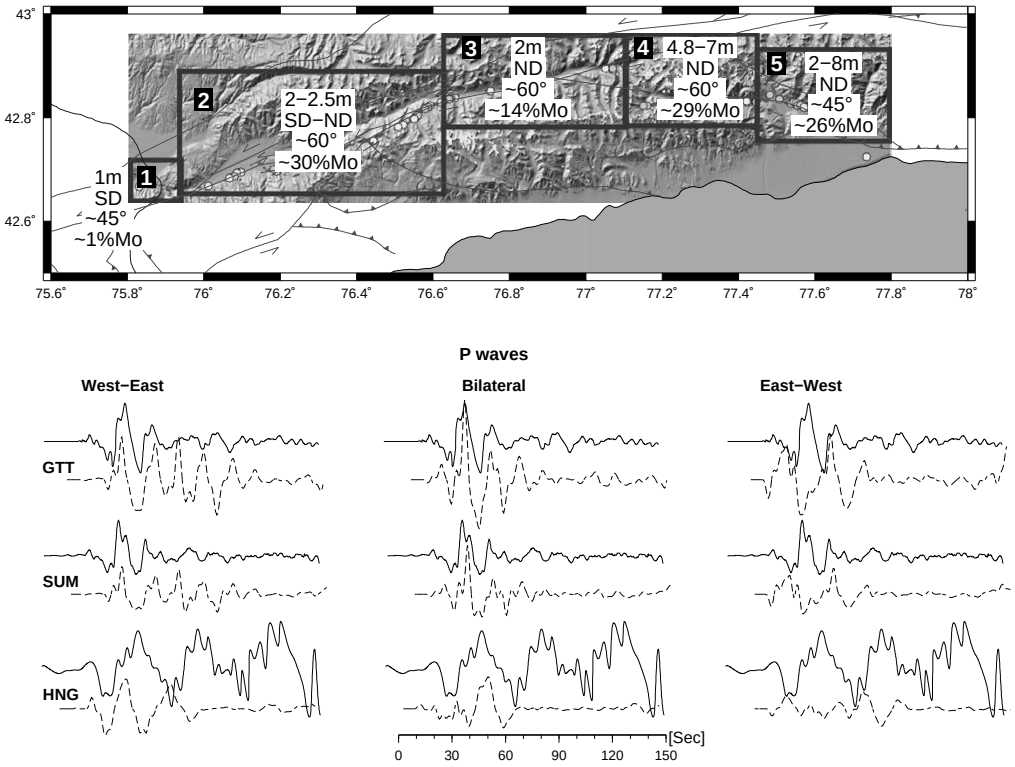

FIGURE 2.13: The representation of the geological source model (after *Arrowsmith et al.* [2005]) for the Chon-Kemin earthquake. The top of the picture (a) shows the map of the epicentre area with the topography map covering the area affected by the surface rupture from the study of *Arrowsmith et al.* [2005]. The segments 1,2,3,4,5 are given as dark gray rectangles according to the *Arrowsmith et al.* [2005] representation, each segments is characterised by a number of parameters shown as a black text on white background in the corresponding rectangle: the first line shows preferred slip given in meter (m); second line gives the fault plane orientation (ND stays for north-dipping, SD- for south-dipping, and the ND-SD is a mixture of both); the third line shows the approximate dip angle; and the last line shows the relative contribution of each segment in to the overall scalar moment of the earthquake in percent (%). The lower part of the plot shows the comparison of the observed data (solid lines) and their synthetic prediction (dashed line) for the proposed source model, for three cases of the rupture propagation: West-East propagating unilateral rupture (from segment 1 to 5); the bilateral propagating rupture from 3 to 1 and to 5 simultaneously; and for the East-West propagating unilateral rupture from segment 5 to 1.

TABLE 2.4: The list of seismic stations used in this study including the information about each institution, which provided the seismic records and the contact person name at the time, when the data were collected.

Station name	Latitude	Longitude	Instrument	Comp [3]	A/U [4]	Received From	Contact Person
API (Apia, Samoa Island)	-13.8072	-171.7500	Wiechert	NS	+/+	Institute of Geophysics, University of Goettingen	Mr. Manfred Herden
				EW	+/+		
				Z	−/−		
DJA (Batavia, Jakarta)	-6.1800	106.7400	Wiechert	NS	+/+	Indonesian Agency for Meteorology, Climatology and Geophysics, Jakarta Indonesia	Dr. Muzli
				EW	+/−		
DBN (De Bilt, Netherlands)	52.1000	5.1833	Wiechert	NS	+/+	INGV Rome, Italy	Silvia Filosa
				EW	+/−		Dr Graziano Ferrari

[3] *Comp* means the component of the instrument

[4] The sign (+) or (−) indicates availability and usage of the seismograms. The first sign shows if the data were available (+) or not (−) the second sign indicates if they were used.

			Bosch-	NS	+/+		
			-Omori	EW	+/+		
DEN (Denver,	39.6767	-104.9483	Wiechert	NS	+/−	USCS, Golden Colorado	Dr. James Dewey
USA)				EW	+/−	(The microfilms archive)	
GTT (Goettingen,	51.5500	9.9667	Wiechert	NS	+/+	Institute of Geophysics,	Mr. Manfred Herden
Germany)				EW	+/+	University of Goettingen	
				Z	+/+		
HAM (Hamburg,	53.5594	9.9811	Wiechert	NS	+/+	Institute of Geophysics,	Prof. Dr. Torsten Dahm
Germany)				EW	+/+	University of Hamburg	
HLG (Helgoland,	54.1794	7.8828	Wiechert	NS	+/+	Institute of Geosciences,	Prof. Dr. Thomas Meier
Germnany)				EW	+/+	University of Kiel	
HNG (Hongo,	35.7111	139.7664	Omori	NS	+/+	USCS, Golden Colorado	Dr. James Dewey
Tokyo, Japan)				EW	+/+	(The microfilms archive).	
				Z	+/−		
CSM (CasaMi.	40.7450	13.9033	Vicentini	NS	+/+	INGV Rome, Italy	Silvia Filosa
Ischia, Italy)				EW	+/+		Dr Graziano Ferrari
PDI (Porto Di	40.7400	13.9433	Vicentini	NS	+/−	INGV Rome, Italy	Silvia Filosa
Ischia,Italy)				EW	+/−		Dr Graziano Ferrari
LEI(Leipzig,	51.3350	12.3917	Wiechert	NS	+/+	Observatory Collm, Inst.	Dr. Siegfried Wendt
Germany)				EW	+/+	of Geophysics and Geology,	
						University of Leipzig	
MNH (Munich,	48.1461	11.6086	Wiechert	NS	+/+	Department of Earth and	Dr. Joachim Wassermann
Germany)				EW	+/+	Environmental Sciences,	
						Ludwig-Maximilians-	
						University	
OTT (Ottawa,	45.3939	-75.7158	Wiechert	NS	+/+	USCS, Golden Colorado	Dr. James Dewey
Canada)				EW	+/+	(The microfilms archive).	
PUL (Pulkovo,	59.7700	30.3200	Galizin	NS	+/−	[*Galitzin*, 1911a]	
USSR)				EW	+/−		
RIV (Riverview,	-33.9833	151.1667	Wiechert	NS	+/+	USCS, Golden Colorado	Dr. James Dewey
Australia)				EW	+/+	(The microfilms archive)	
SIT (Sitka,	57.0500	135.3335	Bosch-	NS	+/+	USCS, Golden Colorado	Dr. James Dewey
Alaska)			-Omori	EW	+/+	(The microfilms archive)	
SLM (San Luis,	38.6300	-90.2300	Wiechert	NS	+/−	USCS, Golden Colorado	Dr. James Dewey
Missouri, USA)				EW	+/−	(The microfilms archive)	
RAV (Ravensburg,	47.7800	9.6100	Conrad	NS	+/+	Institute for Geophysics,	Dr. Rudolf Widmer-
Germany)						University of Stuttgart	Schnidrig
TAR (Taranto,	40.4750	17.2542	Wiechert	NS	+/+	INGV Rome, Italy	Silvia Filosa
Italy)				EW	+/+		Dr Graziano Ferrari
TLO (Toledo,	39.8571	-4.0246	Rebeur-	NS	+/+	National Archives Geodetic	Ms. Marina Lopez Muga
Spain)			-Ehlert	EW	+/+	and Geophysical Data,	
			Milne	EW	+/+	Geophysical Observatory	
						Of Toledo	
VIE (Vienna,	48.2481	16.3617	Wiechert	NS	+/+	INGV Rome, Italy	Silvia Filosa
Austria)				EW	+/+		Dr Graziano Ferrari
UCC (Uccle,	50.7988	4.3586	Wiechert	NS	+/+	(reproduction from a book)	[*Lagrange*, 1911]
Belgium)				EW	+/+		
				Z	+/+		
ZAG (Zagreb,	45.8200	15.9800	Wiechert	NS	+/−	Faculty of Science,	Mr. Ivo Allegretti
Croatia)				EW	+/−	University of Zagreb	

2.8.3 Additional information on earthquake relocation and magnitude

Additional detailed information used to relocate the earthquake and determine the body wave magnitude m_B (Table *2.5*) and the data used to determine the surface wave magnitude M_s presented in extra-table (Table *2.6*).

TABLE 2.5: The station list with all arrival times for all the phases which were available for the Chon-Kemin earthquake from the digitized waveforms and both local and teleseismic bulletins. The table also includes distances and azimuths to all the station, and the amplitude and period values where they were available. If the amplitude and the period columns are empty it means either that the value is not available or, in case of the waveforms, it means that the waveforms were photographed (microfilms) and the true amplitude can not be recovered due to the lack of information about photo-camera.

Station name	Distance[5]	Azimuth	Comp[6]	Phase	Arrival time	T[7]	Amp[8]	m_B	Source
Local bulletins									
TAS (Tashkent,	6.2216	257.2114	-	Pn	23:27:27.00				[*Nikiforov*, 1912]
Uzbekistan)			-	Sn	23:28:55.00				
SVE (Sverdlovsk,	17.4580	328.1534	-	P	23:30:05.00				[*Nikiforov*, 1912]
Russia)			-	S	23:33:37.00				
BLCA (Balakhany,	20.6112	272.2761	-	P	23:30:22.00				[*Nikiforov*, 1912]
Azerbaijan)			-	S	23:34:10.00				
BAK (Baku,	20.6674	272.1159	-	P	23:30:26.00				[*Nikiforov*, 1912]
Azerbaijan)			-						
IRK (Irkutsk,	20.2857	53.4287	-	P	23:30:24.00				[*Nikiforov*, 1912]
Russia)			-	S	23:34:18.00				
KAB (Kabansk,	21.6051	55.0432	-	P	23:31:06.00				[*Nikiforov*, 1912]
Russia)			-	S	23:35:19.00				
PYA (Pyatigorsk,	24.7960	284.2631	-	P	23:31:10.00				[*Nikiforov*, 1912]
Russia)			-	S	23:35:57.00				
Teleseismic bulletins									
DBN (De Bilt,	47.6794	307.4129	EW	P	23:34:27.00	6	130	8.54	[*Koninklijk*, 1915]
Netherlands)			EW	PP	23:36:33.00	11	150	7.93	
			EW	S	23:41:47.00	22	740	8.23	
			NS	SS	23:45:00.00	23	1790	-	
GTT (Goettingen,	45.0291	305.4267	Z	P	23:33:59.00	14	450	8.21	[*Ansel*, 1913]
Germany)			Z	PP	23:36:03.00	17	600	8.45	
			EW	S	23:40:54.00	31	2000	8.51	
			EW	SS	23:44:10.00	14	400	-	
HAM (Hamburg,	44.4690	308.1732	EW	P	23:33:59.00	13	100	7.79	Handwritten bulletin
Germany)			EW	PP	23:36:08.00	14	210	8.03	from Hamburg station,
			EW	S	23:40:50.00	21	220	7.52	found in Hamburg
			EW	SS	23:44:12.00	20	740	-	University library.
POT (Potsdam,	42.9553	305.8468	EW	P	23:33:47.00	3	160	8.40	Seismic Bulletin
Germany)			EW	PP	23:35:48.00	10	500	8.30	from Potsdam Station
			EW	S	23:40:54.00	-	400		received from
			NS	SS	23:43:00.00	-	370		F.S. Uni. Jena
JEN (Jena ,	44.2246	304.1935	Z	P	23:33:49.00	5	62	7.59	Seismic Bulletin
Germany)			Z	PP	23:35:59.00	5	110	8.04	from Jena
			EW	P	23:33:53.00	15	134	7.65	Seismic Station
			EW	PP	23:35:59.00	15	460	8.29	
			EW	S	23:40:30.00	13	154	7.57	
			EW	SS	23:43:50.00	12	426	-	
MNH (Munich,	45.0621	300.3805	-	P	23:34:01.00	-	-	-	
Germany)			-	S	23:40:57.00	-	-	-	
STR (Strassburg,	47.3279	302.1561	-	P	23:34:18.00	-	-	-	
Germany)			-	S	23:41:16.00	-	-	-	
HEI (Heidelberg,	46.4458	302.9112	-	P	23:34:12.00	-	-	-	
Germany)			-	S	23:41:39.00	-	-	-	
HOH (Hohenheim,	46.3710	301.8766	-	P	23:34:18.00	-	-	-	
Germany)			-	S	23:41:30.00	-	-	-	
AAC (Aachen,	47.5904	305.4730	-	P	23:34:23.00	-	-	-	
Germany)			-	S	23:41:28.00	-	-	-	
HNL Honolulu,	98.1976	50.8649	-	P	23:40:06.00	-	-	-	[*Hazard, D. L.* , 1913]
Hawaii, USA)			-	S	23:57:36.00	-	-	-	
SIT (Sitka,	76.5602	17.7488	-	P	23:37:48.00	-	-	-	[*Hazard, D. L.* , 1914]
Alaska, USA)			-	S	23:47:39.00	-	-	-	
OSK (Osaka,	33.3545	269.8345	-	P	23:33:42.00	-	-	-	[*Osaka, Bull.*, 1931]
Japan)			-	S	23:39:42.00	-	-	-	
ZKW (Zi-Ka-Wei,	36.6863	93.8873	-	P	23:32:48.00	-	-	-	[*ZiKaWei, Bull.*, 1915]
China)			-	S	23:39:00.00	-	-	-	
PUL (Pulkovo,	32.9486	317.1148	EW	P	23:32:16.00	-	-	-	(Golytsin (Galitzin),
Russia)			EW	S	23:37:45.00	-	-	-	B. 1911)

[5]Distance is given in degrees [deg]
[6]*Comp* stands for component on which the corresponding amplitude was measured
[7]*T* stands for period in seconds [sec], which corresponds to the measured amplitude
[8]*Amp* stands for amplitude value in micrometers [μm]

OTT (Ottawa,	88.9400	341.3686	NS	P	23:38:36.00	-	-	-	(Golytsin (Galitzin),
Canada)			NS	S	23:49:16.00	-	-	-	B. 1911)
Waveforms									
API (Apia,	114.5731	86.1859	EW	Pdiff	23:40:34.991	15	50	9.54	
Samoa Island)			EW	PP	23:44:36.483	18	125	8.52	
DBN (De Bilt,	47.7607	307.5261	EW	P	23:34:11.087	13	157	8.28	
Netherlands)			EW	PP	23:36:11.415	11	328	8.27	
			EW	S	23:41:16.591	17	804	8.37	
			EW	SS	23:44:23.455	14	2211	-	
GTT (Goettingen,	45.0291	305.4267	Z	P	23:33:59.079	4	118	8.17	
Germany)			Z	PP	23:35:54.736	3.5	84	8.08	
			EW	P	23:33:59.079	13	171	8.02	
			EW	PP	23:35:54.736	15.5	367	8.17	
			EW	S	23:40:53.850	13	547	8.12	
			EW	SS	23:44:03.547	13	493	-	
HAM (Hamburg,	44.4690	308.1732	EW	P	23:34:00.248	4.7	136	8.36	
Germany)			EW	PP	23:35:38.168	8	281	8.35	
			EW	S	23:40:28.378	9	343	8.08	
			EW	SS	23:43:46.456	9	345	-	
HLG (Helgoland,	45.5924	309.6029	EW	P	23:33:45.769	4.5	41	8.06	
Germany)			EW	PP	23:35:42.164	4.5	95	8.12	
			EW	S	23:40:36.326	12	95	7.60	
			EW	SS	23:43:49.788	12	101	-	
HNG (Hongo,	47.8862	76.5531	NS	P	23:34:22.644	-	-	-	
Tokyo, Japan)			NS	PP	23:36:22.350	-	-	-	
			NS	S	23:41:25.884	-	-	-	
			NS	SS	23:44:44.980	-	-	-	
CSM (CasaMi.	46.2820	289.9144	EW	P	23:34:38.188	12	74	7.89	
Ischia, Italy)			EW	PP	23:36:28.133	11	81	7.66	
			EW	S	23:41:24.839	11	345	8.10	
			EW	SS	23:44:25.641	12	974	-	
LEI (Leipzig,	43.7005	304.6639	EW	P	23:34:12.364	3.5	71	8.01	
Germany)			EW	PP	23:35:56.007	6.5	145	8.05	
			EW	S	23:40:28.431	15	170	7.55	
			EW	SS	23:43:26.955	8	123	-	
MNH (Munich,	45.0621	300.3805	EW	P	23:34:01.005	5	96	8.18	
Germany)			EW	PP	23:36:01.110	10	124	7.89	
			EW	S	23:40:24.165	12	264	7.84	
OTT (Ottawa,	88.9400	341.3686	NS	P	23:38:51.359	5	186	8.97	
Canada)			NS	PP	23:42:04.295	6.5	119	8.67	
			NS	SKS	23:49:40.703	9	355	8.39	
			NS	SS	23:55:41.506	-	-	-	
PUL (Pulkovo,	32.9486	317.1148	EW	P	23:32:18.416	18	188	7.92	
Russia)			NS	PP	23:33:15.980	16	274	8.13	
RIV (Riverview,	101.9265	125.3417	NS	Pdiff	23:39:31.951	7	57	8.61	
Australia)			NS	PP	23:43:42.277	7	66	8.37	
			NS	SKS	23:49:58.138	11	111	8.4	
			NS	SP	23:52:39.866	11	170	-	
			NS	ScS	23:58:19.564	-	-	-	
SIT (Sitka,	76.7793	17.6348	NS	P	23:37:32.111	-	-	-	
Alaska)			NS	PP	23:39:38.985	-	-	-	
			NS	S	23:47:44.905	-	-	-	
			NS	SS	23:51:15.489	-	-	-	
RAV (Ravensburg,	46.4313	300.5286	NS	P	23:37:32.111	-	-	-	
Germany)			NS	PP	23:39:38.985	-	-	-	
			NS	S	23:47:44.905	-	-	-	
			NS	SS	23:51:15.489	-	-	-	
TAR (Taranto,	44.1170	288.2451	NS	P	23:34:05.711	3.5	31	7.64	
Italy)			NS	PP	23:35:31.424	5	38	7.68	
			NS	S	23:40:32.073	7	122	7.74	
			NS	SS	23:43:43.655	6	172	-	
TLO (Toledo,	58.8363	297.2077	EW	P	23:35:43.172	5.5	86	8.29	
Spain)			EW	PP	23:38:04.846	6.5	186	8.56	
			EW	S	23:43:55.864	8.7	134	7.79	
			EW	SS	23:48:05.670	8.5	195	-	
VIE (Vienna,	42.0611	299.2679	NS	P	23:33:30.182	6	115	7.98	
Austria)			NS	PP	23:35:19.041	12	399	8.12	
			NS	S	23:42:59.251	12	284	7.87	
UCC (Uccle,	48.6864	306.1149	NS	P	23:34:34.776	-	-	-	
Belgium)			NS	PP	23:36:38.530	-	-	-	
			NS	S	23:41:45.659	-	-	-	
			NS	SS	23:45:19.274	-	-	-	
Average								8.05 ± 0.3	

TABLE 2.6: The amplitude (*Amp*) and period (T) values for the surface waves recorded on five stations. The surface wave magnitudes (3rd column) are calculated with Prague-Moscow formula [*Karnik et al.*, 1962] for each stations and average magnitude M_s is presented with one standard deviation.

Station	T [sec]	Amp [μm]	Ms
RIV	22	326	7.80
OTT	18	558	8.03
CSM	19	1490	7.80
TLO	18	660	8.11
HLG	20	2280	7.96
Average			7.94 $\pm$ 0.15

CHAPTER 3

Source parameters of the M7.3 Sarez-Pamir earthquake of February 18, 1911.

Galina Kulikova[1], *Bernd Schurr*[2], *Frank Krüger* [1], *Elisabeth Brzoska*[3], *Sebastian Heimann*[2]

Published in Geophysical Journal International
2016,
DOI: 10.1093/gji/ggw069

[1]Institute of Earth and Environmental Science, University of Potsdam, K.-Liebknecht-Str. 24/H60, *14476*, Potsdam, Germany.
[2]Helmholtz Centre Potsdam, GFZ German Research Centre for Geosciences.
[3]Institute of Applied Geosciences, KIT Karlsruhe Institute of Technology.

SUMMARY: The M_s ~7.7 Sarez-Pamir earthquake of 18 February 1911 is the largest instrumentally recorded earthquake in the Pamir region. It triggered one of the largest landslides of the past century, building a giant natural dam and forming Lake Sarez. As for many strong earthquakes from that time, information about source parameters of the Sarez-Pamir earthquake is limited due to the sparse observations.
Here the analysis of analogue seismic records of the Sarez-Pamir earthquake is presented. We have collected, scanned and digitized 26 seismic records from 13 stations worldwide to relocate the epicentre, determine the event's depth (~22 km) and magnitude (m_B7.3 and M_s7.7). The unusually good quality of the digitized waveforms allowed their modeling, revealing a NE-striking sinistral strike-slip focal mechanism in accordance with current regional tectonics. The shallow depth and magnitude (M_w7.3) of the earthquake were confirmed. Additionally, we investigated the possible contribution of the landslide to the waveforms and present an alternative source model assuming the landslide and earthquake occurred in close sequence.

3.1 Introduction

The Sarez-Pamir ~M7.7 [*Gutenberg & Richter*, 1954] earthquake occurred on February 18th, 1911 on the Pamir plateau, north-east of Tibet (Figure *2.1*). This earthquake is famous for having triggered one of the largest landslides on Earth [*Ambraseys & Bilham*, 2012]. The landslide flow has completely covered a village - Usoy - with all its inhabitants, houses and animals. Accordingly in some literature this landslide is called Usoy slide [*Preobrazhenskiy*, 1920]. The Usoy landslide has blocked the Murgab river, creating the worlds largest natural dam. The river water started filling up the valley, forming a lake, and by the end of summer 1911 it flooded the Sarez village. Usoy dam and Lake Sarez with its 17 cubic kilometres of stored water have attracted significant attention from the scientific community due to the enormous consequences a possible breach would entail [*Ischuk*, 2006; *Kazakov*, 2004; *Papyrin*, 2001].

According to *Shpilko* [1914], the extend of the Usoy catastrophe was not immediately known to the local government, nor was the fact that the Sarez earthquake and the Usoy landslide happened at the same time. The earthquake and the landslide had destroyed the mountain paths to the district center, interrupting efficient communication and the first information about the catastrophe and rising lake was only received 45 days after the event. When the first commission investigated the lake, oral testimonies stated that the landslide and the earthquake happened at approximately the same time. The fact that the level of Lake Sarez was rising was confirmed and the Sarez villagers were evacuated and relocated. The village was completely flooded by the mid-autumn 1911 [*Shpilko*, 1914].

The first expedition of Preobrazhenskiy I.A., performing geological surveys, mapping and geodetic measurements, was sent to Lake Sarez in 1915. The expedition determined the volume and the mass of the landslide and their work ″Usoy avalanche″ [*Preobrazhenskiy*, 1920] was published in 1920. According to *Preobrazhenskiy* [1920] the estimated volume of the landslide was $2.2km^3$ and the total mass $6 \cdot 10^{12}kg$. These data remain relevant to the present day.

In comparison to the landslide, the Pamir-Sarez earthquake itself attracted less attention from the scientific community until 1915, when Galitzin expressed the idea that there was no earthquake at all and that it was the landslide that was registered on the seismic records. *Galitzin* [1915] calculated, based on *Preobrazhenskiy* [1920] data, the potential energy released by the landslide and concluded that it would be sufficient to produce the seismic amplitudes recorded on Pulkova

seismic station ∼3800 km away. This publication created a long dispute among seismologists at the time, either agreeing [*Klotz*, 1915; *Jeffreys*, 1923] or disagreeing [*Oldham*, 1923; *Jeffreys*, 1924] with Galitzin's idea. *Oldham* [1923] stated that the existence of aftershocks suggests an earthquake source, moreover he argues that the damage and intensity distribution was more typical for a deep earthquake. More recently *Ambraseys & Bilham* [2012] showed that the landslide would probably not be recorded the same way as an earthquake at teleseismic distances due to its much longer source duration. Although we know now that there was an earthquake, its source parameters, i.e. hypocenter and mechanism, are highly uncertain or completely unknown. Being the largest known event in the region, this information is of particular interest to assess regional tectonics.

We have collected historical seismograms and bulletins for the Sarez-Pamir earthquake to learn more about this exceptional event. We scanned and digitized the analogue seismic records and used them together with bulletin information to locate its epicenter and determine its magnitude and depth. Furthermore we employed waveform modeling to determine the focal mechanism, centroid depth and the seismic moment of the earthquake. Additionally, based on examples of modern large landslides, we modeled the Usoy landslide waveforms and investigated how it could have been recorded on the analogue teleseismic records.

3.2 Tectonic setting

The Pamir mountains, located north-east of the Tibetan plateau, are part of the India-Asia collision zone. Pamir crust consists of several terranes that amalgamated on the southern margin of Asia during the late Paleozoic and Mesozoic [*Burtman & Molnar*, 1993; *Schwab et al.*, 2004]. During the Cenozoic collision with India, this crustal package was shortened, reactivating the old sutures as thrust faults, and displaced northward in front of the advancing Indian plate promontory [*Burtman & Molnar*, 1993]. Northward displacement was accommodated by strike-slip systems on the orogene's flanks. In the west the active sinistral Darvaz fault separates the Pamir from the Tajik basin. In the east the dextral Karakorum and Kashgar-Yecheng fault systems presumably translated the Pamir along the Tarim basin's western margin. Currently, Pamir and Tarim basin move at approximately the same speed, rendering these shear zones mostly inactive [*Sobel et al.*, 2011]. Significant syn-tectonic extension is documented in the Pamir plateau by the exhumation of several gneiss domes, but this deformation ceased latest two million years ago [*Robinson et al.*, 2004; *Stübner et al.*, 2013].

In the current deformation regime shortening is localized across Pamir's northern margin at a rate of approximately 1.3-1.5 cm/a [*Zubovich et al.*, 2010; *Ischuk et al.*, 2013]. It is accommodated by thrust faulting across the Pamir Thrust System [*Schurr et al.*, 2014], with the 2008 M6.7 Nura event the most recent of such events [*Teshebaeva et al.*, 2014; *Sippl et al.*, 2014]. In the Pamir interior, where the Sarez-Pamir earthquake presumably occurred, thrusting has ceased and sinistral strike-slip faulting on north-east trending or conjugate planes and to a lesser degree north-south striking normal faulting prevails. This deformation pattern, effecting mostly east-west extension, is in contrast with the long-term cenozoic geological structures, which dominantly recorded north-south shortening along east-west striking thrusts (Figure *3.1*). This change in stress and strain regime is presumably young, and has not yet left its imprint in the structural grain. The only recent fault system of this type that is visible both in the landscape and in the seismicity pattern is the Sarez-Karakul fault system. It strikes NE from Lake Sarez across Lake Karakul to reach the Pamir thrust system (Figure *3.1*). Its surface morphology exhibits en echelon, right-stepping escarpments, with sinistral normal faults also indicated by offset stream channels and fault slip data [*Strecker et al.*, 1995]. It is traced by seismicity with the few available mechanisms indicating

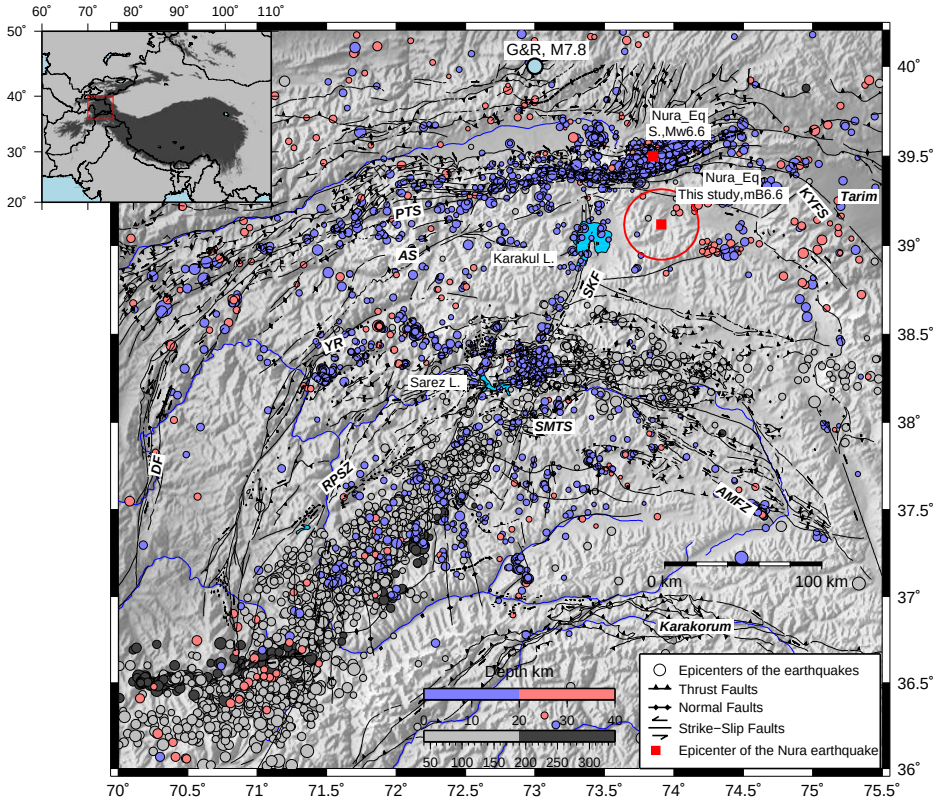

FIGURE 3.1: Seismicity map of the Pamir region. Epicenters are from *Sippl et al.* [2013b], color-coded by depth with color palette (from blue to red) for crustal earthquakes and gray color palette (from white to black) for intermediate depth earthquakes. The active faults described in *Schurr et al.* [2014] are shown as black lines with corresponding kinematics (see legend). The gray circle, marked as G&R,M7.8, represents the epicenter of the Sarez-Pamir earthquake from *Gutenberg & Richter* [1954]. The red rectangle (S.,Mw6.6) indicates epicenter of the Nura earthquake determined in *Sippl et al.* [2014], the red rectangle with an ellipse- the Nura epicenter determined in this study. The the major geological structures mentioned in text named accordingly: SKF- Sarez-Karakul Fault; DF- Darvaz Fault; PTS- Pamir Thrust System; AMFZ- Aksu Murghab Fault Zone; SMTS- Sarez Murghab Thrust System; KYFS- Kashgar-Yecheng Fault Systems; YR- Yazgulem range; AS- Academy of Science range; RPSZ- Rushan-Pshart suture zone. Inset map (top left) shows overview map of the entire India Asia collision (defined by altitude higher than 2500m) with the map extent as red box.

sinistral strike slip faulting [*Schurr et al.*, 2014]. This lineament seems to roughly separate the stable eastern Pamir from the seismically more active western Pamir. The current deformation is thought to reflect gravitational collapse and westward extrusion of Pamir rocks under north-south compression. The east-west extension indicated by Pamir earthquake fault mechanisms and GPS vectors [*Ischuk et al.*, 2013] is balanced by east-west shortening in the Tajik basin.

The Pamir also features an intermediate depth (∼80 - 240 km) seismic zone, which is very rare in continental settings [*Sippl et al.*, 2013b]. The earthquakes form a tight 90° arc (Figure *3.1*) and apparently trace European lithosphere subducting under the Pamir [*Burtman & Molnar*, 1993; *Sippl et al.*, 2013a; *Schneider et al.*, 2013].

3.3 Seismograms collection and digitization

By the beginning of 20th century seismographs developed by the early seismologists -Rebeur-Paschwitz, Ehlert, Wiechert, Omori, Milne, Galizin etc., [*Fréchet & Rivera*, 2012; *Ehlert*, 1898b; *Wiechert*, 1903, 1904; *Omori*, 1899; *Milne*, 1886; *Galitzin*, 1910], were already deployed in observatories worldwide, together forming the first seismic network. However, distribution of the stations was quite heterogeneous, with e.g., clustering in Europe and emptiness in Africa [*Batlló et al.*, 2008], causing large azimuthal gaps in observations for many earthquakes, including the Sarez-Pamir earthquake (Figure *3.2*). Early seismic instruments were mainly one- or two-component horizontal seismometers working as mechanical pendulums (e.g. Wiechert, Bosch-Omori, Vicentini etc.), but first electro-magnetic seismic instruments [Galizin, *Galitzin*, 1910] were also successfully installed in some observatories. Each instrument was characterized by it's own free period, damping and magnification values (Table *3.3*). Before radio timing signals became available in 1920s, the timing of early analogue seismographs was done using local astronomical clocks, inroducing significant uncorrelated errors. The vertical component was developed later [in 1905, *Dewey & Byerly*, 1969] and added as separate instruments afterwards [mostly after 1910, *Wood*, 1921; *McComb & West*, 1931]. The pendulum-type seismographs were typically constructed with a needle fixed on an about 45 cm long metal ″arm″ attached to a moving mass, which recorded the ground motion by scratching on smoked paper fixed on a rotating cylinder.

The Sarez-Pamir earthquake must have been recorded by many seismic stations worldwide, but collecting those seismic records today is difficult. Many seismograms probably did not survive and those which still exist are scattered in local archives of different observatories [*Batlló et al.*, 2008]. Collecting these entails visiting each archive individually, which is complicated due to the necessity for extensive travel and the need of powerful scanning facilities. Nonetheless, in a significant effort we have collected 60 seismograms from 25 different seismic stations for the Sarez-Pamir earthquake. 40 of those records were received from INGV, Rome, which is a great source for historical seismograms from European seismic stations after the EUROSISMOS project [*Michelini et al.*, 2005]. Other seismograms were received by personal contact to different local institutes (see Table *3.3* Appendix *2.8.2* for details).

The paper seismograms were then scanned with high resolution, keeping their original size, to be able to later extract the true amplitudes. Obtaining reliable digital seismograms from those scanned records is a challenging procedure. The Sarez-Pamir earthquake was mainly recorded on old smoked paper, which did not allow an automatic digitizing procedure. Consequently the seismograms were digitized manually using the path tool of GIMP (GNU Image Manipulation Program) [*Kimball & et. al*, 2014] by basically redrawing the whole seismogram. The GIMP output path was then smoothed using Bezier curves, resampled with a constant sampling rate of 0.1s and converted to ASCII text format. The pendulum seismographs introduce a curvature to the waveform registration, which is particularly obvious for large oscillations (Figure *3.3*). We corrected for curvature using the method of *Cadek* [1987] and *Grabrovec & Allegretti* [1994].

Eventually we were able to digitize twenty-six seismograms from thirteen seismic stations, eleven of those stations were located in Europe (Figure *3.2*), one station in Japan and one in Indonesia. This leaves large azimuthal gaps: about 180° on SE-NW and about 90° on N-NE directions. However, the dense network in Europe allows using stations as large aperture seismic array to align and stack the records for further analysis. The European seismic stations, except for DBN, were equipped with Wiechert seismographs and provided generally good quality records, with clear P, S and surface waves. An example of a Wiechert record from a european station - MNH (Munich, Germany) - is shown on Figure *3.3*. The Dutch station DBN and the Japanese station HNG were equipped

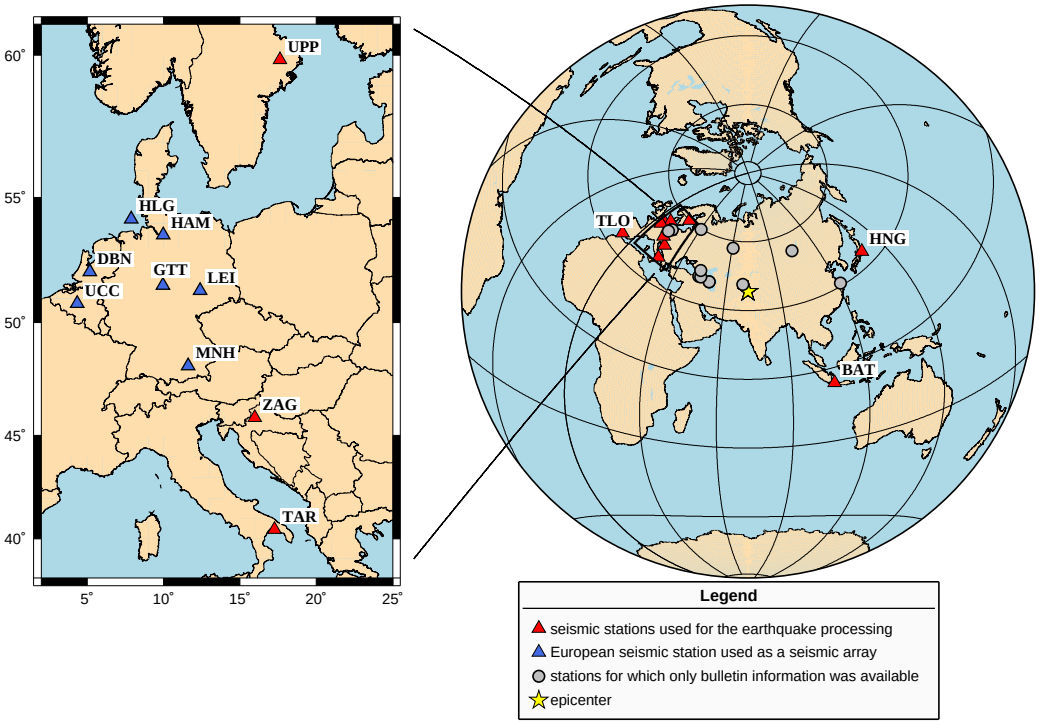

FIGURE 3.2: Seismic stations that have recorded the Sarez-Pamir earthquake. The stations′ distribution is given in the azimuthal equidistant projection; the star at the middle represents the earthquake epicenter; red triangles show the stations which were used in the present study with corresponding station abbreviation name (the station abbreviations are given according to the name of the nearest modern station); the gray circles show the station for which only bulletin information was available. The inset map (left side) shows the seismic station distribution in Europe: blue triangles mark the European stations, which were used as a seismic array, red triangles mark other European stations.

with Bosh-Omori instruments. Their low magnification of only 20, prevented reading the P arrival. The station BAT in Indonesia provided only a north-south component record, which was very oscillatory, probably due to the special site conditions and low damping. Nonetheless all phases could be identified.

TABLE 3.1: Instrument constants for some of analog instrument operating in 1911.

Station [4]	Instrument	Component	Magnification	Damping (h)	Period (T_0[sec])
BAT (Batavia, Djakarta	Wiechert seismograph	NS	193.00	0.45	8.0
Indonesia)	Wiechert seismograph	EW	216.00	0.45	7.6
DBN (De Bilt, Netherlands)	Bosch-Omori	NS	20.00	0.40	18.0
	Bosch-Omori	EW	20.00	0.43	18.0
GTT (Goettingen, Germany)	Wiechert seismograph	NS	152.00	0.40	14.0
	Wiechert seismograph	EW	172.00	0.36	12.6
	Wiechert seismograph	Z	170.00	0.31	4.8
HAM (Hamburg, Germany)	Wiechert seismograph	NS	200.00	0.46	10.0
	Wiechert seismograph	EW	200.00	0.46	10.0
HLG (Helgoland, Germany)	Wiechert seismograph	NS	126.00	0.41	11.5
	Wiechert seismograph	EW	153.00	0.39	11.1
HNG (Hongo, Tokio, Japan)	Omori	NS	20.00	0.40	16.0

[4]Station abbreviation names are given by the authors of this work in three letters, corresponding to the closest modern seismic station name located in this region, however the precise location of the historical station often differ from the modern one.

	Omori	EW	20.00	0.40	16.0
LEI (Leipzig, Germany)	Wiechert seismograph	NS	260.00	0.46	9.6
	Wiechert seismograph	EW	260.00	0.46	9.6
MNH (Munich, Germany)	Wiechert seismograph	NS	190.00	0.46	9.0
	Wiechert seismograph	EW	190.00	0.46	9.0
TAR (Taranto, Italy)	Wiechert seismograph	NS	180.00	0.40	4.5
	Wiechert seismograph	EW	180.00	0.40	4.5
TLO (Toledo, Spain)	Rebeuer-Ehlert	NS	123.00	0.40	7.0
	Rebeuer-Ehlert	EW	122.00	0.40	7.0
UCC (Uccle, Belgium)	Wiechert seismograph	NS	145.00	0.40	10.7
	Wiechert seismograph	EW	165.00	0.37	10.0
	Wiechert seismograph	Z	155.00	0.33	4.8
UPP (Uppsala,Sweden)	Wiechert seismograph	NS	189.00	0.38	9.8
	Wiechert seismograph	EW	191.00	0.38	9.4
ZAG (Zagreb, Croatia)	Wiechert seismograph	NS	200.00	0.45	10.0
	Wiechert seismograph	EW	200.00	0.45	10.0

3.4 Earthquake location and magnitude

3.4.1 Earthquake relocation

Previous studies show different epicenter locations, depths and magnitudes for the Sarez-Pamir earthquake (Figure *3.4*). *Gutenberg & Richter* [1954] suggested the epicenter 200 km north of Lake Sarez (Figure *3.1*). The earthquake was later relocated by more authors, e. g. [*Kondorskaya et al.*, 1982] suggest the epicenter exactly at the eastern edge of Lake Sarez based on macro-seismic data of *Shpilko* [1914] and *Galitzin* [1915], which then also appears in *Kalmetieva et al.* [2009]. *Bindi et al.* [2014] found alternative epicenter locations based on macro-seismic data, after analyzing two datasets [*Semenov & Semenov*, 1958; *Ambraseys & Bilham*, 2012] with a calibrated attenuation model. The ISC GEM [*Storchak et al.*, 2013] located the epicenter close to the northern edge of Lake Sarez, based on arrival times from seismic bulletins. And the study of *Ambraseys & Bilham* [2012] suggested their approximate location about 30 km west from ISC GEM (Figure *3.4*).

In this study we relocated the epicenter of the Sarez-Pamir earthquake using bulletin information and the digitized seismic records. We used the HYPOSAT software [*Schweitzer*, 2001, 2012] with a modified crustal structure from the CRUST 5.1 model [*Mooney et al.*, 1998] and the global velocity model IASPEI91 [*Kennett & Engdahl*, 1991]. The location was calculated with stronger reliance on phase arrival time differences than on the absolute arrival times because of the presumably large absolute timing errors of the old seismographs. However, avoiding absolute arrival times completely was impossible due to the poor azimuthal coverage. Our data set was gleaned from *Nikiforov* [1912], who presented the P and S phase arrival times for the earthquake from eight Russian seismic stations between 3° and 26° away from the epicenter. Additionally, bulletin arrival times from six teleseismic stations (distance from 34° till 47°) and S-P arrival time differences measured directly from the digitized waveforms were available. Details on all phase arrivals used are given in the Table *3.4*, appendix *2.8.2*.

For the final location of the hypocenter we have used nine absolute times and sixty-five arrival time differences. The absolute times were read from the digitized analogue seismograms. This arrival times show good consistency between each other and also agree with arrival times from teleseismic and local bulletins. As a result (Table *3.2*) the epicenter of the Sarez-Pamir earthquake was located at 38.636°N and 72.105°E. The depth of the earthquake was determined at 22 km. However, standard errors are still large with the long axis of the error ellipse reaching 60 km

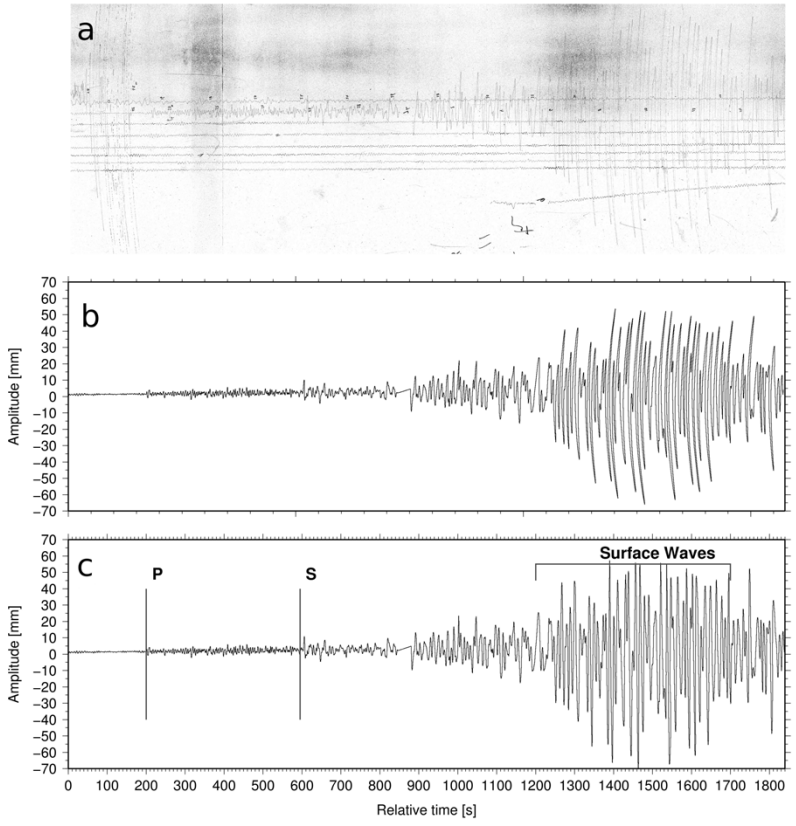

FIGURE 3.3: Example scanned (a) and digitized seismogram before (b) and after (c) curvature correction for the E component of Munich (MNH) station, Germany.

length (Figure *3.1*) and a depth error of 14 km. The error ellipse covers the epicenter proposed by *Ambraseys & Bilham* [2012] and is in good agreement with the intensity distribution map [*Ambraseys & Bilham*, 2012, Fig. 2].

3.4.2 Magnitude calculation

The reported magnitudes of the Sarez-Pamir earthquake range from minimum $M7.1$ in *Kalmetieva et al.* [2009] (calculated from regional seismic observations) to maximum $M7.7$ given by *Gutenberg & Richter* [1954] and confirmed as $M_s7.7$ in *Ambraseys & Bilham* [2012]. Intensity based magnitudes calculated by *Bindi et al.* [2014] are MI_{LH}=7.4, MI_s=7.6, and MI_w=7.2.

The magnitude $M_s7.7$ was calculated from amplitudes and periods of surface waves reported in seismic bulletins at different seismic stations worldwide [for more details see *Ambraseys & Bilham*, 2012] using the Moscow-Prague formula [*Karnik et al.*, 1962]. We had some original copies of those bulletins published in *Schweitzer & Lee* [2003] at hand and in addition the surface wave amplitudes measured on the digitized waveforms (Table *3.5*, appendix *2.8.2*). We also measured surface wave amplitudes for periods between 18 and 22 seconds and confirmed the surface wave magnitude $M_s7.7\pm0.1$ using the Moscow-Prague formula.

Additionally the broadband body wave magnitude m_B [*Bormann & Saul*, 2009; *Bormann et al.*, 2013] was calculated using amplitudes and periods of teleseismic body waves. The magnitude m_B was calculated from the bulletin information only as $m_B7.1\pm0.2$, while the amplitudes measured on

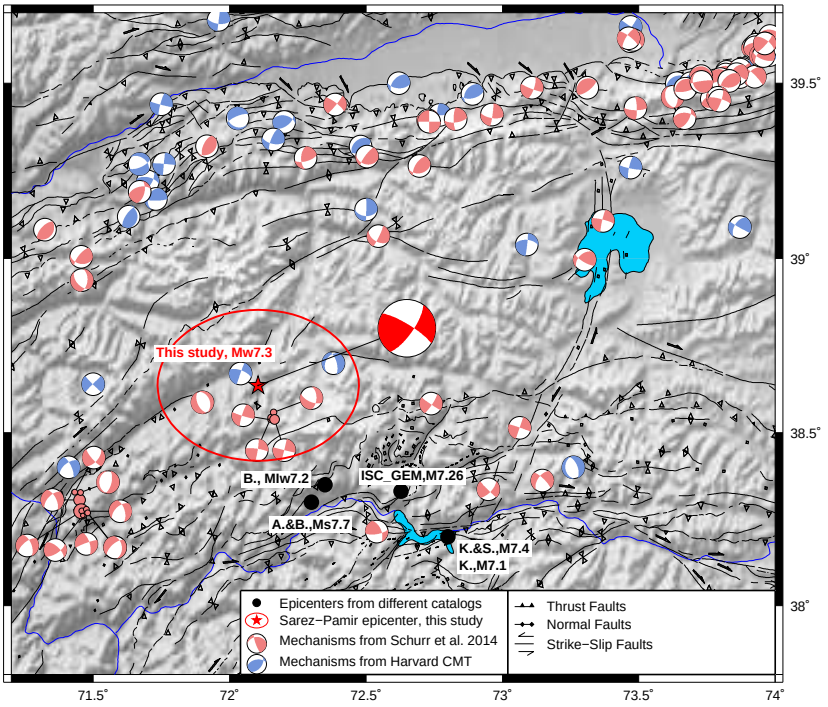

FIGURE 3.4: The topography map of the Pamir region showing the focal mechanisms of all the earthquakes between 1976 and 2015 according *Ekström et al.* [2012] as gray beach-balls; the focal mechanisms determined in *Schurr et al.* [2014] study are shown as blue beach-balls; the epicenter of the Sarez-Pamir earthquake is represented as a red star, with corresponding error ellipse, and the focal mechanism for this earthquake as a red beach-ball. The epicenters of the Sarez-Pamir earthquake determined in other studies are shown as black circles named accordingly: B.,MIw7.2- *Bindi et al.* [2014]; K.,M7.1- *Kalmetieva et al.* [2009]; K.&S.,M7.4- *Kondorskaya et al.* [1982]; A.&B.,Ms7.7- *Ambraseys & Bilham* [2012]; ISC-GEM,M7.26- *Storchak et al.* [2013].

the digitized waveforms resulted in m_B7.3±0.2 (Table *3.4*, appendix *2.8.2*), which agrees well with m_B published by *Ambraseys & Bilham* [2012] based on their teleseismic bulletin information.

TABLE 3.2: The instrumental epicenter location for the Sarez-Pamir earthquake.

	Origin time [hh:mm:ss.s]	Latitude	Longitude	Depth [km]
preferred location	18:40:58.137 ± 4.768	38.636 ± 0.5759	72.105 ± 0.4337	22.22±14.6

3.5 Focal mechanism determination

Determination of the focal mechanism for a historical earthquake using standard procedures like e.g., moment tensor inversion is not straight forward [*Kulikova & Krüger*, 2015] for a number of reasons:

1. The data quality is generally low, with digitized seismograms often having steps and kinks from writing-needle dislocations leading to interpolation problems for digitizing. These steps introduce artificial low frequencies to the recorded true ground displacement, which can bias moment tensor inversion severely.

2. Some single components may be lost and the vertical components were in practically all cases not yet installed in 1911.

3. Imperfect time alignment between different components of the same station hamper the rotation procedure into radial and transverse components.

4. The documented instrument parameters (free period, damping and magnification) sometimes do not fully correspond to the real values, which then biases the restitution to true amplitudes of the seismic records.

All this considered, we decided to avoid the rotation and restitution of the historical seismic records. Instead the focal mechanism was determined by fitting the original waveforms to the synthetic seismograms convolved with the historical instrument response in a Z-N-E coordinate system. The Greens functions were calculated with the reflectivity method [*Fuchs & Müller*, 1971; *Heimann*, 2014a] for different test depths (2-60 km, 2 km steps) for all stations using the IASPEI91 velocity model [*Kennett & Engdahl*, 1991] and origin time determined above (Table *3.2*). The synthetic seismograms were calculated for a double couple point source for all strike, dip and rake angle combinations with a step of 1° and compared to the observed ones. The best fitting (in a least-square sense) mechanism and depth were determined by a grid search.

The free period of the historical instruments varied between 4-20 seconds, which is below or in the range of the corner period of an M7 earthquake. Nonetheless, the body waves were clearly recorded on all the stations except DBN and HNG due to these instruments' low magnification factor. However, those two stations provided good quality records for long period surface waves due to their longer free period (∼20 sec). The european stations, mainly equipped with the Wiechert instrument, also clearly recorded the surface waves, even the ones equipped with very short period instruments (free period between 4 and 7 sec, e.g. TAR, BAT, GTT_Z, UCC_Z).

The frequency content of the body waves fits better the passband of the historical instruments than surface waves. Nevertheless we tried to invert for both wave types; for the body waves in the 10 - 50 seconds and for the surface waves in the 30 - 100 seconds period band. The surface waves inversion did not show an acceptable solution, the misfit function had very low dynamic and a mechanism could not be determined unequivocally. Same situation was observed for joint inversion of surface waves and body waves, because the solution is dominated by surface waves due to their dominant amplitudes. Consequently it was decided to finalize our inversion based on body waves only. The best waveform fit was found for a focal mechanism with strike/dip/rake: 35°/73°/12° and $M_0 = 8.9 \cdot 10^{19} Nm$, M_w7.3 at 30 km depth (Figure *3.5*). Being able to fit the waveforms well with a double couple source eliminates the last doubts, whether there was an earthquake or not. The first estimate on source time duration of the Sarez-Pamir earthquake could be obtained from the duration of P-wave on teleseismic records (e.g. stations in Europe). P-wave records for E and Z components of European stations (Figure *3.5*c) were aligned and stacked together, showning that the source duration does not exceed 30 seconds, which is reasonable for a M_w7.3 earthquake.

The misfit function reveals that dip and rake angles are determined rather well within ±10° precision. But the strike seems less well resolved showing lower dynamics of the misfit than dip and rake (see Figure S1 in the electronic supplement for details). The 5% best solutions for the focal

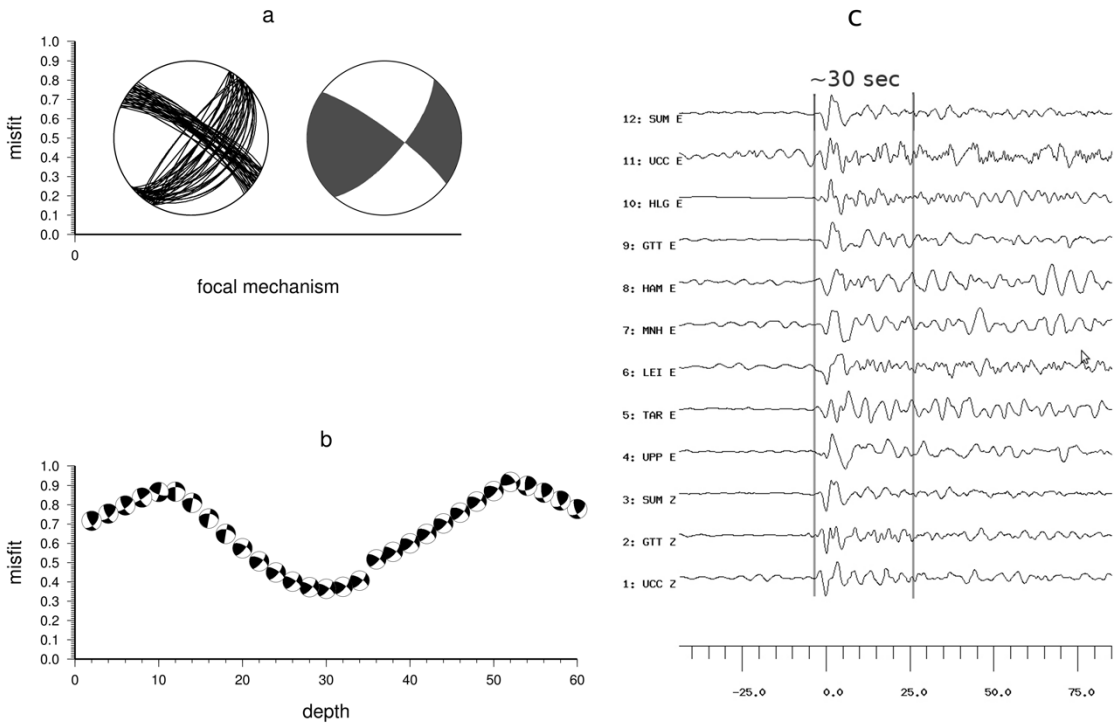

FIGURE 3.5: The results of the focal mechanism grid-search. (a) 5 % best solutions, the black beach ball shows the focal mechanism with the smallest misfit. (b) Misfit function dynamics for the depth of the earthquake, showing minimum for the depths between 26 and 34 km. (c) The P-wave records with corresponding station and component name. The solid gray lines mark the P-wave duration and hence an estimate of the source duration as ∼30 sec. The records are normalized in amplitudes and aligned in time.

mechanism (Figure *3.5* a) show significant variability for the strike. This is probably due to the poor station distribution and thus we give the strike an error estimate of ±30°. The waveform fit (Figure *3.6*) for the mechanism above is good for body-waves with amplitude also matching well. The first onset polarity of the SH waves seems to be reverse for some stations (Figure *3.6*), which might be explained as an artifact introduced by the recording instrument. Although surface waves were excluded in the inversion procedure, the Figure *3.6* reveals that our mechanism shows good waveforms fit for the surface waves as well.

3.6 Usoy landslide

Although it is clear now, not least due to our own analysis, that the seismograms of the Sarez-Pamir event are dominated by an earthquake, some questions on the role of the landslide remain. *Ambraseys & Bilham* [2012] suggested that the landslide could not have been recorded on distant stations because its energy must have been released over a longer time (they suggest at least ∼3 times the earthquake source duration) leading to considerably smaller amplitudes on seismograms compared to the earthquake signal. And this low-frequency signal would have been damped further in the records due to the short-period nature of the historical instruments. Here we try to quantify the possible contribution of the Usoy slide to the recorded seismograms by modeling its source on simulated historical instruments.

The geological studies [*Preobrazhenskiy*, 1920; *Ambraseys & Bilham*, 2012] estimated the parameters of the landslide quite well, allowing to model it as a sliding rock mass. Its weight was estimated at about $6 \times 10^{12}[kg]$, and the slope angle was between 9° and 20°. In addition *Ambraseys & Bilham* [2012] estimated the source duration to be ∼107 seconds and the landslide velocity about $31[m \cdot s^{-1}]$.

It has been shown [*Brodsky et al.*, 2003; *Moretti et al.*, 2012; *Allstadt*, 2013; *Yamada et al.*, 2013] that a landslide signal can be simulated as a combination of a vertical and horizontal single force applied to the ground. We parametrized the force model following *Zhao et al.* [2015], calculating the EW and NS components of the horizontal single force from the strike of the sliding direction and the rest of the Usoy landslide parameters for Greens function calculation. These were then convolved with the instrument responses for synthetic seismograms [*Heimann*, 2014b,a].

This scenario produces about ∼0.4 mm displacement for a station located in Europe (distance ∼45°), which, for example, produces a ∼2.5 cm amplitude on a Wiechert seismograph in GTT (Ǵottingen, Germany) station (magnification 20-50, for long-periods) for the surface waves (see Figure S2, in the electronic supplement). For the Bosch-Omori instrument located in Japan (seismic station HNG) with magnification factor 20 the recorded pulse would be about 1 cm. This means that such displacement should be clearly seen on the analogue seismograms. We have carefully analyzed the analogue records ∼12 hours prior and ∼12 hours after the Sarez-Pamir earthquake and did not find any isolated long period signal similar to the simulated one.

It is possible that the landslide was weaker than the geological studies suggest, too weak to be recorded at all, or that its signal is hidden in the earthquake record. Large Love waves, observed in the Sarez-Pamir earthquake record, could be due to the horizontal force produced by the landslide contribution. To check this possibility we applied beam-forming to the European stations (Figure *3.2*) to enhance the signal-to-noise ratio and separate signals by their slowness. Because only two stations had vertical components, we used the EW component of our array, which is close to the radial direction, for the P waves; for S waves we used the NS components as a proxy for SH (see Figure S3, S4, in the electronic supplement for details). The P waves of the Sarez-Pamir earthquake are followed by another signal, which has a slowness of a P-wave and arrives 120 seconds after the P-wave of the earthquake. This signal is more clearly observed on low-pass filtered records (corner period 20 seconds), indicating that this signal might have been initiated by a low frequency source. The amplitude of the signal would roughly correspond to the P wave amplitude of the simulated Usoy slide. A corresponding signal with the slowness of a PP wave is observed likewise on the waveforms 90 seconds after the P arrival. A similar phase is observed for SH with appropriate timing, although the signal is less clear. The quality of our data does not allow us to make any further statements at this point, however the possibility of the landslide signal being superposed with the earthquake should be considered.

3.7 Discussion

The instrumental seismic record is only little longer than one hundred years, i.e. shorter than most large earthquake recurrence intervals. In the first half of this period, i.e. before establishment of the World-Wide Standardized Seismograph Network (WWSSN), seismographic instruments were diverse and sometimes not well calibrated and timed. Earthquakes from this period could only be described rudimentarily by hypocentre, origin time and magnitude, often plagued with significant uncertainty. This leaves many important earthquakes with very little information. We showed that analogue seismic records from the earliest stage of seismological observation, digitized and re-analyzed with modern tools can still be an important data source extending our knowledge

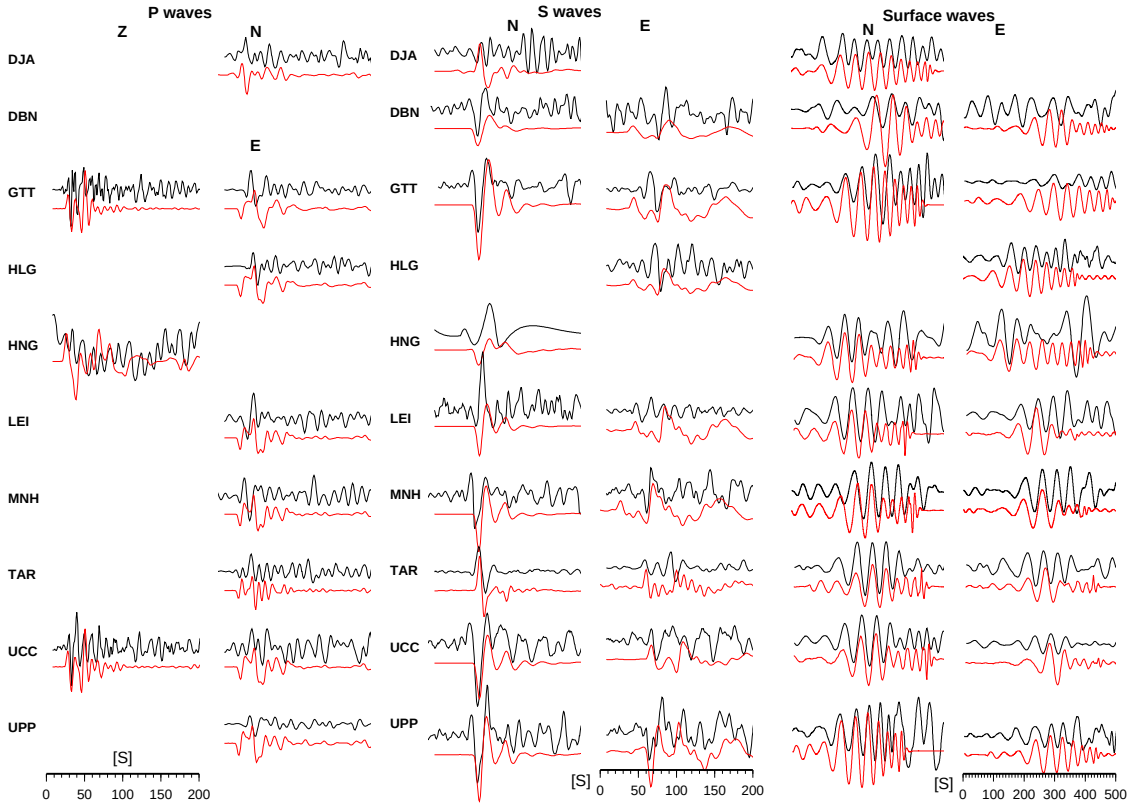

FIGURE 3.6: The synthetic and observed waveforms overlay for the Sarez-Pamir earthquake. The plot shows the synthetic (red lines) and observed (black lines) data overlay for P (a) on Z and E components and S and Surface waves on N and E components.

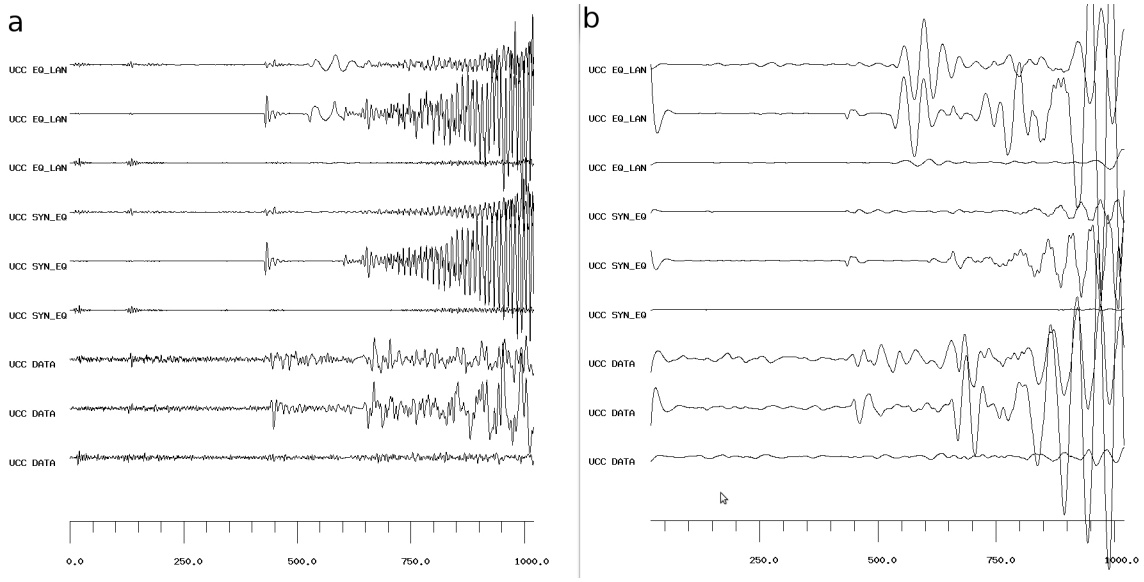

FIGURE 3.7: Seismograms of the seismic station UCC (Uccle, Belgium)for the comparison of the observed seismograms for Sarez-Pamir earthquake (DATA) and the synthetic waveforms for double-couple (DC) source (SYN_EQ) and combination of DC source and landslide source (EQ_LAN). The seismorams are not filtered and not normalized. b) Same as a) but low-pass (40 seconds) filtered.

further into the past. The Sarez-Pamir earthquake is the strongest instrumentally recorded shallow earthquake in the Pamir region and in the Pamir interior no shallow earthquake of magnitude greater than six occurred in the last 50 years, making it a worthwhile target for an in-depth study.

We used digitized seismograms from 13 global stations and seismic bulletins to relocate the epicenter of the earthquake and re-estimate its magnitude and depth. Our location agrees well with the one based on macro-seismic observations [*Ambraseys & Bilham*, 2012; *Bindi et al.*, 2014, Figure *3.4*], also placing it to the west of Lake Sarez. However, both data sets suffer from a west-sided data bias. For the seismic data this is due to the prevalence of European stations. Intensity data also cluster west of Lake Sarez, along the populated western Pamir valleys and in particular along the Bartang valley, whereas the high plateau of the eastern Pamir was largely inhabited during winter and consequently has very few observations [*Bindi et al.*, 2014]. To estimate the bias due to the event-station geometry and Earth model, we relocated the 2008 Nura earthquake with a similar station-phase set as for the Sarez-Pamir earthquake. Although too far away (∼200 km epicentral distance) for a proper master event analysis (Figure *3.1*), the Nura earthquake has the advantage of a precisely known hypocenter [*Sippl et al.*, 2014]. The relocation places the event some 75 km to the south-east, well outside its standard error ellipse. Considering that for this event timing errors are minimal, uncertainties in Pamir-Sarez earthquake location must also be assumed to be significantly larger than suggested by its error ellipse.

We determined several different magnitudes based on amplitude readings and waveform modeling. The body wave magnitude m_B differs slightly (Table *3.4*, appendix *2.8.2*) for amplitudes measured on the digitized waveforms ($m_B 7.3 \pm 0.2$) compared to the one based on the bulletin information ($m_B 7.1 \pm 0.2$). This may be explained by station operators' use of different instrument calibration information compared to the information written in the station books used by us. Similar differences are observed for the surface wave station magnitudes M_S, albeit the small number of surface wave amplitudes in bulletins did not allow a proper magnitude calculation. The M_S determined from the digitized waveforms agrees well with the M_S determined by *Ambraseys & Bilham* [2012], who had more bulletin amplitudes at hand. *Ambraseys & Bilham* [2012] also calculated a surface wave magnitude $M_s 7.4$ from surface wave readings of Milne seismograph recordings alone. Intensity based magnitudes give similar results (M7.2-7.6 using different formulas [e.g. *Bindi et al.*, 2014; *Ambraseys & Bilham*, 2012]). Our M_w of 7.3 based on waveform modeling conforms more to the lower range of estimates.

The exact depth of the earthquake remains a rather uncertain parameter for the Sarez-Pamir earthquake, although it clearly seems to be crustal. This is important, because the central Pamir also features significant intermediate depth seismicity (Figure *3.1*). We compared seismograms of the Sarez-Pamir earthquake and a modern deep earthquake (110 km depth) with nearby epicenters at two close by german stations (Figure S5 electronic supplement). The waveforms of the deep earthquake show clear depth phases, which are absent for the Sarez-Pamir earthquake, which however, features considerably larger surface wave amplitudes, together indicating a shallower source. The depths determined from arrival times and waveform modelling produce a similar result (∼22 km depth), yet with a large uncertainty (16 km standard error for the travel time solution). The seismogenic thickness of the Pamir crust from well located seismicity is about 20 km [*Schurr et al.*, 2014]. It is likely that this is also the depth range that accommodated the Sarez-Pamir rupture.

The focal mechanism of the Sarez-Pamir earthquake fits very well into the current deformation pattern of the Pamir interior recorded recently by moderate earthquakes [*Schurr et al.*, 2014]. They exhibit mostly sinistral strike-slip faulting on NNE to NE trending (or their conjugate) planes, in agreement with our mechanism. The large Pamir-Sarez earthquake corroborates that this is indeed the dominating mode of deformation for the Pamir south of the Pamir thrust system. A

M_w 7.3 strike-slip earthquake has a rupture length of ∼100 km [e.g. *Blaser et al.*, 2010]. There are few known possibly active faults of this dimension, which comply with the epicentre and its uncertainty. *Schurr et al.* [2014] suggested either the Sarez-Murghab thrust system, a roughly east-west trending fault zone re-activating the Rushan-Pshart suture zone, or the sinistral trans-tensional Sarez-Karakul fault system (Figure *3.1*). Our source mechanism would only comply with the latter, which in addition shows young (but undated) scarps and microseismicity [*Schurr et al.*, 2014; *Strecker et al.*, 1995]. Although the epicentre solutions locate the event west of this fault, its uncertainty (particularly considering the relocation test for the Nura earthquake described above) would not eliminate it as the accommodating structure. However, we do not want to rule out that the earthquake occurred on another, unmapped fault. The current seismicity shows several earthquake clusters north and west of Sarez Lake for which available mechanisms all show similar kinematics as the 1911 event, although their dimensions are significantly smaller than its presumed rupture length. But one should also consider that the seismicity pattern may not have been stationary during the last 100 years. A crustal earthquake of this size has probably ruptured to the surface, but no fresh surface scarp has been discovered. The region north and west of Lake Sarez, the Yazgulem and Academy of Science ranges, however, is highly glaciated with some of the highest and most rugged topography, making access for mapping extremely difficult.

The mechanism of the Pamir-Sarez earthquake contributes to the east-west extension under north-south compression typical for the active tectonic regime of the western and central Pamir - but it also accommodates horizontal shear. GPS data quantifies ∼1 cm/a of sinistral shear between the NNW-moving eastern Pamir and the northward ∼stable Tajik depression [*Ischuk et al.*, 2013]. The GPS data set, however, is too sparse to localize this shear. Previous studies have attributed it mostly to the Darvaz fault [*Burtman & Molnar*, 1993]. The Pamir-Sarez earthquake, as well as the other seismicity, may indicate that this shear is in part also taken up by the sinistral strike-slip faulting apparently typical for the western-central Pamir. The recent change in deformation from thrusting to sinistral shear and extension may be caused by the arrival and commencing underthrusting of the northwestern most extent of the Indian lithosphere under the Pamir. Then the Pamir-Sarez earthquake may ultimately be the result of the northward propagating plate boundary between India and Asia at depth.

We do not know when exactly the Usoy landslide occurred. The timing was guessed to be close to the earthquake based on the oral testimonies of two survivors of Usoy village and the large dust cloud people observed in the region directly after experiencing the shaking. It can only be said for sure that the landslide and the earthquake were not more then several hours apart. However, investigating the waveforms of stacked European records we have found a long-period signal 140 seconds after the P wave, and following the PP wave of the earthquake, which may be attributed to the landslide. In this case the landslide signal is very likely to be obscured by the surface waves of the earthquake. Because the historical instrument acts as a high pass filter for the long-period landslide signal, it is hard to distinguish from the surface waves. This could be the reason why waveform inversion of the surface waves did not show the same result as for the body waves. We have modeled the full synthetic waveforms for the Belgian station UCC for our double-couple (DC) source and for a combination of the DC and the landslide (single force) source. The non-filtered waveforms are dominated by the earthquake impulse (Figure *3.7*a), but the low-pass filtered waveforms (40 sec corner) of the combined source (Figure *3.7*b) show slightly better fit to the observed seismograms. The surface waves of the landslide cause a long-period signal, which is not seen for DC-source-only synthetics, but which seems to be present in the observed waveforms.

3.8 Conclusion

The Sarez-Pamir earthquake has been recorded by early analogue seismic stations at regional and teleseismic distances. We collected these seismic records, scanned and digitized them, producing a unique data set of 26 seismograms from thirteen stations worldwide for further analysis. We determined new source parameters based on these seismograms, complementing the previous geologic and macroseismic studies.

The earthquake hypocenter was relocated to 38.636°N and 72.105°E and 22 km depth based on newly read and bulletin arrival times and arrival time differences, which agrees well with macroseismic observations. The different earthquake magnitudes we determined - m_B7.3 , M_s7.7, and M_w7.3 - indicate that the event was slightly smaller than previously assumed, yet still the strongest instrumentally recorded crustal earthquake in the region. For the first time we were able to determine a focal mechanism for this event. Waveform modeling revealed NE striking sinistral strike-slip (or conjugate) faulting in good agreement with the current tectonics of the Pamir interior.

Our study confirms that the majority of the seismic signal of the Sarez-Pamir event is due to the tectonic earthquake. However, we did also find a possible signal that may be due to the slightly delayed landslide. Modeling its contribution based on the landslides' parameters fits the data slightly better than a pure double couple source.

Acknowledgments

We would like to gratefully thank all the people who helped us to collect the historical seismograms: Manfred Herden, Dr. Muzli, Dr. Muksin, Prof. Dr. Torsten Dahm, Marius Kriegerowski, Prof. Dr. Thomas Meier, Annika Fediuk, Kristin Burmeister, Dr. Siegfried Wendt, Pia Buchholz, Dr. Joachim Wassermann, Dr. Rudolf Widmer-Schnidrig, Marina Lopez Muga, Dr. Susana Custodio, Mr. Ivo Allegretti and others. Additionally we are grateful to the EUROSISMOS project and INGV, Rome, especially we thank Dr Graziano Ferrari and Silvia Fillosa and Matteo Quintiliani for their help with the access to the seismograms and digitizing software.

The authors thank Dr. James Dewey and Dr. Josep Batllo for their advice and support in historical seismograms collection and analysis. Our grateful thanks are also extended to Dr. Sebastian Heimann and Tim Sonnemann for providing technical support for this work.

This research has been done in the framework of PROGRESS project (http: //www.earth-in-progress.de /index.35.de.html) and financially supported by the German Federal Ministry of Education and Research.

In this work we have used open source software and would like to gratefully acknowledge: GIMP-; GMT - The Generic Mapping Tools developed by Paul Wessel and Walter H. F. Smith; Seismic Handler (seismic waveform analysis tool) developed by Dr. Klaus Stammler and Dr. Marcus Walther; and Pyrocko (a seismology toolbox and library) developed by Dr. Sebastian Heimann.

3.9 Appendix

TABLE 3.3: The list of seismic stations used in this study including the information about each institution, which provided the seismic records and the contact person name at the time, when the data were collected.

Station name	Latitude	Longitude	Instrument	Comp [5]	A/U [6]	Received From	Contact Person
BAT (Batavia, Jakarta)	-6.1800	106.7400	Wiechert	NS	+/+	Indonesian Agency for Meteorology, Climatology and Geophysics, Jakarta Indonesia	Dr. Muzli
				EW	+/−		
DBN (De Bilt, Netherlands)	52.1000	5.1833	Wiechert	NS	+/+	INGV Rome, Italy	Silvia Filosa
				EW	+/+		Dr Graziano Ferrari
			Bosch- -Omori	NS	+/+		
				EW	+/+		
GTT (Göttingen, Germany)	51.5500	9.9667	Wiechert	NS	+/+	Institute of Geophysics, University of Goettingen	Mr. Manfred Herden
				EW	+/+		
				Z	+/+		
HLG (Helgoland, Germnany)	54.1794	7.8828	Wiechert	NS	+/−	Institute of Geosciences, University of Kiel	Prof. Dr. Thomas Meier
				EW	+/+		
HNG (Hongo, Tokyo, Japan)	35.7111	139.7664	Omori	NS	+/+	USCS, Golden Colorado (The microfilms archive).	Dr. James Dewey
				EW	+/+		
				Z	+/+		
LEI (Leipzig, Germany)	51.3350	12.3917	Wiechert	NS	+/+	Observatory Collm, Inst. of Geophysics and Geology, University of Leipzig	Dr. Siegfried Wendt
				EW	+/+		
MNH (Munich, Germany)	48.1461	11.6086	Wiechert	NS	+/+	Department of Earth and Environmental Sciences, Ludwig-Maximilians- University	Dr. Joachim Wassermann
				EW	+/+		
TAR (Taranto, Italy)	40.4750	17.2542	Wiechert	NS	+/+	INGV Rome, Italy	Silvia Filosa
				EW	+/+		Dr Graziano Ferrari
TLO (Toledo, Spain)	39.8571	-4.0246	Rebeur- -Ehlert	NS	+/+	National Archives Geodetic and Geophysical Data, Geophysical Observatory Of Toledo	Ms. Marina Lopez Muga
				EW	+/+		
			Milne	EW	+/+		
UCC (Uccle, Belgium)	50.7988	4.3586	Wiechert	NS	+/+	INGV Rome, Italy	Silvia Filosa
				EW	+/+		Dr Graziano Ferrari
				Z	+/+		
UPP (Uccle, Belgium)	50.7988	4.3586	Wiechert	NS	+/+	INGV Rome, Italy	Silvia Filosa
				EW	+/+		Dr Graziano Ferrari
ZAG (Zagreb, Croatia)	45.8200	15.9800	Wiechert	NE	+/+	Faculty of Science, University of Zagreb	Mr. Ivo Allegretti
				NW	+/−		

TABLE 3.4: The station list with all arrival times for all the phases which were available for the Sarez-Pamir earthquake from the digitized waveforms and both local and teleseismic bulletins. The table also includes distances and azimuths to all the station, and the amplitude and period values where they were available. If the amplitude and the period columns are empty it means either that the value is not available or, in case of the waveforms, it means that the waveforms were photographed (microfilms) and the true amplitude can not be recovered due to the lack of information about photo-camera.

Station name	Distance[7]	Azimuth	Comp[8]	Phase	Arrival time	T[9]	Amp[10]	m_B	Source
Local bulletins									
TAS (Tashkent, Uzbekistan)	3.844	330.46	-	Pn	18:42:20.00				[*Nikiforov*, 1912]
			-	Sn	18:43:13.00				
BLCA (Balakhany, Azerbaijan)	16.736	285.37	-	P	18:44:52.00				[*Nikiforov*, 1912]
			-	S	18:48:06.00				
BAK (Baku, Azerbaijan)	16.837	284.96	-	P	18:44:49.00				[*Nikiforov*, 1912]
			-	S	18:48:04.00				
SVE (Sverdlovsk, Russia)	20.451	342.85	-	P	18:45:16.00				[*Nikiforov*, 1912]
			-	S	18:48:30.00				
TIF (Tiflis, Russia)	21.118	288.09	-	P	18:45:45.00				[*Nikiforov*, 1912]
			-	S	18:49:44.00				

[5] *Comp* means the component of the instrument

[6] The sign (+) or (−) indicates availability and usage of the seismograms. The first sign shows if the data were available (+) or not (−) the second sign indicates if they were used.

[7] Distance is given in degrees [deg]

[8] *Comp* stands for component on which the corresponding amplitude was measured

[9] *T* stands for period in seconds [sec], which corresponds to the measured amplitude

[10] *Amp* stands for amplitude value in micrometers [μm]

BOR (Borjomi,	22.178	288.40	-	P	18:45:23.00				[*Nikiforov*, 1912]
Russia)			-	S	18:49:23.00				
PYA (Pyatigorsk,	22.467	294.23	-	P	18:46:08.00				[*Nikiforov*, 1912]
Russia)			-	S	18:50:08.00				
IRK (Irkutsk,	26.634	47.17	-	P	18:46:07.00				[*Nikiforov*, 1912]
Russia)			-	S	18:51:00.00				
Teleseismic bulletins									
PUL (Pulkovo,	34.083	323.91	-	P	18:47:45.00				[*Klotz*, 1915]
Russia)									
DBN (De Bilt,	47.378	309.74	EW	P	18:49:43.00	5	8	7.40	[*Koninklijk*, 1915]
Netherlands)			NS	S	18:56:43.00	10	65	7.41	
GTT (Göttingen,	44.182	308.70	Z	P	18:49:21.00	5	12	6.88	[*Ansel*, 1913]
Germany)			Z	PP	18:51:15.00	15			
			EW	P	18:49:21.00	5	10	7.00	
			EW	PP	18:51:15.00	15	15	6.80	
			NS	S	18:55:59.00	9	30	7.02	
			NS	SS	18:59:18.00	12	50		
POT (Potsdam,	42.571	309.51	NS	P	18:49:06.00	3	10	7.22	Seismic Bulletin
Germany)			NS	PP	18:50:02.00	4	16	7.30	from Potsdam Station
			NS	S	18:55:31.00		35		received from
			NS	SS	18:58:04.00		65		F.S. Uni. Jena
JEN (Jena,	43.378	308.08	Z	P	18:49:16.00	5	19	7.08	Seismic Bulletin
Germany)			Z	PP	18:51:04.00	5			from Jena
			EW	P	18:49:16.00	5	8	6.90	Seismic Station
			EW	PP	18:51:04.00	5	12	7.08	received from
			EW	S	18:55:29.00	11	39	7.05	F.S. Uni. Jena
			EW	SS	18:55:29.00	8	22		
HAM (Hamburg,	43.950	311.5900	EW	P	18:49:22.00	6	13	7.04	Handwritten bulletin
Germany)			NS	PP	18:51:04.00	6	9	6.98	from Hamburg station,
			NS	S	18:55:55.00	11	60	7.24	taken from Hamburg
									University archive
ZKW (Zi-Ka-Wei,	41.003	84.2300		P	18:48:37.00				[*ZiKaWei, Bull.*, 1915]
China)			EW	PP	18:50:46.00	3.5	350	(8.5)	
			NS	S	18:55:03.00	8	4350	(9.4)	
			NS	SS	18:58:10.00	13	800		
Average (based only on the amplitudes and periods from the teleseismic bulletins)								7.1 ± 0.2	
Waveforms									
UPP (Uppsala,	40.236	320.56	EW	P	18:48:51.59	6.4	11	6.83	
Sweden)			EW	PP	18:50:20.34	6.4	40	7.39	
			NS	S	18:55:01.78	8	31	7.29	
			NS	SS	18:57:40.71	-	-	-	
TAR (Taranto,	41.631	291.32	EW	P	18:49:18.32	4.4	23	7.43	
Italy)			EW	PP	18:50:46.84	5	55	7.64	
			EW	S	18:55:39.96	9	110	7.59	
			EW	SS	18:58:36.65	-	-	-	
LEI (Leipzig,	42.95	307.99	EW	P	18:49:03.00	8	8	6.70	
Germany)			EW	PP	18:50:44.00	5.9	9	6.90	
			EW	S	18:55:26.00	10	12	6.60	
			EW	SS	18:58:31.00	-	-	-	
GTT (Göttingen,	44.182	308.7	Z	P	18:49:02.70	2.6	12	7.35	
Germany)			Z	PP	18:50:47.65	4.5	14	7.40	
			EW	P	18:49:02.70	2.7	7	7.11	
			EW	PP	18:50:47.65	3.8	18	7.47	
			NS	S	18:55:33.59	10	41	7.12	
			NS	SS	18:58:45.26	-	-	-	
MNH (Munich,	44.251	303.19	EW	P	18:49:18.92	7	10	6.84	
Germany)			EW	PP	18:51:09.30	7	14	7.09	
			NS	S	18:55:41.90	8	44	7.24	
			NS	SS	18:59:08.28	-	-	-	
DBN (De Bilt,	47.378	309.74	NS	S	18:55:40.27				
Netherlands)			NS	SS	18:59:08.46				
UCC (Uccle,	47.957	308.77	Z	P	18:49:37.00	5	8	7.39	
Belgium)			Z	PP	18:51:29.00	3	4	6.97	
			EW	P	18:49:37.00	4.2	5	7.26	
			EW	PP	18:51:29.00	4.6	9	7.07	
			NS	S	18:56:23.00	10	22	7.04	
			NS	SS	18:59:46.82	-	-	-	
BAT (Batavia,	54.763	135.98	NS	P	18:50:46.56	6	5	7.00	
Djakarta,			NS	PP	18:52:44.15	6.5	15	7.27	
Indonesia)			NS	S	18:58:16.81	7.8	29	7.18	
			NS	SS	19:02:06.15	-	-	-	
TLO (Toledo,	57.387	298.25	EW	P	18:51:10.15	3	10	7.70	
Spain)			EW	PP	18:53:19.88	5.6	12	7.55	

			NS	S	18:58:55.44	8	25	7.20
			NS	SS	19:03:16.59	-	-	-
HLG (Helgoland,	45.651	312.14	EW	P	18:49:22.57	5	36	7.76
Germany)			EW	PP	18:51:11.86	5	29	7.56
			NS	S	18:55:53.10	9	71	7.40
			NS	SS	18:58:40.90	-	-	-
ZAG (Zagreb,	42.975	295.80	NE	P	18:48:52.73	4	19	7.38
Croatia)			NE	PP	18:50:27.93	4	37	7.66
			NE	S	18:54:50.00	5	24	7.18
			NE	SS	18:57:54.24	-	-	-
Average (based only on the waveforms amplitudes and periods)								7.3 ± 0.3

TABLE 3.5: The amplitude (*Amp*) and period (T) values for the surface waves recorded on different stations read from the teleseismic bulletins and from the waveforms. The surface wave magnitudes (3rd column) are calculated with Prague-Moscow formula [*Karnik et al.*, 1962] for each stations and average magnitude M_s is presented with one standard deviation.

Station	Comp	Phase	Time	T [sec]	Amp [μm]	Ms
Teleseismic bulletins						
DBN	NS	M	19:09:12.00	18	2800	8.27
GTT	NS	M	18:59:18.00	25	1700	7.86
POT	NS	M	19:06:30.00	10	1500	8.18
JEN	NS	M	19:04:00.00	39	1680	7.65
HAM	NS	M	19:06:42.00	18	740	7.62
ZKW	NS	M	19:08:40.00	16	15600	(8.97)
Average						8.1 ± 0.3
Waveforms						
BAT	NS	LR	19:11:03.13	16	417	7.60
DBN	NS	LR	19:08:10.77	21	602	7.56
GTT	NS	LR	19:06:05.70	22	1073	7.71
HLG	NS	LR	19:06:56.80	21	1123	7.78
HNG	NS	LR	19:09:39.70	25	891	7.71
LEI	NS	LR	19:05:53.25	21	1221	7.78
MNH	NS	LR	19:07:55.65	22	1273	7.79
TAR	NS	LR	19:08:51.75	21	1394	7.82
UCC	NS	LR	19:08:14.70	22	654	7.55
UPP	NS	LR	19:03:14.33	20	1601	7.87
ZAG	NE	LR	19:05:54.72	19	771	7.62
Average						7.7 ± 0.1

Chapter 4

Results for other earthquakes

In this chapter the source parameters of seven further earthquakes were determined. This chapter includes a short description of each earthquake and particular reasons for why it was studied. Then the source parameters, such as epicenter location, depth, magnitude and focal mechanism were newly determined or re-estimated for the earthquakes with the methods presented in Chapter *2*, *3* and Appendix *A*. The general impact of each earthquake on the regional tectonics is discussed in the discussion (Chapter *5*) section.

4.1 1902 Kashgar earthquake

The Kashgar earthquake occurred on August 22, 1902 on the southern margins of the Tien-Shan, near Artix (Atushi) and Kashgar cities in China. The information about this earthquake is very limited (with exception for a few publications in Chinese language [*He et al.*, 2001; *Zhao et al.*, 2001]). *Gutenberg* [1956] assigned magnitude $M_s = 8\frac{1}{4}$ to this earthquake and located it at 40°N and 77°E. Several publications [*Molnar & Ghose*, 2000; *Zhao et al.*, 2000; *Fu et al.*, 2010b] have stated that the earthquake is likely to have thrust mechanism. The publications also claimed that no surface rupture, associated with this earthquake, was found. In the following the instrumental data for the earthquake are analyzed with described above methods in order to determine epicenter location, magnitude, and focal mechanism of the Kashgar earthquake.

The Kashgar earthquake occurred in the very beginning of seismic instrumentation development. Although the original records are not found, some seismograms are printed as example records in books. After searching through the literature 6 seismograms from 3 seismic stations are found. One E component record from seismic station in Leipzig (LEI), Germany is found in *Etzold* [1903]. The seismogram is very clear with large amplitudes, especially for surface waves (clipped record), similar to what was observed for the Chon-Kemin earthquake (see Chapter *2*), which gives the impression that these two earthquakes have the same order of magnitude. But unlike for the Chon-Kemin, strong surface waves of the Kashgar earthquake did not cause instrument failure which indicates that the amplitudes are smaller. Additionally two horizontal component (EW and NS) seismic records from station Laibach, Slovenia, are obtained from *Belar* [1903], with well recorded S and surface waves amplitudes, but absent P wave record. Two publications of Omori, *Omori* [1902] and *Omori* [1903], include reproductions of seismic records in Tokyo, Japan: two EW components with magnification of 10 and 120 and one NS component with magnification of 10. The book reproductions have scale for time with corresponding minute marks, but no scale for amplitude.

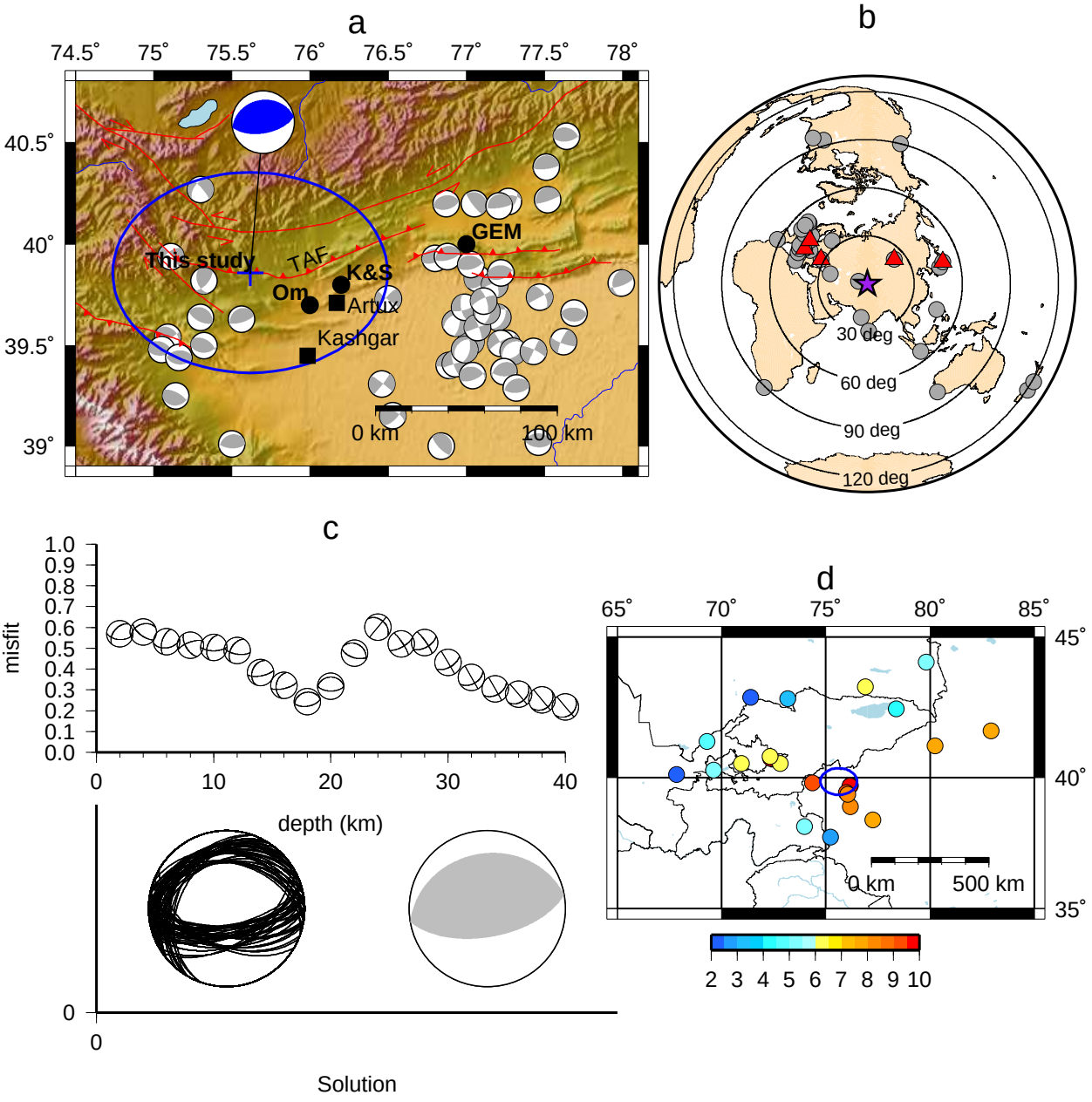
a
74.5˚
75˚
75.5˚
76˚
76.5˚
77˚
77.5˚
78˚
40.5˚
40˚
39.5˚
39˚
This study
TAF
K&S
Om
Artux
Kashgar
GEM
0 km
100 km
b
30 deg
60 deg
90 deg
120 deg
c
misfit
1.0
0.9
0.8
0.7
0.6
0.5
0.4
0.3
0.2
0.1
0.0
0
10
20
30
40
depth (km)
0
0
Solution
d
65˚
70˚
75˚
80˚
85˚
45˚
40˚
35˚
0 km
500 km
2 3 4 5 6 7 8 9 10

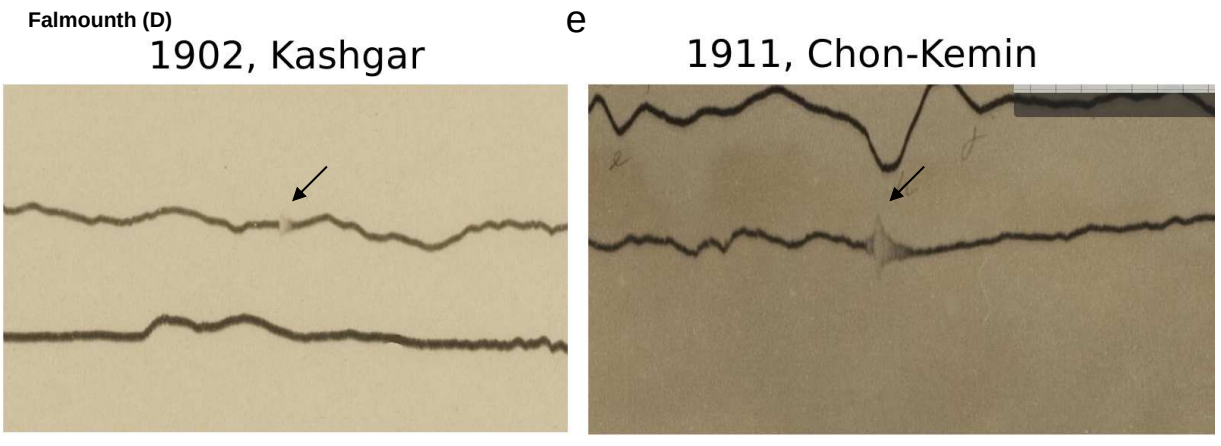
Falmounth (D)
1902, Kashgar
e
1911, Chon-Kemin

FIGURE 4.1: Source parameters determination of the 1902 Kashgar earthquake. a)- Tectonic map of the southern Tien-Shan and Tarim convergence region, the black rectangles show main cities in the area, the black circles show different epicenter locations for the Kashgar earthquake from GEM - *Storchak et al.* [2013], Om. - *Omori* [1907], K&S - *Kondorskaya et al.* [1982], the epicenter determined in this study is marked as blue + with corresponding error ellipse, gray beach balls show focal mechanisms of all the earthquakes from CMT catalog [*CMT*, 2015]. b)- the station distribution map for the Kashgar earthquake, the purple star shows the epicenter location, the gray circles show the stations from which the P wave arrival times were available, red triangles show the station from which the seismograms were obtained. c)- the focal mechanism determination of the Kashgar earthquake, top shows the mechanisms determination for different test depth, the bottom shows the 5% best solutions. d)- the intensity observations map with locations color-coded accordingly, with 10 corresponding to the intensity X, blue ellipse shows the possible epicenter location. e)- magnetograms comparison of the Kashgar (left) and the Chon-Kemin (right) earthquake records at Falmounth station, D component.

However, the maximum amplitudes of each phase are usually given in the text of corresponding book, which allows to scale the seismograms accordingly.

In addition to the seismogram reproductions from books, *Voznesenskiy* [1904] published detailed report about the Kashgar earthquake recording in Irkutsk, Russia. His report includes amplitudes of seismic phases recorded on two different instruments in Irkutsk and also the amplitudes recorded in Nikolaev, Russia. This information is also used in the magnitude calculation and mechanism determination using amplitude ratios. The report of *Voznesenskiy* [1904] also includes the intensity information from 24 locations around the epicenter.

Gutenberg [1956] located the epicenter of the Kashgar earthquake at 40°N and 77°E, this epicenter appears in global seismic catalogs and also in new GEM catalog [Figure *4.1*a *Storchak et al.*, 2013]. Another epicenter often found in the literature is the macroseismic observation based epicenter from *Kondorskaya et al.* [1982] with coordinates 39.8°N and 76.2°E. Unfortunately no detailed seismic bulletins are found for the Kashgar earthquake for precise relocation procedure. However, in 1907, F. Omori [*Omori*, 1907] published a note on the Kashgar earthquake aiming to determine its epicenter (Figure *4.1*a). In this publication he gives arrival times of the earthquake signal at different locations. The information from *Omori* [1907] is combined with the digitized waveforms to determine the epicenter location in this study. It is assumed that the time noted in *Omori* [1907] belongs to P wave arrival, though he did not specify that. P wave arrival times from 38 seismic stations worldwide (Figure *4.1*b) together with 7 arrival time differences are used to relocate the epicenter of the Kashgar earthquake. The epicenter is relocated at 39.859°N and 75.617°E (Figure *4.1*a), but the limited arrival times information results in a large error ellipse. There is not enough data to determine the depth of the earthquake from the bulletins and the digitized waveforms do not show any clear depth phases. *Kondorskaya et al.* [1982] assigned the depth h=40 to this earthquake, apparently based on wide distribution of high intensity (I=X) area. The available intensity observations are very sparse especially on the east (Figure *4.1*d). Three locations show the intensity X [Rossi-Forel scale *Davison*, 1921] along the southern flank of the Tien-Shan for ∼150 km in the east-west direction.

Gutenberg [1956] gave magnitude $M_s = 8\frac{1}{4}$ to the Kashgar earthquake, but this value was later re-estimated and reduced. The macroseismic observation based magnitude presented in *Kondorskaya et al.* [1982] is $M_{macr} = 8.0$ and local magnitude $m_{LH} = 7.9$. The GEM *Storchak et al.* [2013] catalog determined the magnitude $M_w 7.69$ for the earthquake. From the digitized waveforms and information found in books the body wave magnitude $m_B = 7.7 \pm 0.3$ is calculated in this thesis.

There are only three amplitude measurements with period appropriate for M_S determination, using the Prague-Moscow formula [*Karnik et al.*, 1962], from Tokyo and Irkutsk, giving $M_S = 8.0 \pm 0.4$.

Additionally to confirm the magnitude the magnetograms records (see Chapter *A*) of the Kashgar earthquake are compared to those of the Chon-Kemin earthquake. The comparison shows that the magnetogram amplitudes of the Chon-Kemin earthquake are 3 times larger than the Kashgar earthquake amplitudes on the records from station Falmounth (D component, see Figure *4.1*e), and Greenwich (D and H). Assuming the the Chon-Kemin earthquake has magnitude M_w8.0, the 1/3 ratio of amplitudes confirms the magnitude ∼7.7 for the Kashgar earthquake.

The focal mechanism of the Kashgar earthquake is determined by described above amplitude ratios comparison method (Figure *4.1*c), using the digitized waveforms and the amplitude from *Voznesenskiy* [1904]. Despite limited data the fault planes solution was determined successfully as 80°±20°/60°±10°/90°±10°. This focal mechanism agrees with previously reported one in *Molnar & Ghose* [2000] and confirms the trust faulting for the Kashgar earthquake. The mechanism determination for different test depths shows a clear minimum at 18 km depth. Assuming the rupture width of 48 km [based on scaling relations *Blaser et al.*, 2010] the surface rupture is expected, but is not found. However, with poor stations coverage and no clear depths phases the depth determination is rather uncertain. The scalar seismic moment determined from scaling of the waveform is $M_0 = 4 \cdot 10^{20}[Nm]$ (which corresponds M_w7.7).

The analysis of instrumental records of the Kashgar earthquake confirms its magnitude M∼7.7 and the thrust mechanism, which according to scaling relation [*Blaser et al.*, 2010] would produce about 110 km long rupture. Modern lower magnitude earthquakes (gray beach-balls on the Figure *4.1*a) in the region generally indicate north-northwestward under-thrusting of the basement of the Tarim Basin beneath the Tien-Shan [*Molnar & Ghose*, 2000]. *Zhao et al.* [2000] and *Shen et al.* [2013] have stated that the Tuotegongbaizi-Aerpaleike northward dipping thrust fault is responsible for the Kashgar earthquake. This fault has a dimension large enough to produce a magnitude 7.7 earthquake and it agrees well with focal mechanism determined above. This fault cuts through the largest intensity area and propagates further east, consistent with intensity observations.

4.2 1938 Kemin-Chu earthquake

The Kemin-Chu earthquake has occurred on June 20, 1938. The earthquake has caused some local severe damage, landslides and surface cracks along the Big Kemin River [*Wilhelmson*, 1947]. Although no long single surface rupture was found, several cracks up-to 150 m long and with up-to 0.7 m vertical offset were observed around the epicenteral area. This earthquake is of particular interest due to its location on the western most side of the Kemin-Chilik fault zone, western end of surface rupture left by the major 1911 Chon-Kemin earthquake.

Kondorskaya et al. [1982] and *Bindi et al.* [2014] presented source parameters of the Kemin-Chu earthquake based on intensity observations with $M_{IW} = 6.78$ [*Bindi et al.*, 2014]. The seismic bulletins based magnitude M_w=6.7 was assigned to the earthquake by *Storchak et al.* [2013]. No information about focal mechanism of this earthquake was previously reported.

The Kemin-Chu earthquake was not a subject of any individual study previously, subsequently there was no particular collection of seismograms for this earthquake. Seismograms from only 6 seismic stations in Europe (Figure *4.2*b) are collected for this earthquake within the here presented study. The records are good quality analog 3-component seismograms with all the seismic phases

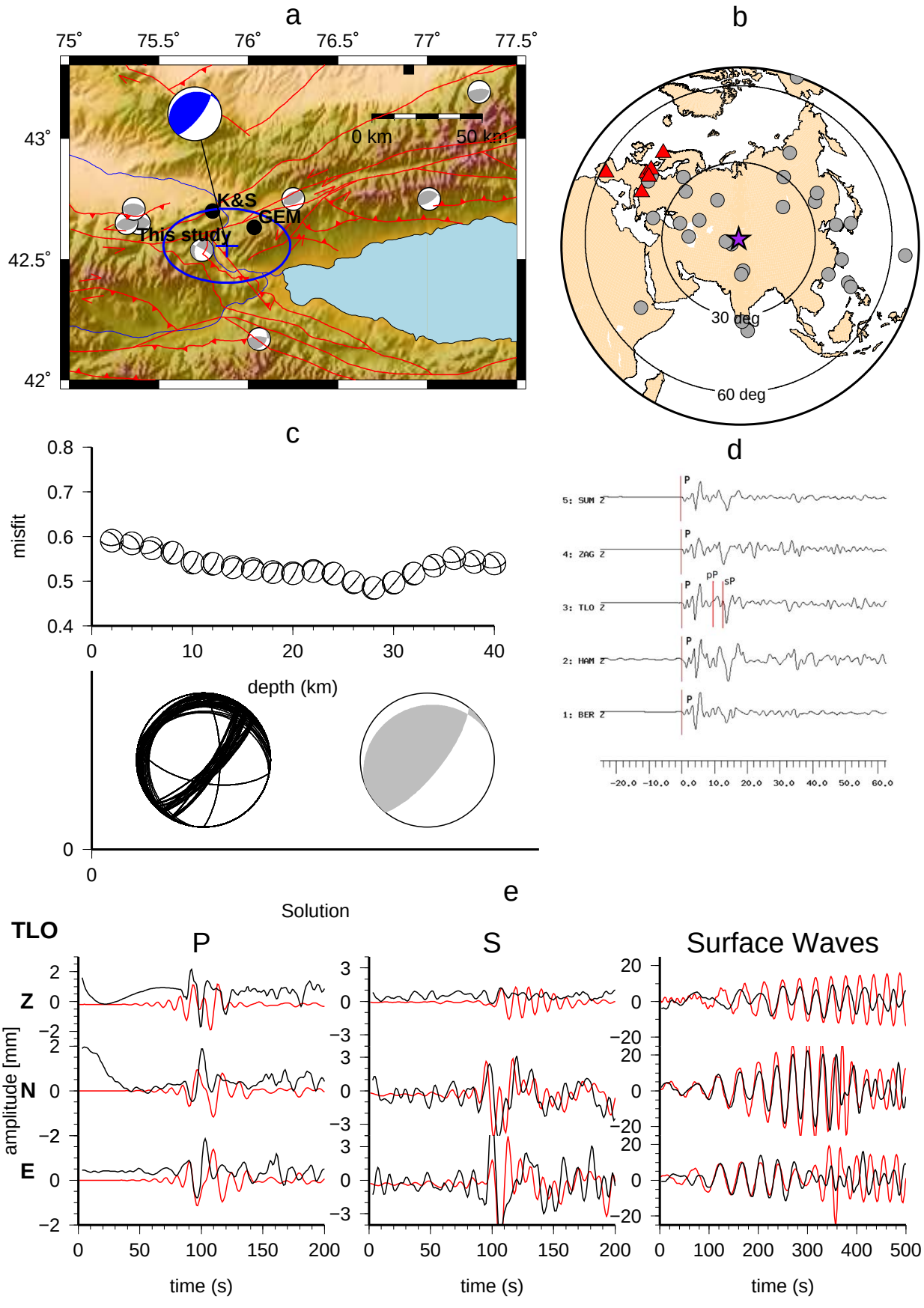
a
75°
75.5°
76°
76.5°
77°
77.5°
43°
42.5°
42°
0 km
50 km
K&S
GEM
This study
b
30 deg
60 deg
c
misfit
0.8
0.7
0.6
0.5
0.4
0
10
20
30
40
depth (km)
0
0
Solution
d
5: SUM Z
4: ZAG Z
3: TLO Z
2: HAM Z
1: BER Z
P
pP
SP
-20.0 -10.0 0.0 10.0 20.0 30.0 40.0 50.0 60.0
e
TLO
P
S
Surface Waves
Z
N
E
amplitude [mm]
time (s)
time (s)
time (s)

FIGURE 4.2: Source parameters determination of the 1938 Kemin-Chu earthquake. a)- Tectonic map of the northern Northern Tien-Shan region, the black rectangles show major cities in the area, the black circles show different epicenter locations of the Kemin-Chu earthquake from GEM - *Storchak et al.* [2013], K&S - *Kondorskaya et al.* [1982], the epicenter determined in this study is marked as blue + with corresponding error ellipse, gray beach balls show focal mechanisms of all the earthquakes from CMT catalog [*CMT*, 2015]. b) -the station distribution map for the Kemin-Chu earthquake, the purple star shows the epicenter location, the gray circles show the stations from which the arrival times are available for relocation, red triangles show the station from which the analog seismograms are obtained. c)- the focal mechanism determination of the Kemin-Chu earthquake, top shows the mechanisms determination for different test depth, the bottom shows the 5% best solutions. d)- The P-wave records with corresponding station and component name. e)- the observed (black) and synthetic (red) waveforms overlay, for the determined focal mechanism, station TLO (Toledo, Spain).

well recorded. These data are digitized and complemented by bulletin information from seismic stations worldwide used to relocate the earthquake epicenter.

The Kemin-Chu earthquake epicenter is relocated at 42.557°N 75.880°E, which is 15 km southwest from the GEM epicenter. The potential depth phases (pP and sP Figure *4.2*d) are marked after the first P wave arrival (pP- 10 seconds after the first P wave onset). These depth phases mean that the earthquake had (Figure *4.2*d) ∼27 km depth. The body wave magnitude $m_B = 6.9 \pm 0.4$ and the surface waves magnitude $M_S = 7.0 \pm 0.3$ are calculated from the digitized waveforms. Full waveform synthetic seismograms are calculated with the reflectivity method for different test depths (Figure *4.2*c). For each seismogram amplitude ratios are determined between P and S phases. In a grid search procedure the simulated recordings are calculated with 10° spacing in strike, dip, and rake angles and then compared to the observed records amplitude ratios. The Kemin-Chu earthquake has thrust mechanism with 250°±30°/20°±10°/120°±10° (Figure ref1938c). It should be mentioned that such station distribution (all the stations located at almost the same distance and azimuth Figure *4.2*b), introduces extra uncertainties in the mechanism determination. The seismic moment $M_0 = 2.9 \cdot 10^{19}[Nm]$ (M_w6.9) is calculated from observed and synthetic waveforms comparison. Estimated from the P-waveforms (Figure *4.2*d, e) the total source time duration is about 10 seconds, which, assuming a rupture velocity of 90% of the upper crustal shear wave velocity, results in about 30 km rupture length for unilateral rupture. This agrees well with rupture length calculated with scaling relations [∼34km, *Blaser et al.*, 2010] for a magnitude 6.9 earthquake. The test for different depth shows minimum misfit at ∼28 km depth, confirming the depth indicated by pP and sP phases.

The obtained fault plane solution suggests a fault plane with either a very shallow or very steep dip angle. *Arrowmith et al.* [2015] found steep fault slopes in the area of the Chu and Chon-Kemin Rivers confluence, where the Kemin-Chu earthquakes epicenter was located. Supposing that this area might have been affected by the Kemin-Chu earthquake, this would explain the focal mechanism obtained above and its steep dip angle. But at the same time along the western most segment of the Chon-Kemin earthquake surface rupture - Dzhil-Aryk section - they found 45° south dipping faulting, which does not fit in the general pattern of the Chon-Kemin rupture and might be associated with the Kemin-Chu earthquake. However, this fault would not agree with the focal mechanism determined in the here presented study.

4.3 1946 Chatkal earthquake

The Chatkal earthquake occurred on November 2, 1946 in Kyrgyzstan. It has been reported by *Kalmetieva et al.* [2009] that all constructions were destroyed in an area of 1500 km^2. The earthquake affected and strongly damaged buildings in the following cities: Osh, Dzhalal-Abad, Tashkent, Andizhan; also there have been large rockfalls, landslides and dammed rivers. No reports of clear surface faulting were found, but cracks with a length of up to 300 m and a width up to 30 m have been reported. This earthquake appears in catalogs with magnitude M7.5 [*Kondorskaya et al.*, 1982; *Storchak et al.*, 2013].

The Chatkal earthquake is the strongest earthquake which occurred in the Fergana region, western Tien-Shan, where the 600 km long Talas-Fergana fault cuts through the Tien-Shan mountain belt. This region has been currently seismically active with moderate sized and smaller earthquakes, which according to *Feld et al.* [2015] have shown reverse and strike-slip faulting. However, there has been no evidence that any of these earthquakes have occurred directly on the Talas-Fergana fault itself. There is an opinion that the Talas-Fergana fault is currently locked and current seismicity occurres along adjoining reverse and strike-slip fault structures. According to *Molnar & Qidong* [1984] there has been a discussion among seismologists that the Talas-Fergana fault itself has been responsible for the Chatkal earthquake. Based on this idea *Molnar & Qidong* [1984] proposed that the Chatkal earthquake had pure right-lateral strike-slip mechanism with strike, dip and rake 330°/90°/180° respectively. In the following this fact is checked by the Chatkal earthquake source parameters re-estimation.

Seismograms from 10 seismic station are collected and digitized for Chatkal earthquake. The same procedure as for the described above earthquakes is applied to the Chatkal earthquake dataset, in order to determine the source parameters. The earthquake epicenter is relocated to 41.463°N and 71.636°E (Figure *4.3*a), the body wave magnitude $m_B 7.4 \pm 0.2$ and surface wave magnitude $M_S 7.5 \pm 0.2$ are determined.

The P wave record of the Chatkal earthquake has shown complicated waveform with additional phases which are hard to interpret (Figure *4.3*d). The same complex pattern is observed in the S waves record, though not so clearly pronounced. Two possible interpretations of this P wave record are discussed. The complicated waveforms could be formed by P and additional pP and sP waves, as shown on the figure Figure *4.3*d. It such case the depth phase pP arrives 18 seconds after the first P, which means that the earthquake had ∼50 km hypocenter depth. I consider this scenario rather unlikely since there have been no reports about upper mantel contribution to the seismicity in this part of the Tien-Shan. Another, more favored in this study interpretation, is that the P wave record indicates a complex structure due the earthquake source. Assuming the multiple sub-events source (as shown for the Chon-Kemin earthquake Chapter *2*) the Chatkal earthquake waveforms can be interpreted as containing at least 3 sub-events, indicating 3 separated fault patches (see Figure *4.3*d, 1,2,3). The third sub-event would explain the arrival of unknown phase marked with question mark on Figure *4.3*d. Another interpretation of this unknown phase could be an early aftershock.

With the amplitude ratios comparison method the focal mechanism of the Chatkal earthquake is determined with strike, dip rake angles 270°±20°/30°±10°/120°±10° respectively, showing pure thrust mechanism at rather shallow ∼10 km depth. Although such a shallow depth of the earthquake is questionable, since no long surface rupture, associated with it, is found. This solution contradicts previously reported strike-slip mechanism for the earthquake. Thereby it argues against the suspicion that the Chatkal earthquake occurred by the strike-slip faulting on the Talas-Fergana

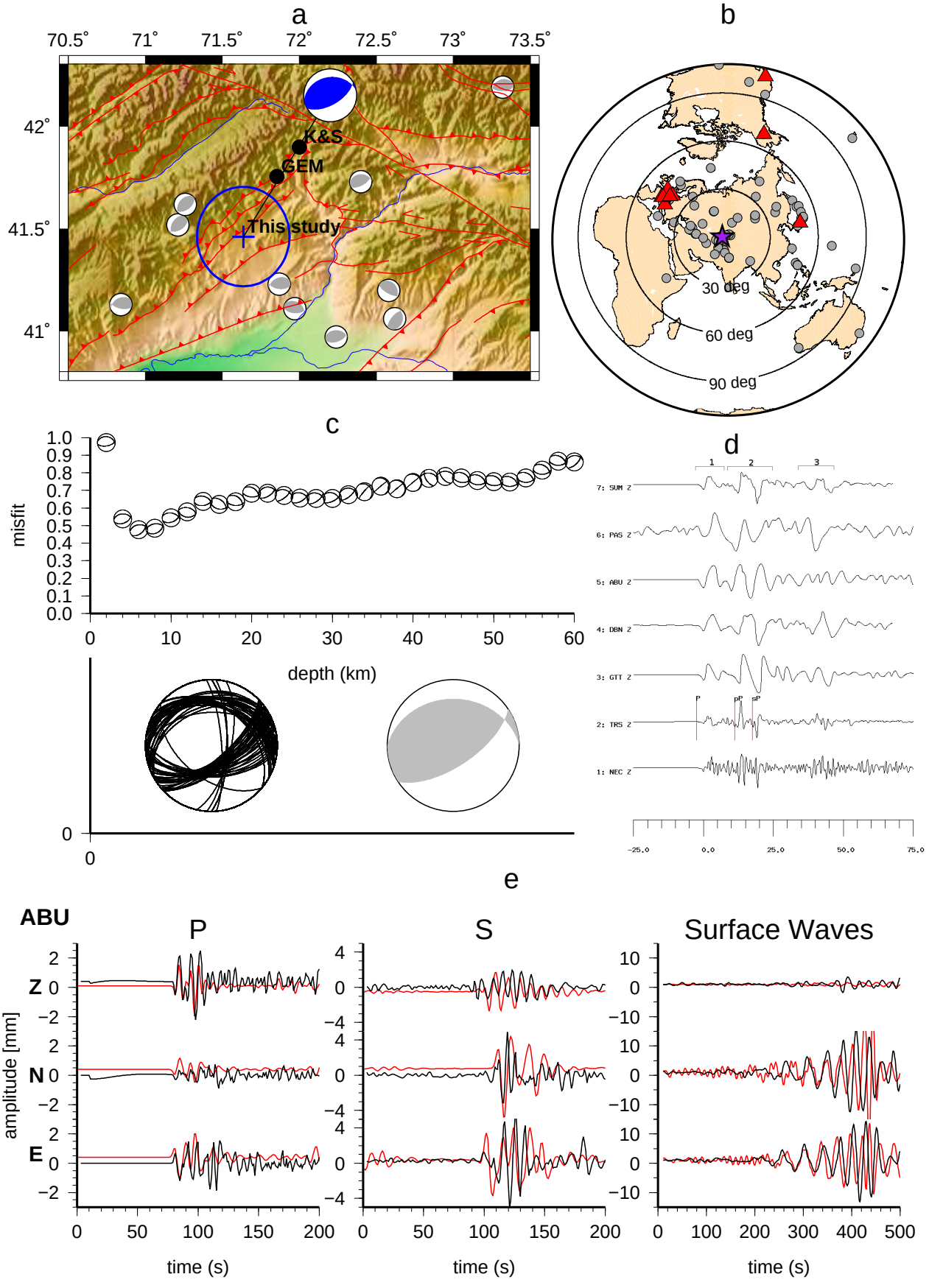
a
70.5˚
71˚
71.5˚
72˚
72.5˚
73˚
73.5˚
42˚
41.5˚
41˚
K&S
GEM
This study
b
30 deg
60 deg
90 deg
c
misfit
depth (km)
d
e
ABU
P
S
Surface Waves
Z
N
E
amplitude [mm]
time (s)

FIGURE 4.3: TSource parameters determination of the 1946, Chatkal earthquake. a)- Tectonic map of the southern Fergana region, the black circles show different epicenter locations of the Chatkal earthquake from GEM - *Storchak et al.* [2013], K&S - *Kondorskaya et al.* [1982], the epicenter determined in this study is marked as blue + with corresponding error ellipse, gray beach balls show focal mechanisms of all the earthquakes from CMT catalog [*CMT*, 2015]. b)- the station distribution map for the Chatkal earthquake, the purple star shows the epicenter location, the gray circles show the stations from which the arrival times are available, red triangles show the station from which the analog seismograms are obtained. c)- the focal mechanism determination of the Chatkal earthquake, top shows the mechanisms determination for different test depth, the bottom shows the 5% best solutions. d)- the P-wave records with corresponding station and component name, pP and sP indicate the potential depth phases and 1,2,3 mark probable sub-events. e)- the observed (black) and synthetic (red) waveforms overlay, for the determined focal mechanism, station ABU (Abuyama, Japan).

fault. The obtained fault plain solution is in a good agreement with the focal mechanisms of the modern moderate sized earthquakes [*Feld et al.*, 2015].

4.4 1970 Sarykamysh and 1978 Zhalanash-Tuup earthquakes

The M6.8, 1970 Sarykamysh and M6.9, 1978 Zhalanash-Tuup earthquakes occurred in the eastern part of the Tien-Shan region, east of the Lake Issyk-Kul (Figure *4.4* and *4.5*). The epicenters of these earthquakes are located only 40 km apart, but the previous studies [*Nelson et al.*, 1987; *Ekström et al.*, 2012] showed that they have absolutely different types of focal mechanisms. The 1970 Sarykamysh earthquake, according to *Nelson et al.* [1987], has thrust mechanism as the majority of the earthquakes in this part of the Tien-Shan. In contrast the 1978 Zhalanash-Tuup earthquake occurred by strike-slip faulting [*Ekström et al.*, 2012], and thereby complemented a few strike-slips registered in the region. Additional interest to the Sarykamysh and Zhalanash-Tuup earthquakes is supported by the fact that they occurred exactly at the turn of analog to digital seismic instrumentation. The 1970 Sarykamysh was still registered only by WWSSN analog seismic stations, whereas the 1978 Zhalanash-Tuup earthquake was already recorded by digital seismic instruments, with even 2 broad-band station records.

4.4.1 1970 Sarykamysh earthquake

The Sarykamysh earthquake occurred on June 5, 1970 near Przhevalsk (Karakol) city in Kyrgyzstan. Like other strong earthquakes in the region it cased severe local damage, surface cracks up to 1.5 m wide, multiple rockfalls and landslides [*Kalmetieva et al.*, 2009]. *Kalmetieva et al.* [2009] located the earthquakes epicenter at 42.52°N 78.73 °E and determined the local magnitude M_{LH}6.8 (Figure *4.4*a).

The Sarykamysh earthquake occurred at the time when the WWSSN was fully operating worldwide, and therefore it was recorded by more then 100 good quality seismic stations. Seismograms from 25 long-period WWSSN stations are collected for the Sarykamysh earthquake. Due to the time consuming digitization process the data from only 10 stations with good distance and azimuth coverage are digitized (Figure *4.4*b). These digitized waveforms combined with bulletin information provided by ISC seismic bulletins [*ISC*, 2015] are used to relocate the earthquake epicenter to 42.529°N 78.712°E, with 16 km hypocenter depth. This epicenter is ∼2 km away from *Kalmetieva*

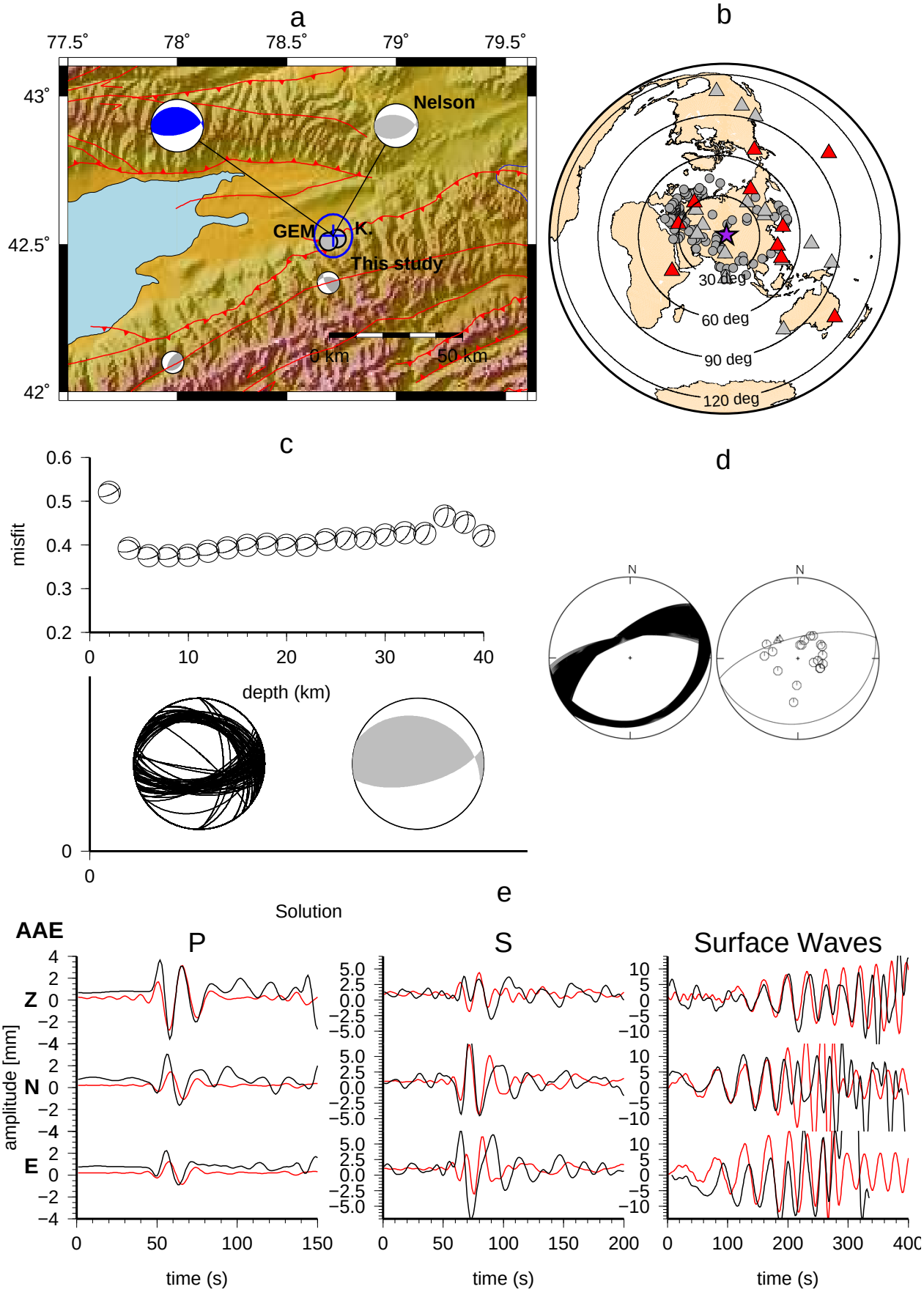
a
77.5˚
78˚
78.5˚
79˚
79.5˚
43˚
42.5˚
42˚
Nelson
GEM
K.
This study
0 km
50 km
b
30 deg
60 deg
90 deg
120 deg
c
misfit
depth (km)
Solution
d
N
N
e
AAE
P
S
Surface Waves
Z
N
E
amplitude [mm]
time (s)
time (s)
time (s)

FIGURE 4.4: Source parameters determination of the 1970 Sarykamysh earthquake. a)- Tectonic map of the epicenter region of Sarykamysh earthquake in the Tien-Shan, east of the Lake Issyk-Kul. the gray circles show different epicenter locations for the Sarykamysh earthquake from GEM - *Storchak et al.* [2013], and K&S - *Kalmetieva et al.* [2009], the epicenter determined in this study is marked as blue + with corresponding error ellipse, small gray beach balls show focal mechanisms of all the earthquakes from CMT catalog [*CMT*, 2015], larger gray beach ball is the mechanism from *Nelson et al.* [1987], and blue beach ball is the mechanism determined in this study. b)- Station distribution map for the Sarykamysh earthquake, the purple star shows the epicenter location, the gray circles show the stations from which the arrival times were available for relocation, red triangles mark the station from which the WWSSN seismograms were digitized and used in this study, the gray triangles mark other WWSSN stations, which also provided seismograms, but were not used. c)- Focal mechanism determination of the Sarykamysh earthquake, top shows the mechanisms determination for different test depths, the bottom shows the 5% best solutions. d)- Focal mechanism determination using first motion polarities from all the stations marked and red and gray triangle on b) e)- Observed (black) and synthetic (red) waveforms overlay, for the determined focal mechanism, station AAE (Adis Abeba, Ethiopia).

et al. [2009] location and ∼1.5 km away from GEM epicenter [*Storchak et al.*, 2015]. The magnitude $m_B = 6.6$ and $M_s = 6.8$ are calculated accordingly.

The focal mechanism of the Sarykamysh earthquake is determined using the amplitude ratios comparison as 280°±10°/30°±10°/110°±10° (Figure *4.4*c). This mechanism is consistent with the solution [277°/53°/108° *Nelson et al.*, 1987] determined by P and SH waveform inversion (Figure *4.4*a). The minimum misfit is observed for the shallow 10 km depth, however the misfit function for different test depths shows very low dynamic. Having good station coverage for the Sarymaysh earthquake allows to determine an alternative focal mechanism of this earthquake using the first motion polarities. The first motion polarities are read from 25 analog seismic records from WWSSN seismic stations. The focal mechanism determined using FOCMEC program [*Arthur Snoke*, 2015] is in a good agreement with both above mention solutions for the strike and rake angles, whereas the dip angle shows strong (up to 40 °) variation.

Unlike early analog seismic instruments the WWSSN seismic stations provided good quality waveforms and better azimuthal coverage. It allows to performs more operations with these data using modern methods and technique. For example clearly read polarities can be used as additional constraint for the focal mechanism. The instruments parameters of the WWSSN station instruments are well known and the time is precise, which allows to invert the waveforms for the focal mechanism determination.

4.4.2 1978 Zhalanash-Tuup earthquake

The Zhalanash-Tuup earthquake occurred on March, 24 1978 near Tuup city, Kyrgyzstan. It was felt on the large territory [*Bindi et al.*, 2014] and had local magnitude $M_{LH} = 7.2$ [*Kalmetieva et al.*, 2009]. The earthquake was recorded by WWSSN stations, and by 6 short-period 1-component (Z) and 7 long-period 3-component digital seismic stations. In addition to that, it was recorded by broad-band seismic station KHC in Prague, Czech Republic and by early Gräfenberg seismic array, Germany (Figure *4.5*c).

Unfortunately any analysis of the Zhalanash-Tuup earthquake is distorted by the fact that it occurred ∼1 hour after M_w7.5 Kuril Island earthquake [*CMT*, 2015] and was recorded on its coda. Therefore the seismic records of the Zhalanash-Tuup earthquake are dominated by long-period late

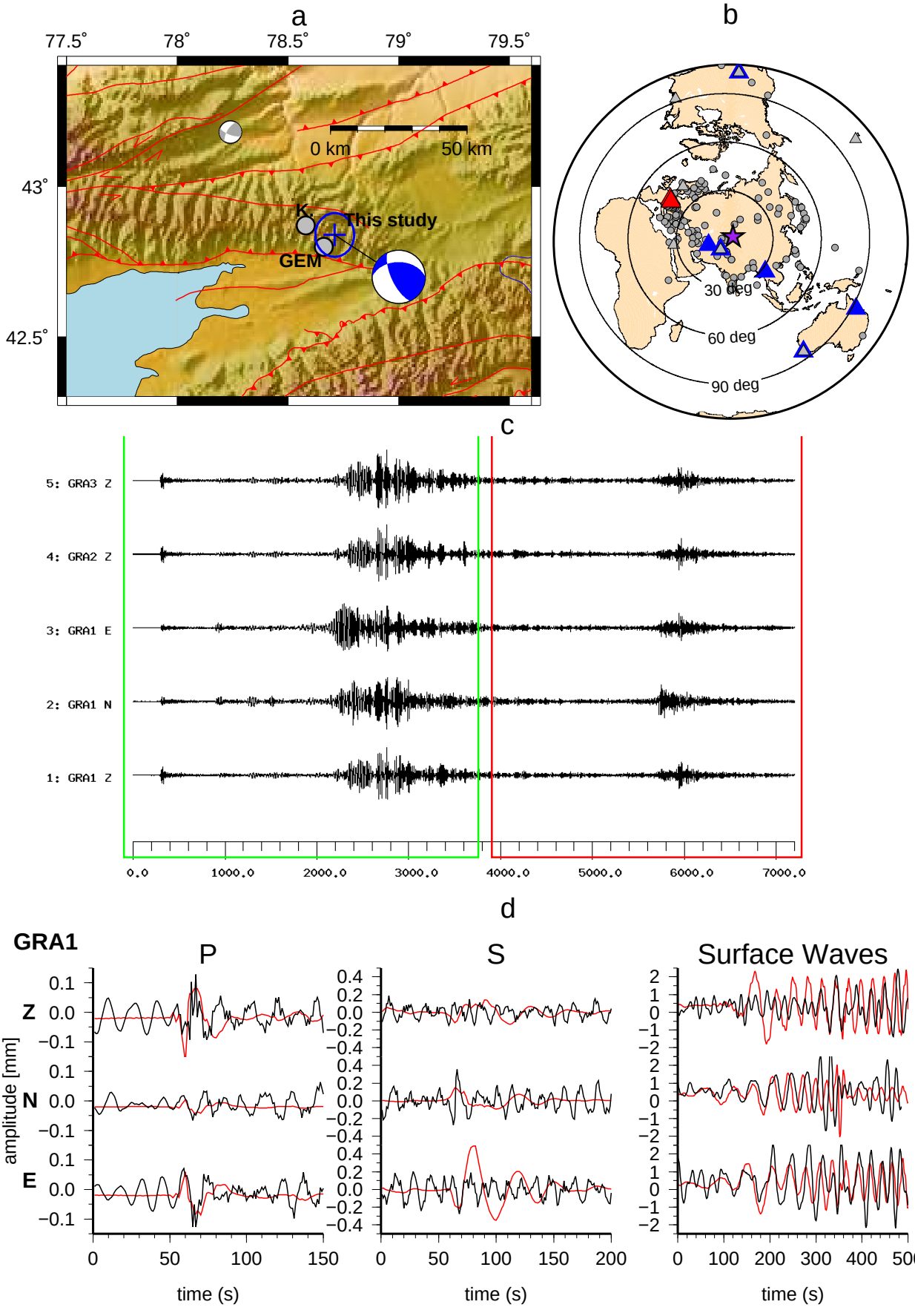
a
77.5˚
78˚
78.5˚
79˚
79.5˚
43˚
42.5˚
0 km
50 km
K
This study
GEM
b
30 deg
60 deg
90 deg
c
5: GRA3 Z
4: GRA2 Z
3: GRA1 E
2: GRA1 N
1: GRA1 Z
0.0
1000.0
2000.0
3000.0
4000.0
5000.0
6000.0
7000.0
d
GRA1
P
S
Surface Waves
Z
N
E
amplitude [mm]
time (s)
time (s)
time (s)

FIGURE 4.5: Source parameters determination of the 1978 Zhalanash-Tuup earthquake. a)- Tectonic map of the epicenter region of the Zhalanash-Tuup earthquake in the Tien-Shan, east of the Lake Issyk-Kul. The gray circles show different epicenter locations for the Zhalanash-Tuup earthquake from GEM - *Storchak et al.* [2013], and K&S - *Kalmetieva et al.* [2009], the epicenter determined in this study is marked as blue + with corresponding error ellipse, small gray beach balls show focal mechanisms of all the earthquakes from CMT catalog [*CMT*, 2015], and blue beach ball is the mechanism of the Zhalanash-Tuup earthquake from the same catalog. b)- Station distribution map for the Zhalanash-Tuup earthquake, the purple star shows the epicenter location, the gray circles show the stations from which the arrival times were available for relocation, red triangles mark the station prividing digital seismic records, blue triangles mark the digital short periods seismic stations, smaller gray triangles mark digital long period stations location. c)- Seismic records of the Zhalanash-Tuup earthquake (red rectangle) with preceding $M_w 7,5$ Kuril island earthquake (green rectangle) recorded at Gräfenberg array, Germany. d)- Observed (black) and synthetic (red) waveforms overlay, for the CMT determined focal mechanism, station GRA1 (Gräfenberg array, Germany).

surface waves of the preceding Kuril Island earthquake. On the long-period seismic stations the Zhalanash-Tuup earthquake is even hard to distinguish. The short-period stations have only one component, and two of them are partially clipped. On the broad-band stations the earthquake is clearly seen, however the records are also dominated by long-periods from earlier earthquake (Figure *4.5*d). The same situation is observed for the analog WWSSN records. Taking the above mentioned bias into account it hard to analyze the Zhalanash-Tuup earthquake with any of the presented in this thesis techniques.

The epicenter of the earthquake is relocated using the few seismograms and mainly the arrival times information from ISC bulletin [*ISC*, 2015]. The relocated epicenter 42.839°N and 78.711°E is just 5 km NNE from the GEM reported epicenter [*Storchak et al.*, 2015]. Further determination of the source parameters cause many difficulties and extremely high errors. It was attempted to determined the focal mechanism of the Zhalanash-Tuup earthquake using amplitude ration comparison, waveform inversion, and even moment tensor inversion, but all the solutions are very unstable and therefore are not presented here.

However the CMT [*Ekström et al.*, 2012] has determined the focal mechanism of the Zhalanash-Tuup earthquake as a strike-slip (Figure *4.5*a). Since no mechanism was determined in this study the observed and synthetic waveform overlay for the CMT mechanism is presented on the (Figure *4.5*d). It shows acceptable waveform-fit for P and Surface waves, but the S waves can hardly be read.

The Zhalanash-Tuup earthquake could have been a very interesting test example for the presented in this thesis methods. However, due to the spoiled waveforms the earthquake could be only partially analyzed.

4.5 1907 Karatag earthquake

The information about the 1907 Karatag earthquake is very limited. It is known from *Kalmetieva et al.* [2009] that a lot of landslides, rockfalls and surface ruptures occurred; 150 settlements were destroyed and more then 1500 people were killed. The most interesting point is that this earthquake appears in local [*Kondorskaya et al.*, 1982; *Kalmetieva et al.*, 2009] and international [*Storchak et al.*, 2013] catalogs with ∼200 km apart located epicenters (Figure *4.6*a). Moreover *Kondorskaya et al.* [1982] and *Kalmetieva et al.* [2009] described this earthquake as having two tremors, first occurred on October 21, 1907 at 04:23:20 and had magnitude M7.4 and the second occurred on the same

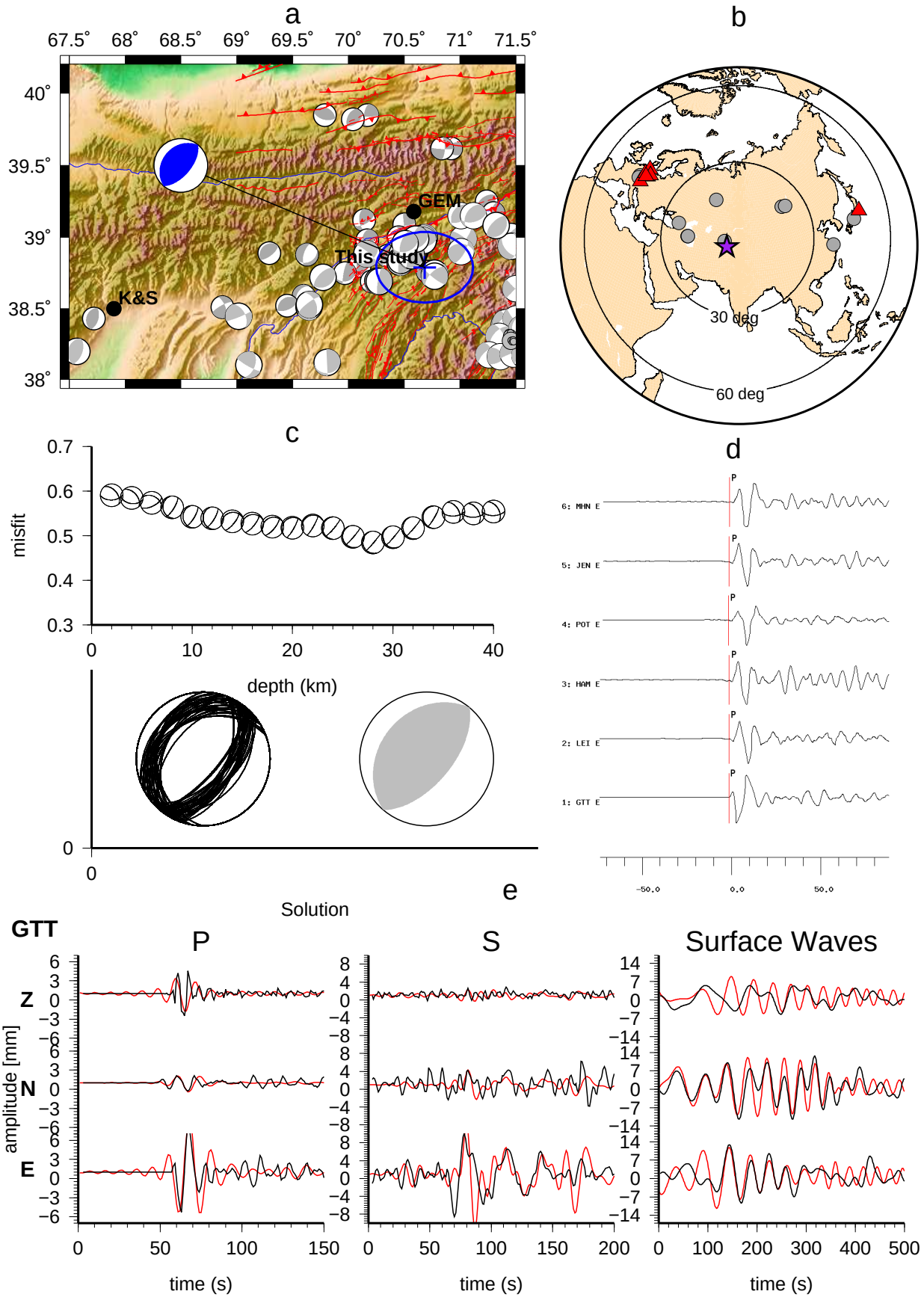
a
67.5˚ 68˚ 68.5˚ 69˚ 69.5˚ 70˚ 70.5˚ 71˚ 71.5˚
40˚
39.5˚
39˚
38.5˚
38˚
GEM
This study
K&S
b
30 deg
60 deg
c
misfit
0.7
0.6
0.5
0.4
0.3
0 10 20 30 40
depth (km)
0
0
d
6: MHN E
5: JEN E
4: POT E
3: HAM E
2: LEI E
1: GTT E
P
−50.0 0.0 50.0
e
Solution
GTT
P
S
Surface Waves
Z
N
E
amplitude [mm]
time (s)
time (s)
time (s)

FIGURE 4.6: Source parameters determination of the 1907, Karatag earthquake. a)- Tectonic map of the southern Tien-Shan and Pamir convergence region, the black circles show different epicenter locations of the Karatag earthquake from GEM - *Storchak et al.* [2013], K&S - *Kondorskaya et al.* [1982], the epicenter determined in this study is marked as blue + with corresponding error ellipse, gray beach balls show focal mechanisms of all the earthquakes from CMT catalog [*CMT*, 2015] and [*Schurr et al.*, 2014]. b)- the station distribution map for the Karatag earthquake, the purple star shows the epicenter location, the gray circles show the stations from which the arrival times were available, red triangles show the station from which the analog seismograms were obtained. c)- the focal mechanism determination of the Karatag earthquake, top shows the mechanisms determination for different test depth, the bottom shows the 5% best solutions. d)- The P-wave records with corresponding station and component name. e)- the observed (black) and synthetic (red) waveforms overlay, for the determined focal mechanism, station GTT (Göttingen, Germany).

day at 04:44 (∼20 min after the first one) with magnitude M7.3. *Kondorskaya et al.* [1982] refers to the fact that two tremors were clearly seen on the european stations.

In this study the seismograms from 7 seismic stations are collected and digitized for the Karatag earthquake, 6 of those station are located in Europe (Figure *4.6*b). Additionally information from seismic bulletins is collected as well. The earthquake epicenter is relocated using 13 absolute arrival times and 36 arrival times differences. The newly located epicenter appeared to be at 38.790°N and 70.683°N with hypocenter depth located at 12 ± 4 km, which is closer to the *Storchak et al.* [2013] solution. The detailed investigation of the analog seismograms and digitized records does not show any additional tremor as it was reported by *Kondorskaya et al.* [1982] and *Kalmetieva et al.* [2009]. There have been no distinguished signal found 20 minutes after the first record (Figure *4.6*e), however this is the arrival time of the SS and the Surface waves on the european stations. Subsequently if the P waves of the second signal are mixed with surface waves of the first one they can not be found. However, the question - how the earlier studies distinguished two tremor sremains open. It could be explained by the fact that at the very beginning of instrumental recording scientists were not used to distinguish all teleseismic phases and may have mistaken the reflected phases (in this case for example SS) for the second seismic signal.

From the digitized waveforms the body wave magnitude $m_B 7.5 \pm 0.2$ and surface wave magnitude $M_S 7.6 \pm 0.3$ are calculated. The digitized seimograms are used to determine the focal mechanism and depth of the earthquake using amplitude ratios. The results show that the Karatag earthquake has thrust mechanism with $40° \pm 20° / 60° \pm 10° / 90° \pm 10°$ strike, dip and rake respectively, with minimum misfit observed for ∼28 km depth. The obtained epicenter location defines the Vakhsh thrust system in the western part of Southern Tien-Shan and Pamir convergence to be responsible for this earthquake. The study of *Schurr et al.* [2014] showed that the Vakhsh thrust system is currently active with moderate size earthquakes and the determined Karatag earthquake focal mechanism is consistent with the active faulting observed in this area.

4.6 1949 Khait earthquake

The Khait earthquake occurred on July 10, 1949 near the Khait village in the Gharm region, Tajikistan. According to *Kondorskaya et al.* [1982] the earthquake reached intensity 10 in the epicenter area accompanied by a number of landslide and surface cracks. It destroyed and severely damaged several villages around the epicenter, one village was buried under large Khait landslide. *Kondorskaya et al.* [1982] gave this earthquake $M_{LH} 7.4$ and hypocenter depth of 18 km and the magnitude $M_w 7.5$ was assigned to it by [*Storchak et al.*, 2013]. It has been discussed by *Schurr*

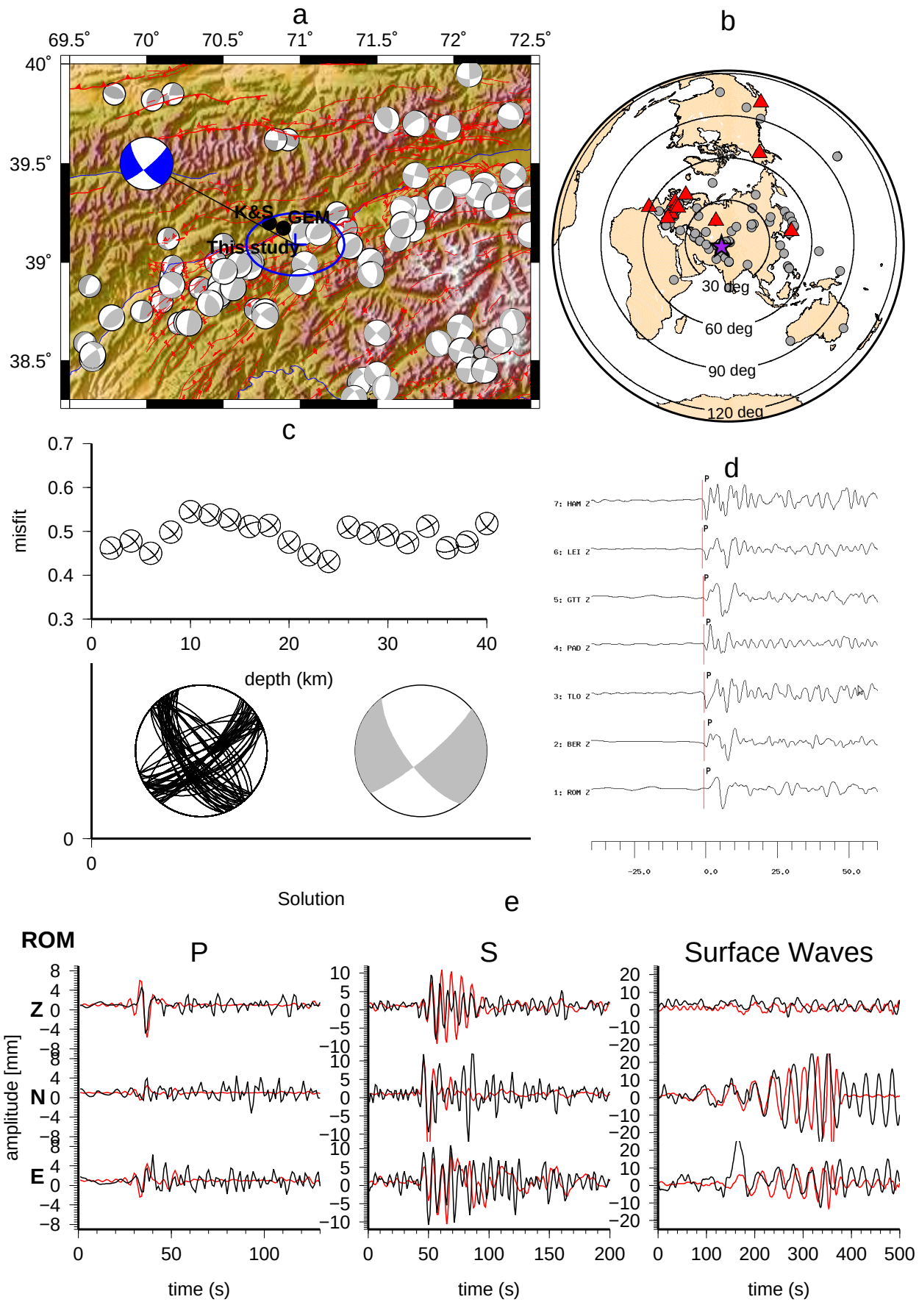
a
69.5°
70°
70.5°
71°
71.5°
72°
72.5°
40°
39.5°
39°
38.5°
K&S
GEM
This study
b
30 deg
60 deg
90 deg
120 deg
c
misfit
0.7
0.6
0.5
0.4
0.3
0
10
20
30
40
depth (km)
0
0
Solution
d
7: HAM Z
6: LEI Z
5: GTT Z
4: PAD Z
3: TLO Z
2: BER Z
1: ROM Z
P
-25.0
0.0
25.0
50.0
e
ROM
P
S
Surface Waves
amplitude [mm]
Z
N
E
time (s)
time (s)
time (s)

FIGURE 4.7: Source parameters determination of the 1949, Khait earthquake. a - Tectonic map of the southern Tien-Shan and Pamir convergence region, the black circles show different epicenter locations of the Khait earthquake from GEM - *Storchak et al.* [2013], K&S - *Kondorskaya et al.* [1982], the epicenter determined in this study is marked as blue + with corresponding error ellipse, gray beach balls show focal mechanisms of all the earthquakes from CMT catalog [*CMT*, 2015] and [*Schurr et al.*, 2014]. b)- the station distribution map for the Khait earthquake, the purple star shows the epicenter location, the gray circles show the stations from which the arrival times were available, red triangles show the station from which the analog seismograms were obtained. c)- the focal mechanism determination of the Khait earthquake, top shows the mechanisms determination for different test depth, the bottom shows the 5% best solutions. d)- The P-wave records with corresponding station and component name. e)- the observed (black) and synthetic (red) waveforms overlay, for the determined focal mechanism, station ROM (Rom, Italy).

et al. [2014] if the Khait earthquake occurred on the Vakhsh thrust system in the Pamir or already on the faults in the Tien-Shan.

The Khait earthquake has been recorded by a large number of stations providing good azimuthal coverage. Seismograms from 42 seismic station are collected for this earthquake, unfortunately only 12 stations (Figure *4.7*b) provided good quality records suitable for digitization. The station from former USSR, located nearer than 3000 km to the epicenter could not be used, because the waveforms exceeded the recordable amplitude range and are simply clipped. The digitized seismograms together with the bulletin information are used to relocate the earthquake epicenter to 39.091° and 70.968° (Figure *4.7*a) and the hypocenter depth to 22 ± 6km which is consistent with previously reported epicenters [*Kondorskaya et al.*, 1982; *Storchak et al.*, 2013] and the macroseismic observations. From the digitized waveforms the body wave magnitude $m_B 7.6 \pm 0.2$ and surface wave magnitude $M_S 7.8 \pm 0.4$ are calculated, which is slightly higher than the values previously reported in the catalogs [*Kondorskaya et al.*, 1982; *Storchak et al.*, 2013].

The strike, dip rake angles of the Khait earthquake focal mechanism were determined using amplitude ratios of the digitized waveforms as 80°±20°/80°±10°/-20°±10° respectively. This fault plane solution shows that the Khait earthquake has occurred on the NE striking dextral (or conjugate) strike-slip faulting with minimum misfit observed for 24 km depth. The seismic moment of the earthquake was $M_0 = 3.2 \cdot 10^{20}[Nm]$ ($M_w 7.6$). This according to scaling relations for a strike-slip fault corresponds to 150 km rupture. However ∼20 seconds source time duration read from P wave record on the Europeans stations (Figure *4.7*d) suggests about 60 km rupture. The rupture agrees well with 60-65 km long maximum intensity area reported by [*Kondorskaya et al.*, 1982; *Storchak et al.*, 2013] and suggests bilateral rupture propagation.

Gubin [1960] stated that the Khait earthquake had reverse mechanism on steeply south dipping, almost vertical plane, which contradicts here presented solution. But the solution shows low misfit and seems to be certain. The current seismicity does not show clearly pronounced strike-slip mechanisms in the epicenteral region of the Khait earthquake, and majority of modern smaller size earthquakes [*Schurr et al.*, 2014] occur by thrust faulting. However, about ∼80 km east of the Khait epicenter a number of strike-slip earthquakes are observed on the NEN striking faults. Although the large epicenter location error is unlikely for the earthquake, it could have occurred on the similar strike-slip fault. The strike-slip structures are expected to form in the region in response to overall compression due to N-S shortening and WNW rotation of the Pamir with respect to Tien-Shan. Therefore it can be concluded that the Khait earthquake mechanism agrees with the regional tectonic.

Chapter 5

Discussion and conclusion

Nowadays, widely distributed digital seismic networks allow quick and accurate determination of source parameters of earthquakes. Modern digital software and communication techniques make it relatively simple to obtain the first information of an earthquake epicenter location, depth, magnitude and focal mechanism within a few minutes after the earthquake occurred. However, for major earthquakes, happening prior to the digital seismic instruments era, the knowledge of the source parameters is limited. This can hardly change with respect to earthquakes, which occurred before the instrumental seismic recording started. But for the earthquakes, which were recoded with analog instruments (end of 19th and beginning of 20th century) the source parameters could be re-estimated and the information database considerably extended.

This study shows the methodology and results of complex analog seismic data analysis in order to obtain source parameters of major ($M > 7$) earthquakes in the tectonically unique Tien-Shan region. In the following the main findings of the performed work are discussed and presented in three subsections; describing the data collection, methodology of analysis and individual earthquakes impact on the regional tectonics. The information contained in these subsections describe the data collection, methodology of analysis and individual earthquakes impact on the regional tectonics.

5.1 Analogue seismic data collection and analysis

Considerable time, devoted to this work, was spent on the analog seismic data collection. Since there is no universal archive of analog seismic records, the records are distributed locally in different institutions worldwide. The preservation of those records requires a lot of space and particular conditions ensuring that the seismograms would remain undamaged. This leads to extra costs for the institutes and observatories archives. Therefore the value and the need of preserving the records is often discussed in the scientific community. Subsequently the risk that the number of available analog seismic records will decrease with time is very high. Thus the chances that such study can be repeated in the future are decreasing. It has been sown in the previous studies that analog seismic records are a great source of information for the historical earthquakes [*Baroux et al.*, 2003; *Stich et al.*, 2005; *Schlupp & Cisternas*, 2007; *Kanamori et al.*, 2010; *Okal*, 2012]. The present study confirms the idea by showing a successful use of the analog data for the strong past century earthquakes analysis.

The table *F.1* (Appendix *F*) gives the contact information of all the organizations, which provided the seismograms for this study including 18 institutions. Mainly, the seismograms were taken and scanned personally by the author of this thesis. Seismograms collection includes traveling to the corresponding archive, finding the necessary record, examining its quality and scanning it. Some institutions do not have scanning facilities and the scanner has to be brought along or the seismograms are photographed. Another very important step in the historical seismograms collection is scanning of the stations books, if available, for instrument parameter information and collecting the seismic bulletins.

For this study more than a 1000 seismograms are collected and scanned, and more than 300 of them are digitized and saved in text format ASCII files. In this work the digitization is done by using a path tool in GIMP (see section *3*). However, any image editor, which can produce a path as a number of points, could perform this job. In the frame-work of this study a software code is developed to convert the digitized path into a time depended seismogram with curvature correction (where it is necessary, for example for Wiechert seismograms). The developed code is simple to use, fast and easy to modify for a needed task. The 1902 Kashgar earthquake, as one of the earliest events, shows that the historical seismograms reproductions from the books can also be digitized and successfully used to determine the parameters of an earthquake.

At the beginning of seismograms collection from the archives it is usually not known how valuable a record from one or another instrument will be in the further analysis. Therefore, from my experience, the following conclusion was drawn about the impact of individual seismic instrument records for the purpose of this study. The good quality record here means that the seismogram is clearly readable with majority of seismic phases well identified. For the large magnitude earthquake (M$>$ 7), analyzed in this study, the best records were provided by Wiehert instrument, located at the epicentral distances between 4000-6000 km, with magnification between 80 and 300. However, for the major earthquakes with the magnitudes closer to 8 the records from station at the distances up to 12000 km could be sufficiently used. The records from Bosh-Omori instruments at the distance range from 4000 to 6000 km are also of a good quality, but due to their low magnification (between 10-20) it is often hard to identify the first arrival, or even the maximum of the P phases. Although Galizin instrument, as the only electromagnetic instrument at the time, providing generally valuable records, is not of much use for this study. The Galizin instruments were located mainly at the distances between 600-2000 km from the study region and due to their high magnification (800-1200) the records are often clipped. However, the Galizin instruments located at larger distances between 9000-11000 km, provided very good quality records.

Overall the seismic stations, at the time period covered by this study, were distributed heterogeneously. Therefore using the dense seismic network in Europe (mainly equipped by Wiechert instruments) as a large aperture seismic array is a very important finding of this study. It allows to align and stack the records, and thus identify the coherent source generated wavelets.

5.2 Methodology of historical earthquakes source parameters re-estimation

The analog seismic data even after being digitized are of a lower quality in comparison to modern digital seismic data. The seismographs of the past, being compared to the modern broadband digital seismic instruments, usually did not have sufficient frequency bandwidth for teleseismic waveform modeling. Moreover, a strong oscillation produced by major earthquakes in many cases provoked a dislocation of the writing needle introducing a step on the seismograms. Interpolation of the

time stamps during digitization is sometimes difficult and introduces small steps and kinks. Such distortion steps bias for instance moment tensor inversion when trying to increase the bandwidth by deconvolving the instrument characteristics. Additionally, the calibration information of the instruments, which was documented manually in the station books, is very often not available or uncertain. Therefore the standard modern source parameters determination techniques can not be directly applied to analyze the analog data. Subsequently it was necessary to develop a set of techniques and methods which allow to determine the parameters of a historical earthquake based on limited dataset.

- - All the named above uncertainties of analog data lead to errors in the focal mechanism determination procedure. However, it has been shown in earlier the studies that amplitude the ratios between different phases can help to significantly constrain the focal mechanism of the earthquake [*Kisslinger*, 1980; *Julian & Foulger*, 1996; *Hardebeck & Shearer*, 2003]. It is obvious that the amplitude ratios remain the most certain information for the historical seismograms. Therefore the focal mechanism is determined using the amplitude ratios only. For the body waves direct and reflected phases are picked (P,PP,S,SS), their amplitudes are measured and the amplitude ratios between different phases are calculated. In a grid search procedure the synthetic records are simulated with 10° spacing in strike, dip and rake angles and their amplitude ratios are compared to the corresponding amplitude ratios of the observed seismograms and a misfit is calculated.

  This method avoids any uncertainties introduced by wrongs timing or instrument characteristics. Amplitude ratios do constrain strike and dip angle but not the sign of the slip vector. For this case the calculation program is designed in a way to be able to employ the first motion polarity information as well when it is available. The performance of the amplitude ratios comparison method is tested for a synthetic example and two modern large continental earthquakes (Appendix *C*), also the influence of the usage of different global velocity models on the method was investigated (Appendix *D*).

- - Additional difficulty in applying standard moment tensor inversion methods is the necessity to rotate the horizontal N and E component seismograms correctly into radial and transverse components in standart moment tensor inversion software. This procedure needs precise time alignment and magnification correction between horizontal N and E components which is often difficult (see Appendix *B*) to obtain. In some cases the true orientation of components seems to deviate from the assumed one (Appendix *B.4*). In order to avoid rotation and restitution (instrument response removal) of the digitized historical seismograms, the synthetic seismograms instead were rotated into the local station ZNE coordinate system and historic seismograph recordings were simulated with given values for damping, free period and magnification of the respective instrument.

- - The fact that geological field observations describing aftermath of an earthquake on the surface can be used as additional source of information to constrain kinematic source parameters is often applied in the historical earthquakes studies [*Schlupp & Cisternas*, 2007; *Kanamori et al.*, 2010; *Okal*, 2012]. In this study the surface damage description, including surface crack locations and size, and the dimension of vertical offsets, are used for kinematic source modeling. The Okada dislocation model [*Okada*, 1985] is employed in order to obtain the theoretical surface rupture parameters based on the determined in this study fault orientation and using scaling relations [*Blaser et al.*, 2010] to calculate fault dimension from its magnitude. This model is then compared to the observed landscape changes as aftermaths of the Chon-Kemin earthquake, and the proposed multiple source model is confirmed.

- – It has been shown in previous studies [*Brodsky et al.*, 2003; *Moretti et al.*, 2012; *Allstadt*, 2013; *Yamada et al.*, 2013] that a landslide signal can be simulated as a combination of vertical and horizontal single forces applied to the ground by a sliding mass (mass of the landslide). In order to distinguish between the earthquake and the landslide signal for the case of the Sarez earthquake the single source model is applied to calculate the Greens functions using FOMOSTO tool in PYROCKO framework [*Heimann*, 2014b,a]. The Greens functions are then used to simulate a set of synthetic seismograms convolved with the instrument response of the corresponding historical instrument. As a result the predicted displacement which such a landslide could produce, and how this displacement would be recorded on a station located at certain place, as well as the possible earthquake-landslide combined records are investigated. Generally the earthquakes are very often accompanied by landslides. There are even the cases when the landslide signal was mistaken for an earthquake one and appeared in the earthquake catalogs, e.g. 2001, Mt. Garmo landslide [*Stark et al.*, 2012]. Here presented results show a possibility to use analog seismic records as an additional source of information for the historical landslide studies.

The set of techniques and methods presented here for the historical earthquakes source parameters determination based on analog seismograms can be also applied for another region in the world where major historical earthquakes occurred and have not been studied based on instrumental data yet. To these regions belongs for example Mongolia, where several $M \geq 7.5$ earthquakes occurred between 1900 and 1970, or the earthquakes in China such as the 1906 Manas earthquake and many others. These methods are likely not restricted to teleseismic distances. They could be adapted for the regional scale for smaller magnitude earthquakes. The amplitude ratios comparison method could be tested for the earthquakes from the past century in Europe, using very dense analog European seismic stations network. For example such earthquakes as $M \leq 7.0$ earthquakes in Italy or 1911, $M_{LH}6.1$ Albstadt earthquake in Germany, and many others could be analyzed.

5.3 Tectonic implication of the results

The above presented methods are successfully applied to determine the source parameters of the 10 largest earthquakes in the Tien-Shan and Pamir region (Figure*5.1*). The newly determined focal mechanisms of major earthquakes, based on the instrumental data, are of crucial importance for the regional tectonics and understanding of deformation processes in the Tien-Shan and Pamir regions.

It is presented in this study that the majority of the earthquakes in the Northern Tien-Shan shows reverse faulting on roughly east-west trending faults, from Kemin-Chilik fault zone extending further till Fergana region as well as east of the Lake Issyk-Kul. This observation is consistent with the modern moderate sized earthquakes [*Ghose et al.*, 1998a] and the current convergence rates in the Tien-Shan [*Zubovich et al.*, 2010]. The faults in the Northern Tien-Shan, which are responsible for the major earthquakes have generally steep dip angles (between 40° and 60°). None of the studied major earthquakes is associated with strike-slip faulting along main structures such as Talas-Fergana fault or Chon-Kemin faults. This confirms earlier reported compressional tectonics of Tien-Shan and the north-south horizontal shortening parallel to the India-Eurasia convergence direction [*Nelson et al.*, 1987; *Ghose et al.*, 1998a; *Feld et al.*, 2015].

Unfortunately the limitations introduce by the analog seismic data quality do not allow to determined the depth of the earthquakes precisely and there is very few identified clear depth phases (pP, sP). However, the presented here modeling reveals that the earthquakes are likely to occur in the

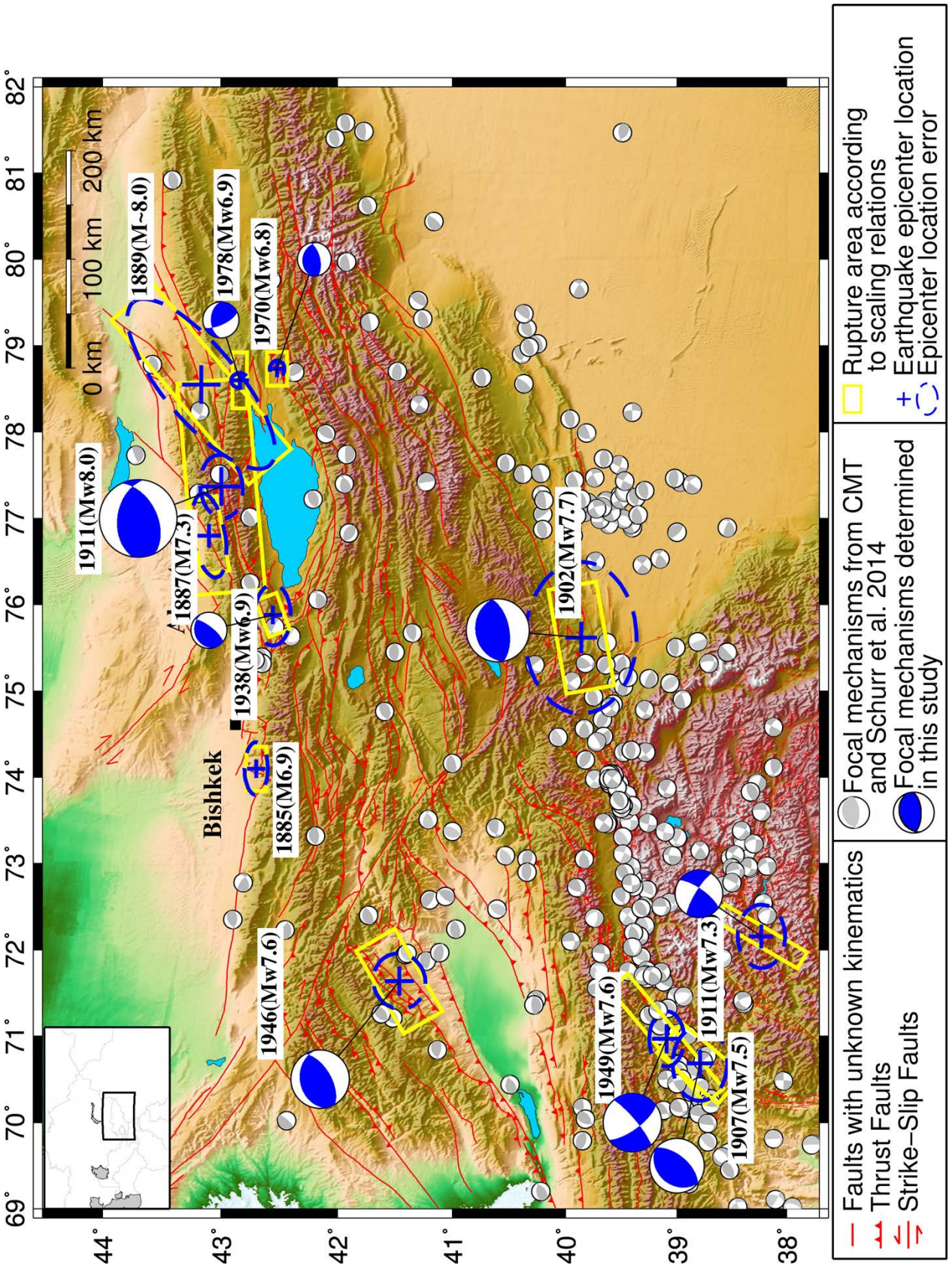
0 km 100 km 200 km
1911(Mw8.0)
1889(M~8.0)
1978(Mw6.9)
1970(Mw6.8)
1887(M7.3)
1938(Mw6.9)
1885(M6.9)
Bishkek
1946(Mw7.6)
1902(Mw7.7)
1949(Mw7.6)
1911(Mw7.3)
1907(Mw7.5)
Faults with unknown kinematics
Thrust Faults
Strike–Slip Faults
Focal mechanisms from CMT and Schurr et al. 2014
Focal mechanisms determined in this study
Rupture area according to scaling relations
Earthquake epicenter location
Epicenter location error
69° 70° 71° 72° 73° 74° 75° 76° 77° 78° 79° 80° 81° 82°
44° 43° 42° 41° 40° 39° 38°

FIGURE 5.1: Tectonic map of the study region with results of the earthquakes source parameters determination. The blue + show the relocated epicenters of the earthquake with corresponding error ellipses in blue. Yellow rectangles around each epicenter show rupture area calculated with scaling relations [*Blaser et al.*, 2010], the rectangles are originated along the strike or, for early events (1885-1889), along the maximum intensity ellipse. The blue beach ball show the focal mechanisms of the earthquakes determined in this study.

upper 20-25 km crust in the middle and western part of the Northern Tien-Shan. Previous studies [e.g. *Alinaghi & Krüger*, 2014] reported the lower crust contribution to the seismicity in eastern part of study area. For example, the centroid depth of the 1978 Zhalanash-Tuup earthquake determined by *Ekström et al.* [2012] is 37.4 km. The only earthquake which left clear long surface rupture signiture, proportional to its predicted from scaling relations size [*Blaser et al.*, 2010], was the 1911 Chon-Kemin earthquake. All other earthquakes do not show clear long scarps and large vertical offsets on the surface. It likely indicates that the hypocenter depth must have exceeded 10 km. However, the absence of surface rupture for such magnitude earthquakes is not singular in the Tien-Shan. It was also observed for other thrust intraplate earthquakes in the world such as 2001 Gujarat (depth 15 km) and 2015 Nepal (depth 12 km) earthquakes. Moreover, based on scaling relations [e.g. *Blaser et al.*, 2010] the rupture width of a magnitude M7.7 thrust earthquake is about 45 km, assuming the 20 km hypocenter depth and 45° dip it could be expected that the earthquake does not rupture to the surface.

For the Pamir region the focal mechanism 1911 Sarez-Pamir earthquake fits very well into the current deformation pattern of the Pamir interior and its margins, defined by recent moderate sized earthquakes [*Schurr et al.*, 2014]. The tectonics along Pamir′s margins is more complex and diverse. For example, the Vakhsh thrust system shows variety from thrust till mostly dextral slip along steep ENE striking planes in the epicentral area of the 1907 Karatag and 1949 Khait earthquakes. It explains the different type of faulting determined for these two nearby earthquakes. All three major earthquakes in the Pamir have been associated with shallow-upper crustal seismicity.

The key conclusions of the here presented work with respect to the impact of each individual earthquake in regional tectonics are discussed in the following:

- - The large magnitude M∼8 of the Chilik earthquake has been confirmed by the instrumental data. This important conclusion is a key finding for the presented study since it affirms that the faults in the Tien-Shan region have produced two magnitude M∼8 earthquakes, (∼120 km apart) within 22 years at the turn of 19th to 20th century.
- - The mechanism of the major Chon-Kemin earthquake is determined, with a constraint for kinematic source model. This model is based on combined analysis of digitized instrumental earthquake records and documented geological data. The suggested kinematic source parameters agree well with the surface rupture observations in the epicenter area.
- - The 1938 Kemin-Chu earthquake mechanism shows that this event has occurred either on a very shallow north-dipping or very steep south-dipping plain. Therefore it can not be associated with the 45° south-dipping fault observed at the western end of the 1911 Chon-Kemin earthquake rupture following *Arrowmith et al.* [2015].
- - The analysis of the 1946 Chatkal earthquake revealed that the earthquake does not have a strike-slip mechanism as it was previously anticipated. It contradicts the idea [*Molnar & Qidong*, 1984] that this earthquake has occurred on the Talas-Fergana strike-slip fault and

therefore agrees with the fact that this large fault has been currently inactive, or locked [*Ghose et al.*, 1998a].

- - The source parameters of the 1970 Sarykamysh are re-estimated in this study, confirming that the earthquake had thrust mechanism. In contrast, the 1978 Zhalanash-Tuup earthquake located only 40 km NNW, has a strike-slip mechanism. These two earthquakes show that two types of faulting present in the region east of Lake Issyuk-Kul. This fact is also confirmed by the current moderate sized seismicity in the region. Although the trust faulting dominates through the Tien-Shan several M>5 strike-slip earthquakes also occurred in the past years east of Lake Issyk-Kul (e.g. Mw6.31990 or Mw6.2 2013 earthquakes).

- – The magnitude M_w and the focal mechanism of the 1902 Kashgar earthquake are for the first time determined based on the instrumental data, though no original paper seismogram existed for this earthquake. This study confirms that the earthquake likely has a smaller magnitude than the previously reported and the fault plane solution presented here is consistent with presumed fault kinematic. The focal mechanism indicated the thrust faulting, which is in a good agreement with presumably responsible Tuotegongbaizi-Aerpaleike northward dipping thrust fault, described in the previous studies [*Zhao et al.*, 2000; *Shen et al.*, 2013].

- - The study of the 1911, Sarez-Pamir earthquake showed that the majority of the recorded seismic signal is due to the tectonic earthquake, and the signal of the landslide has minor contribution if at all. Additionally it was found that the earthquake has strike-slip mechanism on NE striking sinistral strike-slip fault, which is in a good agreement with the current tectonics of the Pamir interior. This study identified the sinistral trans-tensional Sarez-Karakul fault system as the main candidate in the region for being responsible for the Sarez-Pamir earthquake. Although the case when earthquake may have occurred on another, unmapped fault, remains possible as well. The surface trace of the Sarez-Pamir earthquake is not found, which, however, can be explained by fact that the epicenter is located in hard-to-reach area.

- – The 1907, Karatag earthquake was reported in some studies as a double event, consisting of two tremors with 20 minutes time difference and almost the same magnitude. However, the detailed investigation of the instrumental records does not confirm the double event hypothesis. The earthquake occurred in the convergence zone of the Pamir and Southern Tien-Shan and, as it is shown in this study, had thrust mechanism and likely occurred within Vakhsh thrust system. The fault plane solution for the Karatag earthquake is consistent with the focal mechanisms of the modern earthquakes.

- – The 1949 Khait earthquake was also located on the Vakhsh thrust system, however it has shown the dextral strike-slip faulting. This type of faulting is not clearly pronounced for the modern earthquakes in the epicenter area. However, the dextral strike slip earthquakes are observed ∼60 km east of the Khait event epicenter [*Schurr et al.*, 2014]. The strike-slip faulting occurred in the region as a result of westward extrusion in response to overall compression due to N-S shortening. Therefore it can be concluded that the Khait earthquake mechanism agrees with overall tectonic processes.

The Tien-Shan Pamir earthquakes sequence at the turn of the 19th and the 20th century remains a unique tectonic event in the history of seismology. Detailed investigation of the source parameters of these earthquakes reveals a valuable contribution to the general understanding of the large magnitude intracontinetial thrust earthquakes. The findings of this study are also of the crucial importance for estimating the seismic hazard measures in the region of the Tien-Shan. The significance of the presented in this study 10 earthquakes is supported by the fact that the sum of their

scalar seismic moments M_0 is ∼20 times larger than the sum of M_0 of all the CMT catalog [*CMT*, 2015] earthquakes from 1976 till present in the same region.

Outlook

In this study I have investigated 10 strongest earthquakes in the Tien-Shan region between 1885 and 1978, however 24 more earthquakes with magnitude M>6.5 have occurred in the region within that time period. The analog seismic records of those 24 earthquake were collected and partially digitized within this PhD project. Due to time limitation introduced by complicated analog data processing they could not be studied yet. More detailed investigation of the mentioned earthquakes can be done using the here presented methods and would not require very long time.

The interest to the historical seismograms and general historical seismic data preservation currently rises in scientific society. Modern possibilities of data exchange and opened communication on the international level, especially with previously closed countries, allow constant increase of data sources. This could lead to the appearance of new, previously unknown or not accessible, sources of analog seismic data. In such a case, additional information could be obtained for the earthquakes analyzed in this study, which could be directly added to the already obtained results and perhaps improve them.

The error estimation for the presented method introduced by velocity model uncertainty is discussed in the Appendix *E*. However more detailed statistical analysis of the uncertainties of amplitudes ratios comparison method for the focal mechanism and depth determination, could be performed within a Bayesian statistical framework.

Presented here techniques and methods could be applied to obtain more information for other historical large earthquakes in the different regions worldwide. Moreover the methods could be adopted for application on regional scale for smaller magnitudes earthquakes, if the station network distributions allows. For example dense European seismic station coverage from beginning of 1900s allows to determine source parameters of many moderate size earthquakes in Europe.

APPENDIX A

Instrumental magnitude constraints for the July, 11, 1889, Chilik earthquake.

Frank Krüger, Galina Kulikova, Angela Landgraf

Published in Special Publication of Geological Society of London: Seismicity, Fault Rupture and Earthquake Hazards in Slowly Deforming Regions. (eds) Landgraf, A., Hintersberger, E., Kübler, S., & Stein, S. 2015, Vol 432.
DOI: 10.1144/SP432.8

ABSTRACT: A series of large-magnitude earthquakes above 6.9 occurred in the northern Tien-Shan between 1885 and 1911. The Chilik earthquake of July 11, 1889, has been listed with a magnitude of 8.3, based on sparse macroseismic intensities, constrained by reported damage. Despite the existence of several juvenile fault scarps in the epicentral region, that are possibly associated with the 1889 earthquake, no through-going surface rupture having dimensions expected for a magnitude 8.3 earthquake has been located - a puzzling dilemma. Could the magnitude has been overestimated? This would have major implications, not only for the understanding of the earthquake series, but also for regional hazard estimates. Fortunately, a fragmentary record from an early Rebeur-Paschwitz seismometer exists for the Chilik event, recorded in Wilhelmshaven (Germany). To constrain the magnitude, we compare the late coda waves of this record with those of recent events from Central Asia, recorded on modern instruments in Germany and filtered with Rebeur-Paschwitz instrument characteristics. Additional constraints come from disturbances of historic magnetograms that exist from the Chilik and the 1911 Chon-Kemin earthquakes. Scaling of these historic records confirm a magnitude about 8 for the 1889 Chilik earthquake, pointing towards a lower crustal contribution to the fault area.

A.1 Introduction

At the turn of the 19th and 20th centuries, the northern Tien-Shan[1] was hit by a series of large earthquakes [*Ignatiev*, 1885; *Mushketov*, 1891; *Bogdanovich et al.*, 1914, e.g,]. The 1885 (M_s6.9) Belovodskoe event produced considerable damage west of the Kyrgyz capital Bishkek, and was followed in 1887 by a magnitude 7.3 event that destroyed Almaty (previously named Verny). Just two years after these events, the region was struck by the Chilik earthquake east of Verny (commonly assigned M_s 8.3), and in 1911 by the M_w8.0 Chon-Kemin (also called Kebin earthquake) earthquake (Figure *A.1*). Due to the occurrence of these earthquakes in the earliest years of instrumental seismology, the seismographic data base is poor, but some of these events were studied by macroseismic investigations combining collection of eyewitness reports with investigations of primary and secondary landscape response to ruptures and seismic shaking [*Ignatiev*, 1885; *Mushketov*, 1891; *Bogdanovich et al.*, 1914].

The Chilik earthquake occurred on July 11, 1889 (June 30, 1889 Russian old style calendar, valid in Russia until 1918). Unlike other strong earthquakes in the region (the Verny earthquake and the Chon-Kemin earthquake [*Nurmagambetov*, 1999]), it was not additionally studied by a geological expedition [*Mushketov*, 1891]. All information about the earthquake was obtained by testimonies of witnesses collected through questionnaires sent by the ″Russian Geographical Society″ after the earthquake. The epicenter was determined as a center of a maximum intensity ellipse. Based on macroseismic observations that implied intensity X (Rossi-Forel scale) in the epicentral area [*Mushketov*, 1891], the magnitude was estimated to be 8.3±0.5 [*Kondorskaya et al.*, 1982; *Besstrashnov*, 1993] and $8.3^{+0.2}_{-0.1}$ [*Bindi et al.*, 2014]. Furthermore, on the basis of the broad region over which high intensities were observed, and the absence of localized extreme intensities, a hypocenter depth of 40 km was assigned to the earthquake [*Kondorskaya et al.*, 1982; *Kalmetieva et al.*, 2009; *Bindi et al.*, 2014].

[1]Northern Tien-Shan region: in this study we consider not the whole Tien-Shan mountain belt, but its northern part - a rectangular area in the border region between Kazakhstan and Kyrgyzstan, defined by latitude from 42N° to 45N°, and longitude from 74E° to 81E°.

The high magnitude taken together with its intensity-based centroid depth in the lower crust (crustal thickness in the region ranges from 45-55 km [see e.g., *Bindi et al.*, 2014; *Alinaghi & Krüger*, 2014]) would make the Chilik earthquake an unusual event in a zone of continental collision (Figure *A.1*). Surprisingly, despite this high magnitude and several attempts to map the fault, the full extent of a continuous surface rupture that could correspond to an event of this magnitude has not yet been defined with certainty. While juvenile fault scarps with significant large offsets of several meters exist in the epicentral region, they are discontinuous and widely distributed across several neighboring faults [e.g., *Tibaldi et al.*, 1997; *Tibaldi*, 1998; *Abdrakhmatov et al.*, 2015]. In contrast, the M_w8.0 1911 Chon-Kemin earthquake has a remarkable fault scarp with a mapped minimum length of 155 km [*Bogdanovich et al.*, 1914; *Arrowmith et al.*, 2015], and the rupture was possibly up to 200 km long [*Kulikova & Krüger*, 2015]. Moreover, the offsets in 1911 partly exceeded 10 m and the fault scarp is, even after one hundred years, well preserved and visible in the landscape as well as on high-resolution satellite imagery [e.g., *Arrowsmith et al.*, 2005; *Arrowmith et al.*, 2015]. Thus, for the M_s8.3 Chilik earthquake, a surface-rupture length (SRL) between 200 and 300 km with an average displacement between 6.7 and 9.1 meters for thrusting or strike-slip, respectively [e.g., *Blaser et al.*, 2010] could be expected if the earthquake was similar to other continental thrust events.

This apparent discrepancy allows to speculate about the certainty of the available data or the underlying mechanism for that enigmatic event. One possibility could be that the large depth of the earthquake did not allow the rupture to reach the surface for all its length. Recent seismicity, however, is limited to shallow depths and thus, renders a deep source uncertain (Figure *A.1*). A second possibility might be that a complex rupture pattern, involving several segments of neighboring faults and the overall remoteness of the area are the reason that the full rupture has not yet been found. Or, and this issue will be investigated in this study, the intensities, and thus the associated magnitude of about 8.3 have been simply overestimated.

Instrumental data for this event are rare. Although the Chilik earthquake occurred at the very beginning of the seismic instrumentation development, the Chilik earthquake was recorded on a Rebeur-Paschwitz instrument in Wilhelmshaven, Germany. A fragmentary record has been found in a book reproduction [plate 5, *Rebeur-Paschwitz*, 1892b]. However, the seismogram shows a sudden break at the onset of the earthquake and only continues recording about two hours later. We compared this late coda with that of recent large-magnitude events from Central Asia that have been recorded at modern seismic stations in Germany and subsequently been transferred to the characteristics of a Rebeur-Paschwitz instrument.

Mushketov [1891] reported a strong deviation of the magnetic recording instruments in Pavlovsk (Russia) and in Berlin (Germany). Historic magnetograms from similar instruments that operated at different observatories are available. We used records and instrument characteristics from Greenwich and Kew (both Great Britain) for scaling the magnitude of the Chilik earthquake by comparing it to magnetograms of the Chon-Kemin earthquake for which the source parameters are well known [*Kulikova & Krüger*, 2015].

The close look at the historic instrumental data enables us to constrain the moment magnitude of the Chilik earthquake to be about 8. These results contribute to the understanding of this remarkable earthquake and also helps to better define the hazard that such events pose to the population of the area.

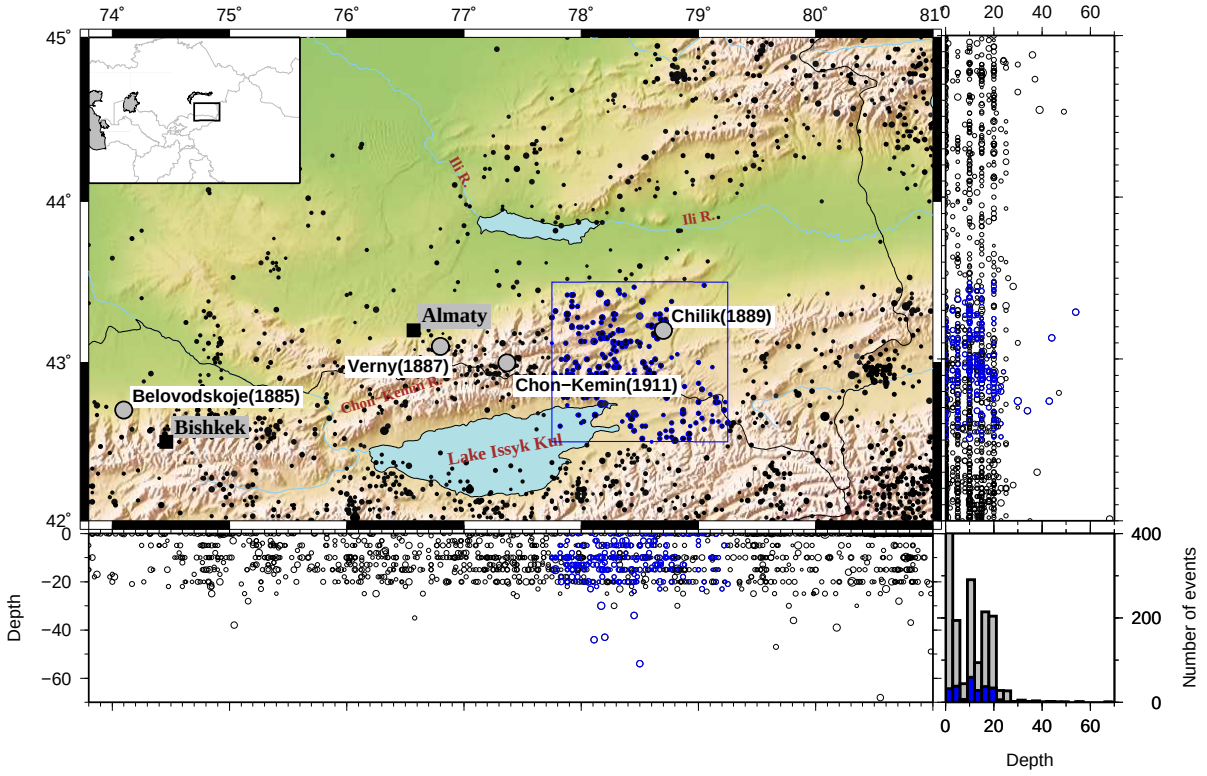

FIGURE A.1: Seismicity map and cross sections of the epicentral area of the Chilik earthquake (black solid line marks political boundaries and lakes). The topography map of the Tien-Shan region with the epicenters (as black circles) of all the earthquakes from 1995 till 2009, according to *Mikhailova et al.* [2015]; blue circles show epicenters of earthquakes in the maximum intensity zone (area marked with blue rectangle); grey circles indicate four most destructive earthquakes in the region with their names and the year of occurence. In latitudinal and longitudinal cross sections the entire seismicity is projected according to the hypocenter depth. The gray histogram in the lower right corner counts the number of events per depth with 10 km steps; the blue overlay histogram shows the same for the region marked with blue box.

A.2 Active faulting in the Chilik area

Seismicity in the Chilik area has recently been characterized by low to moderate magnitudes (Figures *A.1* and *A.2*). Only few large-magnitude events have followed the 1889 earthquake, notably the mentioned 1911 Chon-Kemin earthquake and 1938 (M6.9) Kemin-Chu earthquake [*Kondorskaya et al.*, 1982], and more recently, the Sarykamysch event (1970, M_s6.8), the Zhalanash-Tyup (1978, M_w6.9), and the Baisoorun events (1990, M_w6.3), the epicenter of which are located in the east and north of the Issyk Kul basin (partly seen on Figure *A.2*).

Although the 1889 Chilik event was the largest earthquake of the late 19th century, early 20th century sequence, geological information about the 1889 Chilik event is still sparse. One reason may be that no mapping of earthquake environmental effects was available for this event, rendering any initial investigation in such a remote, alpine, and sparsely populated region difficult.

Holocene faulting in the presumed epicentral area, including faulting that might have been associated with the Chilik earthquake, has been previously mapped by *Tibaldi et al.* [1997] using air photographs and field surveys. The region is characterized by a complex mosaic of active structures (Figure *A.2*), and several segments of these Holocene faults show juvenile fault scarps, visually (with respect to scarp angle, stage of degradation) comparable to the scarps associated with the 1911 event. A natural candidate to accommodate the Chilik earthquake would be the Baisorun Chilik fault (Figure *A.2*), as it is probably part of the inherited Kemin-Chilik shear zone that is located along the Chon-Kemin and Chilik river valleys and marks the boundary between the Zailisky and Kungei ranges [*Tibaldi et al.*, 1997; *Tibaldi*, 1998; *Selander et al.*, 2012]. The western part of this fault system (basically along the Chon-Kemin river) has been activated during the 1911 event [for the complete rupture of the 1911 earthquake see *Bogdanovich et al.*, 1914; *Kulikova & Krüger*, 2015; *Arrowmith et al.*, 2015]. *Bogdanovich et al.* [1914] has also mapped cracks in the uppermost reaches of the Chilik valley, and few cracks associated with mass movements only in discontinuous patches along some downstream reaches of the Chilik valley.

Young fault scarps were observed for instance along the Saty Fault, and also along the Baisorun-Chilik and Beskaragai Faults (Figure *A.2*, marked in red) and represent promising candidates for faulting associated with the 1889 earthquake. This seems reasonable also, because no other large magnitude event has been historically reported, although *Kalmetieva et al.* [2009] claim a magnitude of completeness for events larger than M6.5 since AD 1770. However, combined, these fresh ruptures comprise a length of about 70 km only, with offsets ranging between 3-6 m left-laterally, and 6-8 m vertically for the Saty and Baisorun-Chilik faults (Figure *A.2* A and B) and about 3-4.5 m along the Beskaragai fault, respectively [*Abdrakhmatov et al.*, 2015]. Both faults exhibit steep to near-vertical planes [*Tibaldi et al.*, 1997; *Tibaldi*, 1998], in places bending to shallow dip near the surface, as seen for instance along the Saty fault. Interestingly, the active traces of these faults seem to diverge from a location just west of the supposed Chilik epicenter between the Chilik and Charyn rivers. Whether the scarps reflect a single event or multiple events, cannot be distinguished for the entire mapped fault length. A trench, opened along the Saty segment (at the position of Figure *A.2*Ab), however, revealed only one event [*Abdrakhmatov et al.*, 2015].

An additional young scarp was traced discontinuously for about 30 km in the epicentral area of the (but not associated with) 1978 Zhalanash-Tyup earthquake (see Figure *A.2* for location) by *Crosby et al.* [2007] during field surveys and has been mapped remotely at a length of about 100 km by *Abdrakhmatov et al.* [2015]. The scarp falls into the highest MMI contours of the Chilik event and thus could have been associated with this earthquake [*Crosby et al.*, 2007]. These ruptures near the Kyrgyz/Kazakh border are located at altitudes above 3000 m, in a remote area often snow-covered and characterized by fresh and reworked moraines and glacial lakes. It cannot be excluded that more evidence for young ruptures is still undiscovered.

A.3 Intensity observations

The Chilik earthquake was the third destructive earthquake in the northern Tien-Shan region in the 19th century, and although having the largest magnitude it has caused less damage and fatalities than the Verny and the Belovodskoe earthquakes [*Nurmagambetov*, 1999]. As mentioned above, information about this earthquake came from questionnaires filled out by earthquake witnesses. According to *Mushketov* [1891] printing the forms needed some time and they were eventually sent only in late August, almost two months after the earthquake occurred. This lead *Mushketov* [1891] to express doubts regarding their certainty and precision: *Mushketov* [1891] - ″the quantity and accuracy of received questionnaires certainly depends on the considerable time period which passed

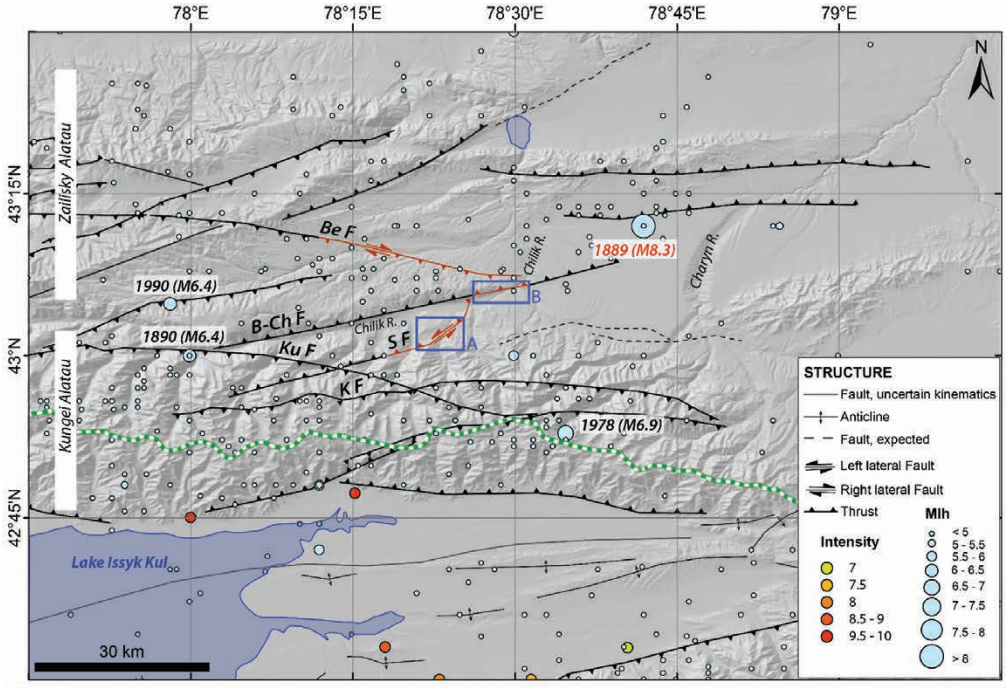
78°E
78°15'E
78°30'E
78°45'E
79°E
43°15'N
43°N
42°45'N
N
Zailisky Alatau
Kungei Alatau
Be F
B-Ch F
Ku F
K F
S F
Chilik R.
Charyn R.
1889 (M8.3)
1990 (M6.4)
1890 (M6.4)
1978 (M6.9)
Lake Issyk Kul
30 km
STRUCTURE
Fault, uncertain kinematics
Anticline
Fault, expected
Left lateral Fault
Right lateral Fault
Thrust
Intensity
7
7.5
8
8.5 - 9
9.5 - 10
MIh
< 5
5 - 5.5
5.5 - 6
6 - 6.5
6.5 - 7
7 - 7.5
7.5 - 8
> 8

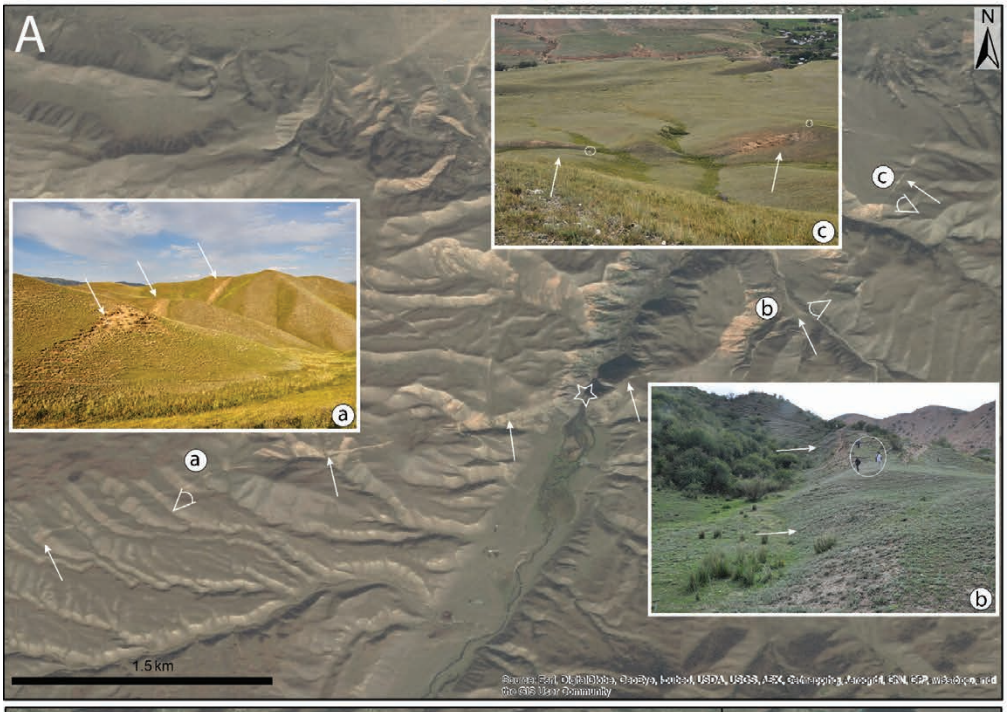
A
N
a
b
c
1.5 km


78°30'E
B
a
b
1.5km

FIGURE A.2: Overview of active faults in the Chilik area on SRTM (Shuttle Radar Topography Mission) hillshade-model. Faults and names are based on *Tibaldi et al.* [1997]; *Tibaldi* [1998]; faults marked in red have been surveyed in the field [*Abdrakhmatov et al.*, 2015], abbreviation are as follows: Be F- Beskaragai fault, S F- Saty fault, B-Ch F- Baisorun Chilik fault. Blue boxes indicate examples of juvenile fault scarps on satellite image and field photo (A and B). Earthquake epicenters are based on *Kalmetieva et al.* [2009] and intensities are those of *Mushketov* [1891] for the 1889 earthquake. (A) Part of the Saty fault with predominantly thrusting on E-W striking, and left transpression on the NNE-SSW striking reaches. Arrows mark the fault trace, the eye symbol indicates the approximate viewing location and direction, and the star depicts the location of a major rockfall at the rupture location that has temporally dammed a lake. Note people for scale (circled) on Photo b and c. (B) Rupture along the Baisorun-Chilik fault. The fresh scarp is best to be seen where it cuts Quaternary alluvial and fluvial sediments. Symbols are similar to (A).

from the day of the earthquake till the day when the questionnaire was filled out, however received information is very valuable material and gives full representation of the earthquake picture″. The data from questionnaires were complemented by information from local newspapers. As a result *Mushketov* [1891] published a detailed report about the earthquake effects at different locations. He then summarized this information in a form of a table with all the villages and cities where the earthquake was felt listed with corresponding intensity according to the Rossi-Forel scale [*Davison*, 1921] and timing of the earthquake according to the local clocks. In addition to the intensity value for each location *Mushketov* [1891] provided a map with the maximum intensity area marked with isolines in the shape of an ellipse stretched from North-East to South-West, covering an area of 18778 km^2, including eastern parts of Zailisky Alatau and Kungei Alatau and extends southwards from Ili river to the coast of lake Issyk-Kul (Figure *A.1*). The epicenter of the earthquake was then determined as the center of this ellipse.

The Rossi-Forel scale [*Davison*, 1921] has it's maximum at intensity value X, which however corresponds to the intensities IX, X, XI and XII in MSK-64 scale [*Ad-hoc Panel*, 1981]. The widely distributed intensity X (Rossi-Forel scale) area lead to the conclusion that earthquakes hypocenter was located at 40 km depth.

There were several attempts to convert the intensity observations for the Chilik earthquake from Rossi-Forel scale to the MSK-64 scale. For example *Januzakov et al.* [2003] converted all the intensities X from Rossi-Forel scale to intensity IX in MSK-64 scale, which was later used by *Bindi et al.* [2014]. *Besstrashnov* [1993] has suggested another conversion, which reached intensity X according to MSK-64. In the present paper, we do not suggest any conversion between intensity scales. Instead, we provide a Table *A.3*, in the appendix *A.8.1*, which includes a short summary about the damage at each observation point with names of the cities and villages at the time of the Chilik earthquake and the modern names of the same places. The table shows the information about damage directly taken from the original report, so that the reader can judge which intensity should correspond to it.

However, independent of the intensity scale used, it is obvious that the observations are sparse. There are two regions where the maximum destruction was observed (Figure *A.3*): between Chilik and Charyn rivers, which is believed by *Mushketov* [1891] to be the true epicenter of the earthquake; and the northern shore of Issyk-Kul lake. *Besstrashnov* [1993] suggests that the severe damage observed on the lake Issyk-Kul site is due to unfavorable site condition and liquefaction near the lake. *Besstrashnov* [1993] pointed out the lack of intensity observations on the East and South-East and suggested that a fault structure laying in between Chilik and Charyn rivers could also be considered responsible for the Chilik earthquake.

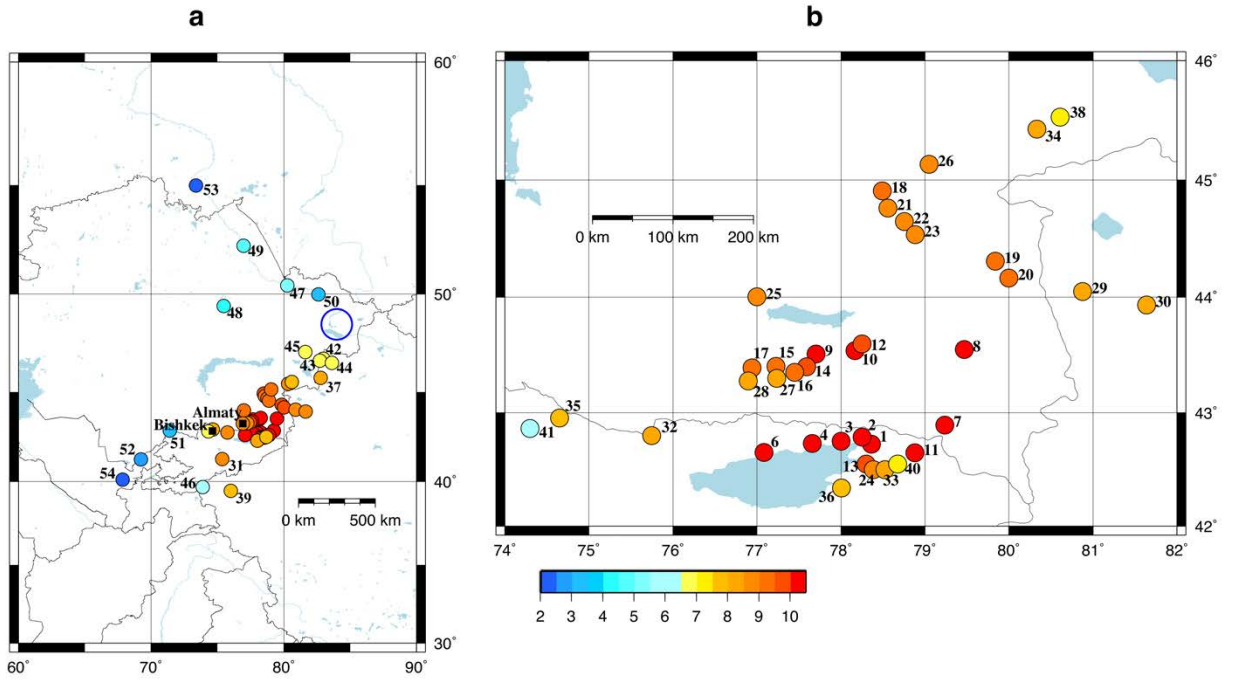

FIGURE A.3: The figure shows intensity assignments for the 1889 Chilik earthquake, color-coded accordingly, and with numbers indicating the places as they are listed in Table *A.3* (Appendix *A.8.1*). The epicenter locations [according to *Mushketov*, 1891] are indicated by black star, the black rectangles show major cities in the region named respectively. The black lines show political boundaries. Panel a) is the map of the whole region where the earthquake was felt, the blue circle indicates an area of low intensity – so called ″seismic island″ (Appendix *A.8.1*) and panel b) is the magnified map of the maximum intensity zone.

A.4 Earthquake source parameters estimation

All information about the Chilik earthquake source parameters is based on the collected eyewitnesses testimonies. However, *Mushketov* [1891] specifically pointed out the incompleteness of collected observations due to sparse settlement in the region. This is also true with respect to the origin time. *Mushketov* [1891] noted the sparseness of the arrival time observations and large differences between them. This is clear from Table *2.2*. There were just two instrumental timing registrations in Pavlovsk (Russia) and Berlin (Germany) and the timing in Almaty was determined from stopped telegraphs station clocks. In five other locations, the timing was also noted using telegraphs clocks. However those observation so little agree with each other, that a precise determination of the origin time of the earthquake based on this information is impossible.

At that time it was also common to note the duration of the earthquakes in different locations, which however appeared to have up to one hour inconsistencies as well. Ultimately, Mushketov (1891) took as the epicenter the center (intersection point of major and minor ellipses axes) of a maximum intensity ellipse [see Figure 1, *Mushketov*, 1891]. The epicenter latitude of 43.17 E° and longitude of 78.55N° was determined, which is very close to the coordinates of the recently published epicenters [*Januzakov et al.*, 2003; *Bindi et al.*, 2014; *Kalmetieva et al.*, 2009] and the origin time 22:14 UTC (universal time). There was no instrumental determination of magnitude for the Chilik earthquake and the existing value is based on macro-seismic observations.

A.4.1 The Rebeur-Paschwitz horizontal pendulum record

Between 1886 and 1895, Ernst von Rebeur-Paschwitz developed three models of horizontal pendulums. The Repsold pendulum became operational in 1888 and was tested in 1889 at two locations in Northern Germany, i. e. in Potsdam and Wilhelmshaven [*Rebeur-Paschwitz*, 1892a]. The pendulum was equipped with an optical mirror so that a light beam could be reflected and used to record the pendulum motion on light sensitive photo paper, clamped on a metal roll. The roll rotated with a speed of 2 cm per hour. The horizontal pendulum was covered by bell-shaped glass to eliminate droughts and to provide thermal insulation (see Figure *A.4*a for a sketch). A detailed description of the instrument and the timeline showing which specific instrument recorded at which location can be found in *Fréchet & Rivera* [2012], where also transfer function parameters like the mechanical free period of the pendulum and measured damping parameters are listed. The test recordings in Potsdam and Wilhelmshaven started simultaneously in March 1889 and lasted until September 1889. After a first analysis of the records, Rebeur-Paschwitz published the first evidence for an earthquake (Japan, April 17, 1889) recorded at teleseismic distance [*Rebeur-Paschwitz*, 1889].

The pendulum in Wilhelmshaven was located in the basement of the naval observatory near the harbor of Wilhelmshaven, 2 m below the surface and attached to a stonewalled pillar which reached 0.9 m deeper. It is mentioned that the motion of the pendulum might be enlarged due to tilt of the pillar caused by 1 m thick layer of sand/peat below the observatory. The orientation of the pendulum was along the meridian (North-South) so that East-West motions of the ground were recorded [*Rebeur-Paschwitz*, 1892a].

Unfortunately, no original Rebeur-Paschwitz records survived. However, reproductions of photo-records can be found in several publications [*Rebeur-Paschwitz*, 1892b, 1893, 1895]. This includes also the reproduction of the Chilik earthquake record in Wilhelmshaven. *Rebeur-Paschwitz* [1892b] shows a plate with an about two day long record (see Figure *A.4*b) of Earth tides (start at 0h, July 10, 1889 GMT noon time, corresponding to 12h, July 10, 1889 universal time and ending at 0h, July 12, 1889 GMT noon time, corresponding to 12 h, July 12, 1889). At 22h 20m 22s universal time, the recording stops seemingly due to too rapid movement of the pendulum. About two hours later five peaks of oscillatory movement are visible. The motion settles to the amplitudes recorded before the onset at about four hours after the onset. *Rebeur-Paschwitz* [1893] published a magnified version of the record encompassing just eight hours, showing more details (Figure *A.4*c). In this publication Rebeur-Paschwitz notes that at both sites (Potsdam and Wilhelmshaven) the record shows a sudden break at 22h 38m universal time. Rebeur-Paschwitz estimated the timing precision to be on the order of 1-3 minutes [*Rebeur-Paschwitz*, 1895]. Unfortunately, no reproduction of the Potsdam record exists.

The time 22h 20m 22s, read from record reproduction (Figure *A.4*c), perfectly matches the likely arrival time of the P-wave of the Chilik earthquake in Germany, assuming the time at the epicenter ∼03:15 according to local observation [*Mushketov*, 1891]. The earthquake was also recorded on the magnetometer in Berlin [*Rebeur-Paschwitz*, 1893], but more than 20 minutes later. We understand this as additional argument that the P-wave onset is responsible for the sharp movement of the pendulum, as magnetometers have a much lower ground motion amplification and are less sensitive to the early P-wave. Thus the magnetometer onset time is likely to correspond to stronger later phases (e.g. surface waves).

The slow motion of the recording drum makes it impossible to follow single swings of the trace. Therefore only envelope amplitudes can be used to compare with synthetic seismograms in the following. Only one absolute photo-paper amplitude is mentioned in [*Rebeur-Paschwitz*, 1892b], i.e. the amplitude of the April 17, 1889 Japan earthquake record was 154 mm. However in the same

publication, we find the amplitudes in 5 mm units (a 5 mm glass grid was used by Rebeur-Paschwitz to measure amplitudes) for hourly amplitude values tabulated for the whole measurement period for Potsdam and Wilhelmshaven. If we use for the April 17 1889 reproduction the amplitude of the reproduction of the Potsdam record (40 mm) and scale it with the reading unit difference between the maximum and minimum hourly amplitudes at 12h and 15h April 17, 1889, given by *Rebeur-Paschwitz* [1892a, page 53](2.3 p, 1 p = 5 mm amplitude), the mentioned 154 mm amplitude can be reproduced within a few mm. The same procedure can be applied to the Chilik record. By scaling the amplitudes on the enlarged reproduction in *Rebeur-Paschwitz* [1893] with the reproduction amplitudes published in *Rebeur-Paschwitz* [1892b] we can scale the former to original photo-paper amplitudes.

Figure *A.5* shows the transfer characteristic of the Rebeur-Paschwitz pendulum in Wilhelmshaven, where we used the values given for the free period of the pendulum in horizontal position (16.0-16.5 s) and the magnification of 54.2, both from *Fréchet & Rivera* [2012, Table 2]. The instrument was constructed without any damping device. The Wilhelmshaven instrument was later on transported to Strasbourg and there slightly modified and reinstalled. In 1892 the exponential decay of amplitude maxima with time during free oscillations was measured [*Rebeur-Paschwitz*, 1892b]. *Fréchet & Rivera* [2012] calculated from these measurements a damping constant $h = 0.0134 - 0.0138$. It is however mentioned that a value of $h = 0.04$ might be more appropriate for the beginning and $h = 0.01$ more appropriate for the end of the measurement.

Inserting $T_0 = 16.25$ s and $h = 0.0134$ in the formula for the response of a mechanical pendulum to ground motion, i.e.:

$$H(\omega) = \frac{G\omega^2}{(-\omega^2 + j\omega 2h\omega_0 + \omega_0^2)} \tag{A.1}$$

- the characteristic of the pendulum can be calculated [*Wielandt*, 2002], where ω is angular frequency, the natural angular frequency $\omega_0 = 2\pi/T_0$ and G is the magnification factor, which in case of the Rebeur-Paschwitz pendulum solely depends on known geometrical features. Figure *A.5* shows clearly the high magnification reached around the resonance frequency.

A.4.2 Mw estimation of the July 11, 1889 Chilik earthquake from the late longperiod coda level

The coda-wave field is built by scattered body and surface waves and in case of the late coda by multiple scattered waves leaving the source in many directions. Several techniques can be found in the literature to estimate the source strength from the level of the late coda waves. An advantage of magnitude estimations based on the amplitudes of late coda waves is the fact that they are less dependent on focal mechanism, variations in event depth and station site factor than estimates based on direct phases [*Mayeda*, 1993; *Mayeda & Walter*, 1996; *Mayeda et al.*, 2003, 2007]. Recent examples for the application of coda based moment magnitude estimations of the scalar seismic moment of regional events in regions with less good station coverage can be found in *Sens-Schönfelder & Wegler* [2006] for GRSN stations and in *Denieul et al.* [2015] for clipped analog seismograms of regional events in France.

In the following, we use broadband records of large magnitude events from Central Asia and a simulation filter for the Rebeur-Paschwitz instrument to measure the amplitude level of the filtered late coda with the aim to derive a scaling relation of the coda level with the seismic moment. Figure *A.6*

shows the E-component of the May 12, 2008, Wenchuan M_w7.8, earthquake (Table *A.5*), recorded at the permanent BSEG station of the German Regional Seismic Network (GRSN) north of Hamburg (Northern Germany) which is equipped with a broadband high gain STS2 seismometer [*Dürbaum & Harjes*, 1986]. The BSEG station is installed since 1995 and has the longest recording time span of the permanent stations in Northern Germany and the best average signal to noise ratio in the mid- and long-period band. The lower trace shows true ground displacement which was obtained by removal of the STS2 instrument response, integration and stabilization by applying a highpass filter at 150 s period. A bar marks the start of the time window corresponding to the coda wave window of the Wilhelmshaven record under the assumption that the break in the pendulum recording is caused by the P-wave and using the epicentral coordinates given in the catalog *Mikhailova et al.* [2015]. In the BSEG displacement record two longperiod arrivals correspond to G2 and R2 mantle waves reaching the BSEG station from the backward direction on the long great circle path. Trace 2 from below shows a Rebeur-Paschwitz pendulum simulation after application of the digital simulation filter. As expected, the simulation is characterized by long oscillations with the free period of the pendulum. The overall magnification is 310 agreeing with the apparent magnification found by *Abe* [1994] for the Rebeur-Paschwitz Wilhelmshaven remanufactured instrument at its new location in Strasbourg [$G = 22.6$, Table 2 in *Fréchet & Rivera*, 2012], [$G_{app} = 159$ in *Abe*, 1994]. Dominant phases like direct P, S and the surface waves can still be identified. However, the longperiod G2 and R2 mantle wave arrivals are completely hidden by late surface wave coda, see inset in Figure *A.6*. In the upper two traces in Figure *A.6*, the envelope and a smoothed version of the envelope are shown. Both traces are characterized by a strong maximum of the surface waves amplitude and a long coda duration of several hours.

Figure *A.7*a shows the GRSN stations in Northern Germany on a map. No broadband station exists at the position of the former naval observatory in Wilhelmshaven, where the original observation took place (no remnants of the observatory exist today, although we could locate its position in Wilhelmshaven). Because of the general higher noise levels in deep sedimentary basins compared to stations on hardrock, only few broadband stations (e.g. BSEG, HLG) are today located in conditions comparable to the Wilhelmshaven station, i.e. in the North German basin. The North German basin comprises up to 8-km thick Permian to Quaternary sediments, deposited in distinguished subbasins and partly exhumed by salt tectonics [e.g., *Henningsen & Katzung*, 2006]. Only recently more stations were installed due to the need to monitor deep gas and oil exploration better (small triangles in Figure *A.7*a). Figure *A.7*b shows all earthquakes in Central Asia since 1992 (installation of the GRSN) with magnitudes $\leq M_w$6.5. All types of focal mechanisms are present. Most earthquakes have shallow depths, however centroid depths down to more than 200 km are reached in the Hindu-Kush region. These earthquakes are used in the following to derive coda amplitude scaling relations for the scalar seismic moment estimation.

Near the epicenter of the Chilik earthquake, we find the August 19, 1992 M_w 7.2 Suusamyr earthquake and the March 24, 1978 M_w6.9 Zhalanash-Tyup earthquake. Unfortunately, both events can not be used for a comparison of the late coda level with the coda level on the Wilhelmshaven record. The Zhalanash-Tyup event records [here we inspected the broadband recordings of the Gräfenberg array in southern Germany, *Korn*, 2002] are dominated by coda of a preceding even stronger event in the Kurile Island region (M_w7.5) which occurred about 77 minutes before. The Suusamyr record shows a strong aftershock just in the beginning of the coda wave time window we want to analyze. However, both events and in addition the smaller M_w6.1 event from January 28, 2013 [directly east of lake Issyk-Kul, 42.6050E°, 79.7080N°, *ISC*, 2015] can be used to pick the maximum of the simulated surface wave envelope to determine an average group velocity of 3.0-3.1 km/s for the envelope maximum of the 16 s period surface waves which dominate the Rebeur-Paschwitz instrument simulations.

For long lapse times of the coda waves, different model types for coda wave propagation predict different characteristics for the coda amplitude level decay. They become distance independent for large lapse times (source - receiver distance small compared to distance traveled by the respective coda wavelet). The coda amplitudes scale linearly with source strength which allows to predict source strength from the coda wave amplitude level [e.g. *Aki & Chouet*, 1975; *Kopnichev*, 1975].

We collected GRSN records for strong recent earthquakes in Central Asia (see Figure *A.7*b) and simulated Rebeur-Paschwitz pendulum records. Then we cut a time window 4900 s after the peak amplitude of the direct surface wave which corresponds to the reappearance of amplitude recordings in the original Wilhelmshaven record 6600 s after the break (supposed to originate due to the P wave onset). We use for this estimate the Chilik earthquake epicenter as determined by the macroseismic interpretation (Figure *A.2*) and the average group velocity for the surface wave peak amplitude arrival of 3.0 km/s determined from the simulated recordings of modern earthquakes in this region. As shown in Figure *A.6*, an envelope trace was calculated and then smoothed with a 300 s moving average. From the original Wilhelmshaven record also the envelope was taken (and smoothed). Subsequently, the integrals of the envelopes of the modern simulations and the original Wilhelmshaven record in time windows starting at 0 and ending at 11000 s (0 s corresponds here to the reappearance of recordings and 11000 s to the latest relative time taken on the Wilhelmshaven record) were calculated for moving time windows of 1800 s, 3600 s and 7200 s length with 50% overlap.

Figure *A.8* shows as example the coda level amplitude integral values for station BSEG compared to the corresponding coda level integral value of the Chilik earthquake on the Wilhelmshaven record. As can be seen, the log of the coda amplitude integral for shallow events (h<40 km) indeed shows linear scaling relative to the log of the scalar seismic moments of the earthquakes. A few deeper events (h>40 km, mainly from Hindu-Kush region (grey circles in Figure *A.8*) show different scaling. Overall, none of the modern events recorded at BSEG produced coda levels similar to the level measured in 1889 in Wilhelmshaven. This can also be clearly seen in Figure *A.9*a where the coda for a time window of 11000 s length starting 4900 s after the surface wave peak amplitude is shown for the largest modern events together with the envelope of the Wilhelmshaven record. Figure *A.9*b shows the coda amplitudes (same time window setting as Figure *A.9*a) for the 25-Apr-2015 Nepal M_w7.8 event at the permanent GRSN stations (lower six traces in Figure *A.9*b) and additionally coda amplitudes at 7 temporary stations (station IGAD is nearest to Wilhelmshaven). The amplitude levels at the temporary stations show more variation up to a factor of 2 compared to the permanent stations which are installed preferentially on the few available rock sites (mainly tops of outcropping salt dome structures, e.g. BSEG, HLG, RUE) in Northern Germany.

Figure *A.10* shows the standard deviations for the axis intercept (Figure *A.10*a) and the gradient of the best fitting straight lines (Figure *A.10*b) for the coda level amplitude integrals for all different time windows relative to the scalar seismic moments in a log-log scale. The smallest standard deviations are found for later time windows starting around one hour after the re-onset of recordings on the Wilhelmshaven record and longer windows. However, for the latest time-window starts, the standard deviations raise again. While the earlier coda windows might still be influenced by direct and single scattered waves, the late window levels especially for the smaller events are probably influenced by the background noise level. A black line in Figure *A.10* marks the latest time where coda amplitudes of the Chilik earthquake in the original Wilhelmshaven record are well above the noise level.

In the final step, we calculate the scalar seismic moment estimate and the corresponding Mw magnitude value for all different coda time windows (modern event simulated records and original Wilhelmshaven record envelope integrals for the time window where the coda amplitudes are well

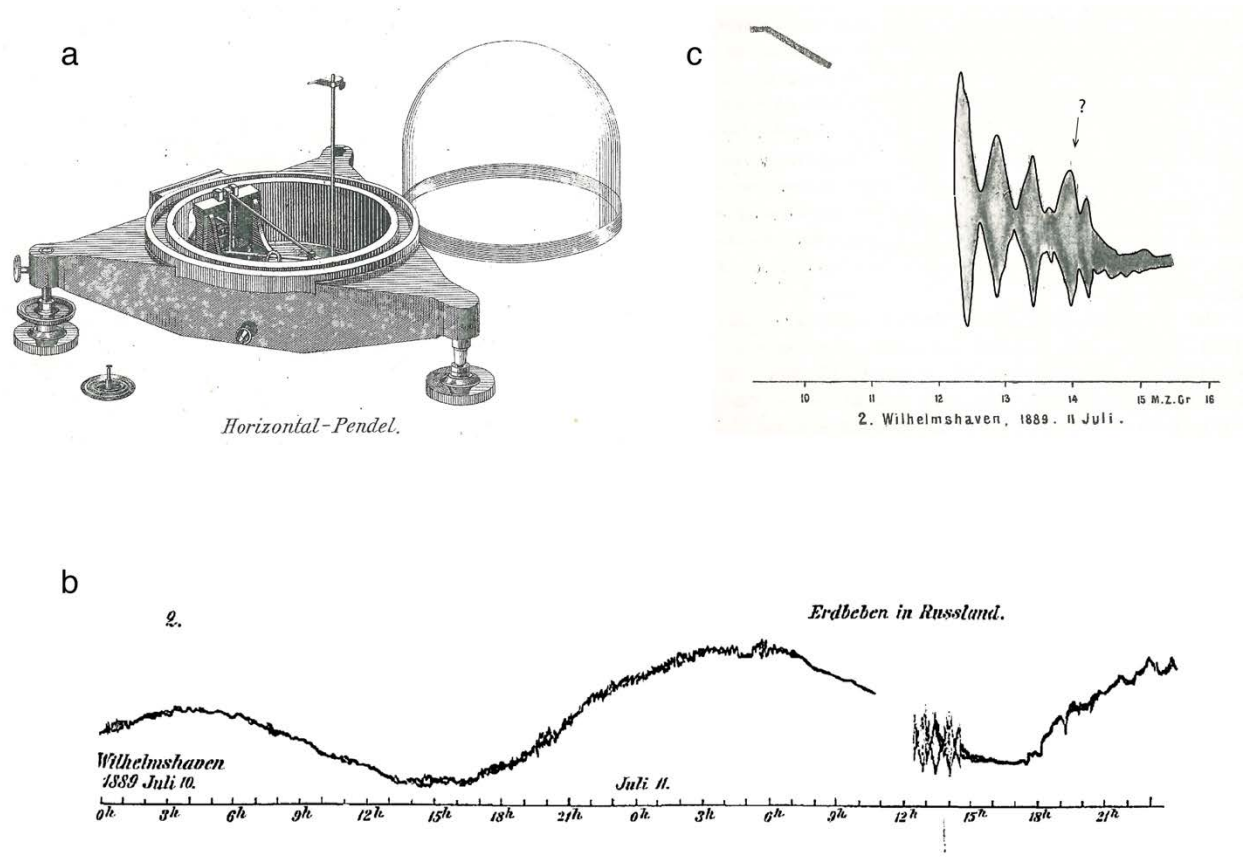

FIGURE A.4: a) Sketch of the Rebeur-Paschwitz pendulum operated in Wilhelmshaven in July 1889 [*Rebeur-Paschwitz*, 1892a]. b) Reproduction of the original record of the 11-July 1889 Chilik earthquake [*Rebeur-Paschwitz*, 1892b]. Time is GMT noon time (12 hours shift relative to universal time). c) magnified reproduction [*Rebeur-Paschwitz*, 1893] with trace envelopes added. A question mark points to the potential arrival time of a strong aftershock following eyewitness reports, see Appendix *A.8.1*.

above the noise level in the Wilhelmshaven record of the Chilik earthquake, see also Figure *A.10*) using the respective straight line parameters. Figure *A.11* shows the M_w estimates for the Chilik event as function of the standard deviation of the respective line fit. Two clusters are visible at about M_w7.5 and M_w8.3. If however, only the smallest standard deviation line fit parameters are used, only the high magnitude values seem likely. These high magnitude values range from 8.0 to 8.7, where mainly the station RGN estimates give the highest M_w estimates.

A.5 Magnetograph recordings of the July, 11, 1889 Chilik earthquakes

Since the mid of the 19th century, continuous record of the geomagnetic field components came in use. Magnetographs had photographic recording systems using films on slowly rotating drums to record the light beam reflected from a tiny mirror mounted on a bar magnet. Around 1889 different variometer types encompassing horizontal and vertical field components as well as declinometers and inclinometers of unifilar and bifilar construction were used all around the world. Some of the

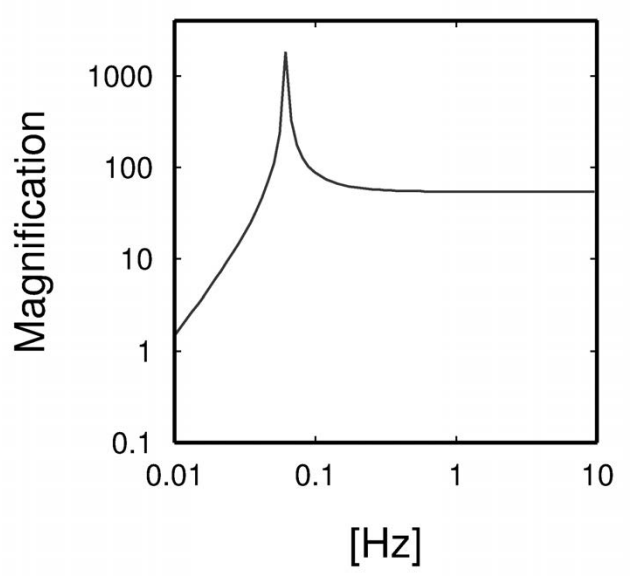

FIGURE A.5: Transfer function of the Rebeur-Paschwitz instrument calculated with the instrument parameters from *Fréchet & Rivera* [2012].

archives hold continuous records of magnetograms since the 19th century. For example, *Batllò et al.* [2005] has shown successful application of magnetograms for the magnitude evaluation of earthquakes occurring prior to digital seismic networks. In the following, we will use magnetograms from British magnetic observatories which are well preserved, scanned and published in digital form by the British Geological Survey (BGS) since 2009 in the *OpenGeoscience* project [*BGS*, 2015].

Early in the history of magnetic measurements, earthquakes were identified as cause for disturbances during magnetic field observations, either by a purely mechanical effect [*Davison*, 1885], or a real magnetic effect [*Moureaux & Mascart*, 1889a,b]. Notes regarding the influence of the waves of the Chilik 1889 earthquake on magnetograph observations, namely those at Pavlosk, near Saint Petersburg, and Berlin, can be found also in the report of *Mushketov* [1891]: ″Deviations were observed in all Maskara magnetographs, in the Wild instruments for registering earth currents and Maskara electrograph for registering air electricity. The Maskara magnetographs and the Wild instruments were installed on a stone column fixed deep in the earth in an underground hall; electrograph was mounted on a special stand on the top floor of a tall tower to the main Observatory building. Deviations in the recordings of the instruments reach 2,5 minutes in the arc, they are most clearly visible in curves of Lloydovy scales (a device which records changes in the vertical component of the magnetic force). This deviations were observed from 00:32 till 00:39 Pavlovsk night time at night of 12 of July, most considerable deviation was at 00:35. The direction of motion was determined from this ratios from SE to NW. In Berlin the deviations of magnetic instruments were also noticed, and in the astronomical observatory oscillation of the instruments, according to Prof. Markuze, were observed on 11 July from 11:27 till 11:53 Berlin noon time.″ [*Mushketov*, 1891, translation by G. Kulikova].

The notes in *Milne et al.* [1898] are of special interest for the analysis of the Chilik earthquake. Here, the Chilik earthquake is event no 2 in a list of earthquakes sent by Milne on two occasions to different magnetic observatories all over the world (mainly in the UK and the British colonies, but also in central and eastern Europe). Positive answers regarding the Chilik earthquake were sent by the observatories in Utrecht, Bombay, Mauritius and Greenwich (note in the Milne report the Chilik earthquake is named ″Quetta earthquake″ probably assuming that the event has happened

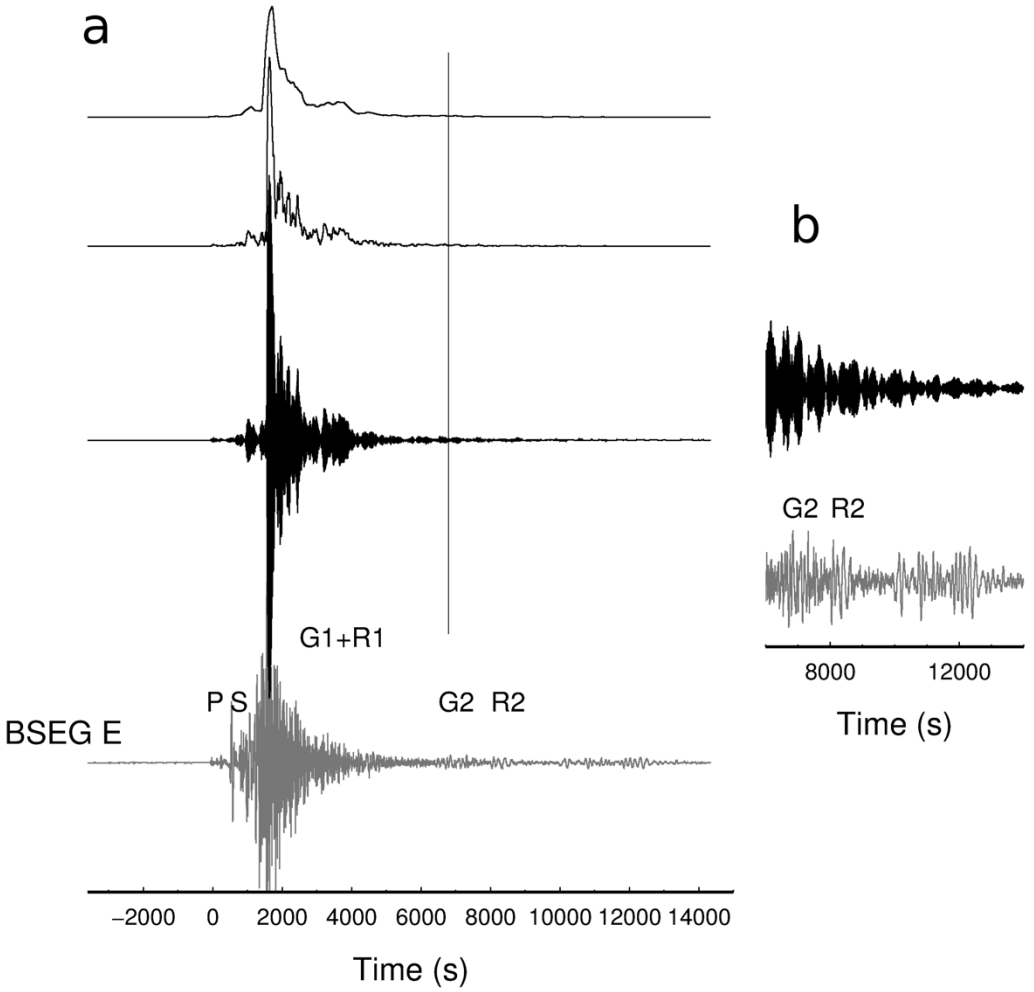

FIGURE A.6: Coda processing example. Lower trace: True ground displacement of the May 12, 2008 Wenchuan M_w 7.8 earthquake recorded on the E-component of GRSN station BSEG where the instrument characteristic of the STS2 seismometer was removed and subsequently integrated to ground displacement, stabilized by highpass filtering at 150 s. Second trace from below: Scaled Rebeur-Paschwitz instrument simulation (scale factor 50 relative to lowest trace). Third trace from below: Envelope of Rebeur-Paschwitz simulation. Upper trace: Same envelope smoothed using 300 s long time window. A black line marks the time window start of coda waves in the Rebeur-Paschwitz pendulum record of the Chilik earthquake. The inset on the right shows the time window between 6000 s and 14000 s where later surface-wave arrivals like G2 and L2 are visible in the broadband record but disappear in the simulation. Scale is adjusted for better visual comparison.

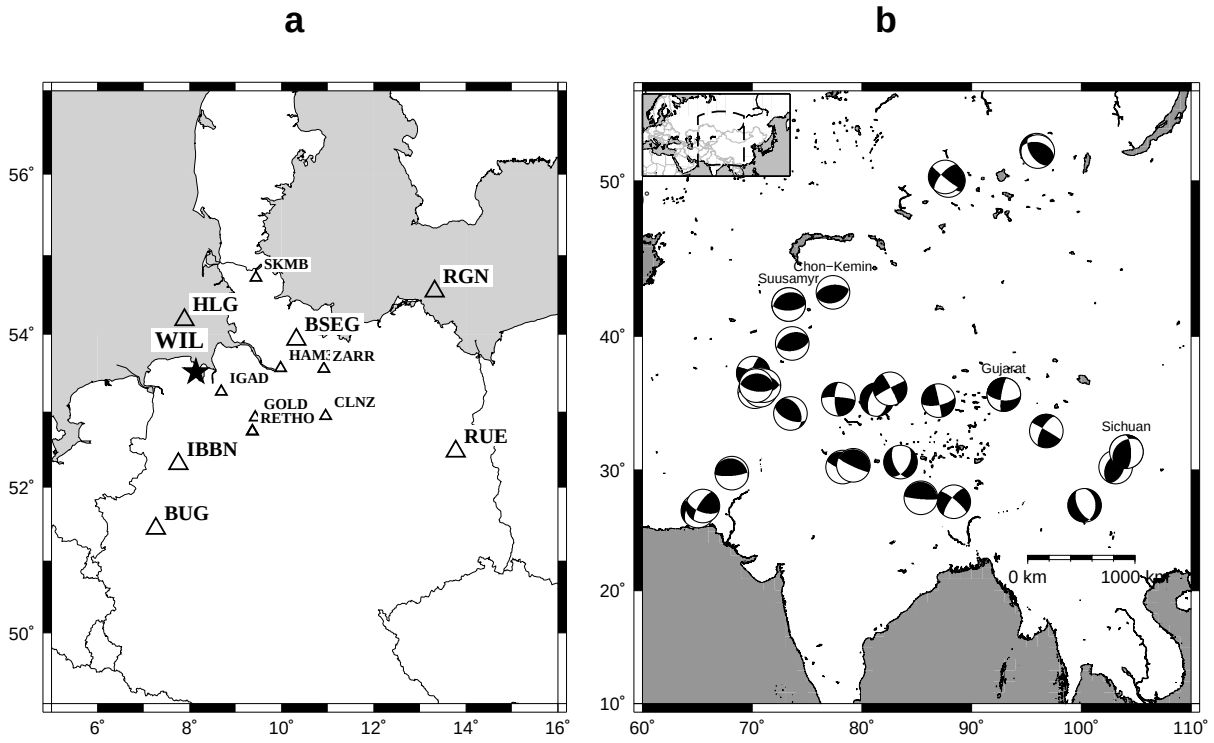

FIGURE A.7: a) Broadband stations of the German Regional Seismic Network (GRSN). Large triangles: permanent stations. Small triangles: temporary stations. b) Focal mechanisms of events with M_w larger or equal to 6.5 in Central Asia since 1992 (installation of high-gain broadband GRSN stations), see also Table *A.5*.

in the seismically active region Quetta in Pakistan). However, inspection of the reported timing reveals that only the onset times at Utrecht and Greenwich can be associated with arrival times of seismic waves of the Chilik earthquake. The onset of disturbance reported from Mauritius and Bombay deviate from arrival times of body or surface waves by several hours. A reproduction of the magnetogram from July 12, 1889 from Bombay was printed and associated with the Chilik earthquake [*Milne et al.*, 1898]. However, the time for the disturbance on the Bombay magnetogram deviates by about eight hours at 7 am on July 12, 1889 and therefore can not be due to the Chilik event. A clock error is unlikely because reproduction related to the June 12, 1897 Shillong earthquake shows correct timing in the sense that the disturbance can be related to the surface wave arrival.

At Utrecht ground motion started on the horizontal field variometer at 10h 39m with maxima at 10h 41m, 10h 52m, 11h 2m and 13h 20m (all pm), while the declination instrument recorded the onset at 10h 42m and maxima at 10h 50m and 11h 1m. It should be noted that in the original report of the Kew geomagnetic observatory (UK) the following note [*Galton*, 1889] is found ″on July 11th between 10 and 11 P.M. the curves registered the passage of tremors from an earthquake which was experienced in Central Asia.″.

Inspection of the historical british magnetograms for July 11, 1889 show that a disturbance at the time of the Chilik earthquake is observable at two out of four observatories and on 3 components

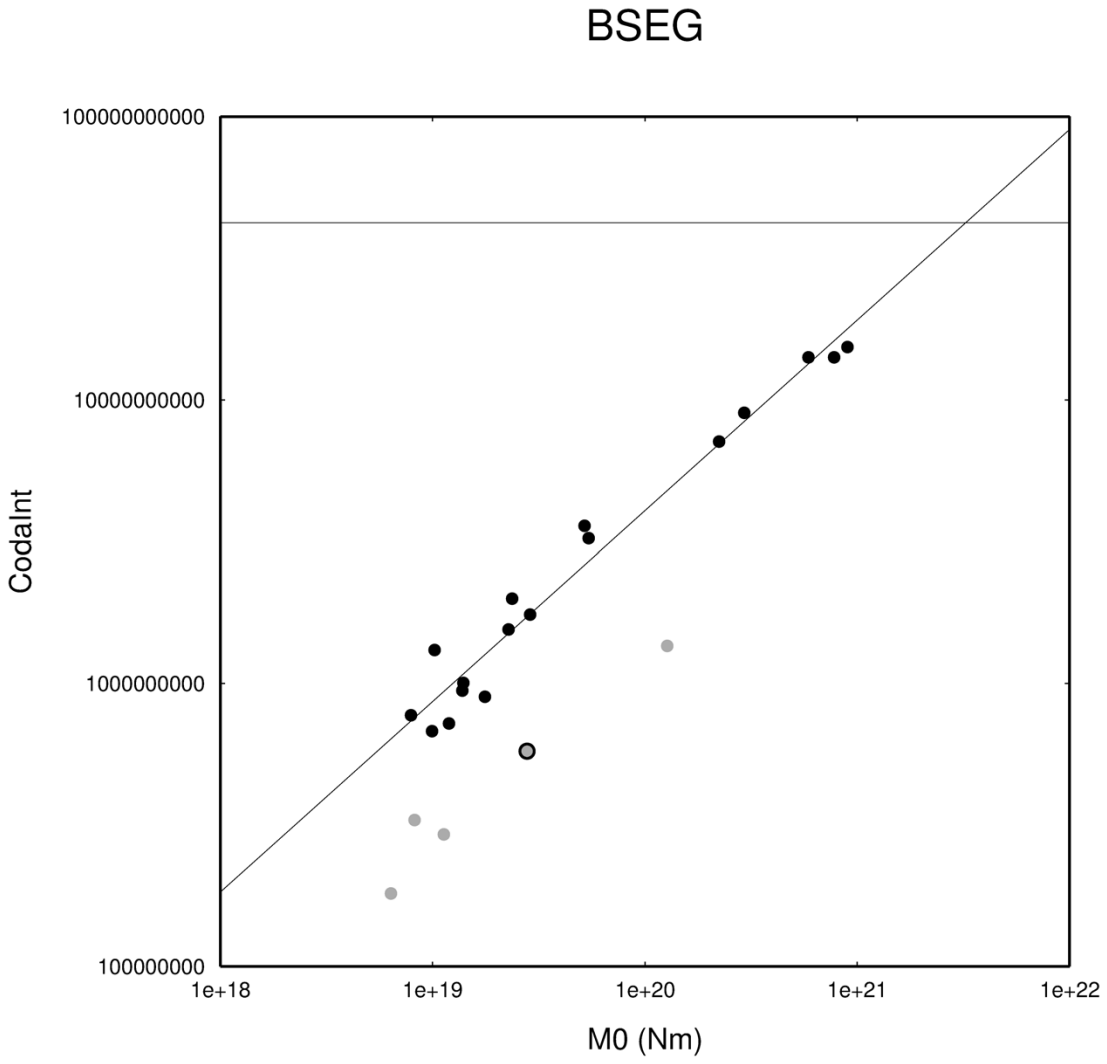

FIGURE A.8: *Log* of coda-amplitude envelope integral starting 5400 s after the peak surface-wave amplitude on the Rebeur-Paschwitz simulated seismogram and a time window length of 5400 s as function of the log of the scalar seismic moment [*CMT*, 2015]. Events with centroid depths shallower than 40 km are plotted with black circles. Events with larger centroid depths are plotted with gray circles (full grey circles correspond to Hindukush events at 184-237 km depth; the grey circle with black edging marks an M_w 6.9 event on September 18, 2011, in northeastern India at 46 km depth, see Appendix A). The horizontal black line corresponds to the log of the coda envelope integral of the Wilhelmshaven record in the corresponding time window. The straight line fit was calculated with the routine FIT [*Press et al.*, 2007] assuming constant and equal standard deviations for the single data points.

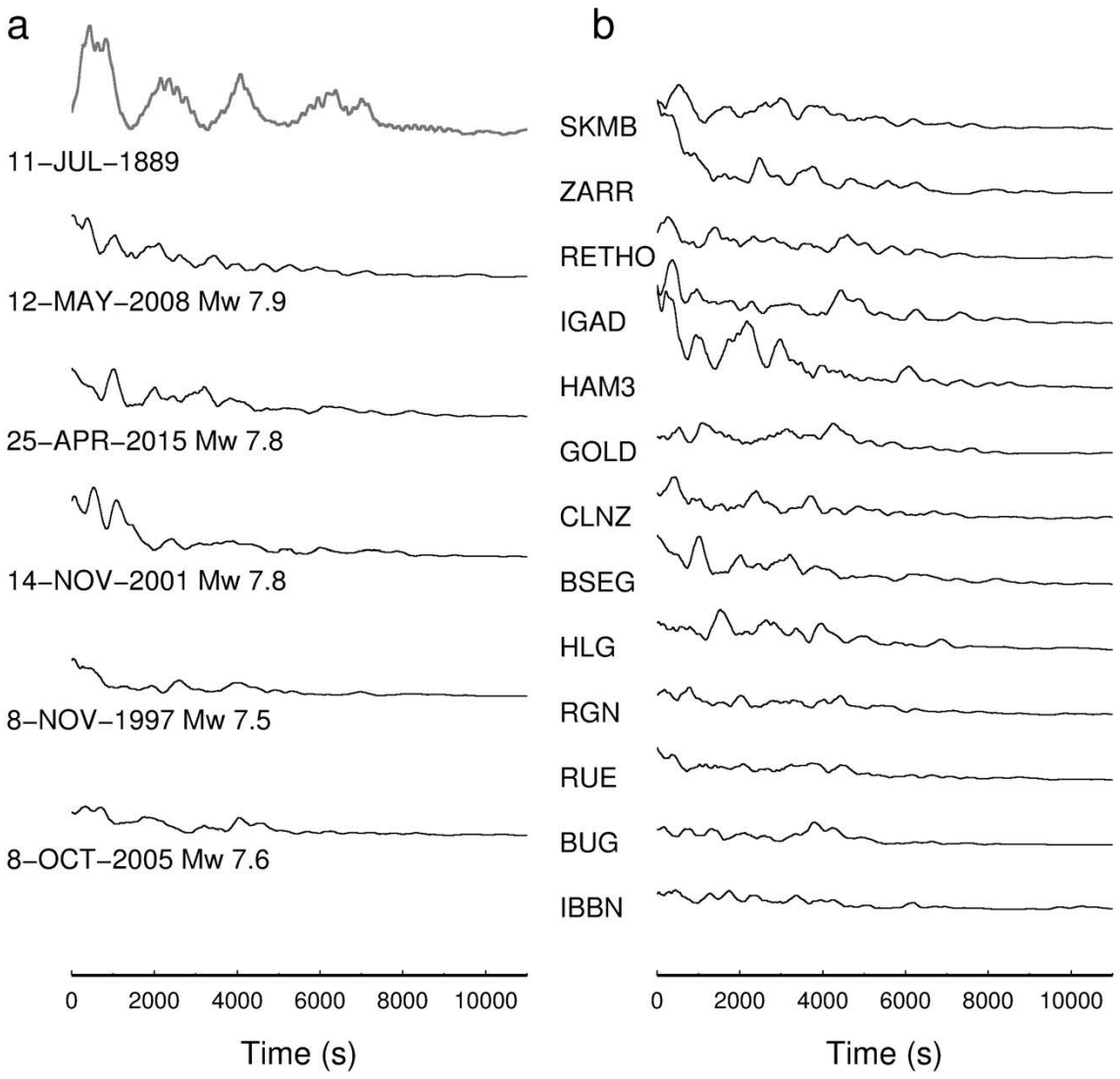

FIGURE A.9: a) Comparison of coda-amplitude envelopes of Rebeur-Paschwitz pendulum simulations of large modern events recorded at BSEG and the Wilhelmshaven original record (uppermost trace) starting 4900 s after the peak surface amplitude on the simulated records. b) Coda envelopes of the April 25, 2015 Nepal, M_w 7.8 earthquake recorded at the permanent and temporary broadband stations in Northern Germany.

(Kew vertical (Z) and horizontal (H) component and Greenwich H component Figure *A.12*). We could also find similar magnetograms and recordings from the mentioned observatories and components for the Jan 3, 1911 Chon-Kemin earthquake, which was recently reanalyzed using waveform modeling of historical seismograms [*Kulikova & Krüger*, 2015]. After a brief review of the theory how a historical magnetometer reacts to seismic waves, we use the arrival times and the relative amplitudes of both earthquakes on the magnetograms to conclude on the magnitude of the Chilik earthquake.

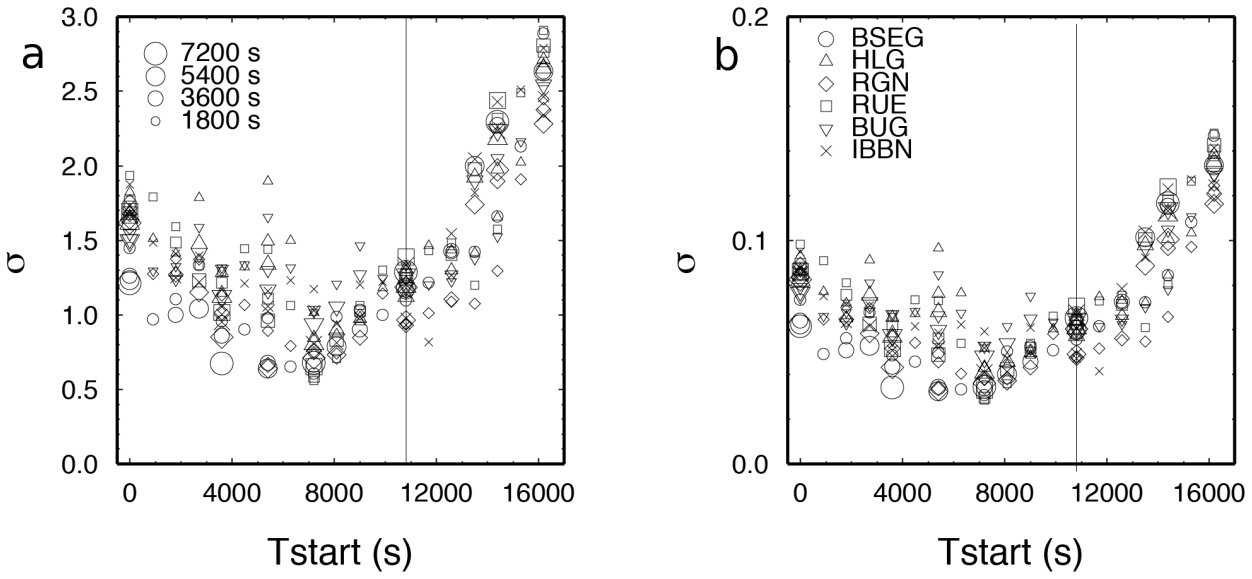

FIGURE A.10: a) Standard deviation σ for the axis intercept of straight line fits to log coda wave amplitude integrals for the permanent stations of the GRSN in Northern Germany as function of the coda window start time. We used moving time windows of 1800s, 3600s, 5400s and 7200s length starting earliest 4900s after the peak surface-wave amplitude on Rebeur-Paschwitz simulated records. The time-window start - Tstart - was increased using 50% overlap for each station and time window length until the time window end reached 20900 s, i.e. 16000 s relative time. A black line marks the last time in the Wilhelmshaven record of the Chilik earthquake, where coda wave amplitudes are safely higher than the background noise level. The size of the symbols scales with the length of the coda time-window used to calculate the integrated coda amplitude. b) same for the standard deviation of the gradient of the straight line fits.

A.5.1 Response of magnetic instruments to earthquake waves

A first discussion of the mechanical effect of seismic waves on compass needles was given by *Davison* [1885]. *Liznar* [1895] and *Reid* [1914] derived mathematical solutions for unifilar and bifilar suspended systems based on the assumption that the attachment points of the pendulum fiber might be slightly different from the bar magnets center of gravity. *Reid* [1914] gave formulas for the amplification and the phase shifts due to ground motion.

A different argument is given by *Eleman* [1966]. Figure *A.12*f shows a sketch of a bar magnet attached to a fiber, exposed to a horizontal force acting on the pivot point of the fiber (i.e. a horizontal ground displacement acting on the support of the whole instrument). For small oscillation angles Ψ the system can be described as a forced oscillator with a characteristic function similar to the one for mechanical seismometers, e.g. equation *A.1*. Because damping is very low (e.g. air friction, eddy currents) the natural period can be approximated by

$$T_0 = 2\pi\sqrt{(\frac{L}{g})} \tag{A.2}$$

- where L is the length of the fiber and g is acceleration due to gravity. *Milne et al.* [1898] reports for T_0 of the bifilar (H component) Greenwich and Kew instruments 42 s and 13.6 s respectively.

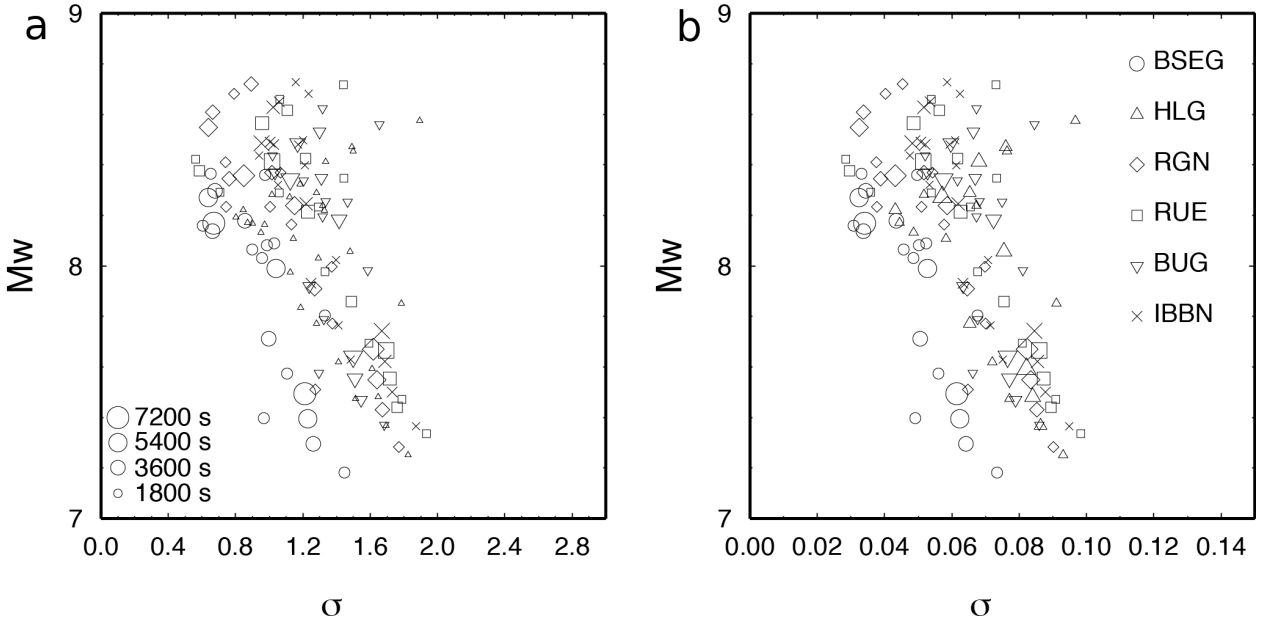

FIGURE A.11: M_w estimate for the Chilik earthquake calculated using the straight line-fit parameters for all different coda time windows for all permanent GRSN stations in Northern Germany. a) as functions of the standard deviation of the axis intercept. b) as functions of the standard deviation of the gradient. The size of the symbols scales with the length of the coda time window used to calculate the integrated coda amplitude. M_w estimates were calculated for all time windows, in which the coda amplitude level of the Wilhelmshaven record of the Chilik earthquake was above the noise level.

The geomagnetic vertical field (Z) will have a component Z Ψ, which introduces a torque which (for small values of ω) causes the magnet to turn until it reaches an equilibrium angle Θ defined by

$$H\theta = Z\psi \tag{A.3}$$

- where H is the horizontal field and where the torsion of the fiber is neglected. More accurate formulas taking friction explicitly into account and also for other basic types of magnetic instruments are given in *Eleman* [1966] and a satisfying quantitative confirmation is demonstrated for a magnetogram of the Mar 28, 1964 Alaska earthquake. Furthermore *Eleman* [1966] shows that the hypothesis of *Liznar* [1895] and *Reid* [1914] leads to the same results if specific approximations are made.

Finally, it should be mentioned that a magnetometer can be regarded as a low sensitivity rotation sensor. The general relation between a displaced material element relative to its original position can be described by

$$u(x + \delta x) - u(x) = \epsilon\delta x + \omega x\delta x \tag{A.4}$$

[e.g. *Aki & Richards*, 2002, page 13], where ϵ is the strain tensor and the rigid body rotation is given by

$$\xi = \frac{1}{2}\nabla \times u(x) \tag{A.5}$$

Following *Cochard et al.* [2006] the rigid body rotation for a double couple source in a homogeneous isotropic medium characterized by P wave velocity v_p, S-wave velocity v_s and density ρ in the farfield is calculated by inserting equation *A.5* in the farfield expression for ground displacement

due to a double couple [*Aki & Richards*, 2002]

$$u(r,t) = \frac{1}{4\pi\rho v_p^3}\frac{A^p}{r}\dot{M}(t-\frac{r}{v_p}) + \frac{1}{4\pi\rho v_s^3}\frac{A^s}{r}\dot{M}(t-\frac{r}{v_s}) \tag{A.6}$$

with A^P and A^S denoting the radiation patterns of P and S waves respectively and $M(t)$ the moment time function of the source as:

$$\xi(r,t) = \frac{-A^{Rot}}{8\pi\rho}[\frac{1}{v_s^4 r}\ddot{M}(t-\frac{r}{v_s}] \tag{A.7}$$

- where A_{rot} denotes the radiation pattern of the rotation term. The farfield rigid body rotation term is therefore smaller than the farfield displacement term by order $1/v_s$. The fact that it is moment acceleration which is recorded by a rotation sensor and not moment rate tends to decrease the effect of body rotation. If thus the bar magnet is twisted around the fiber axis, e.g. the horizontal field component will try to restore the position of the bar magnet relative to the geomagnetic field. The torsional restoring force of the fiber will then cause oscillations with the free period of the system.

A quantitative analysis and comparison of the relative contributions of the above causes of the response of magnetic variometers is beyond this study. Important for the following is that all presented mechanisms are linear in the source strength, i.e. relative magnetogram amplitude can directly be related to scalar seismic moment ratios.

A.5.2 Comparison of the magnetogram amplitudes of Chilik and Chon Kemin earthquake

Table *A.1* shows results of the amplitude analysis of the Kew and Greenwich magnetograms. The earthquake disturbance is best visible on the H component records (see Figure *A.12*) and with less quality on the declination (D) component records. Only for the Chilik earthquake recorded at Kew a signal is also visible on the Z record due to a high noise level on the other Z component records. The reading error on the magnetogram amplitudes is estimated to be on the order of 10% of the maximum amplitude.

The amplitude ratio average between the Chilik and the Chon-Kemin events is 0.83, i.e. the magnetogram data suggest that the moment magnitude of the Chilik earthquake is 0.08 units smaller than that of the Chon-Kemin earthquake (M_w 8.0) and is equal to M_w 7.9 ($\pm$0.1).

Table *A.2* presents arrival time information. Due to the generally low signal to noise ratio it cannot be expected to detect P-wave onsets on the traces. The times of the envelope maxima correspond to the arrival times of surface waves, which can be calculated using the rather precise information available regarding origin time and hypocenter for the Chon-Kemin earthquake [*Kulikova & Krüger*, 2015]. The lower group velocity calculated for the Kew record with 2.9 km/s compared to 3.2 km/s for the maximum of the Greenwich record could be due to the different free periods of the instruments mentioned above coupled with dispersion of the surface waves. The durations of strong surface-wave motion of both the Chilik and Chon-Kemin earthquakes are comparable; again pointing to a similar magnitude of both events.

TABLE A.1: Magnetograms amplitude.

Station	Component	July 11, 1889	January 3, 1911

		amplitude [mm]	amplitude [mm]
Kew	H	12.0	16.2
Greenwich	H	36.7	46.2
Greenwich	D	21.9	22.6

TABLE A.2: Arrival times on magnetograms.

Year	Station	Comp	First onset time time	Max. arrival time	Max. time duration [s]	Group velocity[km/s]
1889	Kew	H	22:41:41	22:44:30	859	
	Greenwich	H	22:16:35	22:35:33	1610	
	Greenwich	D	22:25:34	22:36:09	1354	
1911	Kew	H	23:56:08	23:58:45	754	2.9
	Greenwich	H	23:43:21	23:55:12	1591	3.2
	Greenwich	D	23:49:29	23:55:37	690	

A.6 Discussion

In the following, we discuss the derived constraints for the basic source parameters origin time, epicenter location and centroid depth, focal mechanism and moment magnitude.

A.6.1 Origin time and epicenter location

The abrupt break in the Wilhelmshaven record was observed at 22:10:22 July 11, 1889 (reading error about 1 minute, clock error reported to be 1-3 minutes). We use the epicenter as inferred from macroseismic studies (43.17N°, 78.55E°) to calculate an epicentral distance of 46.8° (the coordinates of the recording pendulum in Wilhelmshaven set to 51.52N°, 8.13E°). A hypocenter depth of 40 km suggests an origin time estimate of 22:11:56.2 July 11, 1889, considering the P-wave travel time in the IASP91 global Earth model [*Kennett et al.*, 1995] to be 505.8 s. Within the mentioned error bounds this matches quite well the origin time of 22:14 July 11, 1889, in the *Mikhailova et al.* [2015] catalog and the reports of stopped local clocks (see Table *2.2*). However, also the origin time uncertainty from the Wilhelmshaven record adds up to 4 minutes, if the timing errors and the uncertain hypocenter location are taken into account. Nevertheless, the assumption that the break in the seismic record is due to the P-wave arrival and not another seismic phase is most consistent with local clock observations (S wave arrival is 409 s later, surface waves arrive about half an hour later). The earthquake was also recorded on the magnetometer in Berlin [*Rebeur-Paschwitz*, 1893], but more than 20 minutes later at 22:33, which is consistent with the arrival of surface waves.

If we use the envelope-maximum arrival time of the surface waves measured on the magnetograms and use the group velocities derived from the magnetograms of the Chon-Kemin earthquake, we can check the differential time (surface wave envelope maximum time on magnetogram minus P-wave onset at Wilhelmshaven station) and compare it with the prediction for the distance to the Chilik

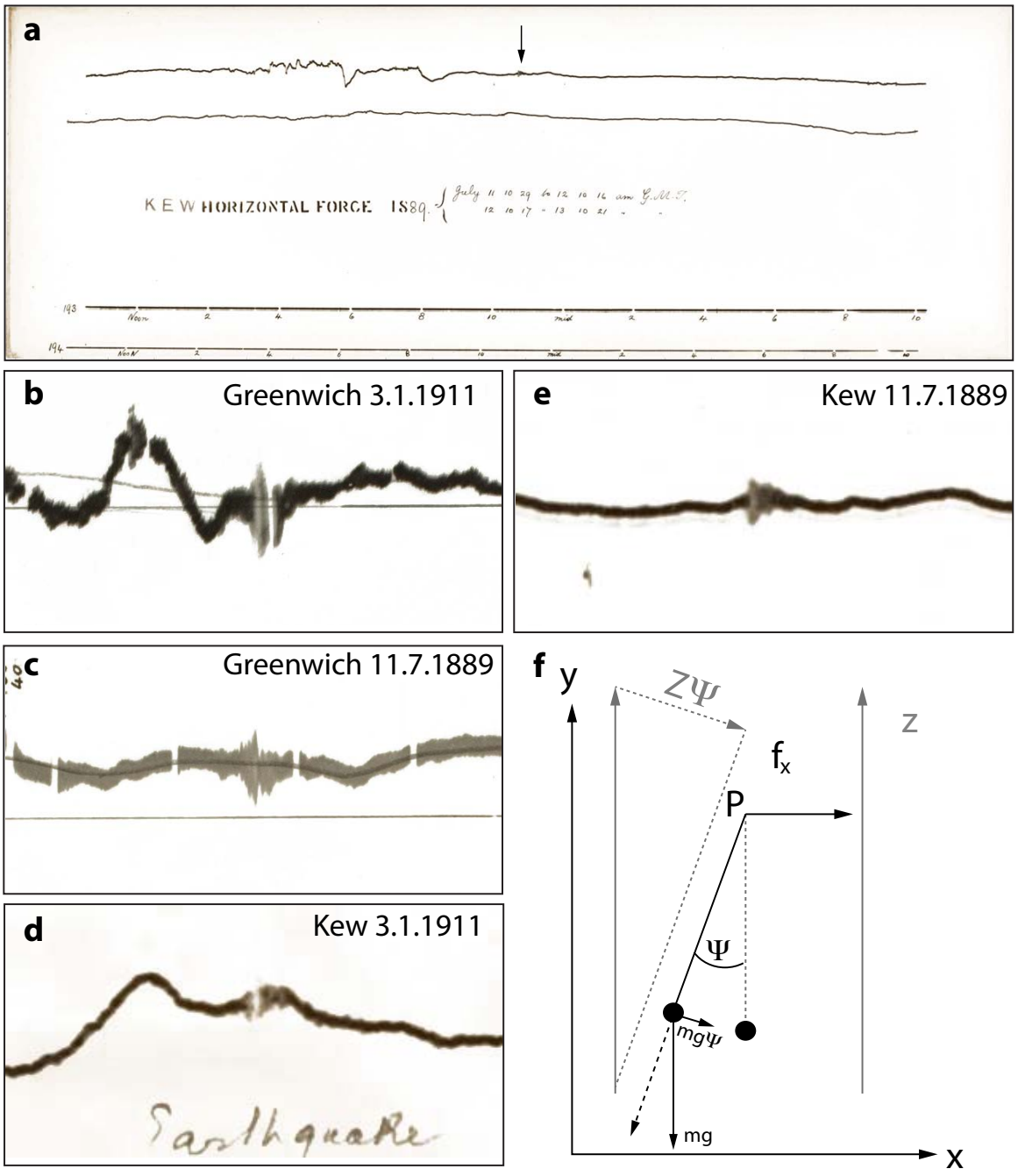

FIGURE A.12: Comparison of magnetometer recordings for the Chilik and the Chon-Kemin earthquakes. Figure a) shows a full magnetogram for the whole day, with arrow indicating the earthquake waveforms. Figures b) and c) are the magnified Greenwich station records for the Chon-Kemin (3.1.1911) and the Chilik (11.7.1889) earthquakes respectively; d) and e) are the Kew station records for the same earthquakes. The plot f) is the sketch, which shows geometry of the magnetic instrument and its response to ground motion, following *Eleman* [1966]. The bar magnet is oriented North-South and seen from magnetic South. P is the pivot point of the fiber attachment. Z is the geomagnetic vertical field component.

hypocenter. Using a distance of 5681 km to Kew and a group velocity of 2.9 km/s (as found for the Chon-Kemin surface wave-train on the magnetogram) the predicted arrival time of the surface wave maximum is 22:44:35 at Kew. This matches almost perfectly the observed arrival time. The same calculation for the Greenwich measurements results in a predicted arrival time of 22:41:25, i.e. about 5 minutes later than the observed arrival time. Considering the time reading error on the Greenwich magnetograms (about 5 minutes) with their lower signal to noise ratio this is still consistent with the assumed hypocenter within the error. However, the mentioned difference time can not be used to improve the epicenter location because of time readings from different instruments with different clocks so that their errors sum up.

A.6.2 Focal mechanism

It was not possible to constrain the focal mechanism of the Chilik event. Derivation of the transfer function of the magnetic instruments would be essential. A relative analysis comparing for instance amplitudes on the H and Z magnetograms for a known focal mechanism with those for the event with unknown mechanism would be only possible with more data.

Geological evidence derived from young fault scarps, potentially associated with the Chilik earthquake, favor a major strike slip component in addition to thrusting. Such a mixed mechanism would be somewhat different than the Chon-Kemin solution [*Kulikova & Krüger*, 2015]. For example, the Zhalanash-Tyup earthquake was a similarly mixed event with an oblique-reverse mechanism. However, a scaled version of the macroseismic intensity distribution of the Zhalanash-Tyup event would not fit the Chilik earthquake damage pattern as shown by *Bindi et al.* [2014]. The recent January 28, 2013, Mw 6.1 [*CMT*, 2015] event east of Lake Issyk-Kul showed even a dominant strike-slip focal mechanism. Oblique motion is not uncommon in the Tien-Shan Mountains, which deform mainly by thick-skinned deformation along steeply dipping reverse faults and basement-cored uplifts [e.g. *Selander et al.*, 2012]. Pre-existing, reactivated shear-zones that are obliquely oriented with respect to the present-day shortening direction seem to accommodate transpression at depth, from which sets of semi-parallel, high-angle reverse faults nucleate and subsequently propagate outwards over time *Selander et al.* [2012]. Steep fault planes or steepening of planes towards depth is also visible in the greater Chilik area [e.g. *Tibaldi et al.*, 1997; *Abdrakhmatov et al.*, 2015], for instance along river cuts, or simply indicated by almost straight fault traces. A steep fault geometry in combination with an atypically small surface rupture length for a M>8 earthquake might pose an additional reason to postulate a deeper source that involved some moment-release in the mid- and/or lower crust.

A.6.3 Moment magnitude and centroid depth

The coda-wave amplitude level is regarded to provide a stable source strength estimate and is much less dependent on the mechanism and the event depth than magnitude determinations based on direct-wave amplitudes [*Denieul et al.*, 2015]. The moment magnitude values estimated from coda-wave-amplitude are larger than the moment magnitude estimated from magnetograms by about 0.3 units. A major uncertainty is the unknown linearity of the Rebeur-Paschwitz pendulum [e.g. the damping coefficient value is mentioned to vary with higher damping of h = 0.04 in the beginning and lower damping of h = 0.01 for larger amplitudes, *Fréchet & Rivera*, 2012]. However, a test with different simulation filters in this damping range shows little effect on the scale of the amplitudes, and if observable at all, accounting for the effect shifts magnitude estimations to slightly larger values. Another uncertainty is the poor information regarding early large aftershocks of the Chilik

earthquake. Very strong aftershocks in the first few hours after the mainshock also would increase the coda level and therefore tend to increase the estimated magnitude value. Aftershock information from eyewitness observations is provided by *Mushketov* [1891] and is presented in translation in Appendix *A.8.1.1.* Indeed, one of the listed aftershocks (see Appendix *A.8.1.1*, first event) could lie within the coda wave analysis window and could correspond to the amplitude maximum at 01:57 on July 12, 1889, see also Figure 4, where we marked a possibly corresponding onset with a question mark. No strong amplitude is visible in the magnetograms at this time, excluding a strong secondary shock. If only those coda time windows are considered, which lie either before or after the mentioned onset in the Wilhelmshaven record, the overall magnitude estimate does not change.

We should furthermore consider that a station site effect at the location of the observatory in Wilhelmshaven might enhance amplitudes of scattered surface waves compared to sites of modern broadband permanent and temporary seismic stations. An indication for such a site effect is the average amplification of Earth tide amplitudes by a factor of about 3 measured at Wilhelmshaven compared to Potsdam (3.1 for 22 common days in July 1889), where we used amplitude reading tabulated in *Rebeur-Paschwitz* [1892b, pages 52-53, 69-70]. Rebeur-Paschwitz suspects that a compressed 1 m thick sand and peat layer underlying the clay layer the pendulum pillar was founded in, might have led to this amplification effect [*Rebeur-Paschwitz*, 1892a, page 43]. Therefore, we suppose that the unknown site effect for mid-period surface waves at the Wilhelmshaven observatory likely contributes to an overestimation of the magnitude possibly in the order of 0.3-0.5 units. Such a station specific amplification effect is observed for instance for station IGAD for the April 15, 2015, Nepal earthquake, see Figure 9b.

We inspected the yearbooks of both Kew and Greenwich observatories [*BGS*, 2015], but found no mentioning of instrumental changes in the years between 1889 and 1911, i.e. the years of the Chilik and the Chon-Kemin earthquakes. The available data therefore enable us to set instrumental constraints for the moment magnitude by a relative comparison of magnetogram amplitudes measured on Kew and Greenwich H (and partially D) component magnetograms. Both amplitude ratios indicate slightly smaller surface-wave amplitudes for the Chilik earthquake compared to the Chon-Kemin earthquake. As mentioned above, both magnetographs had different free periods where the Greenwich magnetograph is more longperiod than the Kew magnetograph. The free period of the Kew magnetograph ($T_0 = 13.6$ s) is likely above the corner period of the Chilik event source spectrum and therefore prone to effects of the extended source, i.e. directivity effects. The free period of 42 s of the Greenwich magnetograph is more suited to measure the seismic moment, but the record is noisier. Both the Kew and the Greenwich observatory have almost the same backazimuth of 67.3° and 67.1° with respect to the Chilik epicenter. It is therefore likely that a mixture of Love and Rayleigh wave amplitudes is observed on the H component magnetogram. It should be mentioned that the possibly different depth and the likely different focal mechanism may bias the amplitude comparison of both earthquakes. With these caveats in mind, we conclude that the magnetogram observations provide evidence that both events were of similar magnitude.

We cannot constrain the hypocenter depth from the available data. The only hint comes from the scaling of the late coda in the Wilhelmshaven record (see Figure *A.6*), because assuming a hypocenter depth in the mantle (e.g. 200 km) would lead to unreasonable large magnitude estimates. It should be mentioned that the M_w 6.9 September 18, 2011 event in northeast India with a centroid depth of 46 km tends to scale similarly as the much deeper Hindukush events with centroid depths ranging from 184 to 237 km, see Figure *A.6.* The lack of observation of extreme localized intensities (assuming that they have not been simply overlooked) and a large continuous surface rupture (assuming that it should have been detectable on satellite images) suggests an event depth in the mid and/or lower crust [*Bindi et al.*, 2014]. There are examples for large continental thrust events (e.g. the M_w 7.6 Gujarat (Bhuj) earthquake or the recent M_w 7.8 Nepal earthquake), which did

not produce major surface ruptures. The latter likely occurred on the low angle Main Himalaya frontal thrust. A similar fault mechanism for the Chilik earthquake cannot be excluded and could perhaps explain the macroseismic observations assuming a centroid depth shallower than 40 km. However, such a focal mechanism seems unlikely given the geological fault mapping results. Only the E-W striking, N-dipping Baisorun-Chilik fault shows primarily dip-slip motion. Rupture along this active fault, however, seems short with respect to the longer fresh rupture traces along the steeply dipping Saty and Beskaragai faults. The Gujarat earthquake occurred in the mid crust with a centroid depth of about 25 km in a region where seismic events in the mid and lower crust are frequently observed [*Bodin & Horton*, 2004]. While there is no high seismicity in the catalog of recent years with hypocenter depths larger than 20 km, there is at least one notable exception, the M_w 6.9 Zhalanash-Tyup earthquake with a centroid depth of 34.7 km as confirmed by broadband body-wave modeling of Gräfenberg array waveforms (not shown). Although this event has not been used in their calculations, *Sloan et al.* [2011] have analyzed and partly relocated the centroid depths of 123 Tien-Shan earthquakes with moment magnitudes > 5.2. They found that lower crustal events are absent within the orogen, but mid-crustal events sporadically occur along the edges of large basins, particularly also south of lake Issyk-Kul [*Xu et al.*, 2006]. Mid-crustal events were found east of lake Issyk-Kul in the intensity X region of the Chilik earthquake, using a temporary regional broadband network [*Xu et al.*, 2006]. Lower crustal events seem common in the Tien-Shan forelands, including the Kazakh platform to the north [*Sloan et al.*, 2011; *Alinaghi & Krüger*, 2014], which is supposedly stronger than other continental areas [see also, *Maggi et al.*, 2000, for modeling results of flexural rigidity]. *Sloan et al.* [2011] explain this earthquake depth distribution with anhydrous crust. The Chilik event occurred not exactly in the foreland, but more or less along the northern rim of the Tien-Shan and crustal rheology in combination with reactivation of inherited faults might well exert the control on the observed seismicity.

A.7 Conclusion

The few instrumental data available for the Chilik earthquake are consistent with the large magnitude estimates resulting from macroseismic studies (M_w 8.0-8.3). The amplitude comparison of longperiod surface waves measured on magnetograms at two observatories in England favor a slightly lower magnitude limit of M_w 8.0. This is consistent with the magnitude estimate from coda amplitudes at Wilhelmshaven, if a station-site factor amplifying mid-period surface waves by a factor of 2-4 is assumed. In addition, the presence of a strong aftershock may contribute to the late coda level recorded at Wilhelmshaven. Taken together with widely distributed and not connected surface rupture patterns which probably can be associated with the Chilik event, this means that a shallow centroid depth in the upper crust is rather unlikely. Overall a centroid depth in the mid or lower crust explains the observations best, consistent with the unusual centroid depth of about 40 km resulting from the macroseismic studies. The eyewitness reports and the geologically inferred surface slip point to a large strike-slip component in contrast to the almost pure thrust focal mechanism type found for the nearby Chon-Kemin earthquake. The Zhalanash-Tyup earthquake shows many of the mentioned characteristics, i.e. an unusual large centroid depth of 34.7 km and a oblique-reverse focal mechanism and is located in the Rossi-Forrel intensity X contour. Modern seismicity presents no further evidence for clusters at lower crustal depth besides the Zhalanash-Tyup event. Because of the potentially severe implications for seismic hazard estimates in intra-continental collision zones in general, we strongly suggest to further investigate potential areas of surface rupture, to date the paleoseismic information, to clarify the regional crustal structure with geophysical methods and to model the stress distribution resulting from the known major

earthquakes. Physical mechanisms for the generation of strong earthquakes in the lower continental crust need clarification.

Acknowledgments

We would like to express gratitude to all the people who helped us to collect the historical seismograms and magnetograms. Particularly we express our very great appreciation to BGS (British Geological Survey) unique collection of historical magnetograms. We are also very grateful to William H.K. Lee for providing open access IRIS webpage ″Seismogram Archives of Significant Earthquakes of the World″, particularly ″British Association for the Advancement of Science: Seismological Investigation, Reports of the Committee″ - from where the information about magnetograph was obtained ($http://ds.iris.edu/seismo-archives/info/historical/baas/$). Special thanks should be given GFZ (German Research Centre for Geosciences, Potsdam) library for providing the historical reports and to Dr. Dino Bindi for his advice and comments on macroseismic observations for the Chilik earthquake. Also we wish to thank Dr. Alexander Strom for providing the unpublished report of *Besstrashnov* [1993] and P. Molnar for providing the microfilms of the *Bogdanovich et al.* [1914] and *Mushketov* [1891].

Additionally we are very gratefully to both our reviewers for their speedy reviews, and friendly and constructive comments. Especially we thank Jim Dewey for the stylistic revision, which considerably improved the language of the manuscript.

This work was funded by the German Federal Ministry of Education and Research and integrated in the Potsdam Research Cluster for Georisk Analysis and Sustainability (PROGRESS: http: //www.earth-in-progress.de /index.35.de.html) and the project TIPTIMON (support code 03G0809).

In this work we have used open source software and would like to gratefully acknowledge: GMT - The Generic Mapping Tools developed by Paul Wessel and Walter H. F. Smith; Seismic Handler (seismic waveform analysis tool) developed by Dr. Klaus Stammler and Dr. Marcus Walther; and GIMP (GNU Image Manipulation Program).

A.8 Appendix

A.8.1 Intensity

The original report contains the description of effects of the Chilik earthquake in different cities and villages near the epicenter region [*Mushketov*, 1891]. The description is limited to the data which were obtained from questionnaires. For densely populated regions, such as larger cities like Verny, there were several observation reports, which provided objective full picture of the damage, whereas in small less populated villages the reports were based on 1-2 witness testimonies. Sometimes, the information was limited to one sentence, e.g. city Lepsy, the report provides just one sentence - ″the earthquake was felt weaker than in neighboring regions (Kopal and Topolevsk), Intensity VII″. No information about particular damage was provided, it is not said how many people felt the earthquake and to what extent. Sometimes the report provided an observation in some regions describing the place as ″in between two ridges″ or ″between two rivers″, and no particular village was assigned to that observation. It is hard to convert such information into a valuable macro-seismic observations map. Subsequently, we have translated the *Mushketov* [1891] report and summarized in a table below, keeping the key information as it appeared in the original text. In order to show

the location of the different cities and villages, we used the old names of those places and using a prerevolutionary (1917) map (The map of Semirechye [*Ilyin*, 1871; *Semirechye*, 1900]. We provided the modern names with corresponding coordinates.

The report also has additional information about damage near lake Issyk-Kul which was not included in table *A.3*. ″ Along the Issyk-Kul shore, the earthquake was felt significantly, the surface cracks, liquefaction and bulging of the ground were observed along all the Issyk-Kul shore up-to the mountains. The cracks reach huge size: up-to five meters wide and one km long; they were also very deep (unknown depth); very often one side of the crack was ∼35 cm higher than the other. Shortly after the earthquake mail correspondence in the region did not function due to the dangerous cracks. They were excessively large on the way from Sazonovka to Uytal on the 10th, 12th and 23th km; and from Uytal to Preobrajenskoe on the 7th, 13th and 22nd km. Also there were many avalanches and landslides on the higher parts along the Issyk-Kul shore. In the lake itself a large wave was formed during the earthquake, which flooded the western shore of the lake. Rivers Tyub, Dzergalan, and Kurmenty changed their course.

Another particularly interesting statement, refers to the so called ″seismic island″ - a place inside the high intensity region, where the earthquake was felt less or not felt at all. *Mushketov* [1891] says: ″ Further NE from Urzharskaya, on the eastern slope of Tarbagatai (about 625 km NE of Verny), in the upper valley of the Irtysh river, the earthquake was much weaker than in the western regions. In the Zaysan quarter (235 km ENE from Urzharskaya and 160 km NE from Bachty), the earthquake was not noticed at all. Because of limited observation it is hard to judge if Zaysan quarter is a seismic island or the earthquake intensity decreases so dramatically crossing Tarbagatai.″

TABLE A.3: Intensity observations (translated by Galina Kulikova from Mushketov(1891)

#	Int. [2]	Old name	Current name	Lat	Lon	Time UTC (Local time)	Effects of the earthquake
1	X	Preobrajenskoe	Tyup, Kyrg.	42.7235	78.3613		Many surface cracks, during the earthquake water came up from those cracks mixed with sand and dirt, the water fountains reach 1.5 meters, suffocating gas was released from the cracks. The bridge over the Tyub river (very stable) was shifted to the left bank by 1.5 meters. All the building made of stones and bricks are destroyed, church half-destroyed. Intensity not less than X.
2	X	Issyk-Kul Monastery	Ak-Bulak, Kyrg.	42.7872	78.2533		The monastery building severely damaged and uninhabitable. The right bank of the nearby river Kurmenty was covered with cracks and the left one collapsed. Intensity X.
3	X	Uytal	Oital (Oytal), Kyrg.	42.7500	78.0000		All the buildings completely destroyed, 8 people killed and 2 severely injured. Many large surface cracks. Intensity X.
4	X	Sazonovka	Ananyevo, Kyrg.	42.7300	77.6600		In the village and around it many cracks up to 1.5 meters wide, one side of those cracks is higher than the other by 35 cm. 21 persons severely injured. Intensity X.
5	X	Tyraygyrskaya volost	[3]	See Cholpon-Ata.			Huge rock masses fell down the slopes killing people and animals, 39 people died and 2 severely injured. Intensity X.
6	X	Cholpon-Ata	Cholpon-Ata, Kyrg.	42.6500	77.0838		See Tyraygyrskaya volost
7	X	Region between rivers Charyn and Karkara	Set to the village Karkara in Kaz. at approximately same location.	42.8914	79.2372		Here was a trade camp, people could not remain standing, and were thrown away for several meters. Intensity X. Between Chilik river valley crossing river Uch-Merke and Charyn near division of Zailiysky and Kungei Alatau the mountain road was completely destroyed. In the upper Chilik river valley and Asy river valley severe destruction were observed.
8	X	Chundzhi	Chundzha (Shonzhi), Kaz.	43.5500	79.4667	22:35 (03:35) not checked	Partially stone buildings were destroyed, cracks in all the houses, chimneys broke everywhere. Near the spring flowing into a ravine 30 cm wide cracks were observed. Intensity X. About 10 km W from Chundzhi dust cloud was seen all day, apparently a lot of landslides occurred here. This place is believed to experience the strongest shaking.
9	X	Malovodnoe	Baydibek-biya, Kaz.	43.5106	77.7028		All the house destroyed, including Russian wooden ones. Intensity X.

[2]Intensity according to Rossi-Forel scale read from *Mushketov* [1891]

[3]Region covering North and North-West part of the Issy-Kul lake. Approximately from modern Grigorievka on the East til Balykchu on the West having Issy-Kul lake coast as a South boundary and Chon-Kemin river as Nort boundary Intensity observation point is set to Cholpon-Ata.

10	X	Koramskayakaya volost	Set to the central village Koram, Kaz.	43.5409	78.1643		All 2500 houses destroyed. But all constructions were made of clay. 21 persons died. Intensity X.
11	X	Dzhergalanskaya lowland	Jergalan, Kyrg.	42.6474	78.8780		The whole lowland (about 1.5 km wide) was covered with cracks, filled with sand and water. Later thousands of craters were formed, from 15 till 30 cm deep and up to 6 meters in diameter. The water flow was very strong, so that 20 goats and a yurt of one nomad was buried under the sand. Three bridges (wooden, 30-40 meters long) across Jergalan river were absolutely broken. Intensity X.
12	IX-X	Chilik, Kazakstan	Shelek, Kazakstan	43.5978	78.2496	22:15 (03:15) not checked	All the houses and buildings including stone constructions were strongly destructed by shaking, everywhere chimneys and ovens fell down, the walls were covered by cracks, also cracks were observed in the earth (direction from E to W). Intensity IX-X.
13	IX-X	Dachi (near Przhevalsk), Kyrg.	Pristan'-Przheval'sk,Kyrg.	42.5500	78.3000		Many changes in the Earth's surface, the coastline torn and lowered down, forming star-like cracks, the coast was flooded, many soil flows and landslides were observed. Liquefaction was observed all over the region as well as many surface cracks, all the houses at least half-destroyed. People could not remain standing. Intensity IX-X.
14	IX-X [4]	Turgen	Turgen, Kaz.	43.4006	77.5933		The church and many stone houses destroyed. Intensity IX-X.
15	IX	Karasuyskayakaya, tarachinskoy volosti	Baiterek (Alexeevka), Kaz.	43.4028	77.2250		Stronger than in Verny. Almost all the houses destroyed. Intensity IX.
16	IX	Nadejdinkoe (Issyk)	Esik, Kaz.	43.3500	77.4500		The earthquake was considerably weaker, All the buildings remain standing, the cracks in the wall were observed. Intensity IX.
17	IX	Kuyankuz	Qoyankus,Kaz.	43.3917	76.9405		The post office stone building completely destroyed, in another building half wall collapsed, many walls were covered with cracks. Water appeared in the wells, though earlier they were empty. Intensity reached IX.
18	IX	Karabulak	Karabulak, Kaz.	44.9089	78.4922		In the church an icon attached to the western wall with 30 cm long spikes, fell and was thrown to the middle of the building.
19	IX	Borohudzir	Not found, village about 20km NW from Zharkent	44.3104	79.8375		Half of the buildings was destroyed. 5 km NE of Borohudzir many cracks up to 35 cm wide were observed on the river Shum site.
20	IX	Zharkent	Zharkent, Kaz.	44.1667	80.0000	22:25 (03:25) from stopped station clocks	All the state buildings were destroyed, though they were all built from adobe brick. The ovens and chimneys collapsed everywhere. Taking into account the number of landslides and avalanches it is believed to have intensity IX.

[4]The intensity in the text of *Mushketov* [1891] report is IX-X, but the summary table in the same report gives intensity X.

21	VIII-IX [5]	Djhangyz-Agach	Zhalgyzagash, Kaz.	44.7633	78.5587		All the brick houses were destroyed. Intensity VIII-IX.
22	VIII-IX [5]	Tsaritsinkoe	Budennovskoe, Kaz.	44.6484	78.7553		All the brick houses were destroyed. Intensity VIII-IX.
23	VIII-IX [5]	Lugovoe	Terysakan, Kaz.	44.5361	78.8842		All the brick houses were destroyed. Intensity VIII-IX.
24	VIII-IX	Przhevalsk	Karakol, Kyrg.	42.5000	78.3833	22:20 (03:20) not checked	People woke up because of banging bricks, falling chimneys and shaking. Earth cracks were not observed in Przhevalsk itself, half of the building were damaged. A lot of cracks were observed in the walls of houses, given intensity VIII to IX.
25	VIII-IX	Iliyskoe	Iliysk, Kaz.	44.0033	76.9986	22:15 (03:15) Telegraph clocks	Also stronger than in Verny, a lot of oblique cracks in the wall. In the soft ground the cracks were observed till 1 meter depth. Intensity VIII-IX.
26	VIII-IX	Kopal	Kapal, Kaz.	45.1333	79.0500	22:00 - 22:15 (03:00 - 03:15) not checked	Some brick buildings were destroyed, chimneys collapsed. Intensity not less than VIII-IX.
27	VIII	Talgar (Sofiyskoe), Kaz.	Talgar, Kaz.	43.3000	77.2333	22:15 (03:15) approxi-mately	The houses (mainly wooden) survived, the destructions are minimal. Intensity VIII.
28	VIII	Verniy, Kaz.	Almaty, Kaz.	43.2775	76.8958	22:15 (03:15) Telegraph clocks.	The damage is not strong, in a few houses the chimneys collapsed. The shaking was more severe in the lower - North part of the city, same as in 1887. Intensity VIII.
29	VIII	Suydun	Shuiding Zhén (Shuiding), China	44.0500	80.8753		All the houses (clay wattle and daub) destroyed, many dead people. Intensity not less than VIII. East of that region no information is available.
30	VIII	Kuldzha	Gulja, China	43.9352	81.6394		same as Suydun
31	VIII	Narinskoe	Narin, Kyrg.	41.2951	75.3415	21:50 (02:50) checked with Sun clocks	Before the main shaking typical noise was heard, similar to the bubbling of water and then louder noise similar to firework. After the earthquake for half an hour people heard loud individual bangs from the Issyk-Kul site. Many houses had cracked walls, stoves and chimneys; ceiling beams were broken. However, cracks in the earth were not observed, but rockfalls were observed in the surrounding mountains. In the direction of Issyk-Kul lake these rockfalls continued longer and dust clouds were observed in the NE direction. The water in the ponds and the river Naryn rose. Intensity VIII.
32	VIII	Narybulak (Karabulak Tokmakskogo uezda)	Karabulak, Kyrg.	42.7990	75.7489	22:10 (03:10)	First strong noise was heard from SSE, then shaking started, first light and then strong. The damage was considerable, the cracks were till 2.2 cm wide, the ovens and chimneys were destroyed

[5] The intensity in the text of *Mushketov* [1891] report is VIII-IX, but the summary table in the same report gives intensity IX.

33	VIII	Teploklyuchenskoe	Teploklyuchenka, Kyrg.	42.5002	78.5251		124/132 houses had severe cracks, ovens and chimneys collapsed. Intensity VIII.
34	VIII	Topolevskiy	Topolevka, Kaz.	45.4287	80.3313		Partially destroyed and severely damaged stone building. Intensity VIII.
35	VII-VIII	Alamedin	Alamedin. Kyrg.	42.9547	74.6490		The buildings were damaged.
36	VII-VIII	Olivkino	Kyzyl Suu, Kyrg.	42.3395	78.0068		1/7 of all the building were severely damaged. The cracks were observed in the walls of stone building, the chimneys and ovens fall everywhere.
37	VII-VIII	Barlyk	Birliktau (mountain peak), China	45.7432	82.7632		There was a significant arrival of water in the springs. One shabby building collapsed. Intensity VII-VIII.
38	VII	Lepsy (Lepsinsk)	Lepsy (Lepsinsk), Kaz.	45.5270	80.6105		The earthquake was felt weaker than in neighboring regions (Kopal and Topolevsk), Intensity VII.
39	VII	Kashgar	Kashgar, China	39.4704	75.9898		There were cracks in the buildings. Typical hum was heard. Intensity VII.
40	VII	Derges	Zhergez, Kyrg.	42.5488	78.6740		The earthquake was considerably weaker than in Przhevalsk, small cracks in the house walls and chimneys.
41	VI	Sukuluk	Sokuluk, Kyrg.	42.8603	74.3002	22:00 (03:00)	All people woke up, the water in wells rose, the bangs were heard from the E. The animals were very disturbed. Intensity VI.
42	VI	Chuguchak	Qoqek, China	46.7460	82.9798		The earthquake was felt significantly. Intensity VI.
43	VI	Bakhty	Bakhty, Kaz.	46.6568	82.7303	22:12 (03:12) checked via sun time	Effects of the earthquake were insignificant, no cracks in the walls. Only crumbling plaster and the clatter of dishes were observed. Intensity VI.
44	VI	Durbundzhin	Emin, China	46.5254	83.6287		The earthquake was felt significantly. Intensity VI.
45	VI	Urzharskaya	Urzhar, Kaz.	47.0875	81.6319	23:15 (04:15) checked with sun clocks	Sleeping people woke up, the dishes fell out of cupboards. The clocks stopped, animals expressed anxiety. Intensity VI.
46	V-VI	Irkeshtam	Irkeshtam, Kaz.	39.6784	73.8985	22:05 (03:05)	All sleeping people woke up. The dishes in the cupboard clanged, but no damage was observed, no underground hum was heard. The intensity V-VI.
47	V	Semipalatinsk	Semey, Kaz.	50.4233	80.2508	22:40 (03:40)	3 people woke up. Light shaking was observed in the houses, lamps and candlelights wavered. Dishes clinked in the cupboards. Intensity V.
48	IV	Karkaraly	Karkaralinsk, Kaz.	49.4159	75.4776	22:15 (03:15) Telegraph clocks	Not everyone noticed the earthquake, there was specific hum, and unstable objects fell down. Intensity IV.
49	III-IV	Pavlodar	Pavlodar, Kaz.	52.2871	76.9675	22:30 (03:30)	Not everyone noticed the earthquake. Those who did not sleep described the earthquake as undulation motion, no hum was heard, candlelight and clock pendulums swayed, one-store house was shaking. People praying in a mosque run out, because the building was shaking. One person woke up with his family, because of noise produced by swinging clock pendulums. Intensity III-IV

50	III	Ust-Kamenogorsk	Oskemen, Kaz.	49.9757	82.6024	22:10 (03:10)	No damage, but the earthquake was felt as 2 shocks. Intensity III.
51	III	Aulie-Ata	Taraz, Kaz.	42.8993	71.3992	21:50 (02:50) checked with Telegraph clock	Was noticed only by not sleeping people indoors. Intensity III.
52	II-III	Tashkent	Tashkent, Uzbekistan	41.2667	69.2167	21:50 (02:50) checked with Sun clock	The earthquake was felt weakly, about 2-3 minutes duration. The window glasses and dishes in the cupboards clanged. Hanging objects were swinging. Only people who did not sleep felt it. Intensity II-III.
53	II	Omsk	Omsk, Russia	54.9880	73.3661	22:30 (03:30)	The beams were swinging in the church and a strongly swaying water in the river in the absence of wind was observed. Intensity up to II.
54	II	Djizak	Jizzakh, Uzbekistan	40.1158	67.8422		The earthquake was noticed by very few people, also who were not sleeping. The intensity did not exceed II.

A.8.1.1 Aftershocks information

Here we present the translation of the original *Mushketov* [1891] report, regarding aftershocks of the Chilik earthquake. All the times are given in local time. With respect to the Chilik earthquake aftershocks the following information was collected:

In Verny	
strong quake noticed	12 July at 7 o'clock in the morning (local time)
week quake	13 July ″ 3^h 54^m ″
week quake	13 July ″ 4^h 58^m ″
a quake with preceding underground hum	14 July ″ 3^h 45^m ″
week quake	14 July ″ 7^h 30^m ″
week quake without hum	14 July ″ 9^h 37^m ″

In Zharkent the shaking repeated often following the Chilik earthquake, at the same time as in Verny. Generally they were felt stronger than in Verny. The strongest one on July 14.

In Przhevalsk the earthquake repeated at 6^h 44^m, on July 12, all day light shaking was felt, the strongest was observed on July 13 at night and at 3 pm.

In Kopal at 6^h 24^m and 7^h 56^m the earthquake repeated. But the underground hum was heard only during the first one.

In Sukuluk aftershock at 6^h 16^m on July 12.

In Chilik the aftershocks were often and were observed till October.

In Karabuk aftershocks occurred several times on July 12, and during the following 8 days.

A.8.2 List of earthqukes in Central Asia.

TABLE A.5: M_w ≥6.5 events used for coda level analysis

Date	time	latitude [N°]	longitude [E°]	depth [km]	M_0[6][dyn·cm]	M_w	Name[7]
August 19, 1992	02:04:45.8	42.19	73.32	17	7.68e+26	7.3	Suusamyr, Kyrgyzstan
August 9, 1993	12:42:58.3	36.48	70.47	213.7	3.58e+26	7	
February 3, 1996	11:14:31.8	27.15	100.28	15	9.94e+25	6.6	
November 19, 1996	10:44:52.3	35.45	77.86	15	2.37e+26	6.9	
February 27, 1997	21:08:13.6	29.74	68.13	15.3	5.20e+26	7.1	

[6]Scalar seismic moment of an earthquake

[7]These are the names, which were given to some earthquakes of particular interest.

November 8, 1997	10:03:03.4	35.33	86.96	16.4	2.23e+27	7.5	
May 30, 1998	06:22:36.9	37.38	70.08	24.1	7.89e+25	6.6	
March 28, 1999	06:22:36.9	37.38	70.08	24.1	7.89e+25	6.6	
November 8, 1999	16:45:46.2	36.48	70.81	237.2	6.37e+25	6.5	
November 14, 2001	09:27:15.9	35.8	92.91	15	5.90e+27	7.8	Gujarat (Bhuj), India
March 3, 2002	12:08:23.6	36.57	70.42	228.5	1.27e+27	7.4	
September 27, 2003	11:33:36.2	50.02	87.86	15	9.38e+26	7.3	
October 1, 2003	01:03:30.0	50.24	87.59	15	1.13e+26	6.7	
April 5, 2004	21:24:04.5	36.52	70.84	183.5	1.13e+26	6.6	
October 8, 2005	03:50:51.5	34.38	73.47	12	2.94e+27	7.6	
December 12, 2005	21:47:48.4	36.45	71.06	210.2	8.20e+25	6.5	
March 20, 2008	22:33:12.1	35.43	81.37	12	5.43e+26	7.2	
May 12, 2008	06:28:40.4	31.44	104.1	12.8	8.97e+27	7.9	Sichuan (Wenchuan) China,
August 25, 2008	13:22:08.5	30.61	83.51	17.3	1.39e+26	6.7	
October 5, 2008	15:53:01.1	39.5	73.64	12	1.40e+26	6.7	Nura, Kyrgyzstan
January 3, 2009	20:23:23.6	36.44	70.36	205.6	9.17e+25	6.6	
April 13, 2010	23:49:45.8	33.05	96.79	15.7	2.53e+26	6.9	
September 18, 2011	12:40:59.9	27.44	88.35	46	2.78e+26	6.9	
December 27, 2011	15:22:03.8	51.78	95.91	19.5	1.38e+26	6.6	
February 26, 2012	06:17:24.3	51.69	96	20.5	1.19e+26	6.7	
April 20, 2013	00:02:53.1	30.22	103.12	21.9	1.02e+26	6.6	
September 24, 2013	11:30:08.4	26.7	65.04	12	5.59e+27	7.7	
September 28, 2013	07:34:12.2	27.11	65.5	15	2.28e+26	6.8	
February 12, 2014	09:19:57.6	36.22	82.57	18.3	2.87e+26	6.9	
April 25, 2015	06:11:58.4	27.77	85.37	12	7.76e+27	7.8	Nepal
April 26, 2015	07:09:21.7	27.56	85.96	17.4	1.76e+26	6.7	

Appendix B

Difficulties and challenges in historical data processing

Working with historical seismograms was a very challenging task and there are a number of aspects to take into account. Some of those difficulties made it impossible to use the seismograms, even where they were available. This is why data from only 18 stations out of 23 available, were used. The explanation of the potential difficulties found in historical seismogram processing and ways to overcome them are detailed below.

B.1 Paper records quality

The paper seismograms or microfilm scans sometimes have low quality and which can make digitization difficult. For example the records of station SLM and DEN (Table *2.4*) belong to that category. The seismogram is too dark making the contrast level too low for a successful digitization moreover, where no arrival is visible the seismograms lack timing; and the components are not marked (Figure *B.1*), so the seismogram could not digitized.

B.2 Instrument configuration limitations

The mechanical pendulum instruments had relatively narrow amplitude range which they could be registered, thus strong oscillations could not be recorded. This effect is more obvious for the seismometers with higher gain. Moreover the teleseismic records are long and registered on more

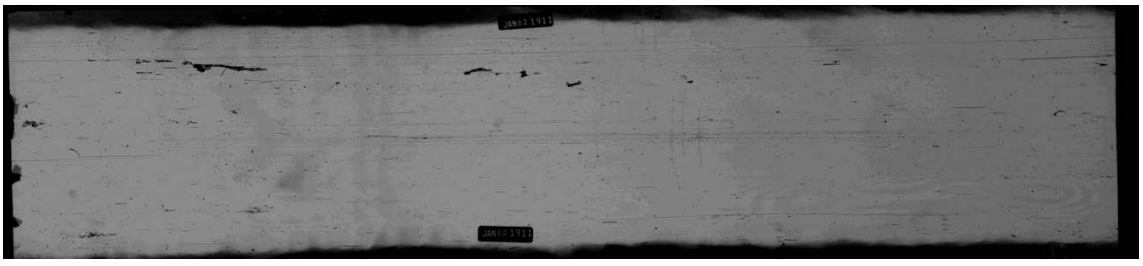

FIGURE B.1: Example of a bad quality seismogram which cannot be digitized. The record is from SLM seismic station (Wiechert instrument), both components are present on the record but not marked.

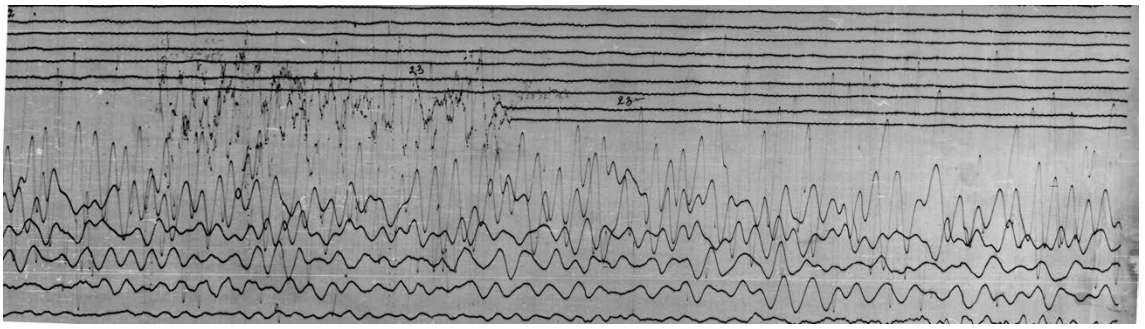

FIGURE B.2: Example of a seismogram with high gain which cannot be digitized due to high amplitudes and overlap between the traces, the record is from PUL seismic station (Galitzin instrument, NS component) with magnification factor 856.

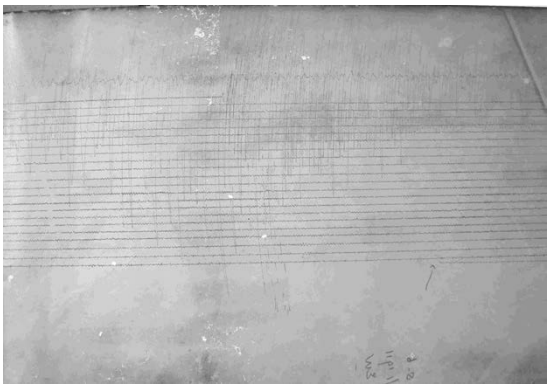

FIGURE B.3: Example of a seismogram with overlap between the traces, the record is from DJA seismic station (Wiechert instrument, NS component) the recorded earthquake can not be identified the first arrival of the Chon-Kemin earthquake can not be found.

than one trace of the paper seismogram, which leads to the overlap between the waveforms. These effects were observed on the seismograms from PUL (Figure *B.2*) station, ZAG station and DJA station (Figure *B.3*): the records are clipped completely and the traces overlapped, which made digitization impossible.

The same effect is observed for surface waves on the majority of the station in Europe (DBN (Bosch-Omori), GTT, HAM, HLG, LEI, MNH, TAR, TLO (Rebeur-Ehlert), VIE, UCC): all good quality records, but surface waves on the horizontal components are clipped and the records cannot be digitized after the S-waves. Consequently the surface waves recorded on the European seismic stations could not be used in the determination of the focal mechanism of the earthquake and the estimation of the surface wave magnitude.

In some cases the strong oscillation produced by this major earthquake caused mechanical destruction of the instrument. For example; the writing needle was replaced during registration of the earthquake introducing a step (jump) in the seismogram (Figure *B.5*), or the writing mechanism of the instrument was damaged resulting in one-sided recording (Figure *B.4*). Although those records can be digitized they may introduce errors in further processing, which is very undesirable.

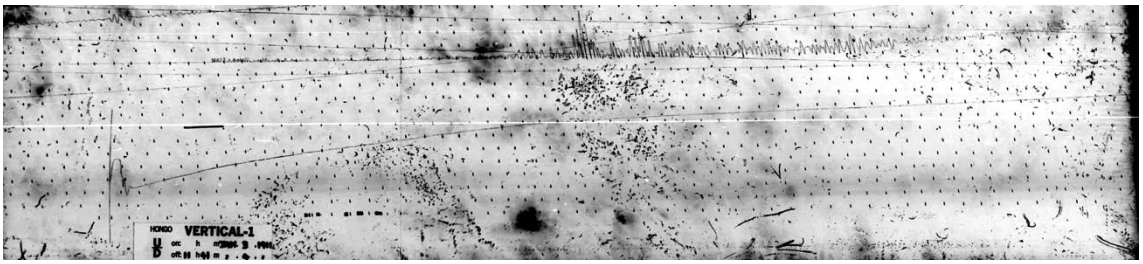

FIGURE B.4: Example of a HNG seismic station seismogram (Omori instrument, Z component) when the instrument was damaged and could not record the complete signal. The record can be digitized but is not usable.

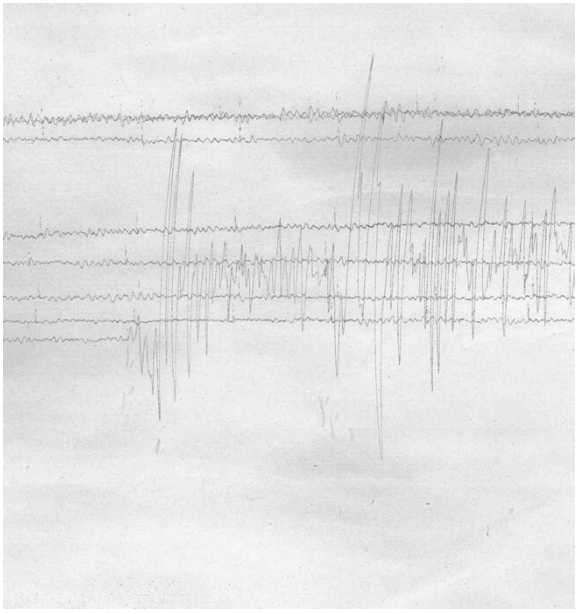

FIGURE B.5: Example of a step in a seismic record as a result of needle dislocation, the record is from DBN seismic station (Wiechert instrument, EW component).

B.3 Timing problems

Timing is one of the serious problems for historical seismograms. On some of the records time was not marked at all, only the date and the Chon-Kemin was recognised only by a guess to be the largest recorded earthquake of the day. The lack of a universal clock resulted in the time difference for the different stations. In this case stations where timing was marked and corresponded to the bulletin information for the same stations were used as a reference (e.g. HAM, MHN).

Moreover in some cases mechanical pendulums registering ground motion were not two component seismometers but two independent one-component seismographs one oriented NS and another one oriented EW with separate timing. Although the time marks are superposed into both seismograms at constant intervals, but obviously there might be uncertainty in their synchroneity (Figure *B.6*) as well as in the postulate of constant drum speed between time marks [*Stich et al.*, 2005]. The time marks on the seismograms appear as gaps in the record every minute ("minute marks") and larger gaps every hour ("hour marks"). Usually those gaps can be filled during digitization [*Schlupp & Cisternas*, 2007] by the data extrapolation, but sometimes the time marks are too large leading to the loss of some parts of the waveforms (Figure *B.7*).

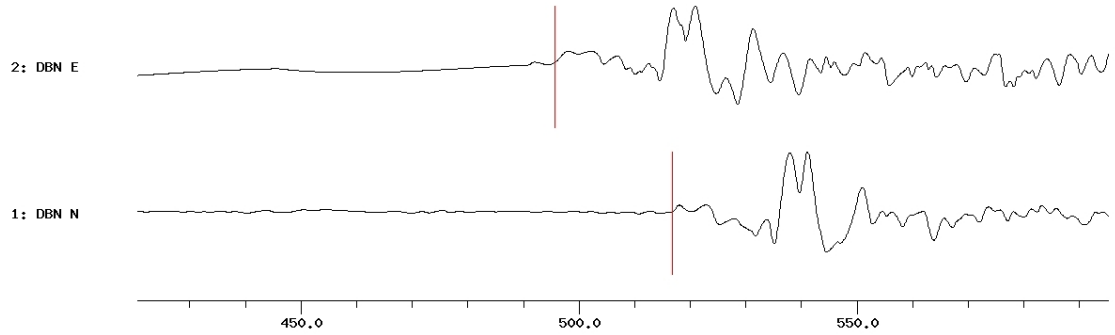

FIGURE B.6: Example of time disagreement of two horizontal components for the same station, the record is from DBN seismic station (Bosch-Omori instrument).

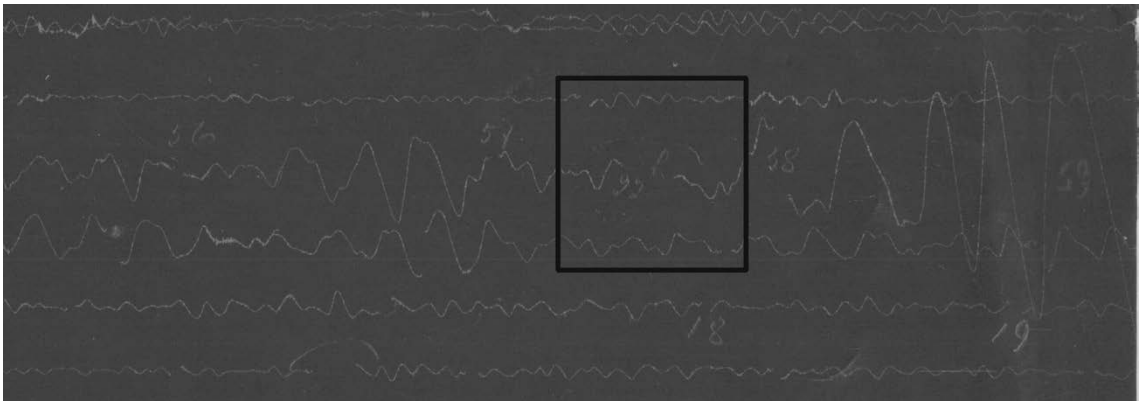

FIGURE B.7: Example of a big hour mark interrupting the waveform (the black square). The record is from API seismic station (Wiechert instrument, NS component).

B.4 Polarity issues

The amplitude ratio comparison method determines strike, dip and rake angles, but it would show the same misfit for normal and reverse faulting, so there would be two possible rake angles. The first motion polarities are very important in fixing the fault plane orientation in that case. The polarity of the arriving phase is sometimes hard to read on a historical record. But even if it is possible, the orientation of the instrument was not always marked on the paper seismogram, thus it is difficult to identify the direction of the recording system. This could mean that the paper sheet can be rotated 180° in both directions without any evidence of the preferred orientation, however the relative orientation of all three components with respect to each other is known. Using particle motion analysis the orientation of the all ZNE components with respect to each other can be constrained for both possible mechanisms, because the backazimuth direction of the P-wave is known. The comparison of relative polarities, estimated from particle motion analysis to the observed waveforms relative polarities from a three component station (e.g. station GTT), then constrains the true focal mechanism.

Appendix C

Additional information on focal mechanisms determination

In order to test the performance of focal mechanism determination using only amplitude ratios for the Chon-Kemin earthquake we run three tests on: a synthetic event and two modern earthquakes[1], where the focal mechanism is known. For the synthetics test an earthquake was simulated with certain mechanism and depth, keeping exactly the same source-receiver configuration as for the Chon-Kemin earthquake, the data were then convolved with corresponding instrument characteristics to reproduce the Chon-Kemin earthquake dataset. For two modern example earthquakes the station distribution was also reproduced as closely as possible to the Chon-Kemin earthquake, and the seismograms were modified by deconvolving the modern instrument characteristics and applying the corresponding historical instrument. For all three test earthquakes the synthetics were simulated in the same grid search procedure, with 10° degree spacing (to save the computation time), the observed and synthetic waveforms amplitude ratios were compared and the mechanism with the smallest misfit was determined.

C.1 Synthetic test

An earthquake with focal mechanism str/ dip/ rake= 280°/ 40°/ 100° and the depth of 26 km was simulated for the same source-receiver configuration as the Chon-Kemin earthquake. As a result of amplitude ratios comparison the focal mechanism was determined correctly (Figure *C.1*b) as well as the depth (Figure *C.1*c). The right side of the Figure *C.1* shows the misfit function dynamics for strike, dip and rake angle respectively, which shows a very obvious minimum for the true mechanism. The test showed that the mechanism of a synthetic earthquake can be successfully determined by amplitude comparison method as well as the depth of this earthquake.

C.2 Wenchuan Earthquake

The second test was performed for the Wenchuan earthquake which had a thrust mechanism and large magnitude [*Ekström et al.*, 2012; *Yagi et al.*, 2012; *USGS*, 2014c]. The Wenchuan earthquake (also known as Sichuan earthquake or the Great Sichuan Earthquake,) occurred on May 12, 2008

[1]This study does not aim to provide any analysis of those modern earthquakes, the earthquakes are just used as examples and the previous studies on those earthquakes are used as references.

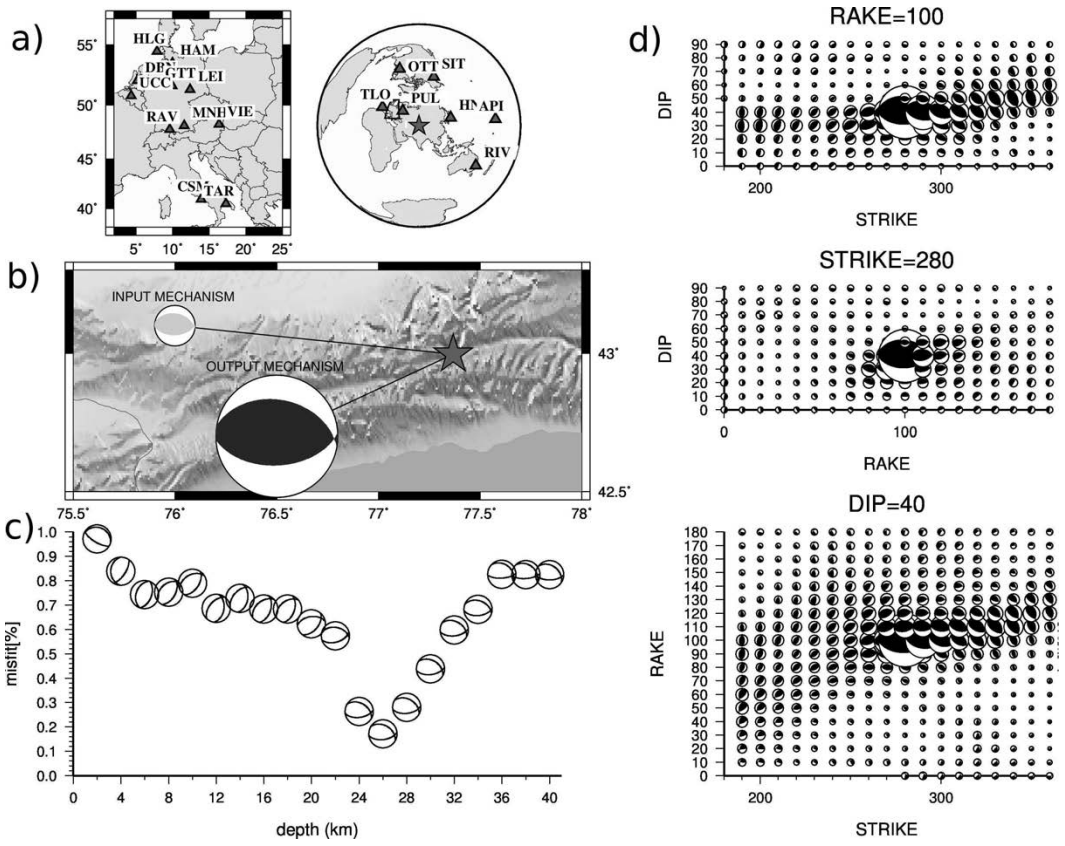

FIGURE C.1: The results of focal mechanism determination for the synthetic test earthquake based on the amplitude ratios comparison method. The upper left figure (a) shows the station distribution for all the stations used. The middle left figure (b) shows the tectonic map of the region; the epicentre is marked with the star; the grey beach ball shows the input focal mechanisms; the black beach ball shows the focal mechanism determined by the amplitude ratios comparison. The lower left plot (c) shows the misfit function dynamics depending on the depth of the earthquake, showing a clear minimum for the input depth 26 km. The three plots on the right side (d) represent the misfit function dynamics for the given rake, strike and dip accordingly

in Sichuan province, China, epicentre 30.986°N, 103.364°E [*USGS*, 2014c]. The earthquake had magnitude Mw7.9 [*USGS*, 2014c] and the focal mechanism of this earthquake according to *USGS* [2014c] is 238°/ 59°/ 128° or according to *Ekström et al.* [2012] 229°/ 33°/ 141°, the depth of the earthquake varies between 12 and 19 km in different studies [*Ekström et al.*, 2012; *Hwang et al.*, 2011; *Yagi et al.*, 2012; *USGS*, 2014c]. According to different studies the earthquake rupture length was between 210 [*Hwang et al.*, 2011] and 300 [*Yagi et al.*, 2012] km, and the source time duration between 70 [*Hwang et al.*, 2011] and 125 [*Yagi et al.*, 2012] seconds, although the exact numbers differ in different studies, but the range of these parameters remains the same and makes this earthquake comparable in size to the Chon-Kemin earthquake.

The focal mechanism determined with amplitude ratios comparison method for the Wenchuan earthquake (Figure *C.2*) was 250°/ 40°/ 140°, which is consistent with both *USGS* [2014c] and *Ekström et al.* [2012] solutions. The depth is likely to be between 16 and 26 km (corresponding to minimum misfit Figure *C.2*c), which is in a acceptable range for such a large earthquake and also consistent with other studies. The test for the Wenchuan earthquake confirms that the amplitude ratios comparison method can successfully determine the focal mechanism of a major thrust earthquake using teleseismic waveforms. The depth determination is less certain, but the range of appropriate depths can be constrained as well.

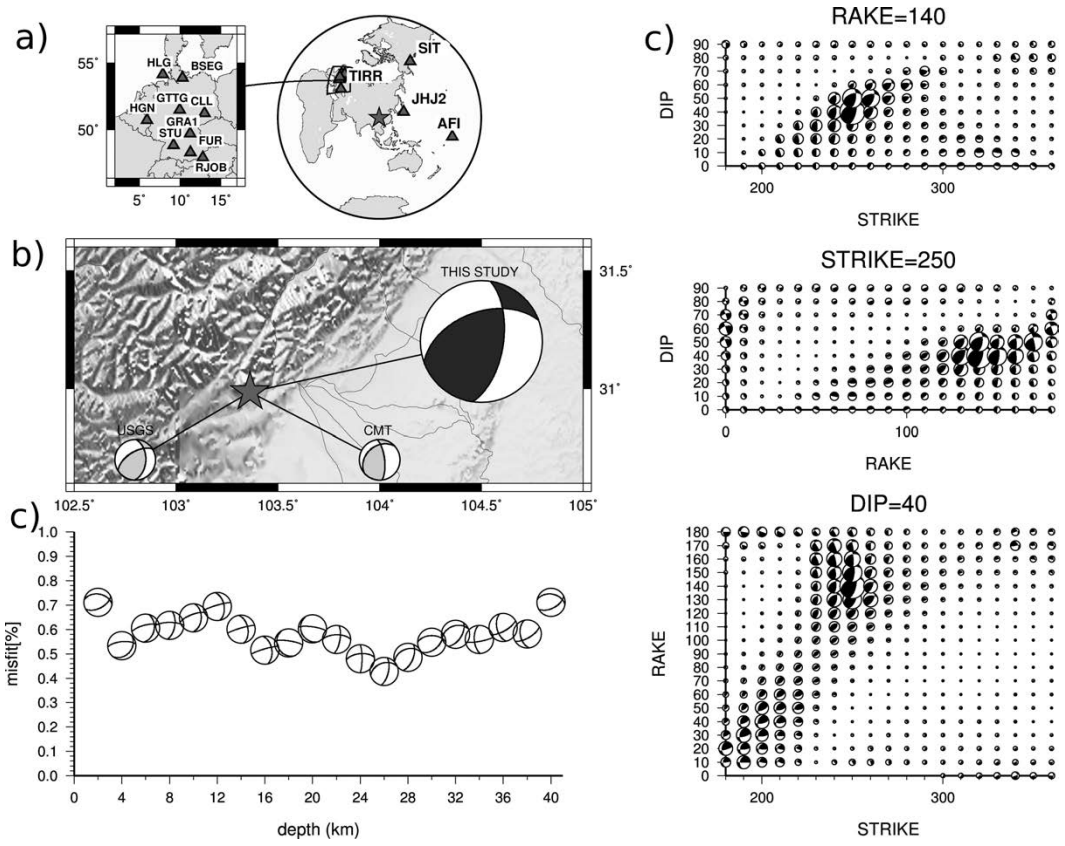

FIGURE C.2: The results of focal mechanism determination for the Wenchuan earthquake based on the amplitude ratios comparison method. The upper left figure (a) shows the station distribution for all the station, used. The middle left (b) is tectonic map of the region; the epicentre is marked with the star; the grey beach balls show the focal mechanisms determined *USGS* [2014c] and *Ekström et al.* [2012]; the black beach ball shows the focal mechanism determined in this study. The lower left plot shows the misfit function dynamics depending on the depth of the earthquake, showing a weak minimum for the depth between 16 and 26 km. The three plots on the right (d) side represent the misfit function dynamics for the given rake, strike and dip accordingly.

C.3 Balutchestan earthquake

The third test was performed for a strike slip earthquake with large magnitude. For this test we chose the Balutchestan earthquake which occurred in Pakistan on September 24, 2013. According to *USGS* [2014b] the earthquake's epicentre was located at 26.951°N 65.501°E, magnitude was Mw7.7 and the focal mechanism of this earthquake was 134° /86° /136° [*USGS*, 2014b] or 130° /87° /129° [*Ekström et al.*, 2012], the depth differs between 12 and 23 km [*USGS*, 2014b].

The focal mechanism obtained by amplitude ratios comparison (Figure *C.3*) was 140° /80° /120°, the minimum misfit is observed for the depth between 12 and 18 km, which is in a good agreement with the information reported by [*USGS*, 2014b] and [*Ekström et al.*, 2012]. This test also proves that the amplitude ratios comparison can be used to determine the focal mechanism of a major strike slip earthquake using the teleseismic data.

All three test have shown good performance of the amplitude ratios comparison method, for the synthetic test as well as for both real earthquakes. However from the misfit function distribution it is obvious that the method has uncertainties of about 10° in dip and rake and up to 20° in strike.

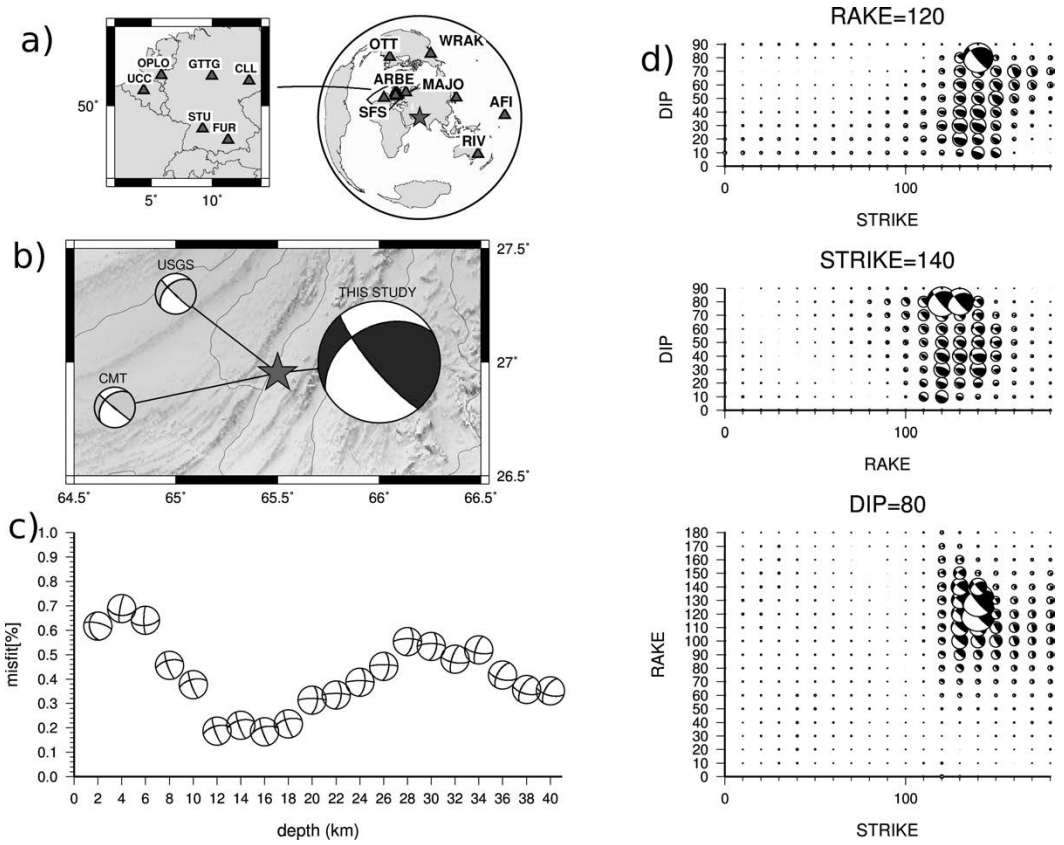

FIGURE C.3: The results of focal mechanism determination for the Pakistan earthquake based on the amplitude ratios comparison method. The upper left figure (a) shows the station distribution for the stations used. The middle left (b) is tectonic map of the region; the epicentre is marked with the star; the grey beach balls show the focal mechanisms determined *USGS* [2014b] and *Ekström et al.* [2012]; the black beach ball shows the focal mechanism determined in this study. The lower left plot (c) shows the misfit function dynamics depending on the depth of the earthquake, showing a minimum for the depth between 12 and 18 km. The three plots on the right side (d) represent the misfit function dynamics for the given rake, strike and dip accordingly.

Appendix D

The velocity model uncertainties estimation

The focal mechanisms of the earthquakes presented in this thesis are determined using the amplitude ratios comparison of the observed and synthetic waveforms. In order to estimate the performance of

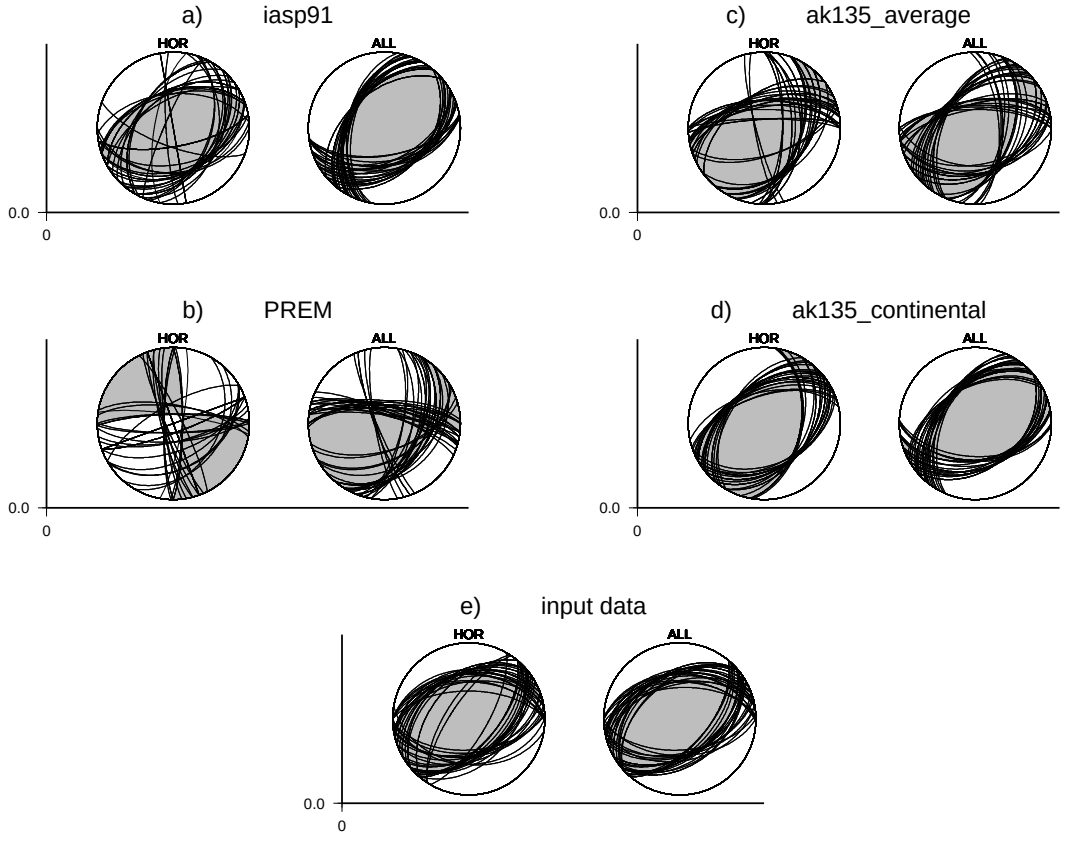

FIGURE D.1: Test of different global velocity models for the amplitude ratios comparison using: a)-d) the results for each velocity model named accordingly. HOR - shows the calculation using only horizontal components amplitude comparison, and ALL- stand for calculations using the amplitudes from all three components. e) – shows the results for the input data case, meaning that different velocity models are applied at the source and receiver sites, as it was done for the input data, therefore the misfit is 0.

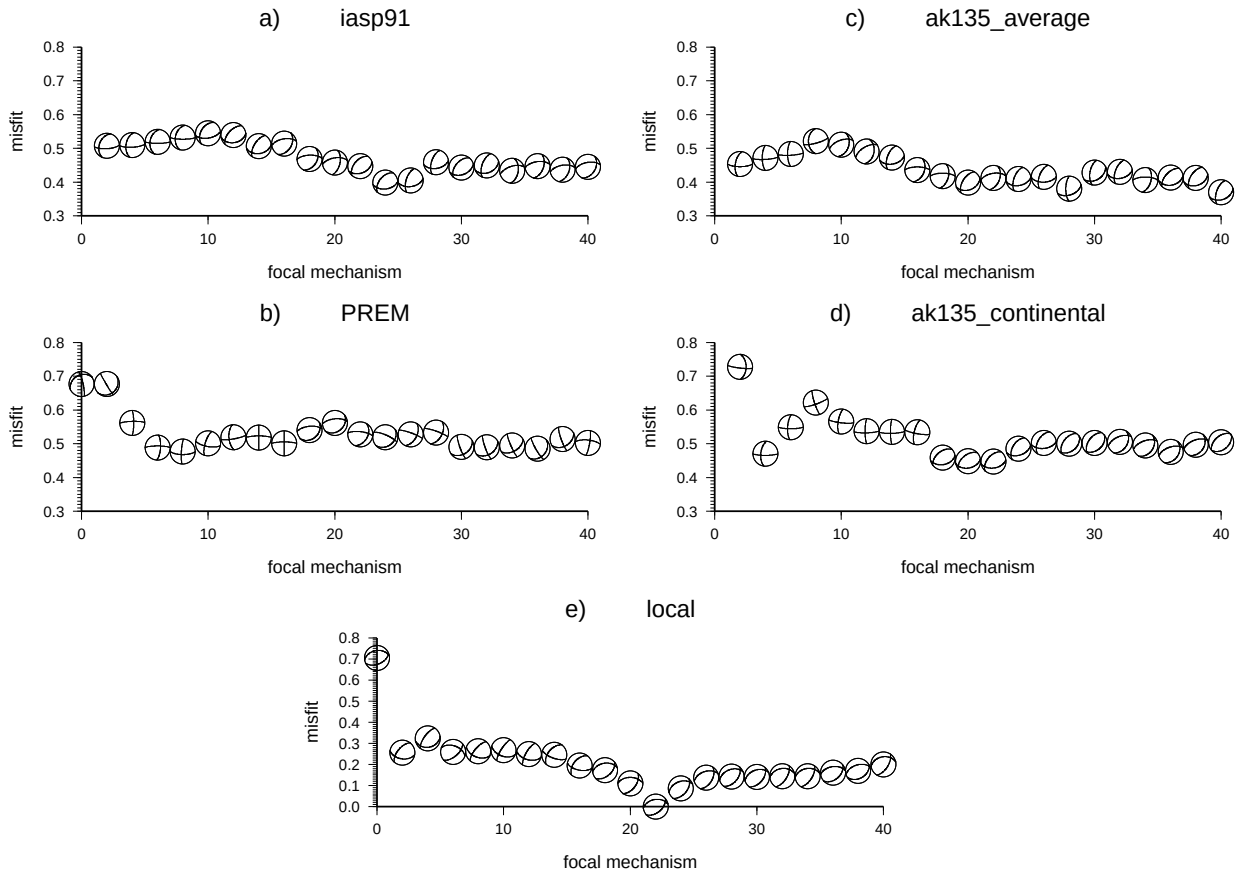

FIGURE D.2: Same as Figure *D.1*, but for different test depths

this method it is necessary to evaluate the uncertainties introduced by usage of global velocity model in the Greens functions calculation. To do that a synthetic test was set up. The waveforms for a synthetic earthquake are modeled with the following parameters: epicenter location at 42.0°N and 77°E, hypocenter depth 22 km and seismic moment $M_0 = 5.0 \cdot 10^{20}[Nm]$ (M_w7.3), and 50°/50°/70° strike, dip and rake resectively.

The modeling is done using QSEIS - code for calculating synthetic seismograms [*Wang*, 1999] with possibility to employ different shallow structures at source and receiver site. The velocity model suggested by *Alinaghi & Krüger* [2014] is used for the source site and AK135 [*Kennett et al.*, 1995] (continental) velocity model for the receiver site. Seismic waveforms, produced for the synthetic event, are then treated as the observed input data for determination of focal mechanism using amplitude rations comparison, as described in Chapter *2*.

In a grid search procedure the amplitude ratios are compared and minimum misfit is determined. Four different global velocity models PREM [*Dziewonski & Anderson*, 1981], IASPEI91 [*Kennett*, 1991], AK135 average and continental [*Kennett et al.*, 1995; *Bormann*, 2012] are tested, and the results are presented on the Figure *D.1*. Two different types of test are set up, first using only horizontal components (HOR Figure *D.1*) of the seismograms and second using all 3 components (ALL Figure *D.1*). This test is necessary since for early 1900s records vertical component is often not available. The best performance is shown by the AK135 continental and the IASPEI91 velocity models. The fault orientation is determined using first motion polarities to fix the rake angle.

The same test as described above is done for different depths. The minimum misfit for the correct 20±2 km depth is found using AK135 continental velocity model (Figure *D.2*d). The IASPEI91 model showed minimum misfit for 24-26 km depth (Figure *D.2*a), which is also close to the right value. However, overall misfit function dynamic with respect to depth is relatively low (Figure *D.2*).

The velocity model uncertainties estimation demonstrates that using the AK135 continental velocity model the mechanism of the earthquake can be determined with 10°/10°/10° uncertainties for the strike, dip, and rake respectively. The IASPEI91 velocity model has 10°/10°/30° uncertainties for the same parameters. These two velocity models perform best also for mechanism determination for different test depths, with slightly better result for the AK135. Based on this test the AK135 continental model is used as preferred in the focal mechanism determination procedure in the here presented study.

Appendix E

Additional data for different earthquakes

This appendix provides additional information and data for the earthquakes presented in Chapter *4*. The information is presented in tables. First table for each earthquake gives the arrival times for each phase used for epicenter location, and the amplitudes and the periods for m_B calculation. Additionally two tables are presented for each earthquake containing data for M_S and M_w determination. For the early earthquakes (1902 and 1907) the first table includes all the arrival times which were collected from the digitized waveforms and the bulletins. For later earthquakes (1938-1949) the tables are only showing the information from the waveforms. The bulletin information from *Storchak et al.* [2015] and other bulletins was also used to relocate these earthquakes, but it was not included in the tables presented here, because of being to long for a printed copy. The tables for two latest earthquakes (1970, 1978) are also excluded from this attachment for the same reason. This information can be provided electronically upon request.

E.1 1902 Kashgar earthquake

TABLE E.1: The station list with all arrival times for all the phases which were available for the 1902 Kashgar earthquake from the digitized waveforms and *Omori* [1907]. The table also includes distances and azimuths to all the stations, and the amplitude and period values where they are available. If the amplitude and the period columns are empty, it means either that the value is not available or, in case of the waveforms, it means that the true amplitude can not be read.

Station name	Distance[1]	Azimuth	Comp[2]	Phase	Arrival time	T[3]	Amp[4]	m_B	Source
Local bulletins									
TAS	4.888	267.05	-	P	03:02:12.000				
IRK	21.938	51.72	-	P	03:05:24.000				
BOM	22.931	187.23	-	P	03:05:24.000				
TIF	23.062	280.31	-	P	03:05:14.000				
NIKH	31.432	294.63	-	P	03:07:00.00				
KOD	31.437	176.82	-	P	03:04:48.000				
PAVL	32.981	318.55	-	P	03:07:48.000				
BUD	40.028	298.11	-	P	03:09:20.000				
TRI	43.999	297.03	-	P	03:08:17.000				
HAM	44.372	308.72	-	P	03:07:55.000				
PDI	45.599	290.34	-	P	03:10:05.00				
RDP	46.069	292.15	-	P	03:08:30.000				
CAT	46.083	285.74	-	P	03:08:59.000				
QCI	46.341	295.36	-	P	03:08:53.000				
OSA	46.644	78.24	-	P	03:09:04.00				
STR	46.996	302.64	-	P	03:08:00.00				
PAV	47.222	297.83	-	P	03:08:52.000				
MAN	47.449	110.97	-	P	03:09:04.00				
UCC	48.391	306.44	-	P	03:09:06.00				
EDI	51.024	314.71	-	P	03:09:30.000				
PAIH	51.701	314.92	-	P	03:10:10.000				
SHID	51.795	307.91	-	P	03:10:12.000				

DJA	55.51	141.52	-	P	03:09:54.000			
PER	82.106	146.48	-	P	03:13:36.000			
VCTH	88.59	12.63	-	P	03:10:00.00			
CTO	91.9	224.44	-	P	03:14:48.000			
TNT	92.079	342.25	-	P	03:25:48.000			
BALH	95.506	338.83	-	P	03:24:30.000			
SFDH	107.967	237.06	-	P	03:09:06.00			
CHR	121.348	122.27	-	P	03:20:36.000			
WEL	121.614	119.06	-	P	03:29:00.00			
CDIH	146.524	274.79	-	P	03:19:30.000			
LEI	44.5144	299.2	EW	P	03:07:53.448	4.7	30	7.6
LEI	44.5144	299.2	EW	PP	03:09:49.281	7.8	288	8.37
LEI	44.5144	299.2	EW	S	03:14:47.958	8	173	7.84
LEI	44.5144	299.2	EW	SS	03:18:36.395			-
HNG	49.259	74.86	NS	P	03:10:07.15	7.1	22	7.59
HNG	49.259	74.86	NS	PP	03:11:15.08	12.3	33	7.23
HNG	49.259	74.86	EW	S	03:17:04.77	9.2	109	7.77
LAI	43.389	297.25	EW	P	03:07:50.00			
LAI	43.389	297.25	EW	PP		9	48	7.53
LAI	43.389	297.25	NS	S		9	162	7.76
LAI	43.389	297.25	EW	SS				
Median								7.68 ± 0.3
Average								7.71 ± 0.3

TABLE E.2: The amplitudes (*Amp*) and the periods (T) for the surface waves recorded on three stations, read from, the waveforms, reports, and books [*Omori*, 1907; *Etzold*, 1903; *Voznesenskiy*, 1904]. The surface wave magnitude (3rd column) is calculated with Prague-Moscow formula [*Karnik et al.*, 1962] for each station and average magnitude M_s is presented with one standard deviation.

Station (Instrument)	T [sec]	Amp [μm]	Ms
IRK1 (Milne)	17	438	7.67
IRK2 (Bosch-Omori)	22	3750	8.47
HNG (Bosch-Omori)	18	734	7.81
Median			7.81 ± 0.4
Average			7.98 ± 0.4

TABLE E.3: Scalar moment and moment magnitude determination for the 1902 Kashgar earthquake

#	Station	M_0	M_w
1	LAI	2.02E+20	7.50
2	LEI	3.14E+20	7.63
3	HNG	4.41E+20	7.73
4	IRK1	5.17E+20	7.78
5	IRK2	9.83E+20	7.96
	Average	4.41±3.0E+20	7.73±0.2
	Median	4.91±3.0E+20	7.72±0.2

[1]Distance is given in degrees [deg]
[2]*Comp* stands for component on which the corresponding amplitude was measured
[3]T stands for period in seconds [sec], which corresponds to the measured amplitude
[4]*Amp* stands for amplitude value in micrometers [μm]

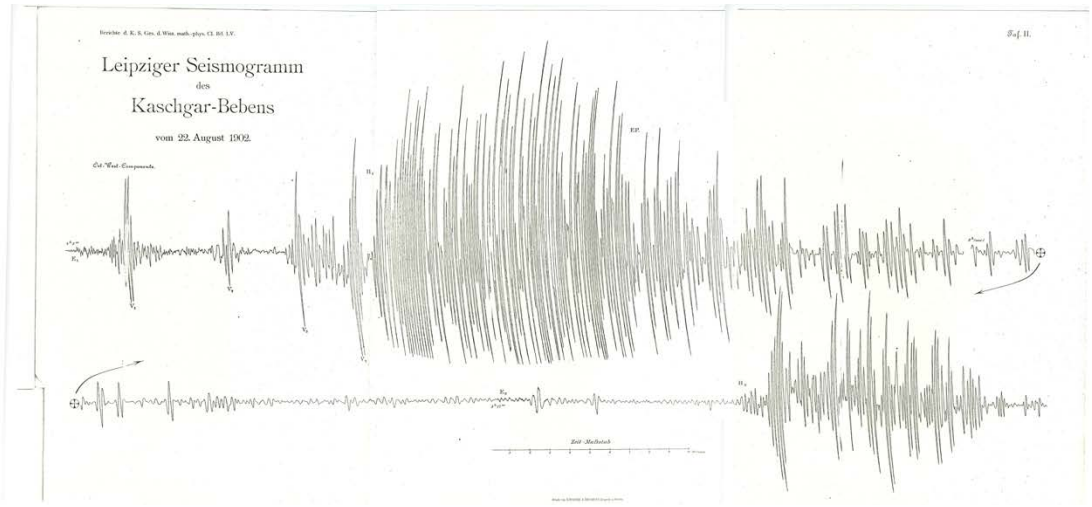

FIGURE E.1: Example of a seismogram reproduction for 1902 Kashgar earthquake, the record is from Leipzig seismic station in Germany, found in *Etzold* [1903].

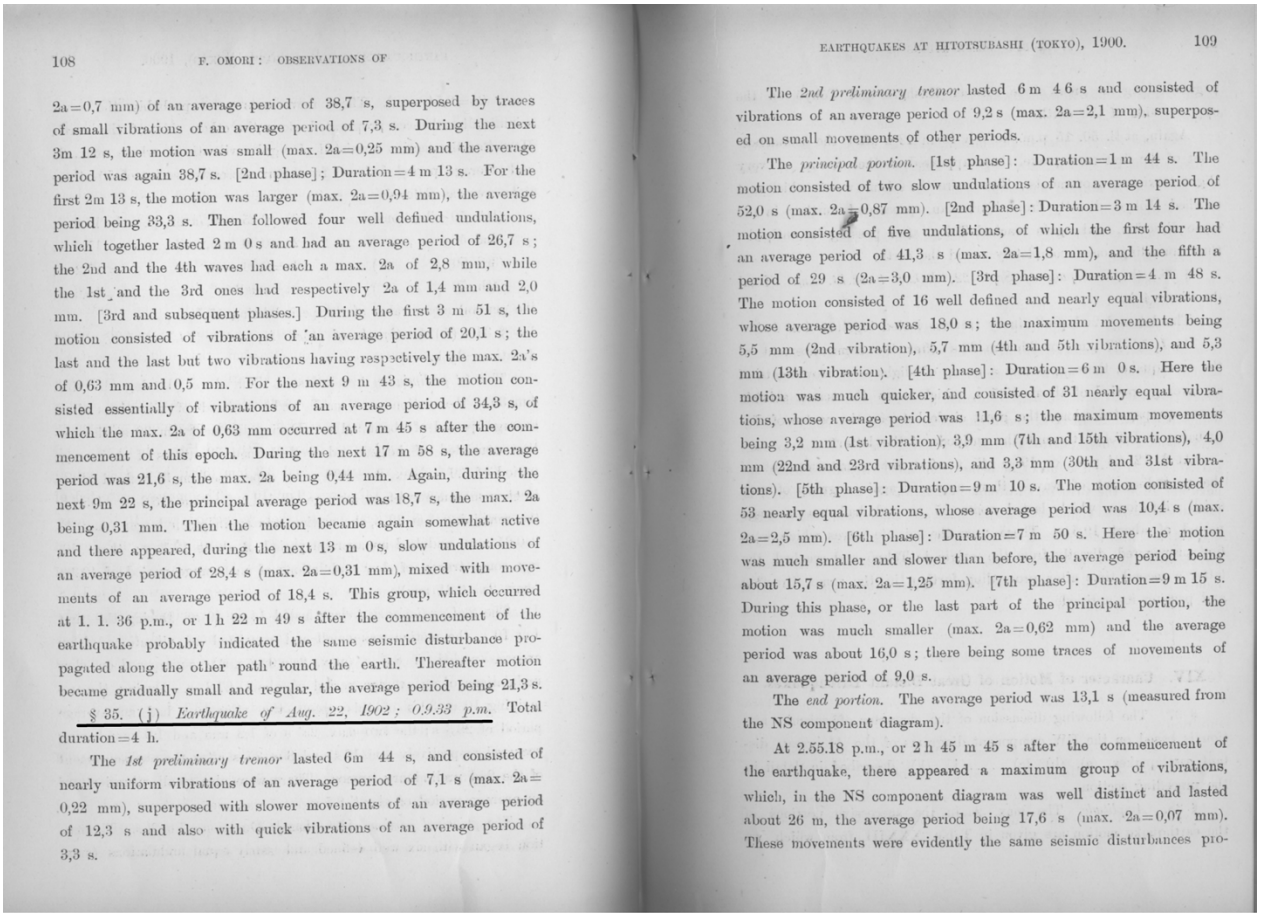

108 F. OMORI: OBSERVATIONS OF

2a=0,7 mm) of an average period of 38,7 s, superposed by traces of small vibrations of an average period of 7,3 s. During the next 3m 12 s, the motion was small (max. 2a=0,25 mm) and the average period was again 38,7 s. [2nd phase]; Duration=4 m 13 s. For the first 2m 13 s, the motion was larger (max. 2a=0,94 mm), the average period being 33,3 s. Then followed four well defined undulations, which together lasted 2 m 0 s and had an average period of 26,7 s; the 2nd and the 4th waves had each a max. 2a of 2,8 mm, while the 1st and the 3rd ones had respectively 2a of 1,4 mm and 2,0 mm. [3rd and subsequent phases.] During the first 3 m 51 s, the motion consisted of vibrations of an average period of 20,1 s; the last and the last but two vibrations having respectively the max. 2a's of 0,63 mm and 0,5 mm. For the next 9 m 43 s, the motion consisted essentially of vibrations of an average period of 34,3 s, of which the max. 2a of 0,63 mm occurred at 7 m 45 s after the commencement of this epoch. During the next 17 m 58 s, the average period was 21,6 s, the max. 2a being 0,44 mm. Again, during the next 9m 22 s, the principal average period was 18,7 s, the max. 2a being 0,31 mm. Then the motion became again somewhat active and there appeared, during the next 13 m 0 s, slow undulations of an average period of 28,4 s (max. 2a=0,31 mm), mixed with movements of an average period of 18,4 s. This group, which occurred at 1. 1. 36 p.m., or 1 h 22 m 49 s after the commencement of the earthquake probably indicated the same seismic disturbance propagated along the other path round the earth. Thereafter motion became gradually small and regular, the average period being 21,3 s.

§ 35. (j) *Earthquake of Aug. 22, 1902; 0.9.33 p.m.* Total duration=4 h.

The *1st preliminary tremor* lasted 6m 44 s, and consisted of nearly uniform vibrations of an average period of 7,1 s (max. 2a=0,22 mm), superposed with slower movements of an average period of 12,3 s and also with quick vibrations of an average period of 3,3 s.

EARTHQUAKES AT HITOTSUBASHI (TOKYO), 1900. 109

The *2nd preliminary tremor* lasted 6 m 46 s and consisted of vibrations of an average period of 9,2 s (max. 2a=2,1 mm), superposed on small movements of other periods.

The *principal portion.* [1st phase]: Duration=1 m 44 s. The motion consisted of two slow undulations of an average period of 52,0 s (max. 2a=0,87 mm). [2nd phase]: Duration=3 m 14 s. The motion consisted of five undulations, of which the first four had an average period of 41,3 s (max. 2a=1,8 mm), and the fifth a period of 29 s (2a=3,0 mm). [3rd phase]: Duration=4 m 48 s. The motion consisted of 16 well defined and nearly equal vibrations, whose average period was 18,0 s; the maximum movements being 5,5 mm (2nd vibration), 5,7 mm (4th and 5th vibrations), and 5,3 mm (13th vibration). [4th phase]: Duration=6 m 0 s. Here the motion was much quicker, and consisted of 31 nearly equal vibrations, whose average period was 11,6 s; the maximum movements being 3,2 mm (1st vibration), 3,9 mm (7th and 15th vibrations), 4,0 mm (22nd and 23rd vibrations), and 3,3 mm (30th and 31st vibrations). [5th phase]: Duration=9 m 10 s. The motion consisted of 53 nearly equal vibrations, whose average period was 10,4 s (max. 2a=2,5 mm). [6th phase]: Duration=7 m 50 s. Here the motion was much smaller and slower than before, the average period being about 15,7 s (max. 2a=1,25 mm). [7th phase]: Duration=9 m 15 s. During this phase, or the last part of the principal portion, the motion was much smaller (max. 2a=0,62 mm) and the average period was about 16,0 s; there being some traces of movements of an average period of 9,0 s.

The *end portion.* The average period was 13,1 s (measured from the NS component diagram).

At 2.55.18 p.m., or 2 h 45 m 45 s after the commencement of the earthquake, there appeared a maximum group of vibrations, which, in the NS component diagram was well distinct and lasted about 26 m, the average period being 17,6 s (max. 2a=0,07 mm). These movements were evidently the same seismic disturbances pro-

FIGURE E.2: Example of an earthquake description found in *Omori* [1903] book for the 1902 Kashgar earthquake from station in Tokyo, Japan.

E.2 1907 Karatag earthquake

TABLE E.4: The station list with all arrival times for all the phases which were available for the 1907 Karatag earthquake from the digitized waveforms. The table also includes distances and azimuths to all the station, and the amplitude and period values where they were available. If amplitude and period columns it means that the true amplitude can not be read.

Station name	Distance	Azimuth	Comp	Phase	Arrival time	T	Amp	m_B	Source
Local bulletins									
TAS	2.055	324.79			04:24:18				
IRK	26.163	50.15			04:29:18				
IRK	26.163	50.15			04:33:30				
BUD	37.763	299.43			04:31:12				
BUD	37.763	299.43			04:37:02				
UPP	38.566	319.57			04:31:06				
UPP	38.566	319.57			04:37:07				
VIE	39.433	301.04			04:30:40				
VIE	39.433	301.04			04:36:52				
ZAG	40.103	297.37			04:31:26				
GRA	40.23	299.39			04:31:20				
GRA	40.23	299.39			04:36:38				
ZKW	41.602	85.53			04:31:34				
ZKW	41.602	85.53			04:38:12				
PAD	42.998	297.72			04:31:37				
PAD	42.998	297.72			04:38:00				
RDP	43.405	292.35			04:31:29				
RDP	43.405	292.35			04:38:13				
STR	44.998	303.11			04:31:56				
STR	44.998	303.11			04:38:43				
MAN	50.354	105.02			04:33:06				
MAN	50.354	105.02			04:40:30				
OSA	50.775	74.04			04:33:13				
OSA	50.775	74.04			04:40:42				
MIZ	52.967	66.5			04:33:19				
DJA	56.411	135.49			04:33:24				
DJA	56.411	135.49			04:41:24				
SIT	81.149	14.13			04:36:22				
PER	82.558	142.71			04:37:00				
CTO	87.819	221.24			04:37:00				
OTT	90.173	337.17			04:37:00				
GTT	43.04	306.92	EW	P	04:31:40	6	34.60	7.26	
GTT	43.04	306.92	EW	PP	04:33:21	8	49.42	7.49	
GTT	43.04	306.92	EW	S	04:38:13	13	95.05	7.37	
GTT	43.04	306.92	EW	SS	04:38:13	32	75.00	-	
HAM	42.805	309.72	Z	P	04:31:43	7	88.46	7.80	
HAM	42.805	309.72	Z	PP	04:38:15	12	207.69	8.04	
HAM	42.805	309.72	EW	S	04:31:43	16	165.38	7.51	
HAM	42.805	309.72	EW	SS	04:38:15	-	-		
MNH	42.588	301.72	Z	P	04:31:33				
MNH	42.588	301.72	Z	PP	04:37:58				
MNH	42.588	301.72	EW	S	04:31:33				
MNH	42.588	301.72	EW	SS	04:37:58				
POT	41.03	307.8	Z	P	04:31:24	12	56	7.37	
POT	41.03	307.8	Z	PP	04:37:47				
POT	41.03	307.8	EW	S	04:31:24	24	220	7.56	
POT	41.03	307.8	EW	SS	04:37:47				
LEI	41.565	306.29	EW	P	04:31:28	6	48.73	7.61	
LEI	41.565	306.29	EW	PP	04:37:23	10	117.54	7.77	
LEI	41.565	306.29	EW	S	04:31:28	10	58.08	7.36	
LEI	41.565	306.29	EW	SS	04:37:23	-	-	-	
JEN	42.121	305.83	EW	P	04:31:35	12	48.5	7.45	
JEN	42.121	305.83	EW	PP	04:38:00				
JEN	42.121	305.83	EW	S	04:31:35	24	89.5	7.31	
JEN	42.121	305.83	EW	SS	04:38:00	-	-	-	
HNG	53.812	70.48	Z	P	04:33:13.00	12	50.00	7.32	
HNG	53.812	70.48	Z	PP	04:35:15.00				
HNG	53.812	70.48	NS	S	04:40:42.00	18	130.00	7.46	
HNG	53.812	70.48	NS	SS	04:44:12.00				
Median								7.50 ± 0.3	
Average								7.53 ± 0.3	

TABLE E.5: The amplitudes (*Amp*) and the periods (T) of the surface waves of the 1907 Karatag earthquake. The surface wave magnitude (3rd column) is calculated with Prague-Moscow formula [*Karnik et al.*, 1962] for each station and average magnitude M_s is presented with one standard deviation.

Station (Instrument)	T [sec]	Amp [μm]	Ms	
1	GTT	16	246.976	7.41
2	LEI	17	596.000	7.75
3	MNH	18	421.488	7.58
4	HAM	19	536.000	7.67
5	POT	19	198.000	7.21
6	JEN	18	397.000	7.55
7	HNG	22	446.000	7.63
Median			7.58 $\pm$0.2	
Average			7.54 $\pm$0.2	

TABLE E.6: Scalar moment and moment magnitude determination for the 1907 Karatag earthquake

#	Station	M_0	M_w
1	GTT	2.14E+27	7.58
2	LEI	8.96E+26	7.39
3	MNH	3.55E+27	7.58
4	HAM	3.20E+27	7.50
5	POT	3.18E+26	7.62
6	JEN	1.69E+27	7.77
7	HNG	1.14E+27	7.66
	Average	1.85$\pm$2.0E+20	7.48$\pm$0.2
	Median	1.69$\pm$2.0E+20	7.45$\pm$0.2

E.3 1938 Kemin-Chu earthquake

TABLE E.7: The station list with all arrival times for all the phases which were available for the 1938 Kemin-Chu earthquake from the digitized waveforms. The table also includes distances and azimuths to all the station, and the amplitude and period values where they were available. If amplitude and period columns it means that the true amplitude can not be read.

Station name	Distance	Azimuth	Comp	Phase	Arrival time	T	Amp	m_B	Source
Local bulletins									
HAM	43.721	307.83	Z	P	23:58:36.750	2	15.5	7.4	
HAM	43.721	307.83	Z	PP	00:00:21.820	5	29.4	7.5	
HAM	43.721	307.83	NS	P	23:58:36.750	2.5	15.2	7.5	
HAM	43.721	307.83	NS	PP	00:00:21.820	5	25.8	7.5	
HAM	43.721	307.83	NS	S	00:05:10.060	7	23.7	7.0	
HAM	43.721	307.83	NS	SS	00:08:28.29	-	-	-	
HAM	43.721	307.83	EW	P	23:58:36.750	5	15.8	7.2	
HAM	43.721	307.83	EW	PP	00:00:21.820	5	39.3	7.7	
HAM	43.721	307.83	EW	S	00:05:10.060	7	15.3	6.8	
HAM	43.721	307.83	EW	SS	00:08:28.29	-	-	6.8	
GTT	44.187	305.15	EW	P	23:59:01.72	3	5.8	-	
GTT	44.187	305.15	EW	PP	00:00:54.76	5.6	15.3	7.2	
GTT	44.187	305.15	EW	S	00:05:44.05	9.1	9.7	6.5	
GTT	44.187	305.15	EW	SS	00:09:00.95	-	-	-	
GTT	44.187	305.15	NS	P	23:59:01.72	5.3	3.6	6.5	
GTT	44.187	305.15	NS	PP	00:00:54.76	5.9	3.7	6.6	
GTT	44.187	305.15	NS	S	00:05:44.05	7.5	5.6	6.4	
GTT	44.187	305.15	NS	SS	00:09:00.95	-	-	-	
LEI	42.775	304.28	EW	P	23:58:29.41	3.1	3.0	6.7	

LEI	42.775	304.28	EW	PP	00:00:12.59	10.2	14.7	7.0
LEI	42.775	304.28	EW	S	00:04:55.92	8.8	10.8	6.6
LEI	42.775	304.28	EW	SS	00:07:55.97	-	-	-
LEI	42.775	304.28	NS	P	23:58:29.41	6.1	2.8	6.4
LEI	42.775	304.28	NS	PP	00:00:12.59	4.55	3.1	6.6
LEI	42.775	304.28	NS	S	00:04:55.92	7.9	5.0	6.3
LEI	42.775	304.28	NS	SS	00:07:55.97	-	-	-
BER	44.751	318.31	EW	P	23:58:48.78	4.3	8.0	7.0
BER	44.751	318.31	EW	PP	00:00:33.54	5.6	17.6	7.3
BER	44.751	318.31	EW	S	00:05:26.48	7	17.1	6.9
BER	44.751	318.31	EW	SS	00:08:32.19	-	-	-
BER	44.751	318.31	NS	P	23:58:48.78	4.8	3.1	6.5
BER	44.751	318.31	NS	PP	00:00:33.54	7	4.3	6.6
BER	44.751	318.31	NS	S	00:05:26.48	7.8	7.7	6.5
BER	44.751	318.31	NS	SS	00:08:32.19	-	-	-
BER	44.751	318.31	Z	P	23:58:48.78	2.4	28.2	7.6
BER	44.751	318.31	Z	PP	00:00:33.54	3.2	22.0	7.5
ZAG	42.029	295.43	EW	P	23:58:22.98	3.2	13.5	7.3
ZAG	42.029	295.43	EW	PP	23:59:59.45	5.7	32.4	7.6
ZAG	42.029	295.43	EW	S	00:04:44.82	9	12.5	6.6
ZAG	42.029	295.43	EW	SS	00:07:42.02	-	-	-
ZAG	42.029	295.43	NS	P	23:58:22.98	2.1	7.9	7.3
ZAG	42.029	295.43	NS	PP	23:59:59.45	4.9	10.3	7.1
ZAG	42.029	295.43	NS	S	00:04:44.82	9	9.4	6.5
ZAG	42.029	295.43	NS	SS	00:07:42.02	-	-	-
ZAG	42.029	295.43	Z	P	23:58:22.98	2.7	9.6	7.0
ZAG	42.029	295.43	Z	PP	23:59:59.45	3.8	13.9	7.3
TLO	57.834	296.48	EW	P	00:00:26.71	9	5.0	6.4
TLO	57.834	296.48	EW	PP	00:02:34.37	9	6.3	6.6
TLO	57.834	296.48	EW	S	00:08:23.39	12	7.3	6.3
TLO	57.834	296.48	EW	SS	00:12:17.29	-	-	-
TLO	57.834	296.48	NS	P	00:00:26.71	9	2.6	6.2
TLO	57.834	296.48	NS	PP	00:02:34.37	9	3.0	6.3
TLO	57.834	296.48	NS	S	00:08:23.39	12	4.8	6.1
TLO	57.834	296.48	NS	SS	00:12:17.29	-	-	-
TLO	57.834	296.48	Z	P	00:00:26.71	3	5.4	6.8
TLO	57.834	296.48	Z	PP	00:02:34.37	3	2.0	6.5
Median								6.87 ± 0.4
Average								6.80 ± 0.4

TABLE E.8: The amplitudes (*Amp*) and the periods (T) of the surface waves of the 1938 Kemin-Chu earthquake. The surface wave magnitude (3rd column) is calculated with Prague-Moscow formula [*Karnik et al.*, 1962] for each station and average magnitude M_s is presented with one standard deviation.

Station (Instrument)	T [sec]	Amp [μm]	Ms	
1	HAM	25	209	7.15
2	GTT	21	163	7.12
3	LEI	20	85	6.85
4	BER	19	337	7.48
5	ZAG	20	78	6.80
6	TLO	19	82	6.99
Median			7.06 ±0.3	
Average			7.06 ±0.3	

TABLE E.9: Scalar moment and moment magnitude determination for the 1938 Kemin-Chu earthquake

#	Station	M_0	M_w
1	HAM	6.84E+26	7.16
2	GTT	1.30E+26	6.68
3	LEI	2.64E+26	6.88
4	BER	4.71E+26	7.05
5	ZAG	3.71E+26	6.98
6	TLO	1.85E+26	6.78

Average	3.17±2.0E+19	6.94±0.2
Median	2.90±2.0E+19	6.91±0.2

E.4 1946 Chatkal earthquake

TABLE E.10: The station list with all arrival times for all the phases which were available for the 1946 Chatkal earthquake from the digitized waveforms. The table also includes distances and azimuths to all the station, and the amplitude and period values where they were available. If amplitude and period columns it means that the true amplitude can not be read.

Station name	Distance	Azimuth	Comp	Phase	Arrival time	T	Amp	m_B	Source
Local bulletins									
ABU	49.456	75.974	Z	P	18:37:11.55	7	11.35	7.36	
ABU	49.456	75.974	Z	PP	18:39:02.69	9	8.40	6.82	
ABU	49.456	75.974	NS	S	18:44:27.16	8	42.86	7.33	
ABU	49.456	75.974	NS	SS	18:47:36.60	8	82.86	-	
GTT	42.407	305.249	Z	P	18:36:18.0	5	19.00	7.48	
GTT	42.407	305.249	EW	PP	18:37:59.0	5	45.00	7.75	
GTT	42.407	305.249	EW	S	18:42:38.0	7	66.00	7.47	
GTT	42.407	305.249	EW	SS	18:47:01.0	9	68.00	-	
HUA	138.820	306.377	Z	Pdiff	18:48:03.0	12	7.50	6.80	
HUA	138.820	306.377	Z	PP	18:50:49.0	15	54.12	7.56	
HUA	138.820	306.377	NS	S	19:09:17.0	16	48.24	7.78	
DBN	45.175	306.999	Z	P	18:36:39.34	8.5	25	7.37	
DBN	45.175	306.999	Z	PP	18:38:27.95	8.5	37	7.44	
DBN	45.175	306.999	EW	S	18:43:07.79	8.5	50	7.27	
DBN	45.175	306.999	EW	SS	18:46:27.42	9	66	-	
TRS	41.390	295.755	Z	P	18:36:08.89	2.2	88	8.11	
TRS	41.390	295.755	Z	PP	18:37:42.80	5.9	48	7.41	
TRS	41.390	295.755	EW	S	18:41:57.13	5	71	7.75	
TRS	41.390	295.755	EW	SS	18:45:09.72	6	76	-	
NEC	45.496	299.647	Z	P	18:36:50.0	4	14	7.44	
NEC	45.496	299.647	Z	PP	18:38:38.0	4	24	7.58	
NEC	45.496	299.647	EW	S	18:43:45.0	6	67	7.55	
NEC	45.496	299.647	EW	SS	18:46:47.42	6	74	-	
BAS	44.926	300.193	Z	P	18:36:46.0	7	43	7.69	
BAS	44.926	300.193	Z	PP	18:38:40.0	9	34	7.38	
BAS	44.926	300.193	EW	S	18:43:18.0	10	97	7.49	
COL	69.280	16.940	Z	P	18:39:30.40	9	15	7.62	
COL	69.280	16.940	Z	PP	18:42:02.83	10	17	7.44	
COL	69.280	16.940	NS	S	18:48:16.77	15	46	7.38	
COL	69.280	16.940	NS	SS	18:53:02.53	17	49	-	
PAS	103.918	8.556	Z	P	18:42:20.74	10	5	7.32	
PAS	103.918	8.556	Z	PP	18:46:30.85	7	17	7.67	
PAS	103.918	8.556	NS	S	18:53:50.69	14	24	7.53	
PAS	103.918	8.556	NS	SS	19:01:29.69	16	35	-	
JEN	41.530	304.100	Z	P	18:39:16.00	4.0	34	7.43	
JEN	41.530	304.100	Z	PP	18:41:06.00	4.5	37	7.41	
JEN	41.530	304.100	EW	S	18:45:49.00	7	55	7.41	
JEN	41.530	304.100	EW	SS	18:48:59.00	7	54	-	
Median								7.44 ± 0.3	
Average								7.47 ± 0.3	

TABLE E.11: The amplitudes (*Amp*) and the periods (T) of the surface waves of the 1946 Chatkal earthquake. The surface wave magnitude (3rd column) is calculated with Prague-Moscow formula [*Karnik et al.*, 1962] for each station and average magnitude M_s is presented with one standard deviation.

Station (Instrument)	T [sec]	Amp [μm]	Ms

1	ABU	19	278.09	7.45
2	PAS	25	126.62	7.34
3	COL	19	295.94	7.64
4	DBN	18	604.57	7.77
5	GTT	18	441.33	7.60
6	JEN	18	283.98	7.40
7	NEC	18	289.96	7.45
8	BAS	20	447.27	7.59
9	HUA	22	269.44	7.86
Median			7.59 ±0.2	
Average			7.56 ±0.2	

TABLE E.12: Scalar moment and moment magnitude determination for the 1946 Chatkal earthquake

#	Station	M_0	M_w
1	JEN	2.62E+27	7.58
2	ABU	1.37E+27	7.39
3	GTT	2.66E+27	7.58
4	HUA	1.99E+27	7.50
5	DBN	2.98E+27	7.62
6	TRS	4.99E+27	7.77
7	NEC	3.41E+27	7.66
8	BAS	2.18E+27	7.53
9	COL	2.42E+27	7.56
10	PAS	3.25E+27	7.64
	Average	2.79±2.0E+20	7.60±0.2
	Median	2.64±2.0E+20	7.58±0.2

E.5 1949 Khait earthquake

TABLE E.13: The station list with all arrival times for all the phases which were available for the 1949 Khait earthquake from the digitized waveforms. The table also includes distances and azimuths to all the station, and the amplitude and period values where they were available. If amplitude and period columns it means that the true amplitude can not be read.

Station name	Distance	Azimuth	Comp	Phase	Arrival time	T	Amp	m_B	Source
Local bulletins									
BER	45.283	320.178	Z	P	04:01:56.0	3	22.02	7.57	
BER	45.283	320.178	Z	PP	04:03:19.0	3	37.59	7.80	
BER	45.283	320.178	EW	S	04:08:36.0	9	107.00	7.58	
BER	45.283	320.178	EW	SS	04:08:39.0	-	-	-	
DBN	46.333	308.839	Z	P	04:02:02.0	3	17.14	7.56	
DBN	46.333	308.839	Z	PP	04:03:50.0	5	21.36	7.33	
DBN	46.333	308.839	EW	S	04:08:54.0	5	30.57	7.39	
DBN	46.333	308.839	EW	SS	04:12:44.0	-	-	-	
ROM	44.052	292.756	Z	P	04:01:41.0	5	59.47	7.58	
ROM	44.052	292.756	Z	PP	04:03:05.0	5	32.47	7.51	
ROM	44.052	292.756	EW	S	04:08:19.0	12	253.00	7.92	
HUA	139.672	302.663	Z	Pdiff	04:13:04.0	9	21.00	7.37	
HUA	139.672	302.663	EW	PP	04:16:04.0	10	27.00	7.43	
HUA	139.672	302.663	EW	SS	04:20:32.0	12	54.00	7.95	
PAD	43.613	298.125	Z	P	04:01:35.00	3	25.00	7.42	
PAD	43.613	298.125	Z	PP	04:03:26.00	6	39.00	7.41	
PAD	43.613	298.125	EW	S	04:03:26.00	6	167.00	7.94	
PAS	106.708	7.851	Z	P	04:07:58.00	5	4.08	7.71	
PAS	106.708	7.851	Z	PP	04:12:09.00	5	19.45	7.99	
PAS	106.708	7.851	NS	S	04:18:28.00	5	44.12	8.15	
HAM	43.183	310.326	Z	P	04:01:48.00	5	51.00	7.51	
HAM	43.183	310.326	Z	PP	04:03:38.00	5	59.00	7.67	

HAM	43.183	310.326	EW	S	04:08:28.00	8	102.00	7.61
LEI	41.963	306.812	Z	P	04:01:24.00	4	48.00	7.58
LEI	41.963	306.812	Z	PP	04:03:04.00	5	78.00	7.69
LEI	41.963	306.812	EW	S	04:07:45.00	7	94.00	7.63
GTT	43.444	307.416	Z	P	04:01:32.00	4	45.00	7.55
GTT	43.444	307.416	Z	PP	04:03:16.00	7	65.00	7.57
GTT	43.444	307.416	EW	S	04:03:16.00	9	87.00	7.49
TLO	56.222	296.554	Z	P	04:03:17.00	5	13.00	7.21
TLO	56.222	296.554	Z	PP	04:04:09.00	5	23.00	7.56
TLO	56.222	296.554	EW	S	04:11:06.00	6	45.00	7.48
COL	72.026	16.328	Z	P	04:04:58.00	9	34.00	7.48
COL	72.026	16.328	Z	PP	04:07:39.00	12	41.00	7.63
COL	72.026	16.328	NS	S	04:14:21.00	15	65.00	7.64
ABU	50.812	73.406	Z	P	04:02:43.00	9	56.00	7.49
ABU	50.812	73.406	Z	PP	04:04:22.00	12	59.00	7.39
ABU	50.812	73.406	NS	S	04:10:04.00	16	98.00	7.39
Median								7.56 ± 0.2
Average								7.59 ± 0.2

TABLE E.14: The amplitudes (*Amp*) and the periods (T) of the surface waves of the 1949 Khait earthquake. The surface wave magnitude (3rd column) is calculated with Prague-Moscow formula [*Karnik et al.*, 1962] for each station and average magnitude M_s is presented with one standard deviation.

Station (Instrument)	T [sec]	Amp [μm]	Ms	
1	BER	16	623	7.83
2	DBN	16	282	7.50
3	ROM	19	647	7.76
4	HUA	27	86	7.28
5	PAS	25	145	7.41
6	HAM	19	600	7.72
7	LEI	16	617	7.79
8	GTT	18	1223	8.05
9	COL	25	588	7.83
10	ABU	22	1083	7.99
Median			7.77 ±0.2	
Average			7.72 ±0.2	

TABLE E.15: Scalar moment and moment magnitude determination for the 1949 Khait earthquake

#	Station	M_0	M_w
1	BER	2.00E+27	7.50
2	DBN	5.72E+27	7.80
3	ROM	2.14E+27	7.52
4	HUA	1.05E+28	7.98
5	PAD	5.68E+27	7.80
6	PAS	2.01E+27	7.50
7	HAM	1.93E+27	7.49
8	LEI	1.24E+27	7.36
9	GTT	1.76E+27	7.46
10	TLO	4.89E+27	7.76
11	COL	5.20E+27	7.78
12	ABU	4.23E+27	7.72
	Average	3.19±2.5E+20	7.64±0.2
	Median	3.95±2.5E+20	7.70±0.2

Appendix F

Contact information

TABLE F.1: The contact information of the institutions which provided historical analog seismic records for this study.

#	Institution	Contact Person	Seismograms recieved via
1	Institute of Geophysics, University of Göttingen	Mr. Manfred Herden	Received by post, scanned in Potsdam and sent back
2	Indonesian Agency for Meteorology, Climatology and Geophysics, Jakarta Indonesia	Dr. Muzli	Photographed in Indonesia and brought to Potsdam by Dr. Muksin
3	INGV Rome, Italy	Silvia Filosa Dr Graziano Ferrari	Provided scanned copies of the seismograms via ftp server
4	USCS, Golden Colorado (The microfilms archive)	Dr. James Dewey	Personal travel to the institution archive Scanning facilities are evaluable in situ
5	Institute of Geophysics, University of Hamburg	Prof. Dr. Torsten Dahm	Personal travel to the institution archive Scanning facilities are evaluable in situ
6	Institute of Geosciences, University of Kiel	Prof. Dr. Thomas Meier	Personal travel to the institution archive Scanning facilities are evaluable in situ
7	Earthquake Research Institute University of Tokyo	Hiroshi Tsuruoka	Provided scanned copies of the seismograms via ftp server
8	Observatory Collm, Institute of Geophysics and Geology, University of Leipzig	Dr. Siegfried Wendt	Personal travel to the institution archive with own scanning facilities
9	National Archives Geodetic and Geophysical Data, Geophysical Observatory Of Toledo	Ms. Marina Lopez Muga	Provided scanned copies of the seismograms via ftp server
10	Faculty of Science, University of Zagreb	Mr. Ivo Allegretti	Provided scanned copies of the seismograms via ftp server

11	Institute for Geophysics, University of Stuttgart	Dr. Rudolf Widmer- Schnidrig	Personal travel to the institution archive Seismograms were photographed
12	Department of Earth and Environmental Sciences, Ludwig-Maximilians- University	Dr. Joachim Wassermann	Personally taken from the archive scanned in Potsdam and sent back
13	Institute of Geosciences Friedrich-Schiller- University, Jena	Christine Luge	Copies of the seismograms were received by post
14	CGUC - Geophysical Institute University of Coimbra	Dr. Susana Custódio	Personally taken from the archive scanned in Potsdam and sent back
15	Ecole et Observatoire des Sciences de La Terre, University of Strasbourg	Prof. Dr. Luis Rivera	Personal travel to the institution archive Scanning facilities are evaluable in situ
16	Department of Earth Science University of Bergen	Prof. Lars Ottemøller	Personal travel to the institution archive Scanning facilities are evaluable in situ
17	Geophysical Institute, China Earthquake Administration (CEA)	Liu Jie and Qiyuan	Provided scanned copies of the seismograms via e-mail
18	Central Institute for Meteorology and Geodynamics Vienna University of Technology	Helmut Hausmann	Provided scanned copies of the seismograms via e-mail for a fee

Bibliography

Abdrakhmatov, K., Walker, R., Campbell, G., Elliott, A., Hillemann, C., Hollingsworth, J., Landgraf, A., Mukambayev, A. and, R. M., & Sloan, A., 2015, Surface rupturing of the 1889 Chilik (Mw 8.2) earthquake and hazard in the interior of Asia., in preparation.

Abdrakhmatov, K. E., Aldazhanov, S. A., Hager, B. H., Hamburger, M. W., Herring, T. A., Kalabaev, K. B., Makarov, V. I., Molnar, P., Panasyuk, S. V., Prilepin, M. T., Reilinger, R. E., Sadybakasov, I. S., Souter, B. J., Trapeznikov, U. A., Tsurkov, V. Y., & Zubovich, A. V., 1996. Relatively recent construction of the Tien–Shan inferred from GPS measurements of present-day crustal deformation rates, *Nature*, **384**(6608), 450–453.

Abdrakhmatov, K. E., Djanuzakov, K. D., & Delvaux, D., 2002. Active Tectonics and Seismic Hazard of the Issyk-Kul Basin in the Kyrgyz Tian-Shan, In *Lake Issyk-Kul: Its Natural Environment*, pp. 147–160, eds. Klerkx, J. & Imanackunov, B. Springer Netherlands, NATO Science Series.

Abdrakhmatov, K. E., Strom, A. L., Delvaux, D., Havenith, H. B., & Vittori, E., 2013. Temporary clustering of strong earthquakes of Northern Tien–Shan., *Communication of the Institute of Seismology, National Academy of Sciences of the Kyrgyz Republic.*, **1**, 3–9.

Abe, K., 1981. Magnitudes of large shallow earthquakes from 1904 to 1980, *Physics of the Earth and Planetary Interiors*, **27**, 72–92.

Abe, K., 1994. Instrumental magnitudes of historical earthquakes, 1892 to 1898., *Bulletin of the Seismological Society of America*, **84**(2), 415–425. Available at: `http://www.bssaonline.org/content/84/2/415.abstract`, Last accessed on May 2, 2015.

Abe, K. & Noguchi, S., 1983. Determination of magnitude for large shallow earthquakes 1898-1917, *Physics of the Earth and Planetary Interiors*, **32**, 45–59.

Ad-hoc Panel, 1981. Report of the ad-hoc panel of experts on updating the MSK-64 intensity scale., *Gerlands Beiträge zur Geophysik*, **90**, 261–268.

Agnew, D. C., 2002. History of Seismology, In *IASPEI international handbook of earthwuake engineering seismology*, pp. 3–13, ed. Lee, W. H. K. Academic Press.

Aki, K. & Chouet, B., 1975. Origin of coda waves: Source, attenuation, and scattering effects., *Journal of Geophysical Research*, **80**(23), 3322–3342. doi: 10.1029/JB080i023p03322, Available at: `http://dx.doi.org/10.1029/JB080i023p03322`.

Aki, K. & Richards, P., 2002. *Quantitative Seismology.*, Geology (University Science Books).: Seismology, University Science Books.

Alinaghi, A. & Krüger, F., 2014. Seismic array analysis and redetermination of depths of earthquakes in Tien-Shan: implications for strength of the crust and lithosphere., *Geophysical Journal International*, **198**(2), 1111–1129. doi: 10.1093/gji/ggu141, Available at: `http://gji.oxfordjournals.org/content/198/2/1111.abstract`, Last accessed on August 4, 2015.

Allstadt, K., 2013. Extracting source characteristics and dynamics of the August 2010 Mount Meager landslide from broadband seismograms, *Journal of Geophysical Research: Earth Surface*, **118**(3), 1472–1490. ISSN 2169-9011, doi: 10.1002/jgrf.20110, Available at: `http://dx.doi.org/10.1002/jgrf.20110`.

Ambraseys, N. & Bilham, R., 2012. The Sarez-Pamir Earthquake and Landslide of 18 February 1911, *Seismological Research Letters*, **83**(2), 294–314. doi: 10.1785/gssrl.83.2.294, Available at: `http://srl.geoscienceworld.org/content/83/2/294.short`, Last accessed on December 12, 2014.

Ansel, A., 1913. *Seismic registrations in Goettingen in the 1911.* From the news of the Royal Society of Sciences in Goettingen, Mathematics-Physics Class 1913., Presented by E Wiechert at the sitting on 20 July 1912, in German.

Arrowmith, J., Crosby, C., Korjenkov, A., Mamyrov, E., Povolotskaya, I., Guralnik, B., & Landgraf, A., 2015. Surface rupture of the 1911 Kebin (Chon-Kemin) earthquake, Northern Tien Shan, Kyrgyzstan., In *Seismicity, Fault Rupture and Earthquake Hazards in Slowly Deforming Regions.*, p. 432, eds. Landgraf, A., Hintersberger, E., Kübler, S., & Stein, S. Geological Society, London, Special Publications, submitted.

Arrowsmith, J., Crosby, C., Korjenkov, A., Mamyrov, E., & Povolotskaya, I., 2005. *Surface rupture of the 1911 Kebin (Chon-Kemin) earthquake, Northern Tien-Shan, Kyrgyzstan.* Eos Trans. AGU, 86(52), Fall Meet. Suppl., Abstract T51F-05, Power Point Presentation, Available at: `http://activetectonics.la.asu.edu/N_tien_shan/N_tien_shan.html`, Last accessed on August 4, 2015.

Arthur Snoke, 2015. Package for determining and displaying earthquake focal mechanisms., Available at: `https://seiscode.iris.washington.edu/projects/focmec`, Last accessed on September 10, 2015.

Avouac, J. P., Tapponnier, P., Bai, M., You, H., & Wang, G., 1993. Active thrusting and folding along the northern tien shan and late cenozoic rotation of the tarim relative to dzungaria and kazakhstan, *Journal of Geophysical Research: Solid Earth*, **98**(B4), 6755–6804. ISSN 2156-2202, doi: 10.1029/92JB01963, Available at: `http://dx.doi.org/10.1029/92JB01963`, Last accessed on August 4, 2015.

Baroux, E., Pino, N. A., Valensise, G., Scotti, O., & Cushing, M. E., 2003. Source parameters of the 11 june 1909, lambesc (provence, southeastern france) earthquake: A reappraisal based on macroseismic, seismological, and geodetic observations, *Journal of Geophysical Research: Solid Earth*, **108**(B9).

Batlló, J., 2014. Historical Seismometer, In *Encyclopedia of Earthquake Engineering*, pp. 1–31, eds. Beer, M., Kougioumtzoglou, I. A., Patelli, E., & Au, I. S.-K. Springer Berlin Heidelberg. doi: 10.1007/978-3-642-36197-5_171-1, Available at: `http://dx.doi.org/10.1007/978-3-642-36197-5_171-1`.

Batllò, J., Arrazola, D., & Ugalde, A., 2005. Using magnetograms for earthquake magnitude evaluation, *Eos, Transactions American Geophysical Union*, **86**(48), 498–498. ISSN 2324-9250, doi: 10.1029/2005EO480003, Available at: `http://dx.doi.org/10.1029/2005EO480003`, Last accessed on August 4, 2015.

Batlló, J., Stich, D., & Maciá, R., 2008. Quantitative Analysis of Early Seismograph Recordings, In *Historical Seismology*, pp. 385–402, eds. Fréchet, J., Meghraoui, M., & Stucchi, M. Springer Netherlands, Modern Approaches in Solid Earth Sciences.

Belar, A., 1903. Monatsbericht für Jänner 1902der Erdbebenwarte an der k.k. Staats-Oberrealschule in Laibach., In *Die Erdbebenwarte.*, pp. 172–173, ed. Belar, A. Laibach Druck von Ig. v. 1901/02. Kleinmayr & Fed. Bamberg Im Verlage des Herausgebers., In German.

Besstrashnov, V., 1993. *Report on the results of seismogeological investigations in the area of the Mainak water-power plant on the Charyn River.* Hydroproject Association, Unpublished Report, in Russian.

BGS, 2015. Historical UK magnetic observatory magnetograms and yearbooks., British Geological Survey, Available at: `http://www.bgs.ac.uk/data/Magnetograms/home.html`, Last accessed on August 4, 2015.

Bindi, D., Parolai, S., Gómez-Capera, A., Locati, M., Kalmetyeva, Z., & Mikhailova, N., 2014. Locations and magnitudes of earthquakes in central asia from seismic intensity data., *Journal of Seismology*, **18**(1), 1–21. ISSN 1383-4649, doi: 10.1007/s10950-013-9392-1, Available at: `http://dx.doi.org/10.1007/s10950-013-9392-1`.

Blaser, L., Krüger, F., Ohrnberger, M., & Scherbaum, F., 2010. Scaling relations of earthquake source parameter estimates with special focus on subduction environment., *Bulletin of the Seismological Society of America*, **100**(6), 2914–2926. doi: 10.1785/0120100111, Available at: `http://www.bssaonline.org/content/100/6/2914.abstract`, Last accessed on August 4, 2015.

Bodin, P. & Horton, S., 2004. Source Parameters and Tectonic Implications of Aftershocks of the Mw 7.6 Bhuj Earthquake of 26 January 2001., *Bulletin of the Seismological Society of America*, **94**(3), 818–827. doi: 10.1785/0120030176, Available at: `http://www.bssaonline.org/content/94/3/818.abstract`, Last accessed on August 4, 2015.

Bogdanovich, K. I., Kark, I. M., Korol'kov, B. Y., & Mushketov, D. I., 1914. *Earthquake in Northern district of Tien-Shan, 22 December 1910 (4 January 1911).*, p. 250, in Russian.

Bormann, P., 2012. Global 1-D Earth models, In *New Manual of Seismological Observatory Practice 2 (NMSOP-2)*, pp. 1–11, ed. Bormann, P. Deutsches GeoForschungsZentrum GFZ, Potsdam. doi: 10.2312/GFZ.NMSOP-2_DS_2.1.

Bormann, P. & Saul, J., 2009. Earthquake magnitude, *Meyers, R. A. (Eds.), Encyclopedia on Complexity and Systems Science, Springer*, pp. 2473–2496.

Bormann, P., Baumbach, M., Bock, G., Grosser, H., Choy, G. L., & Boatwright, J., 2009. Seismic Sources and Source Parameters, In *New Manual of Seismological Observatory Practice (NMSOP)*, pp. 1 – 94, ed. Bormann, P. Deutsches GeoForschungsZentrum GFZ, Potsdam.

Bormann, P., Wendt, S., & DiGiacomo, D., 2013. Seismic Sources and Source Parameters, In *New Manual of Seismological Observatory Practice 2 (NMSOP2)*, pp. 1–259, ed. Bormann, P. Deutsches GeoForschungsZentrum GFZ, Potsdam.

Brodsky, E. E., Gordeev, E., & Kanamori, H., 2003. Landslide basal friction as measured by seismic waves, *Geophysical Research Letters*, **30**(24). ISSN 1944-8007, Available at: `http://dx.doi.org/10.1029/2003GL018485`, Last accessed on May 1, 2015.

Burtman, V. S., 2013. The geodynamics of the Pamir-Punjab syntaxis, *Geotectonics*, **47**(1), 31–51. ISSN 0016-8521, doi: 10.1134/S0016852113010020, Available at: `http://dx.doi.org/10.1134/S0016852113010020`, Last accessed on August 15, 2015.

Burtman, V. S. & Molnar, P., 1993. Geological and geophysical evidence for deep subduction of continental crust beneath the pamir, *Geological Society of America Special Papers*, **281**, 1–76. doi: 10.1130/SPE281-p1.

Cadek, O., 1987. Studying earthquake ground motion in Prague from Wiechert seismograph records, *Gerl. Beitr. Geoph.*, **96**, 438–447.

Chen, W.-P. & Molnar, P., 1977. Seismic moments of major earthquakes and the average rate of slip in central Asia, *Journal of Geophysical Research*, **82**(20), 2945–2969. ISSN 2156-2202, doi: 10.1029/JB082i020p02945, Available at: `http://dx.doi.org/10.1029/JB082i020p02945`, Last accessed on August 4, 2015.

CMT, 2015. Global Centroid-Moment-Tensor (CMT) Catalog., CMT catalog web search, Available at: `http://www.globalcmt.org/CMTsearch.html`, Last accessed on August 15, 2015.

Cochard, A., Igel, H., Schuberth, B., Suryanto, W., Velikoseltsev, A., Schreiber, U., Wassermann, J., Scherbaum, F., & Vollmer, D., 2006. Rotational Motions in Seismology: Theory, Observation, Simulation., In *Earthquake Source Asymmetry, Structural Media and Rotation Effects.*, pp. 391–411, eds. Teisseyre, R., Majewski, E., & Takeo, M. Springer Berlin Heidelberg. doi: 10.1007/3-540-31337-0_30, Available at: `http://dx.doi.org/10.1007/3-540-31337-0_30`.

Crosby, C., Arrowsmith, J., Korjenkov, A., Guralnik, B., Mamyrov, E., & Povolotskaya, I., 2007. *The Hunt for Surface rupture from the 1889 Ms8.3 Chilik earthquake, Northern Tien-Shan, Kyrgyzstan and Kazakhstan.* Eos Trans. AGU, 88(52), Fall Meet. Suppl., Abstract T23D-1635, Poster Presentation, Available at: `http://activetectonics.la.asu.edu/N_tien_shan/N_tien_shan.html`, Last accessed on August 4, 2015.

Dahm, T. & Krüger, F., 1999. Higher-degree moment tensor inversion using far-field broad-band recordings: theory and evaluation of the method with application to the 1994 bolivia deep earthquake, *Geophysical Journal International*, **137**(1), 35–50.

Dahm, T. & Krüger, F., 2014. Moment tensor inversion and moment tensor interpretation, In *New Manual of Seismological Observatory Practice 2 (NMSOP-2)*, pp. 1–37, ed. Bormann, P. Deutsches GeoForschungsZentrum GFZ, Potsdam.

Dahm, T., Krueger, F., Stammler, K., & Yuan, X., 2004. *Moment tensor inversion - a practical for beginners.*

Davison, C., 1885. IV.-On a Possible Cause of the Disturbance of Magnetic Compass-Needles during Earthquakes., *Geological Magazine (Decade III)*, **2**, 210–211. doi: 10.1017/S0016756800151945, Available at: `http://journals.cambridge.org/article_S0016756800151945`, Last accessed on August 4, 2015.

Davison, C., 1921. On scales of seismic intensity and on the construction and use of isoseismal lines, *Bulletin of the Seismological Society of America*, **11**(2), 95–130. Available at: `http://www.bssaonline.org/content/11/2/95.short`, Last accessed on August 4, 2015.

Delvaux, D., Abdrakhmatov, K. E., Lemzin, I. N., & Strom, A. L., 2001. Landslides and surface breaks of the 1911 Ms 8.2 Kemin earthquake, *Russian Geology and Geophysics*, **42**, 1167–1177.

Denieul, M., Sèbe, O., Cara, M., & Cansi, Y., 2015. Mw Estimation from Crustal Coda Waves Recorded on Analog Seismograms., *Bulletin of the Seismological Society of America.* doi: 10.1785/0120140226, Available at: `http://www.bssaonline.org/content/early/2015/03/05/0120140226.abstract`.

Dewey, J. & Byerly, P., 1969. The early history of seismometry (to 1900), *Bulletin of the Seismological Society of America*, **59**(1), 183–227.

Dost, B. & Haak, H., 2002. *A comprehensive description of the KNMI seismological instrumentation*, De Bilt, The Netherlands : Koninklijk Nederlands Meteorologisch Instituut, Includes bibliographic references.

Dürbaum, H. & Harjes, H., 1986. *Zehn Jahre Gräfenberg-Array.*, Mitteilung XV der Senatskommission für geowissenschaftliche Gemeinschaftsforschung, VCH Verlagsgesellschaft D-6940 Weinheim, Germany, p. 172, Schrittmacher der Breitband-Seismologie, in German.

Dziewonski, A. M. & Anderson, D. L., 1981. Preliminary reference earth model, *Physics of the Earth and Planetary Interiors*, **25**(4), 297–356. ISSN 0031-9201, doi: http://dx.doi.org/10.1016/0031-9201(81)90046-7, Available at: `http://www.sciencedirect.com/science/article/pii/0031920181900467`.

Ehlert, R., 1898a. Horizontalpendelbeobachtungen im Meridian zu Strassburg i. E.-Von April bis Winter 1895., *Beiträge zur Geophysik*, **3**, 131–209, in German.

Ehlert, R., 1898b. Compilation, explanation and critical evaluation of the most important seismometer with particular reference to its practical usefulness., *Beiträge zur Geophysik*, **3**, 350–475, in German.

Ekström, G., Nettles, M., & Dziewónski, A., 2012. The global CMT project 2004-2010: Centroid-moment tensors for 13,017 earthquakes., *Physics of the Earth and Planetary Interiors*, **200-201**(0), 1–9. doi: http://dx.doi.org/10.1016/j.pepi.2012.04.002, Available at: `http://www.sciencedirect.com/science/article/pii/S0031920112000696`, Last accessed on August 4, 2015.

Eleman, F., 1966. The Response of Magnetic Instruments to Earthquake waves., *Journal of geomagnetism and geoelectricity*, **18**(1), 43–72. doi: 10.5636/jgg.18.43.

Etzold, F., 1903. *Die von Wicherts astatischem Pendelseismometer in der Zeit vom 15. Juli bis 81. December 1902 in Leipzig gelieferten Seismogramme von Fernbeben.* . Abdruck aus den Berichte der math.-phys. Klasse der Königl. Sächs. Gesellschaft der Wissenschaften zu Leipzig, Leipzig, pp. 22–38, Sitzung vom 2. Februar 1903., mit Tafel II, In German.

Feld, C., Haberland, C., Schurr, B., Sippl, C., Wetzel, H.-U., Roessner, S., Ickrath, M., Abdybachaev, U., & Orunbaev, S., 2015. Seismotectonic study of the fergana region (southern kyrgyzstan): distribution and kinematics of local seismicity, *Earth, Planets and Space*, **67**(1). doi: 10.1186/s40623-015-0195-1, Available at: `http://dx.doi.org/10.1186/s40623-015-0195-1`, Last accessed on August 4, 2015.

Ferrari, G., 1992. *Two hundred years of seismic instruments in Italy, 1731-1940*, SGA Storia-Geofisica-Ambiente, Istituto nazionale di geofisica (Italia).

Fréchet, J. & Rivera, L., 2012. Horizontal pendulum development and the legacy of Ernst von Rebeur-Paschwitz, *Journal of Seismology*, **16**(2), 315–343, Springer Netherlands. ISSN 1383-4649, doi: 10.1007/s10950-011-9272-5, Available at: `http://dx.doi.org/10.1007/s10950-011-9272-5`, Last accessed on August 4, 2015.

Fu, B., Ninomiya, Y., & Guo, J., 2010a. Slip partitioning in the northeast pamir–tian shan convergence zone, *Tectonophysics*, **483**(3–4), 344–364. ISSN 0040-1951, doi: http://dx.doi.org/10.1016/j.tecto.2009.11.003, Available at: `http://www.sciencedirect.com/science/article/pii/S0040195109006222`, Last accessed on September 10, 2015.

Fu, Z., Lü, X., Jin, X., Dai, Y., Shao, H., & Hao, P., 2010b. Discussion on the Abnormally Low Active Fault Slip Rate of the M_S8.0 Wenchuan Earthquake, *Earthquake Research In China*, **24**(3), 272–276.

Fuchs, K. & Müller, G., 1971. Computation of Synthetic Seismograms with the Reflectivity Method and Comparison with Observations, *Geophysical Journal of the Royal Astronomical Society*, **23**(4), 417–433.

Galitzin, G. B., 1910. *Über einen neuen Seismographen für die Vertikal-Komponente des Bodenbewegung: Von Fürst B. Galitzin (Golicyn)*, Buchdr. d. Kais. Akad. d. Wiss.

Galitzin, G. B., 1911a. Das Erdbeben vom 3.- 4. Januar 1911, *Bulletin de l'Académie Impériale des Sciences de St.-Pétersbourg. VI série*, **5**, 127–136, in German, Fürst B. Galitzin (Golicyn).

Galitzin, G. B., 1911b. *Über ein neues aperiodisches Horizontalpendel mit galvanometrischer Fernregistrierung: Von Fürst B. Galitzin (Golicyn)*, St. Petersburg: Kaiserl. Akademie der Wissensch., In German.

Galitzin, G. B., 1915. On the earthquake of 18th february 1911., *Proceedings of the Imperial Academy of Sciences. VI series.*, **9**(10), 991–998.

Galitzin, G. B., Reinfeldt, C., & Hecker, O., 1914. *Vorlesungen über Seismometrie*, St. Petersburg: Kaiserl. Akademie der Wissensch., In German.

Galton, F., 1889. Report of the Kew Committee for the Year Ending October 31, 1889., *Proceedings of the Royal Society of London*, **46**(280-285), 474–495. doi: 10.1098/rspl.1889.0054, Available at: `http://rspl.royalsocietypublishing.org/content/46/280-285/474.short`, Last accessed on August 4, 2015.

Ghose, S., Hamburger, M. W., & Ammon, C. J., 1998a. Source parameters of moderate-sized earthquakes in the tien shan, central asia from regional moment tensor inversion, *Geophysical Research Letters*, **25**(16), 3181–3184. ISSN 1944-8007, doi: 10.1029/98GL02362, Available at: `http://dx.doi.org/10.1029/98GL02362`, Last accessed on August 30, 2015.

Ghose, S., Hamburger, M. W., & Virieux, J., 1998b. Three-dimensional velocity structure and earthquake locations beneath the northern tien shan of kyrgyzstan, central asia, *Journal of Geophysical Research: Solid Earth*, **103**(B2), 2725–2748. ISSN 2156-2202, doi: 10.1029/97JB01798, Available at: `http://dx.doi.org/10.1029/97JB01798`, Last accessed on August 30, 2015.

Grabrovec, D. & Allegretti, I., 1994. On the digitizing of historical seismograms, *Geofizika*, **11**, 27–31.

Gray, T., 1883. On Gray and Milne′s Seismographic Apparatus, *Quarterly Journal of the Geological Society*, **39**(1-4), 218–223. doi: 10.1144/GSL.JGS.1883.039.01-04.17, Available at: `http://jgslegacy.lyellcollection.org/content/39/1-4/218.abstract`.

Gubin, I. E., 1960. Regularities of Seismic Activity in the territory of Tajikistan., *Academy of Sciences Publishing House, Moscow*, pp. 279–303, In Russian.

Gutenberg, B., 1956. Great earthquakes 1896-1903, *Eos, Transactions American Geophysical Union*, **37**(5), 608–614. ISSN 2324-9250, doi: 10.1029/TR037i005p00608, Available at: `http://dx.doi.org/10.1029/TR037i005p00608`, Last accessed on September 4, 2015.

Gutenberg, B. & Richter, C. F., 1954. *Seismicity of the earth and associated phenomena / by B. Gutenberg and C.F. Richter*, Princeton University Press Princeton, N. J, 2nd ed.

Hardebeck, J. L. & Shearer, P. M., 2003. Using S/P amplitude ratios to constrain the focal mechanisms of small earthquakes, *Bulletin of the Seismological Society of America*, **93**(6), 2434–2444.

Hazard, D. L. , 1913. *Results of observations made at the Coast and Geodetic Survey Magnetic Observatory near Honolulu, Hawaii 1911 and 1912.* Govt. Print. Off., U.S. Coast and Geodetic Survey. Department of Commerce and Labor. Coast and Geodetic Survey. O.H. Tittmann, superintendent.

Hazard, D. L. , 1914. *Results of observations made at the Coast and Geodetic Survey Magnetic Observatory at Sitka, Alaska.* Govt. Print. Off., U.S. Coast and Geodetic Survey. Department of Commerce and Labor. Coast and Geodetic Survey. O.H. Tittmann, superintendent.

He, Y.-M., Zheng, T.-Y., & Shan, X.-J., 2001. March 19, 1996 Artux Xinjiang Earthquake: A Simple Unilateral Rupture Event, *Chinese Journal of Geophysics*, **44**(4), 506–514. ISSN 2326-0440, doi: 10.1002/cjg2.168, Available at: `http://dx.doi.org/10.1002/cjg2.168`, Last accessed on September 4, 2015.

Heimann, S., 2014a. *Fomosto: a tool to manage pre-calculated Green's function stores.* GFZ German Research Center for Geosciences, Helmholtz-Zentrum Potsdam, Germany, Available at: `http://emolch.github.io/pyrocko/current/fomosto.html`, Last accessed on November 1, 2014.

Heimann, S., 2014b. *Pyrocko - a seismology toolbox and library.* GFZ German Research Center for Geosciences, Helmholtz-Zentrum Potsdam, Germany, Available at: `http://emolch.github.io/pyrocko/`, Last accessed on November 1, 2014.

Henni, P. & Lawrie, K., 1999. *The National Seismological Archive WWSSN Microfilm Collection [Final Report]: British Geological Survey, Seismology Series, Technical Report WL/99/18*, British Geological Survey, Available at: `http://www.earthquakes.bgs.ac.uk/hazard/pdf/wl9918.pdf`.

Henningsen, D. & Katzung, G., 2006. *Einfuhrung in die Geologie Deutschlands.*, Springer Spektrum, p. 234, in German.

Howell, B. F. J., 1990. An introduction to seismological research : History and development, pp. 57–72, Chapter 4.

Hwang, R.-D., Chang, J.-P., Wang, C.-Y., Wu, J.-J., Kuo, C.-H., Tsai, Y.-W., Chang, W.-Y., & Lin, T.-W., 2011. Rise time and source duration of the 2008 M_W 7.9 Wenchuan (China) earthquake as revealed by Rayleigh waves, *Earth, Planets, and Space*, **63**, 427–434.

Ignatiev, I., 1885. *Earthquakes in Tokmak district in 1885.* Isviestia, Russian Geographical Society, in Russian.

Ilyin, A., 1871. Map of Semirechye Area., In *Detailed Atlas of the Russian Empire with plans to major cities, consisting of 70 maps.*, ed. Ilyin, A. Cartographic Institution Publisher, in Russian. Available at: `http://www.krasplace.ru/wp-content/uploads/2009/atlas1871/map64.jpeg`.

ISC, 2015. *International Seismological Centre On-line Bulletin.* Int. Seis. Cent, Thatcham, United Kingdom, Available at: `http://www.isc.ac.uk/iscbulletin/search/bulletin/`, Last accessed on September 15, 2015.

Ischuk, A., 2006. Usoy natural dam: problem of security (lake Sarez, Pamir moutains, Tadjikistan, *Italian Journal of Engineering Geology and Environment*, **Special Issue 1**, 189–192. doi: 10.4408/IJEGE.2006-01.S-26.

Ischuk, A., Bendick, R., Rybin, A., Molnar, P., Khan, S. F., Kuzikov, S., Mohadjer, S., Saydullaev, U., Ilyasova, Z., Schelochkov, G., & Zubovich, A. V., 2013. Kinematics of the pamir and hindu kush regions from gps geodesy, *Journal of Geophysical Research: Solid Earth*, **118**(5), 2408–2416. ISSN 2169-9356, doi: 10.1002/jgrb.50185, Available at: `http://dx.doi.org/10.1002/jgrb.50185`, Last accessed on September 10, 2015.

Januzakov, K., Omuraliev, M., Omuralieva, A., Ilyasov, B. I., & Grebennikova, V. V., 2003. *Strong earthquakes of the Tien-Shan (within the Kyrgyzstan territory and adjacent regions of the countries of Central Asia).* Ilim, Bishkek, p 216., ISBN 5-8355-1335-6.

Jeffreys, H., 1923. The Pamir earthquake of 18 February 1911, in relation to the depths of earthquake foci., *Monthly Notices of the Royal Astronomical Society Geophysical Supplement 1*, pp. 22–31.

Jeffreys, H., 1924. *The Earth.* Cambridge: Cambridge University Press, 278 pp., 1st ed.

Julian, B. R. & Foulger, G. R., 1996. Earthquake mechanisms from linear-programming inversion of seismic-wave amplitude ratios, *Bulletin of the Seismological Society of America*, **86**, 972–980.

Kalmetieva, Z., Mikolaichuk, A., Moldobekov, B., Meleshko, A., Jantaev, M. M., & Zubovich, A. V., 2009. *Atlas of earthquakes in Kyrgyzstan.*, Bishkek CAIAG - 2009, p. 75, Editor-in-chief of English version: Dr. H.B. Havenith.

Kanamori, H., Rivera, L., & Lee, W. H. K., 2010. Historical seismograms for unravelling a mysterious earthquake: The 1907 Sumatra Earthquake, *Geophysical Journal International*, **183**, 358–374.

Karnik, V., Kondorskaya, N. V., Riznitchenko, J. V., Savarensky, E. F., Soloviev, S. L., Shebalin, N. V., Vanek, J., & Zatopek, A., 1962. Standardization of the earthquake magnitude scale, *Studia Geophysica et Geodaetica*, **6**, 41–48.

Kazakov, N., 2004. *Russian geologists on lake Sarez.* A collection of the publications related to the lake Sarez and Usoy avalanche., Available at: `http://www.nikzdaru.com/`, Last accessed on May 2, 2015.

Kennett, B. L. N., 1991. *IASPEI 1991 Seismological Tables*, Research School of Earth Sciences,Australian National University.

Kennett, B. L. N. & Engdahl, E. R., 1991. Traveltimes for global earthquake location and phase identification, *Geophysical Journal International*, **105**(2), 429–465.

Kennett, B. L. N., Engdahl, E. R., & Buland, R., 1995. Constraints on seismic velocities in the Earth from traveltimes., *Geophysical Journal International*, **122**(1), 108–124. doi: 10.1111/j.1365-246X.1995.tb03540.x, Available at: `http://gji.oxfordjournals.org/content/122/1/108.abstract`, Last accessed on August 4, 2015.

Kimball, S. & et. al, 2014. *GIMP - GNU Image Manipulation Program*, GIMP is a freely distributed piece of software., Available at: `http://www.gimp.org/`, Last accessed on December 12, 2014.

Kisslinger, C., 1980. Evaluation of s to p amplitude rations for determining focal mechanisms from regional network observations, *Bulletin of the Seismological Society of America*, **70**(4), 999–1014.

Klotz, O., 1915. Earthquake of february 18, 1911, *Bulletin of the Seismological Society of America*, **5**(4), 206–213.

Kondorskaya, N., Shebalin, N., & World Data Center A, f. S. E. G., 1982. *New Catalog of Strong Earthquakes in the U.S.S.R. from Ancient Times Through 1977.*, p. 609, Report (World Data Center A for Solid Earth Geophysics), Available at: `ftp://ftp.ngdc.noaa.gov/hazards/publications/Wdcse-31.pdf`, Last accessed on August 4, 2015.

Koninklijk, N., 1915. *Seismic registrations in De Bilt.* Koninklijk Nederlands Meteorological Instituut, 108., Journal, magazine : National government publication : Dutch, Utrecht : Kemink and Zoon, 1915-1943.,in German.

Kopnichev, Y. F., 1975. A model of generation of the tail of the seismogram., *Dok. Acad. Nauk, SSSR*, **222**, 333–335, english Translation.

Korn, M., 2002. *Ten Years of German Regional Seismic Network (GRSN): Report 25 of the Senate Commission for Geosciences.*, DFG, Wiley-VCH Verlag GmbH, p. 299.

Kulikova, G. & Krüger, F., 2015. Source process of the 1911 M8.0 Chon-Kemin earthquake: investigation results by analogue seismic records., *Geophysical Journal International*, **201**(3), 1891–1911. doi: 10.1093/gji/ggv091, Available at: `http://gji.oxfordjournals.org/content/201/3/1891.abstract`.

Lagrange, E., 1911. The earthquake of January 3-4 1911., *Ciel et Terre*, **32**, 40, in French.

Lee, William H.K., 2011. Seismogram Archives of Significant Earthquakes of the World. The USGS WWFC Pilot Scanning Project. , Available at: `http://ds.iris.edu/seismo-archives/projects/`, Last accessed on September 28, 2015.

Liznar, J., 1895. *Einfluss des Erdbebens vom April 1895 auf die Magnetographen in Pola und Wien nebsteinigen Bemerkungen ber die Wirkung der Erdbeben auf magnetische Variationsapparate überhaupt.*, Meteor. Zeitschrift, XII, pp. 261–267, in German.

Maggi, A., Jackson, J., McKenzie, D., & Priestley, K., 2000. Earthquake focal depths, effective elastic thickness, and the strength of the continental lithosphere., *Geology*, **28**(6), 495–498. doi: 10.1130/0091-7613(2000)28⟨495:EFDEET⟩2.0.CO;2, Available at: `http://geology.gsapubs.org/content/28/6/495.abstract`, Last accessed on August 4, 2015.

Makarov, V., Alekseev, D., Batalev, V., Bataleva, E., Belyaev, I., Bragin, V., Dergunov, N., Efimova, N., Leonov, M., Munirova, L., Pavlenkin, A., Roecker, S., Roslov, Y., Rybin, A., & Shchelochkov, G., 2010. Underthrusting of tarim beneath the tien shan and deep structure of their junction zone: Main results of seismic experiment along manas profile kashgar-song-köl, *Geotectonics*, **44**(2), 102–126. ISSN 0016-8521, doi: 10.1134/S0016852110020020, Available at: `http://dx.doi.org/10.1134/S0016852110020020`, Last accessed on August 4, 2015.

Mayeda, K., 1993. mb(LgCoda): A stable single station estimator of magnitude., *Bulletin of the Seismological Society of America*, **83**(3), 851–861. Available at: `http://www.bssaonline.org/content/83/3/851.abstract`, Last accessed on August 4, 2015.

Mayeda, K. & Walter, W. R., 1996. Moment, energy, stress drop, and source spectra of western United States earthquakes from regional coda envelopes., *Journal of Geophysical Research: Solid Earth*, **101**(B5), 11195–11208. doi: 10.1029/96JB00112, Available at: `http://dx.doi.org/10.1029/96JB00112`, Last accessed on August 4, 2015.

Mayeda, K., Hofstetter, A., O'Boyle, J. L., & Walter, W. R., 2003. Stable and Transportable Regional Magnitudes Based on Coda-Derived Moment-Rate Spectra, *Bulletin of the Seismological Society of America*, **93**(1), 224–239. doi: 10.1785/0120020020, Available at: `http://www.bssaonline.org/content/93/1/224.abstract`, Last accessed on August 4, 2015.

Mayeda, K., Malagnini, L., & Walter, W. R., 2007. A new spectral ratio method using narrow band coda envelopes: Evidence for non-self-similarity in the Hector Mine sequence., *Geophysical Research Letters*, **34**(11), pp. L11303(1-5). doi: 10.1029/2007GL030041, Available at: `http://dx.doi.org/10.1029/2007GL030041`, Last accessed on August 4, 2015.

McComb, H. E. & West, J. C., 1931. *Bulletin Of The National Research Council., List of Seismologic Stations of the World.*, Published by The National Research Council of The National Academy of Sciences Washington D.C, Number 82, Second edition.

Michelini, A., De Simoni, B., Amato, A., & Boschi, E., 2005. Collecting, digitizing, and distributing historical seismological data, *EOS, Transactions American Geophysical Union*, **86**(28), 261–266. ISSN 2324-9250, doi: 10.1029/2005EO280002.

Mikhailova, N., Mukambayev, A., Aristova, I., Kulikova, G., Ullah, S., Pilz, M., & Bindi, D., 2015. Central Asia earthquake catalogue from ancient time to 2009., *Annals of Geophysics*, **58**(1), pp. S0102(1–9). doi: 10.4401/ag-6681, Available at: `http://www.annalsofgeophysics.eu/index.php/annals/article/view/6681`, Last accessed on August 4, 2015.

Milne, J., 1886. *Earthquakes and Other Earth Movements*, International scientific series, D. Appleton and company, Book from the collections of: New York Public Library, Digitizing sponsor: Google.

Milne, J. & Gray, T., 1882. On seismic experiments, *Philosophical Transactions of the Royal Society of London*, **173**, 863–883.

Milne, J., Shinobu, H., & Plummer, W. E., 1898. Seismological Investigation.- Third Report of the Committee., In *Reports of the Seismological Investigation Committee.*, pp. 179–276, ed. Milne, J. British Association for the Advancement of Science. Available at: `http://ds.iris.edu/seismo-archives/info/historical/baas/BAAS1898.pdf`.

Molnar, P. & Ghose, S., 2000. Seismic moments of major earthquakes and the rate of shortening across the tien shan, *Geophysical Research Letters*, **27**(16), 2377–2380. ISSN 1944-8007, doi: 10.1029/2000GL011637, Available at: `http://dx.doi.org/10.1029/2000GL011637`, Last accessed on August 4, 2015.

Molnar, P. & Qidong, D., 1984. Faulting associated with large earthquakes and the average rate of deformation in central and eastern Asia, *Journal of Geophysical Research: Solid Earth*, **89**(B7), 6203–6227. ISSN 2156-2202, doi: 10.1029/JB089iB07p06203, Available at: `http://dx.doi.org/10.1029/JB089iB07p06203`, Last accessed on August 4, 2015.

Molnar, P. & Tapponnier, P., 1975. Cenozoic Tectonics of Asia: Effects of a Continental Collision: Features of recent continental tectonics in Asia can be interpreted as results of the India-Eurasia collision, *Science*, **189**(4201), 419–426.

Mooney, W. D., Laske, G., & Masters, T. G., 1998. CRUST 5.1: A global crustal model at 5°x 5°, *Journal of Geophysical Research*, **103**(B1), 727–747.

Moretti, L., Mangeney, A., Capdeville, Y., Stutzmann, E., Huggel, C., Schneider, D., & Bouchut, F., 2012. Numerical modeling of the Mount Steller landslide flow history and of the generated long period seismic waves, *Geophysical Research Letters*, **39**(16), L16402. ISSN 1944-8007, doi: 10.1029/2012GL052511, Available at: `http://dx.doi.org/10.1029/2012GL052511`.

Moureaux, M. & Mascart, M., 1889a. Sur les relations qui peuvent exister entre les perturbations magnetiques et les tremblements du terre du 30 Mai 1889., *C.R. CVIII*, p. 1189, in French.

Moureaux, M. & Mascart, M., 1889b. Sur la cause de certains troubles observes sur les courbes des magnetographes., *C.R. CIX*, pp. 272–274, in French.

Müller, G., 1985. The reflectivity method - a tutorial, *Journal of Geophysics - Zeitschrift Für Geophysik*, **58**(1-3), 153–174.

Mushketov, I. V., 1890. *Verny earthquake 28 May (9 June) 1887 y.* Works of the geological committee, Commissionaires of the geological committee, in Russian.

Mushketov, I. V., 1891. *Materials for investigation of earthquakes in Russia.* Annex to the 27th volume of tidings of the Imperial Russian Geographical Society, in Russian.

Nelson, M. R., McCaffrey, R., & Molnar, P., 1987. Source parameters for 11 earthquakes in the tien shan, central asia, determined by p and sh waveform inversion, *Journal of Geophysical Research: Solid Earth*, **92**(B12), 12629–12648. ISSN 2156-2202, doi: 10.1029/JB092iB12p12629, Available at: `http://dx.doi.org/10.1029/JB092iB12p12629`, Last accessed on September 10, 2015.

Nikiforov, P. M., 1912. *Bulletin of the Permanent Central Seismic Commission.*, St. Petersburg, Russia, in Russian.

Nurmagambetov, A., 1999. *Seismic history of Almaty.*, Publishing House "LEM", Almaty, p. 68, in Russian.

Okada, Y., 1985. Surface deformation due to shear and tensile faults in a half-space, *Bulletin of the Seismological Society of America*, **75**(4), 1135–1154.

Okal, E. A., 2012. The south of java earthquake of 1921 september 11: a negative search for a large interplate thrust event at the java trench, *Geophysical Journal International*, **190**(3), 1657–1672.

Oldham, R. D., 1923. The pamir earthquake of 18th february, 1911, *Quarterly Journal of the Geological Society*, **79**(1-4), 237–245.

Oliver, J., 1961. On the long period character of shear waves, *Bulletin of the Seismological Society of America*, **51**(1), 1–12.

Omori, D. F., 1903. *Horizontal Pendulum Observation of Earthquakes at Hitotsubashi (Tokyo) 1900*, Imperial Earthquake Investigation Committee, pp. 109–111.

Omori, F., 1899. *Horizontal Pendulums for Registering Mechanically Earthquakes and Other Earth-movements*, Tokyo.

Omori, F., 1902. A horizontal pendulum tromometer, *Publications of the Earthquake Investigation Committe in foreign language*, **12**, 1–7. Available at: `http://ci.nii.ac.jp/naid/110006606629/en/`, Last accessed on September 4, 2015.

Omori, F., 1907. Note on the Kashgar (Turkestan) Earthquake of Aug. 22, 1902, In *Bulletin of the Imperial Earthquake Investigation Committee*, vol. 1, pp. 161 – 166, ed. Omori, F. Disaster prevention Committee and Imperial Earthquake Investigation Committee. Available at: `http://id.nii.ac.jp/0021/00009378`.

Oreshin, S., Vinnik, L., Peregoudov, D., & Roecker, S., 2002. Lithosphere and asthenosphere of the tien shan imaged by s receiver functions, *Geophysical Research Letters*, **29**(8), 32–1–32–4. ISSN 1944-8007, doi: 10.1029/2001GL014441, Available at: `http://dx.doi.org/10.1029/2001GL014441`, Last accessed on August 4, 2015.

Osaka, Bull., 1931. *The Seismological Bulletin in Osaka from 1882 to 1929.* The Osaka Meteorological Observatory.

Papyrin, L., 2001. Sarez catastrophe geophysical forecast, *Publishing house "Science World", Moscow, 2001.*, pp. 183–194, in Russian.

Phinney, R. A., 1961. Leaking modes in the crustal waveguide: 1. The oceanic PL wave, *Journal of Geophysical Research*, **66**(5), 1445–1469.

Pintore, S., Quintiliani, M., & Franceschi, D., 2005. TESEO: A Vectoriser of Historical Seismograms, *Comput. Geosci.*, **31**(10), 1277–1285.

Powell, T. & Fries, D., 1964. *Handbook: World-wide Standard Seismograph Network*, Acoustics and Seismics Laboratory, Institute of Science and Technology, The University of Michigan, Ann Arbor, Michigan., p. 500.

Preobrazhenskiy, I. A., 1920. *Usoy avalanche.* Printed by order of the Geological Committee., Resolution of the Presence of the Geological Committee December 1, 1915 (In Russian).

Press, W. H., Teukolsky, S. A., Vetterling, W. T., & Flannery, B. P., 2007. *Numerical Recipes 3rd Edition: The Art of Scientific Computing.*, Cambridge University Press, New York, NY, USA, 3 edition.

Rebeur-Paschwitz, v. E., 1889. The Earthquake of Tokio, April 18, 1889., *Nature*, **40**, 294–295. doi: 10.1038/041032a0.

Rebeur-Paschwitz, v. E., 1892a. Über Horizontalpendel-Beobachtungen in Wilhelmshaven, Potsdam und Puerto Orotava auf Teneriffa., *Astronomische Nachrichten*, **130**(13-14), 193–216, in German. doi: 10.1002/asna.18921301302, Available at: `http://dx.doi.org/10.1002/asna.18921301302`, Last accessed on August 4, 2015.

Rebeur-Paschwitz, v. E., 1892b. *Das Horizontalpendel und seine Anwendung zur Beobachtung der absoluten und relativen Richtungs-Aenderungen der Lothlinie: Ergebnisse einiger mit Unterstützung der Königlich Preussischen Akademie der Wissenschaften in den Jahren 1889-1892 auf den Observatorien zu Wilhelmshaven und Potsdam sowie in Puerto Orotava auf Teneriffa ausgeführter Beobachtungsreihen.*, vol. Band LX of **Nova Acta der Ksl. Leop.-Carol. Deutschen Akademie der Naturforscher**, Druck von E. Blochmann & Sohn in Dresden. Für die Akademie in Commission bei Wilh. Engelmann in Leipzig, in German.

Rebeur-Paschwitz, v. E., 1893. Über die Aufzeichnung der Fernewirkungen von Erdbeben., *Petermanns Mitteilungen*, **9**(39), 201–212, in German, page 203.

Rebeur-Paschwitz, v. E., 1895. *Horizontalpendel-Beobachtungen auf der Kaiserlichen Universitäts-Sternwarte zu Strassburg 1892 - 1894 (Mit Tafel I - IV und 14 Holzschnitten).*, Beiträge zur Geophysik. Hgg. v. Georg Gerland 2, Schweizerbart, E., pp. 211 – 536, in German.

Reid, H. F., 1914. The free and forced vibrations of a suspended magnet: Concluded., *Terrestrial Magnetism and Atmospheric Electricity*, **19**(4), 189–203. doi: 10.1029/TE019i004p00189, Available at: `http://dx.doi.org/10.1029/TE019i004p00189`, Last accessed on August 4, 2015.

Richter, C. F., 1958. *Elementary seismology.*, W. H. Freeman and Company, San Francisco.

Robinson, A. C., A. Yin, C. E., Manning, T. M., Harrison, S.-H., Zhang, & Wang, X.-F., 2004. The giant Shakhdara migmatitic gneiss dome, Pamir, India-Asia collision zone: 2. Timing of dome formation, *Geological Society of America Bulletin*, **116**(7/8), 953–973. doi: 10.1130/B25375.1.

Scherbaum, F., 2007. *Of Poles and Zeros: Fundamentals of Digital Seismology*, Springer, Modern Approaches in Geophysics, 2nd edition.

Schlupp, A. & Cisternas, A., 2007. Source history of the 1905 great Mongolian earthquakes (Tsetserleg, Bolnay), *Geophysical Journal International*, **169**, 1115–1131.

Schneider, F., Yuan, X., Schurr, B., Mechie, J., Sippl, C., Haberland, C., Minaev, V., Oimahmadov, I., Gadoev, M., Radjabov, N., Abdybachaev, U., Orunbaev, S., & Negmatullaev, S., 2013. Seismic imaging of subducting continental lower crust beneath the Pamir, *Earth and Planetary Science Letters*, **375**, 101–112. ISSN 0012-821X, doi: http://dx.doi.org/10.1016/j.epsl.2013.05.015, Available at: `http://www.sciencedirect.com/science/article/pii/S0012821X13002537`, Last accessed on September 4, 2015.

Schurr, B., Ratschbacher, L., Sippl, C., Gloaguen, R., Yuan, X., & Mechie, J., 2014. Seismotectonics of the Pamir, *Tectonics*, **33**(8), 1501–1518, 2014TC003576. ISSN 1944-9194, doi: 10.1002/2014TC003576, Available at: `http://dx.doi.org/10.1002/2014TC003576`, Last accessed on September 10, 2015.

Schwab, M., Ratschbacher, L., Siebel, W., McWilliams, M., Minaev, V., Lutkov, V., Chen, F., Stanek, K., Nelson, B., Frisch, W., & Wooden, J. L., 2004. Assembly of the Pamirs: Age and origin of magmatic belts from the southern Tien Shan to the southern Pamirs and their relation to Tibet, *Tectonics*, **23**(4), TC4002(1–31). ISSN 1944-9194, doi: 10.1029/2003TC001583, Available at: `http://dx.doi.org/10.1029/2003TC001583`, Last accessed on September 4, 2015.

Schweitzer, J., 2001. Hyposat - an enhanced routine to locate seismic events, *Pure and Applied Geophysics*, **158**(1-2), 277–289.

Schweitzer, J., 2003. 79.24 Germany. German National Report - Part A. Early German contributions to modern seismology., In *International Handbook of Earthquake and Engineering Seismology*, vol. 81, Part B, pp. 1347–1352, eds. William H.K. Lee, Hiroo Kanamori, P. C. J. & Kisslinger, C. Academic Press, International Geophysics.

Schweitzer, J., 2012. *HYPOSAT/ HYPOMOD*. (GFZ) German Research Center for Geosciences, Potsdam, User Manual.

Schweitzer, J. & Lee, W., 2003. 88 Old Seismic bulletins to 1920: A collective heritage from early seismologists, In *International Handbook of Earthquake and Engineering Seismology*, pp. 1665–1723, eds. William H.K. Lee, Hiroo Kanamori, P. C. J. & Kisslinger, C. Academic Press, International Geophysics.

Selander, J., Oskin, M., Ormukov, C., & Abdrakhmatov, K., 2012. Inherited strike-slip faults as an origin for basement-cored uplifts: Example of the Kungey and Zailiskey ranges, Northern Tian Shan., *Tectonics*, **31**(4), pp. TC4026(1–22). ISSN 1944-9194, doi: 10.1029/2011TC003002, Available at: `http://dx.doi.org/10.1029/2011TC003002`, Last accessed on August 4, 2015.

Semenov, P. & Semenov, V., 1958. Catalog of earthquakes felt on the territory of Tajikistan for the period 1865-1940, and 1941-1952 years, Academy of Sciences Tadzh.SSR, Stalinabad.

Semirechye, 1900. Map of the parishes in Semirechye area., in Russian, Available at: `http://clubklad.ru/maps/4985/`, Last accessed on June 10, 2015.

Sens-Schönfelder, C. & Wegler, U., 2006. Radiative transfer theory for estimation of the seismic moment., *Geophysical Journal International*, **167**(3), 1363–1372. doi: 10.1111/j.1365-246X.2006.03139.x, Available at: `http://dx.doi.org/10.1111/j.1365-246X.2006.03139.x`, Last accessed on August 4, 2015.

Shen, J., Bai, M., & Shi, G., 2013. A Brief Introduction to the Seismotectonic Map of Xinjiang and Its Neighborhood., *Earthquake Research In China*, **27**(3), 411–426.

Shirokova, E. I., 1974. Detailed study of the stresses and fault planes at earthquake foci of Central Asia., *Izv. Acad. Sci. USSR, Phys. Solid Earth.*, **1**(11), 22–36, in Russian.

Shpilko, G. A., 1914. *The 1911 earthquake in Pamirs and its effects. (Chronological certificate and report on the results of the Pamir squad expedition).* Proceedings of the Imperial Russian Geographical Society., Volume L. Petrograd. 1914., Compiled by the Head of Pamir squad, General Staff, Lieutenant Colonel Shpilko. (In Russian).

Simpson, D. W., Hamburger, M. W., Pavlov, V. D., & Nersesov, I. L., 1981. Tectonics and seismicity of the toktogul reservoir region, kirgizia, ussr, *Journal of Geophysical Research: Solid Earth*, **86**(B1), 345–358. ISSN 2156-2202, doi: 10.1029/JB086iB01p00345, Available at: `http://dx.doi.org/10.1029/JB086iB01p00345`, Last accessed on August 15, 2015.

Sippl, C., Schurr, B., Tympel, J., Angiboust, S., Mechie, J., Yuan, X., Schneider, F., Sobolev, S., Ratschbacher, L., & Haberland, C., 2013a. Deep burial of Asian continental crust beneath the Pamir imaged with local earthquake tomography, *Earth and Planetary Science Letters*, **384**, 165–177. ISSN 0012-821X, doi: http://dx.doi.org/10.1016/j.epsl.2013.10.013, Available at: `http://www.sciencedirect.com/science/article/pii/S0012821X13005761`, Last accessed on September 4, 2015.

Sippl, C., Schurr, B., Yuan, X., Mechie, J., Schneider, F. M., Gadoev, M., Orunbaev, S., Oimahmadov, I., Haberland, C., Abdybachaev, U., Minaev, V., Negmatullaev, S., & Radjabov, N., 2013b. Geometry of the Pamir-Hindu Kush intermediate-depth earthquake zone from local seismic data, *Journal of Geophysical Research: Solid Earth*, **118**(4), 1438–1457. ISSN 2169-9356, doi: 10.1002/jgrb.50128, Available at: `http://dx.doi.org/10.1002/jgrb.50128`, Last accessed on August 20, 2015.

Sippl, C., Ratschbacher, L., Schurr, B., Krumbiegel, C., Rui, H., Pingren, L., & Abdybachaev, U., 2014. The 2008 nura earthquake sequence at the pamir-tian shan collision zone, southern kyrgyzstan, *Tectonics*, **33**(12), 2382–2399. ISSN 1944-9194, doi: 10.1002/2014TC003705, Available at: `http://dx.doi.org/10.1002/2014TC003705`, Last accessed on September 4, 2015.

Sloan, R. A., Jackson, J. A., McKenzie, D., & Priestley, K., 2011. Earthquake depth distributions in central asia, and their relations with lithosphere thickness, shortening and extension, *Geophysical Journal International*, **185**(1), 1–29. ISSN 1365-246X, doi: 10.1111/j.1365-246X.2010.04882.x, Available at: `http://dx.doi.org/10.1111/j.1365-246X.2010.04882.x`.

Sobel, E. R., Schoenbohm, L. M., Chen, J., Thiede, R., Stockli, D. F., Sudo, M., & Strecker, M. R., 2011. Late Miocene–Pliocene deceleration of dextral slip between Pamir and Tarim: Implications for Pamir orogenesis, *Earth and Planetary Science Letters*, **304**(3-4), 369–378. ISSN 0012-821X, doi: http://dx.doi.org/10.1016/j.epsl.2011.02.012.

Stark, C. P., Wolovick, M., & Ekstrom, G., 2012. Glacier surge triggered by massive rock avalanche: Teleseismic and satellite image study of long-runout landslide onto RGO Glacier, Pamirs, *AGU Fall Meeting Abstracts*, p. A7, Provided by the SAO/NASA Astrophysics Data System. Available at: `http://adsabs.harvard.edu/abs/2012AGUFM.C32A..07S`.

Stich, D., Batlló, J., Maciá, R., Teves-Costa, P., & Morales, J., 2005. Moment tensor inversion with single-component historical seismograms: The 1909 Benavente (Portugal) and Lambesc (France) earthquakes, *Geophysical Journal International*, **162**, 850–858.

Storchak, D., Giacomo, D. D., Engdahl, E., Harris, J., Bondár, I., Lee, W., Bormann, P., & Villasenor, A., 2015. The isc-gem global instrumental earthquake catalogue (1900–2009): Introduction, *Physics of the Earth and Planetary Interiors*, **239**, 48 – 63, ISC-GEM Catalogue. ISSN 0031-9201, doi: http://dx.doi.org/10.1016/j.pepi.2014.06.009, Available at: `http://www.sciencedirect.com/science/article/pii/S003192011400154X`.

Storchak, D. A., Di Giacomo, D., Bondár, I., Engdahl, E. R., Harris, J., Lee, W. H. K., Villaseńor, A., & Bormann, P., 2013. Public Release of the ISC–GEM Global Instrumental Earthquake Catalogue (1900–2009), *Seismological Research Letters*, **84**(5), 810–815.

Strecker, M. R., Frisch, W., Hamburger, M. W., Ratschbacher, L., Semiletkin, S., Samoruyev, A., & Sturchio, N., 1995. Quaternary Deformation in the Eastern Pamirs, Tajikistan and Kyrgyzstan, *Tectonics*, **14**(5), 1061–1079. doi: 10.1029/95TC00927.

Stübner, K., Ratschbacher, L., Weise, C., Chow, J., Hofmann, J., Khan, J., Rutte, D., Sperner, B., Pfänder, J. A., Hacker, B. R., Dunkl, I., Tichomirowa, M., Stearns, M. A., & members, P. T., 2013. The giant Shakhdara migmatitic gneiss dome, Pamir, India-Asia collision zone: 2. Timing of dome formation, *Tectonics*, **32**(5), 1404–1431. ISSN 1944-9194, doi: 10.1002/tect.20059, Available at: `http://dx.doi.org/10.1002/tect.20059`, Last accessed on September 4, 2015.

Tapponnier, P. & Molnar, P., 1979. Active faulting and cenozoic tectonics of the Tien Shan, Mongolia, and Baykal Regions, *Journal of Geophysical Research: Solid Earth*, **84**(B7), 3425–3459. ISSN 2156-2202, doi: 10.1029/JB084iB07p03425, Available at: `http://dx.doi.org/10.1029/JB084iB07p03425`, Last accessed on September 10, 2015.

Teshebaeva, K., Sudhaus, H., Echtler, H., Schurr, B., & Roessner, S., 2014. Strain partitioning at the eastern Pamir-Alai revealed through SAR data analysis of the 2008 Nura earthquake, *Geophysical Journal International*. doi: 10.1093/gji/ggu158, Available at: `http://gji.oxfordjournals.org/content/early/2014/06/03/gji.ggu158.abstract`.

Tibaldi, A., 1998. Effects of topography on surface fault geometry and kinematics: examples from the Alps, Italy and Tien-Shan, Kazakstan., *Geomorphology*, **24**(2), 225–243.

Tibaldi, A., Graziotto, E., Forcella, F., & Gapich, V. H., 1997. Morphotectonic indicators of Holocene faulting in central Tien Shan, Kazakstan, and geodynamic implications., *Journal of Geodynamics*, **23**(1), 23–45, Provided by the SAO/NASA Astrophysics Data System. doi: 10.1016/S0264-3707(96)00021-X.

USGS, 2014a. *Earthquake Archive Search and URL Builder*. NEIC, National Earthquake Information Center, U.S. Geological Survey, National Center, USA, http:// earthquake.usgs.gov/earthquakes/search/.

USGS, 2014b. *M7.7 - 61km NNE of Awaran, Pakistan (BETA)*. U.S. Geological Survey, National Earthquake Information Center, Available at: `http://comcat.cr.usgs.gov/earthquakes/eventpage/usb000jyiv`, Last accessed on November 9, 2014.

USGS, 2014c. *Magnitude 7.9 - EASTERN SICHUAN, CHINA*. U.S. Geological Survey, National Earthquake Information Center, Available at: `http://earthquake.usgs.gov/earthquakes/eqinthenews/2008/us2008ryan`, Last accessed on November 9, 2014.

Vinnik, L., Reigber, C., Aleshin, I., Kosarev, G., Kaban, M., Oreshin, S., & Roecker, S., 2004. Receiver function tomography of the Central Tien Shan, *Earth and Planetary Science Letters*, **225/1-2**, 131 – 146.

Vinnik, L. P., Roecker, S., Kosarev, G. L., Oreshin, S. I., & Koulakov, I. Y., 2002. Crustal structure and dynamics of the tien shan, *Geophysical Research Letters*, **29**(22), 4–1–4–4, 2047. ISSN 1944-8007, doi: 10.1029/2002GL015531, Available at: `http://dx.doi.org/10.1029/2002GL015531`, Last accessed on August 4, 2015.

Voznesenskiy, A. V., 1904. List of earthquake observations by Irkutsk Magnetic Meteorological Observatory, In *Proceedings of the East-Siberian department of the Imperial Russian Geographical Society published by Editing Committee Volume XXXIV, 1903, N1*, pp. 11–18, ed. Kolmin, N. Steam typo-lithography of Makushin P. and Posohin V., Printed upon request of the East Siberian department of the Imperial Russian Geographical Society under the supervision of the editing committee, In Russian and French, the publication was access as a scanned copy via Scientific library of the Irkutsk public University. Available at: `http://library.isu.ru/`.

Wadsworth, J., 1942. The Wiechert Vertical Seismograph: An Improved Design, *Geophysical Journal International*, **5**, 48–53. ISSN 1365-246X, doi: 10.1111/j.1365-246X.1942.tb00445.x, Available at: `http://dx.doi.org/10.1111/j.1365-246X.1942.tb00445.x`.

Wang, R., 1999. A simple orthonormalization method for stable and efficient computation of green's functions, *Bulletin of the Seismological Society of America*, **89**(3), 733–741. Available at: `http://www.bssaonline.org/content/89/3/733.abstract`, Last accessed on September 28, 2015.

Wiechert, E., 1903. Theory of automatic seismographs. The Royal Society of Sciences in Göttingen., 128, Weidmannsche bookstore, Berlin., in German.

Wiechert, E., 1904. An astatic higher sensitivity pendulum for mechanical registration of earthquakes, *Beiträge zur Geophysik*, **VI**, 435–450, in German.

Wielandt, E., 2002. Chapter 18: Seismometry., In *International Handbook of Earthquake and Engineering Seismology.*, vol. 81, Part A of **International Geophysics**, pp. 283 – 304, eds. William H.K. Lee, Hiroo Kanamori, P. C. J. & Kisslinger, C. Academic Press. doi: http://dx.doi.org/10.1016/S0074-6142(02)80221-2, Available at: `http://www.sciencedirect.com/science/article/pii/S0074614202802212`.

Wilhelmson, P. M., 1947. *Kemin-Chu earthquake, 21 June 1938.*, Publisher Academy of Sciences KazSSR, Alma-Ata, p. 39, in Russian.

Wood, H. O., 1921. *Bulletin Of The National Research Council., A List of Seismologic Stations of the World.*, The National Research Council of The National Academy of Sciences, Washington D.C , Part 7, No. 15.

Xu, Y., Roecker, S. W., Wei, R., Zhang, W., & Wei, B., 2006. Analysis of seismic activity in the crust from earthquake relocation in the central Tien Shan., *Bulletin of the Seismological Society of America*, **96**(2), 737–744. doi: 10.1785/0120030220, Available at: `http://www.bssaonline.org/content/96/2/737.abstract`, Last accessed on August 4, 2015.

Yagi, Y., Naoki, N., & Kasahara, A., 2012. Source process of the 12 may 2008 wenchuan, china, earthquake determined by waveform inversion of teleseismic body waves with a data covariance matrix, *Earth, Planets and Space*, **64**.

Yamada, M., Kumagai, H., Matsushi, Y., & Matsuzawa, T., 2013. Dynamic landslide processes revealed by broadband seismic records, *Geophysical Research Letters*, **40**(12), 2998–3002. ISSN 1944-8007, doi: 10.1002/grl.50437, Available at: `http://dx.doi.org/10.1002/grl.50437`.

Zhao, J., Moretti, L., Mangeney, A., Stutzmann, E., Kanamori, H., Capdeville, Y., Calder, E. S., Hibert, C., Smith, P. J., Cole, P., & LeFriant, A., 2015. Model Space Exploration for Determining Landslide Source History from Long-Period Seismic Data, *Pure and Applied Geophysics*, **172**(2), 389–413.

Zhao, R.-b., Li, J., & Shen, J., 2000. The preliminary study on active faults and paleo-earthquakes in the north fringe of Kashi depression, *Acta Seismologica Sinica*, **13**(3), 351–355. ISSN 1000-9116, doi: 10.1007/s11589-000-0045-4, Available at: `http://dx.doi.org/10.1007/s11589-000-0045-4`, Last accessed on September 4, 2015.

Zhao, R.-b., Shen, J., & Li, J., 2001. Preliminary study on the deformation features and seismogenic model of the 1902 Artux, Xinjiang earthquake of $M_s = 8\frac{1}{4}$., *Journal of Seismology and Geology*, **23**(4), 493–500, in Chinese.

ZiKaWei, Bull., 1915. *Bulletin Observations, Year 1911, Seismology, Chang-Hai.* Magnetic, Meteorological and Seismological Observatory Zi-Ka-Wei (China), Zi-Ka-Wei (China), in French.

Zubovich, A. V., Wang, X.-q., Scherba, Y. G., Schelochkov, G. G., Reilinger, R., Reigber, C., Mosienko, O. I., Molnar, P., Michajljow, W., Makarov, V. I., Li, J., Kuzikov, S. I., Herring, T. A., Hamburger, M. W., Hager, B. H., Dang, Y.-m., Bragin, V. D., & Beisenbaev, R. T., 2010. GPS velocity field for the Tien Shan and surrounding regions, *Tectonics*, **29**(6), TC6014(1–23). ISSN 1944-9194, doi: 10.1029/2010TC002772, Available at: `http://dx.doi.org/10.1029/2010TC002772`, Last accessed on August 4, 2015.